Effects on the free surface of a turbulent flow

Pablo Gutiérrez-Matus

Thèse de Doctorat de l'École Polytechnique

Spécialité: *Physique*

présentée par

Pablo Gutiérrez

pour l'obtention du grade de

Docteur de L'École Polytechnique

Effets induits en surface par un écoulement turbulent

*

Thèse soutenue publiquement le **12 septembre 2013** devant le jury composé de:

M.	Sébastien	Aumaître	CEA-Saclay	(Co-directeur de thèse)
M.	Mickaël	Bourgoin	LEGI, Grenoble	(Rapporteur)
M.	Olivier	Cadot	ENSTA	(Rapporteur)
M.	Christophe	Clanet	École Polytechnique	(Examinateur)
M.	François	Daviaud	CEA-Saclay	(Directeur de thèse)
M.	Willem	van de Water	Eindhoven Univ. Tech.	(Examinateur)

Laboratoire **SPHYNX**,
Service de Physique de l'État Condensé, IRAMIS, DSM
CEA Saclay

Acknowledgments / Remerciements / Agradecimientos

I first acknowledge the institutions that funded my thesis work: CONICYT (from the Chilean government); the Embassy of France in Chile; Triangle de la Physique; and ANR, under the grant TURBULON.

Then I thanks Olivier Cadot and Mickaël Bourgoin for referring the manuscript. I really appreciated the scientific discussion we had during the thesis defense, together with Christophe Clanet and Willem van de Water. I thanks all of you again for the attention you paid to my work and for all your suggestions to improve the manuscript.

I thanks Anne Tanguy and François Ladieu for the very useful comment you gave me to improve the thesis presentation.

I thanks François Daviaud for directing the thesis, where you essentially encouraged us[1] to freely follow the way our research took... although suggesting me a very reasonable schedule which, nonetheless, I had never respected. So I thank you also for your patience, and for the valuable scientific remarks you gave us during this period.

I thanks Sébastien for his enormous generosity in time, energy and ideas. In my career, I expect to keep your scientific –and particularly experimental– rigor and criticism, together with your passion for simple arguments and analyses. On the other hand, I will always remember how kindly your welcomed us[2] during our stay in France.

As the main experiment was conducted at SPEC, this work benefited from the fundamental support of Vincent Padilla, Cecile Wiertel-Gasquet, Patrick Meininger, Dominique Duet and Jean–Claude Tack; and from discussions with Jean Boisson, Marco Bonetti, Bérengère Dubrule, Eric Herbert and Gilbert Zalcser.

I also appreciated more circumstantial discussions –especially during visits to our lab– that gave us new ideas or confirmed our intuitions. Without being exhaustive, I can mention Jean Christophe Geminard, Romain Monchaux, Frederic Moisy, Michael Berhanu, Rodrigo Soto, Claudio Falcón and Leonardo Gordillo.

I thanks the –not already mentioned– members of the TURBULON collaboration, for instance for the stimulating discussions we had about wave turbulence: Luc Deike, Timothée Jamin, Benjamin Miquel, Guillaume Ducrozet, Eric Falcon, Stéphan Fauve, Claude Laroche, François Petrelis, Benoit Semin... and very specially to Félicien Bonnefoy, who received us at Nantes, did most of the job, and still gave us nice addresses to go for diner.

I thanks the "stagier(e)s" who contributed –directly or not– to our experiment: Alexis Soulier, Aurelie Heyries, Daphne Heyries, Ippei Joillot, Mooez Ferjani and Romain Graziani.

I acknowledge the people that kindly allowed me (and sometimes the whole scientific community) to use their MATLAB codes. I can mention Rodrigo Hernandez, Raphaël Candelier, Eric Herbert, Nicholas Ouellette, Daniel Blair, Eric Dufresne and Frederic Moisy.

I also thanks Nicolas Mujica, who kindly hosted me in the LMFE (Chile) to work in a granular project.

Je tiens à remercier Eric Vincent pour m'avoir accueilli au sein du Service de Physique de l'État Condensé (SPEC), ainsi que Olivier Dauchot comme le chef du Groupe Instabilités et Turbulence (GIT) à l'époque. J'apprécie beaucoup les efforts faits –avec Sébastien– pour me trouver un statut compatible avec mon absence d'employeur (difficulté supplémentaire au CEA). Et à cet propos, je remercie la patience démontré par le GIT qu'en solidarité avec moi est allait pendant des mois à cette cantine dégueulasse qui est la 2 (que d'ailleurs je ne trouve pas aussi

[1] us = me and Sébastien.

[2] us = me, Claudia & Simón.

mal, mais voila pourquoi Marco ne mange plus jamais à la cantine). Ensuite, je remercie aussi à François (D.) qui, après Eric comme chef du SPEC, prend le soin de gérer le labo dans ces temps adverses. Egalement je remercie François (L.) qui s'occupe actuellement du SPHYNX, et dont j'apprécie énormément sa manière de faire sans trop de bruit (sauf pour nous sortir des blagues millénaires de Coluche). Je remercie également les personnes du SPEC que m'ont toujours aide avec des points techniques ou administratives: Corinne Kopec–Coelho, Nathalie Royer, Pierre Janvier et Nadine Genand–Riondet.

En remercient tout particulièrement Mme. Lemarechal et Mme. Ferret, je remercie aussi l'ensemble du personnel de l'École doctorale de l'X, pour m'avoir facilité les taches administratives usuelles, ainsi qu'avoir allégé les lourds dossiers pour obtenir ou renouveler titres de séjours, récépissés, etc. De la même façon, je remercie Science–Accueil, pour m'avoir orienté à mon arrivé en France.

J'ai adoré l'ambiance du groupe (GIT–puis–SPHYNX) et comment chacun y contribue à sa façon. Je remercie vous tous. En plus de la physique, ici j'ai appris des choses que l'on ne trouverai jamais sur un programme d'études: comment bien tasser le café; ou à apprécier la bonne culture française du genre *Les Inconnues*, ou les lectures en deuxième et troisième dégrée d'*Asterix*. Je remercie aussi Elisabeth Bouchaud, avec qui j'ai eu le plaisir de partager le bureau pendant deux ans.

Je remercie aux thésards du groupe: ceux avec qui j'ai commencé la thèse: Corentin Coulais, Corentin Herbert et Boudoin Saint–Yves; ceux avec qui je l'ai finit: Brice Saint–Michel, Simon Thalabard et Sandrine Ngo; ainsi que ceux avec qui j'ai partagé pendant moins de temps: Jullien Deisegne, Gilles Collet et Martin Mihelich. J'ai des excellents souvenirs du temps passé au labo, où dans des confs dans des endroits lointains, où même en attendant le RER B, qu'arrive dans 02 minutes.

Et si bien on ne le considère pas assez sur les papiers, cette thèse aurais marché beaucoup moins bien sans l'aide de Vincent. Je remercie énormément le talent que tu as démontré dans la conception des montages expérimentaux, et encore plus pour ton amitié et générosité.

Antes de continuar, debo confesar el alivio que me produce el poder escribir mal sin que me de vergüenza (puede existir otra barrera idiomática?).

Dicho esto, quiero agradecer a los amigos y familiares que se animaron a cruzar el charco y nos visitaron. Recuerdo particularmente a Juan Carlos y a Pablo Riquelme.

Agradezco a la comunidad chileno/latina instalada en Francia y alrededores, por estar ahí recordando el terruño. Puedo mencionar a Miguel Trejo, Suomi Ponce, Leonardo Gordillo, Valeria Sequeida, Flo Muñoz, Cristobal Arratia, Romina Bossa–Abiven, Yves Abiven, Francisco Martinez, Victor Romero, Belén Rojas, Pablo Rojas, Eduardo Rojas (ojo que no son hermanos), Marcelo Gatica, Mirla Gatica (aquí si) y Daniela Peñailillo.

Agradezco enormemente a mi familia –a mis padres y a mis hermanas– por su apoyo incondicional, tanto desde la lejanía como desde la cercanía (aunque en el fondo yo se que ustedes hubieran preferido que yo siguiera en Francia... pero no, yo retorno al país natal). Agradezco también a Claudia por su apoyo.

Dedico este trabajo a Simón Gutiérrez, con quien comparto el gusto de jugar con agua. Espero con ansias nuestro reencuentro, y que podamos ir a recorrer juntos los ríos, lagos y mares del sur de Chile.

Contents

Chapter 1

General Introduction

Most of the earth's crust corresponds to water in contact with air: oceans, lakes and rivers. Therefore, this interface plays a major role in the mass, momentum an heat transfers within the atmosphere. On small scales, mass and heat transfer is mediated by turbulence, specially by wave breaking [1; 8]. When waves break, they drive air allowing exchanges of oxygen and carbon dioxide, which are crucial for aquatic life. On larger scales, the amounts of gas exchanged in this process have significant effects on weather and, perhaps, on climate[1].

In natural environments, turbulence is also related with subsurface currents, with the influence of bottom topography and with the interaction with solid structures or boundaries. One of these situations –in which turbulence is not created at the surface– is illustrated in figure 1.1–top: it is a picture of a vortex detached from the rear of a boat traveling in otherwise calm water. But aside the vortex, one may also notice: (i) in the bottom–right corner, closer to the boat, there are some very irregular deformation zones *separated* by irregular lines. They are characteristic of upwelling and downwelling motion, produced here by the rapid motion of the boat's impellers. (ii) On the left of the vortex, there are some gravity waves produced by the natural motion of the boat, which seem to be perturbed by the vortex indeed. These different features are typical surface expressions of a turbulent flow.

This picture also recall another particularity of the air–water interface, very well stated by D. H. Peregrine when he wrote about his *fascination of fluid mechanics* [7]:

> Our perception of the world is dominated by our vision. The commonest fluids, air and water, are transparent, so we most readily see the interface between them. The air–water interfaces of clouds, and rain, of streams, rivers, lakes and the seas are vital elements in most of the natural scenes we enjoy.

Beyond this poetic view of the air–water interface, it comes a more concrete question: What is the relation between the deformation visible on the surface, and the turbulence

[1] It is very difficult to state the contribution of turbulence in such a global and slowly evolving variable as climate. It is because much different physico-chemical processes are involved. However, turbulence has undeniable influence on some of them, for instance: on the air-water fluxes of carbon dioxide (see [4; 11]); on aquatic life (both because water aeration and nutrients' transport); and on the fraction of reflected solar radiation (dependent on the air–water interface roughness; see [2]).

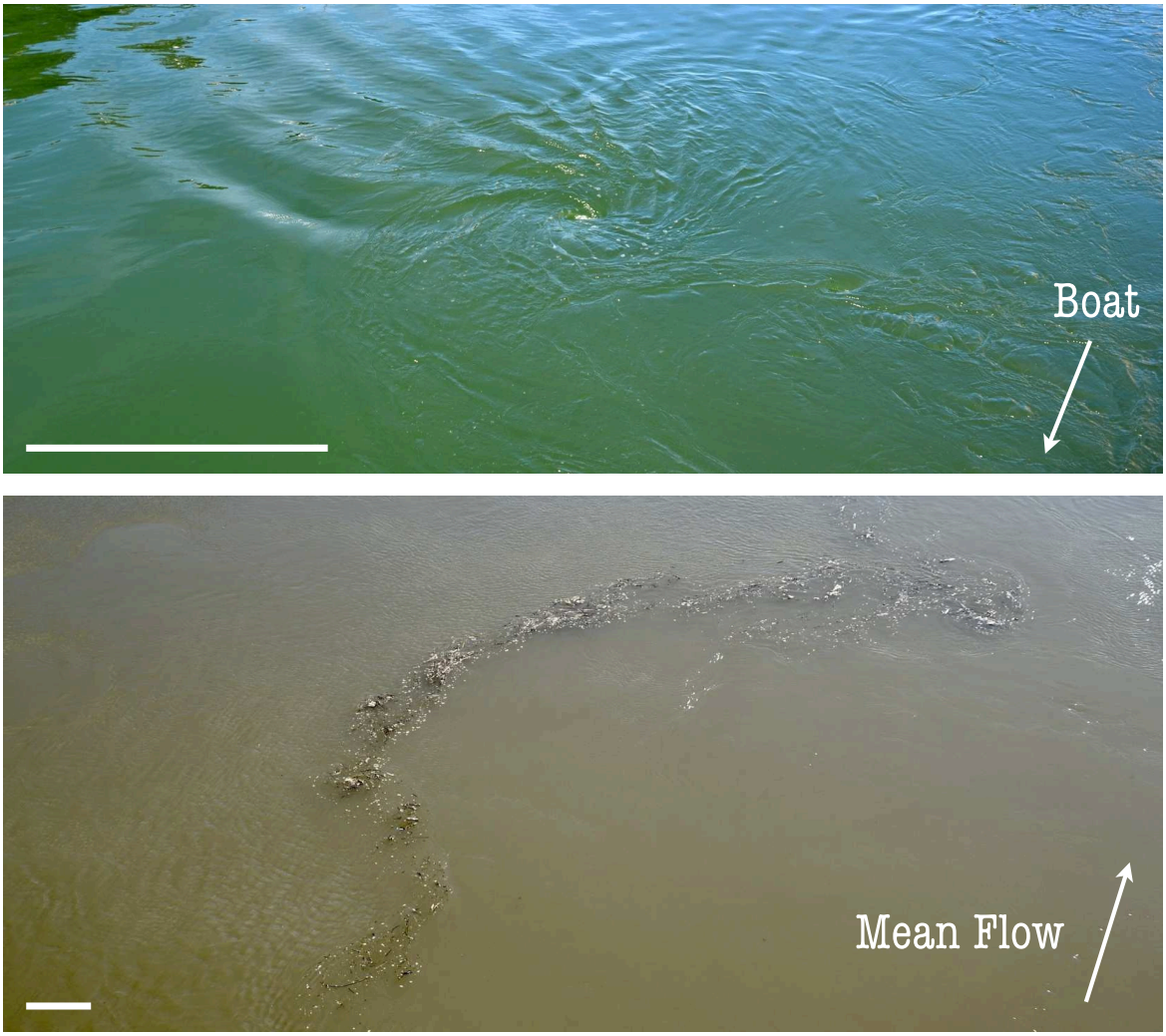

Figure 1.1: Surface manifestations of turbulence. Top: detachment of a vortex at the rear of a boat in a calm river (Saint–Martin channel in Paris). Picture taken from the boat. Bottom: rotten wood (+ some foam) is advected by the current of Saone river. Picture taken from the *Pont de la Feuillée* in Lyon. White bars on the right correspond to a very rough estimates of 1 meter.

which is beneath? Indeed, this question motivates active research in oceanography [3; 10; 12]. Nowadays satellites provide frequent, global and well resolved observations of surface variables, although the equally relevant sub-surface turbulence is much more elusive.

Turbulence plays a major role in another oceanic–environmental subject: It strongly affect the transport of nutrients and pollutants [8]. This is illustrated by figure 1.1–bottom: a picture of the Saone river taken after a period on intense rains and winds. It resulted in an increased water flux (in the direction indicated by the arrow), carrying important amounts of rotten wood. In this particular situation, one can observe that wood (together with some foam) is very concentrated in a particular region of the flow,

that may be related with a stronger vorticity[2]. The transport of organic matter by flows and turbulence is relevant to aquatic life, as it rules the concentration and distribution of nutrients for zones irrigated by a river, for instance. On the other hand, long–term–persistent inorganic matter is also transported by fluid flows. Indeed, winds and large scale oceanic currents induce an enormous cumulation of plastic litters [9], with ecological consequences not completely evaluated –but already not encouraging–. Therefore, more knowledge about the physical processes involved on turbulent transport of floating particles is desirable in order to develop strategies to deal with such pollution.

The goal of this manuscript is to present our experimental study on *surface manifestations of a turbulent flow*.[3] In particular it concerns (i) the statistics of the surface deformation, produced by turbulent motion, (ii) the effect of turbulence on externally excited surface waves, and (iii) the dynamics of particles floating on the surface of a turbulent flow. It is organized as follows:

In the next chapter we develop some connections between sound and free surface flows: one may think the air–water interface (or any other interface) as an elastic sheet that experience expansions and compressions as a consequence of fluid motion. Thus, the interface is compressible even if the underlying fluid is incompressible.

Still is chapter 2, we then give a proper introduction to turbulence, as it is the context of this thesis. Particular attention is given to the relation between turbulence and free surface flows.

In chapter three, we present the experimental setup that makes this study possible. After giving the physical parameters involved in the experiment, we discuss the dynamical regimes to be expected on the light of dimensionless numbers. Finally we present the measurement techniques, applied in order to access the velocity field and the deformation of the surface.

The first chapter devoted to experimental results is chapter 4, in which we discuss the different regimes available to our setup, together with their main properties.

In chapter 5, we focus on the possibility of wave generation by a turbulent flow, where the velocity field is primarily horizontal. There is a prediction of spontaneous generation of sound by turbulent motion [5; 6], which by analogy was extended to horizontal flows in shallow water. Therefore it is pertinent to ask the question about the possibility to observe such a wave generation in our finite depth experimental configuration. With this question in mind, we study in detail the surface deformation that is produced as a consequence of the turbulent motion in our experiment.

A strongly related problem is addressed in chapter 6. It concerns the influence of turbulence on wave propagation. Here again the problem was first considered in the acoustical context, with the question about how sound propagates in heterogeneous media. Thus, this time we mechanically excite monochromatic waves on the surface of our liquid, and we study how these waves are affected by the turbulent background.

Then, in chapter 7 we focus our attention on the dynamics of particles floating on the

[2]The picture make little justice to such dynamical process, contrary to direct observation where the concentration on vortices appeared clearly. A representative movie is available upon request.

[3]I borrow this sentence from the title of an article by M. S. Longuet–Higgins (JFM, 1996), although it does not have a direct connexion with this manuscript.

free surface of a turbulent flow. As light particles are constrained to rest at the surface of the fluid, they experience the motions of the surface as an effective compressibility. After observing and characterizing the consequences of compressibility on particles, we discuss the possible sources of them.

Finally, in last chapter we give a summary of our results, together with some general conclusions. Then, future research directions are proposed.

1.1 Bibliography

[1] Banner, M. L., and Peregrine, D. H. Wave breaking in deep water. *Annual Review of Fluid Mechanics 25* (1993), 373–397.

[2] Gill, A. E. *Atmosphere-Ocean Dynamics*. Academic Press, 1982.

[3] Isern–Fontanet, J., Lapeyre, G., Klein, P., Chapron, B., and Hecht, M. W. Three-dimensional reconstruction of oceanic mesoscale currents from surface information. *Journal of Geophysical Research 113* (2008), C09005.

[4] Jähne, B., and Haussecker, H. Air-water gas exchange. *Annual Review of Fluid Mechanics 30* (1998), 443–468.

[5] Lighthill, M. J. On sound generated aerodynamically. I. General theory. *Proceedings of the Royal Society A 211* (1952), 564–587.

[6] Lighthill, M. J. On sound generated aerodynamically. II. Turbulence as a Source of Sound. *Proceedings of the Royal Society A 222* (1954), 1–32.

[7] Peregrine, D. H. The fascination of fluid mechanics. *Journal of Fluid Mechanics 106* (1981), 59–80.

[8] Thorpe, S. A. *An Introduction to Ocean Turbulence*. Cambridge University Press, 2007.

[9] U. S. Environmental Protection Agency. Marine Debris in the North Pacific. 2011.

[10] Wang, J., Flierl, G. R., LaCasce, J. H., McClean, J. L., and Mahadevan, A. Reconstructing the Ocean's Interior from Surface Data. *Journal of Physical Oceanography 43* (2013), 1611–1626.

[11] Zappa, C. J., Raymond, P. A., Terray, E. A., and McGillis, W. R. Variation in surface turbulence and the gas transfer velocity over a tidal cycle in a macrotidal estuary. *Estuaries 26* (2003), 1401–1415.

[12] Zhang, L., and Sun, C. A geostrophic empirical mode based on altimetric sea surface height. *Science China, Earth Sciences 55* (2012), 1193–1205.

Chapter 2

Turbulence and free surface flows

In this chapter we give a more precise introduction to turbulent flows with free surface. We start by developing an analogy between free surface flows and compressible flows (section 2.1). As the analogy has no need of turbulence concepts, we keep those ones to subsequents sections.

In section 2.2, we give the set of equations valid for incompressible viscous fluids, and we recall the ideas of classical–homogeneous–isotropic turbulence for three dimensional flows. This context represent the basis for any turbulence theory, although some of they assumptions have to be removed when considering particular applications. Therefore, in section 2.3 we move to turbulence in two dimensional flows as –in principle– it is more pertinent to our experiments. However, the limitations of their concepts are addressed.

Then, we return to free surface flows. After giving the mathematical formulation (Navier Stokes equations + boundary conditions), we consider a qualitative description of the phenomenology observed in turbulent flows with free surface. Finally, we consider some attempts of giving quantitative predictions for turbulent free surface flows, in the sense of the well known counterparts of classical turbulence.

2.1 The compressible free surface of an incompressible fluid flow

As it will be shown by different experimental results, one can understand the phenomenology of a free–surface–turbulent–flow as an effective compressibility on its surface, even if the fluid under study is incompressible. In this situation, it is tempting to develop some analogies with compressible flows. To do so, we consider now some features of compressible fluids.

2.1.1 Sound

Sound is perhaps the most clear manifestation of compressibility. It consist in pressure variations that propagate through a medium with a speed c. For liquids and gases, one can actually derive the wave equation [1; 32] from both the momentum conservation equation

(Euler equation):

$$\frac{D\mathbf{u}}{Dt} = \frac{\partial \mathbf{u}}{\partial t} + (\mathbf{u}\cdot\nabla)\,\mathbf{u} = -\frac{\nabla p}{\rho}, \tag{2.1}$$

and mass conservation equation

$$\frac{D\rho}{Dt} + \rho\nabla\cdot\mathbf{u} = \frac{\partial \rho}{\partial t} + \nabla(\rho\mathbf{u}) = 0, \tag{2.2}$$

where $\mathbf{u} = (u_1, u_2, u_3)$ is the velocity, $D/Dt = \partial/\partial t + \mathbf{u}\cdot\nabla$ is the material derivative, p is the pressure and ρ the fluid density. From last equation (the expression on the left), one can see that any change in fluid density (and consequently on its volume) is compensated by the term $\nabla\cdot\mathbf{u}$. Thus, this term can be understood as the fluid compressibility.

We consider a small perturbation $(\mathbf{u}, \rho, p)$ from the state of zero velocity and homogeneous density ρ_0 and pressure p_0. For irrotational flows, one has $\mathbf{u} = \nabla\phi$, with ϕ the so-called velocity potential. The linearized version of equation (2.1) gives a relation between the pressure and the potential $\rho_0\partial\phi/\partial t = p_0 - p$ and the linearized version of (2.2) connects density to the potential $\partial\rho/\partial t + \rho_0\nabla^2\phi = 0$.

By assuming a relation between changes of pressure and density [32] that links them by a dependence $p = p(\rho)$, and linearizing pressure around $\rho = \rho_0$, it can be obtained that $\partial p/\partial t = p'(\rho_0)\partial\rho/\partial t$. The natural consequence of this relation is an equation for ϕ,

$$\frac{\partial^2\phi}{\partial t^2} = c^2\nabla^2\phi, \tag{2.3}$$

that is in fact the well known wave equation. Here $c^2 = \partial p/\partial\rho|_{\rho_0}$ is the velocity of wave propagation, or sound velocity. This general expression already gives useful information: for a given variation of pressure, the smaller is the variation of density (i.e. small compressibility), the larger is the sound velocity. From thermodynamic arguments on the other hand [32], one has $c^2 = \gamma_h RT$ for perfect gases, where R is the gas constant, T is temperature and γ_h the ratio of specific heats, close to 1.4 for air at typical pressure and temperature conditions. Therefore, sound velocity depends only on the equilibrium conditions of the system: all perturbations travel with the same velocity c. In other words, sound waves are non–dispersive, in opposition (for instance) to gravity waves in the surface of a fluid, where a dependence on the wave-number explicitly appears.

In our construction, we neglected the contribution of gravity *a priori*. This is because it appears to be unimportant for wavelengths smaller than c^2/g [32], corresponding approximately to 12 km in air, and 200 km in water. These wavelengths justify the approximation, as they are much larger that ordinary sound waves.

As sound velocity is characteristic of the medium and usually constant, it is useful to consider motion velocities in comparison to sound velocity, by defining the Mach number

$$M = \frac{U}{c},$$

where U is the velocity of the corresponding motion in the medium. Sound velocity is given by the compressibility of the medium, thus, the more U approaches c, the more important are the effect of compressibility in the motion. When $U \ll c$, on the contrary, compressibility effects are negligible.

2.1.2 A formal analogy in incompressible fluids: *sound* waves in shallow water

For all practical situations water can be assumed as incompressible, given the enormous value of sound velocity on it[1]. In spite of this, one can establish a formal analogy with sound in the shallow water limit. It holds when the height of the fluid $h(x, y, t)$ is very small in comparison to a characteristic wavelength λ.

Under this condition, the total vertical acceleration of the surface (Du_3/Dt) is negligible compared to gravity [1]. Thus the Euler equations become

$$\frac{Du_1}{Dt} = \frac{\partial u_1}{\partial t} + u_1\frac{\partial u_1}{\partial x} + u_2\frac{\partial u_1}{\partial y} + u_3\frac{\partial u_1}{\partial z} = -\frac{1}{\rho}\frac{\partial p}{\partial x}, \tag{2.4}$$

$$\frac{Du_2}{Dt} = \frac{\partial u_2}{\partial t} + u_1\frac{\partial u_2}{\partial x} + u_2\frac{\partial u_2}{\partial y} + u_3\frac{\partial u_2}{\partial z} = -\frac{1}{\rho}\frac{\partial p}{\partial y} \tag{2.5}$$

and

$$p = p_0 + \rho g(h - z), \tag{2.6}$$

from which we can state that the r. h. s. terms on (2.4) and (2.5) do not depend on z:

$$\frac{Du_1}{Dt} = -g\frac{\partial h}{\partial x}, \qquad \frac{Du_2}{Dt} = -g\frac{\partial h}{\partial y}. \tag{2.7}$$

Therefore, the rate of change of u_1 and u_2 following fluid particles is also independent on z. In other words the initial dependence is conserved in time.

An usual hypothesis to derive shallow water equations is to consider u_1 and u_2 as being initially independent of z. Thus, the terms $\partial u_1/\partial z$ and $\partial u_2/\partial z$ become zero. Equations (2.7) reduce to:

$$\frac{\partial \mathbf{u}_\perp}{\partial t} + (\mathbf{u}_\perp \cdot \nabla_\perp)\mathbf{u}_\perp = -g\nabla_\perp h, \tag{2.8}$$

with $\mathbf{u}_\perp = (u_1, u_2)$ and $\nabla_\perp = (\partial/\partial x, \partial/\partial y)$.

On the other hand, one has incompressibility

$$\nabla \cdot \mathbf{u} = 0, \tag{2.9}$$

that can be integrated over the height

$$\begin{aligned} 0 &= \int_0^h \left\{ \frac{\partial u_1}{\partial x} + \frac{\partial u_2}{\partial y} + \frac{\partial u_3}{\partial z} \right\} dz \\ &= \frac{\partial}{\partial x}\int_0^h u_1 dz + u_1\frac{\partial h}{\partial x} + \frac{\partial}{\partial y}\int_0^h u_2 dz + u_2\frac{\partial h}{\partial y} + u_3\Big|_h , \end{aligned}$$

where we took into account that $h = h(x, y)$ on the limits of the integral, and we assumed a flat bottom where velocities vanish. We can complement this equation by noticing that

[1]Sound velocity in water is $c \sim 1400$ m/s and $c = 340$ m/s in air [32].

$u_3|_h$ is given by the so-called kinematic boundary condition, valid on the free surface (to be considered in section 2.4),

$$\frac{\partial h}{\partial t} + u_1 \frac{\partial h}{\partial x} + u_2 \frac{\partial h}{\partial y} = u_3,$$

to obtain

$$\frac{\partial}{\partial x}\int_0^h u_1 dz + \frac{\partial}{\partial y}\int_0^h u_2 dz + \frac{\partial h}{\partial t} = \nabla_\perp \cdot \int_0^h \mathbf{u}_\perp dz + \frac{\partial h}{\partial t} = 0. \tag{2.10}$$

As we assumed earlier that u_1 and u_2 are independent of z, we obtain

$$\frac{\partial h}{\partial t} + \nabla_\perp (h\mathbf{u}_\perp) = 0. \tag{2.11}$$

Equations (2.8) and (2.11) are the shallow water equations. They can be rewritten by considering variables integrated over the fluid depth, $\tilde{p} = \rho g h^2/2$ and $\tilde{\rho} = \rho h$ [30], as:

$$\frac{\partial \mathbf{u}_\perp}{\partial t} + (\mathbf{u}_\perp \cdot \nabla_\perp)\mathbf{u}_\perp = -\frac{\nabla_\perp \tilde{p}}{\tilde{\rho}} \tag{2.12}$$

and

$$\frac{\partial \tilde{\rho}}{\partial t} + \nabla_\perp (\tilde{\rho}\mathbf{u}_\perp) = 0. \tag{2.13}$$

They have the very same structure of equations (2.1) and (2.2), although we are restricted here to the plane (x, y). *Sound* waves carried by the *pressure* $\tilde{p}$ propagate in the bidimensional plane producing variations of the *density* $\tilde{\rho}$. Expansions and compressions of $\tilde{\rho}$ can only represent variations of the local height h.

Another remarkable property of waves in shallow water is its propagation velocity. As for sound waves that are governed for equivalent equations, we expect to observe non-dispersive waves here again. This is indeed the case as $c^2 = \partial\tilde{p}/\partial\tilde{\rho} = g\tilde{\rho}/\rho = gh$. For a fluid layer of 0.5 cm thickness, the sound velocity is 22 cm/s, much smaller than sound speed in water. The Mach number $U/\sqrt{gh}$ in this context is called the Froude number[2], which is usually not small.

As for sound, complex phenomena are expected when M is or order 1. Over reflexion of waves when they encounter a shear layer seems possible both for sound [36; 46] and for shallow water [21]. In shallow water it was indeed observed experimentally [22], although it appears to be difficult to keep the shallow water limit and other instabilities make difficult the interpretation of results.

2.1.3 More analogies in incompressible fluids: Free surface flows

Shallow water equations hold for very specific conditions, not always easily reached in experiments. However, mass conservation generally holds and it allows to discuss more analogies with sound, although a true relation does not really exist. To discuss those informal analogies is indeed the aim of this section and, to some extent, of this thesis.

[2]In what follows (starting from section 2.4), we rather use a definition of the Froude number related to U^2/gh, as it comes more naturally from free surface boundary conditions.

2.1.3.1 Surface deformation at the free surface

Although shallow water equations (2.8) and (2.11) were obtained under suitable approximations (and with the assumption of an inviscid fluid), equation (2.10) is more general. It comes from the integration of incompressibility condition, subjected to the kinematic boundary condition. Thus it holds for liquids of any depth, regardless of fluid viscosity and the presence of surface tension. By considering the mean velocity over the height $\overline{u} = (\int_0^h u\, dz)/h$, one can express equation (2.10) as,

$$\nabla_\perp \cdot \overline{\mathbf{u}_\perp} = -\frac{1}{h}\left(\frac{\partial h}{\partial t} + (\overline{\mathbf{u}_\perp} \cdot \nabla_\perp)h\right). \tag{2.14}$$

Because of vertical integration, only horizontal compressibility has a meaning. Thus it could be relevant to our experiment, where the flow is expected to be primarily horizontal. As for shallow water, the more general equation (2.14) indicates the connection between height fluctuations and horizontal compression/expansion. The spatiotemporal evolution of h depends on the stabilizing influence of gravity and surface tension.

One way to evaluate the effects of compressibility is by looking the dynamics of floating objects.

Some years ago, it was observed [19; 33] that particles cluster in the presence of standing waves induced by the Faraday instability. It was argued that the mechanism responsible for clustering was surface tension, coupled to the spatial modulation of wave amplitudes. One can interpret the argument as follows: Standing waves are steeper at nodes than at antinodes. On the other hand, as the motion is periodic, capillary forces can only depend on the absolute value of local steepness [33]. Consequently, the force is inhomogeneous and its spatial distribution is defined by the wave pattern. At the same time, it rules the long–time motion of particles. Few comments can be made at this point:

- The analysis is valid only for stationary wave patterns, in which long–time effects could be observed. That makes the particularity of the mechanism. Indeed, it also appears to be dependent on particles filling fraction [47].
- It seems clear, anyway, that an heterogenous force induce an effective compressibility on particles. However, as the force is fixed by the wave pattern, there is no restitution mechanism allowing the complete analogy with sound.

A related, statistical analysis was proposed by Herterich & Hasselmann in the eighties [27], developed in the oceanographical context. They generalize the concept of Stokes drift[3] to a random field of gravity waves. Again, a long–time effect of this drift is an horizontal diffusion of tracers, that can explain clustering of matter at some scales.

Perhaps the common point of these two examples is that they correspond to long–time effects produced by waves. This is relevant to floating objects, as clustering can be induced on them. Also, as we are dealing with waves, both examples can be considered using a potential theory.

[3]Stokes drift is experienced by fluid parcels close to the surface –and by any other floating object– under the presence of traveling waves: after one period, the fluid parcel experience a slight spacial variation compared to its original position. It follows the direction of the traveling wave, an it can represent an important source of (slow) motion.

2.1.3.2 Downward and upward flows

Cressman and Goldburg [12] considered a very natural relation that holds for incompressible flows:

$$\nabla_\perp \cdot \mathbf{u}_\perp = -\frac{\partial u_3}{\partial z}, \tag{2.15}$$

which is valid in the whole fluid volume, in particular on the surface. This expression links two–dimensional compressibility to vertical velocity gradients.

For shallow flows with motion principally in two dimensions, vertical velocity gradients are produced as a secondary motion, as noticed, for instance, by Kamp [28]. Indeed, he gives estimates for the horizontal divergence and associate positive values to upward flows (together with negative values to downward flows).

Again, the compressibility effect can be revealed by floating particles: as upward and downward motion encounter the free surface, it generate hills and subduction zones (see the features on the right–bottom in figure 1.1–top). Floating particles, which are constrained to rest on the free surface, travel over expansion and compression zones, thus experience clustering.

In opposition to wavy motions described in the previous section, here the source of compressibility is fundamentally *rotational*. Indeed Kamp suggested –again for shallow flows– that upward flows are concentrated in vorticity dominated regions of the primary flow [28].

2.1.3.3 The effect of object's inertia

The dynamics of several interacting *particles* attracts a lot of attention nowadays, because of its intrinsic industrial and ecological interest: Fuel drops in cars injectors; transport of pollutants in air and water; cloud's formation, etc. The related phenomena of preferential concentration was considered since the sixties, as notices in [39].

One way to understand preferential concentration is to consider the relation between particle's velocity $\mathbf{v}_p$ and the surrounding velocity $\mathbf{u}$ [35; 4] :

$$\nabla \cdot \mathbf{v}_p = (\beta - 1)\tau_s \nabla[(\mathbf{u} \cdot \nabla)\mathbf{u}], \tag{2.16}$$

where $\beta = 3\rho_f/(\rho_f + 2\rho_p)$ comes from the mismatch between the fluid density ρ_f and the particle density ρ_p. For a particle radius a and kinematic viscosity ν, the Stokes time $\tau_s = a^2/(3\nu\beta)$ represents a characteristic time over which the flow velocity $\mathbf{u}$ is *filtered* by the particle. In [35], this equation originally comes from an asymptotic analysis for small particle inertia. As it could be expected, perfect match of densities, or a particle radius equal to zero, imply $\nabla \cdot \mathbf{v}_p = 0$, although *particle*'s velocity is certainly undefined in the last case. In more realistic cases, however, there exists some density mismatch and a nonzero Stokes time, and this is at the origin of preferential concentration in turbulent flows [38; 39; 24].

Equation (2.16) differs from (2.14) and (2.15), in the sense that it primarily concern particles, but also the underlying flow. Equations (2.14) and (2.15) only concern the flow. They concern particles only if particles are there.

Although these considerations do not need turbulence *a priori* to be relevant, they have all been developed in that context [27; 12; 35; 4; 38; 24]. Therefore, now we consider turbulence in more detail.

2.2 *Classical* Turbulence in three dimensions

For incompressible Newtonian fluids in three dimensions, one has the incompressibility condition

$$\nabla \cdot \mathbf{u} = 0, \tag{2.17}$$

with $\mathbf{u} = (u_1, u_2, u_3)$ the fluid velocity in the Eulerian description. It results from mass conservation equation (2.2) when the fluid has a constant, homogeneous density.

Next we have the Navier-Stokes (NS) equation:

$$\rho \left(\frac{\partial \mathbf{u}}{\partial t} + (\mathbf{u} \cdot \nabla)\, \mathbf{u} \right) = -\nabla p + \mu \nabla^2 \mathbf{u} + \mathbf{f}, \tag{2.18}$$

where p is the pressure, $\mu = \rho\nu$ is the dynamic viscosity and ν is the kinematic viscosity. $\mathbf{f}$ represents an external force. In particular, $\mathbf{f}$ may include gravity. However, as gravity is a conservative force, it can be included in the so-called *dynamic pressure* $p_d = p + \rho g z$ (with g the gravity acceleration) replacing the usual pressure term.

2.2.1 Dimensionless Navier Stokes equation

In order to gain some intuition about the physical parameters involved in equation (2.18), it is necessary to work with dimensionless variables. We first exclude external forcing in order to do a general description. Let us rewrite the physical variables in this way: $\mathbf{r} = L_0 \tilde{\mathbf{r}}$, in which $\mathbf{r}$ has the usual dimensions of length. We have introduced here L_0: the typical length scale of the problem. Thus $\tilde{\mathbf{r}}$ is a dimensionless variable associated to distances and (to the inverse of) gradients. Now we will proceed in the same way with the other variables: $\mathbf{u} = U_0 \tilde{\mathbf{u}}$, with U_0 the typical velocity scale of the problem. $t = L_0/U_0 \tilde{t}$ and $p = \rho U_0^2 \tilde{p}$. When there is an external forcing, it usually imposes L_0 and U_0 (the example of our experiment is given in section 3.2). If we now apply this change of variables to equation (2.18), we get:

$$\frac{\partial \tilde{\mathbf{u}}}{\partial \tilde{t}} + (\tilde{\mathbf{u}} \cdot \tilde{\nabla})\, \tilde{\mathbf{u}} = -\tilde{\nabla} \tilde{p} + \frac{\nu}{U_0 L_0} \tilde{\nabla}^2 \tilde{\mathbf{u}}, \tag{2.19}$$

in which every term is dimensionless. In particular, a dimensionless group –the *Reynolds* number– appears naturally:

$$Re = \frac{U_0 L_0}{\nu}, \tag{2.20}$$

in which all the dimensional information of the flow is contained.

A more concrete presentation of Re is postponed to section 3.2, after giving concrete values to U_0, L_0 and ν in connection to our experiment. However, at this stage we can notice:

- The Reynolds number can be seen as the ratio between two time scales $Re = \tau_\nu/\tau_u$ where τ_ν is the one associated with viscous dissipation, and τ_u the one associated with advection. Thus, when the viscous time is small compared to the advection time (small Re), viscosity controls the dynamics. When the advection time is smaller (large Re), advection controls the dynamics. The case of $Re \gg 1$, implies strong separation of time scales (and length scales).

- The competition between time scales can be also interpreted in reference to the Navier Stokes equation, recalling that advection comes from the nonlinear term $(\mathbf{u} \cdot \nabla)\,\mathbf{u}$ and viscosity from the linear one $\nu\nabla^2\mathbf{u}$. Thus, for viscosity dominated flows, nonlinearity does not play significant role. On the contrary, when Re is large, nonlinearity is the key in the motion and energy transfers.

2.2.2 Scaling laws in fully developed turbulence

We are now in position to briefly discuss the ideas about the inertial range of turbulence. Although these ideas come from Kolmogorov and his paper of 1941 (usually referred as K41), we chose to closely follow the development carried out by Phillips [44], published in a special issue celebrating the 50 years of K41.

Let us start from the equation for the energy, as obtained from (2.18) [23],

$$\frac{d}{dt}\left\langle \frac{1}{2}u^2 \right\rangle = -\nu\langle|\nabla \times \mathbf{u}|^2\rangle, \tag{2.21}$$

where $u = |\mathbf{u}|$ and brackets denote the average over the whole flow domain. In the inviscid case, this is a conservation equation. The Navier Stokes equation, on the other hand, is dissipative because of the viscosity ν. We can, however, develop the analysis in terms of scales (wave–numbers), as proposed by Phillips [44]. Here,

$$\left\langle \frac{1}{2}u^2 \right\rangle = \int_0^\infty E(k)dk,$$

and

$$\frac{\partial E(k)}{\partial t} = -\frac{\partial \varepsilon(k)}{\partial k} - 2\nu k^2 E(k), \tag{2.22}$$

with $E(k)$ the turbulent energy spectrum, k the norm of $\mathbf{k}$ in the wave number space (we assume isotropy) and $\varepsilon(k)$ the spectral flux through wave–number k. Their units are $[E(k)] = L^3/T^2$, $[k] = L^{-1}$ and $[\varepsilon(k)] = L^2/T^3$, respectively.

We are now interested in the inertial range of turbulence. As we already saw, for high Re, there is a strong separation between the scale L_0 –at which energy is supplied to the system– and the scale of dissipation l_D. By definition, the inertial range is far enough from both L_0 and l_D. Consequently, the intermediate scale k^{-1} is not much affected by distant wave numbers but only by closer ones, which enter into play because of nonlinearity. Also, the timescale associated to that scale, say $t_k = u_k^{-1} \cdot k^{-1}$ is much larger than dissipative ones. Therefore, we expect the scales in the inertial range to be statistically stationary, thus $\partial E(k)/\partial t \approx 0$.

As, from equation (2.22) one can see that dissipation becomes relevant only at large k, therefore the term proportional to k^2 is negligible in the inertial range and ε appears to be scale–independent. However, one can find its value by integration:

$$\varepsilon_0 = 2\nu \int_0^\infty k^2 E(k) dk,$$

with ε_0 the rate at which energy is dissipated in the system. It has dimensions $[\varepsilon_0] = L^2T^{-3}$ and it could be related both to the energy injection scale $L_0 \sim U_0^3/\varepsilon_0$ and to the one of dissipation $l_D \sim u_D^3/\varepsilon_0$. For the dissipative scale l_D, however, the term with ν is the only important in the r.h.s. of equation (2.22) and it is comparable to the l.h.s. term. Thus, dimensionally we obtain $l_D \sim (\nu^3/\varepsilon_0)^{1/4}$ that can be expressed in terms of the Reynolds number in a way that shows clearly the scale separation for large Re,

$$l_D \sim Re^{-3/4} L_0. \tag{2.23}$$

For the inertial range, following the first similarity hypothesis of Kolmogorov, we consider as relevant dimensional parameters are ε_0, ν, k and $E(k)$. By evoking the Buckingham Π-Theorem for these parameters –with dimensions L and T– we find two dimensionless numbers: $\Pi_1 = E(k)/\varepsilon_0^{-2/3} k^{5/3}$ and $\Pi_2 = k l_D$ with $\Pi_1 = F(\Pi_2)$. From equation (2.23), however, one can see that for large Re, $k l_D = \Pi_2 \to 0$, making this dimensionless parameter dynamically irrelevant [5]. Thus Π_1 is constant ($= A$) and we end up with the celebrated Kolmogorov spectrum

$$E(k) = A\, \varepsilon_0^{2/3} k^{-5/3}. \tag{2.24}$$

2.3 Two dimensional turbulence

Two dimensional (2D) turbulence concerns flows which can be readily described by only two components. To some extent it was inspired by the geophysical interest of oceans and atmosphere, as they *horizontal*[4] extensions are much larger than the vertical one. Thus the dynamics could be expected to be well described by horizontal components. Also –at the beginning– 2D turbulence was inspired by the enormous gain in computing time when performing numerical simulations.

It appears that these two motivations deserve more discussion nowadays: 2D models of the ocean are capable to explain some of its important features, but an important part of the ocean-atmosphere energy transfer comes from vertical fluxes of mass and momentum; concerning computational time, it always help to ignore one component to perform computations, but the price of loosing important physics is too high in some contexts. Moreover, in real situations (particularly in experiments), it is much more difficult to get a truly 2D flow than a 3D one.

However, since the first developments of the 2D turbulence theory, it becomes clear that, compared to classical turbulence, 2D turbulence has remarkable properties, in particular the absence of vortex stretching. Indeed it exhibits the phenomenon called *dual cascades:*. It can be argued that the energy ($\langle \mathbf{u}^2 \rangle/2$, with $\mathbf{u}$ the velocity) goes from

[4]In this context, horizontal means perpendicular to the local gravity.

the forcing wavenumber k_F to lower wavenumber (larger scales), although the so-called enstrophy ($\langle\Omega^2\rangle/2$, with $\Omega = (\nabla \times \mathbf{u})|_z$ the vertical vorticity) goes from k_F to larger wavenumbers (smaller scales). In these conditions, there are two scalings for the energy spectrum, depending on the wavenumber:

$$E(k) \sim k^{-5/3} \quad \text{for} \quad k < k_F \quad \text{and} \quad E(k) \sim k^{-3} \quad \text{for} \quad k > k_F. \tag{2.25}$$

These unique properties of 2D turbulence made it a fundamental subject of scientific research.

A fact that also contributed to the standing of 2D turbulence, is that some physical mechanisms naturally enhance bidimensionality, when starting from an isotropic initial state. To date, there are three known mechanisms that produce this effect: (i) strong uniform magnetic fields [51]; (ii) density stratification [34; 42], and (iii) global rotation [37].

Moreover, these three mechanisms appear naturally when dealing with the fluid dynamics in geophysical and astrophysical contexts.

Because of its intrinsic relevance and its unusual properties, there were many efforts to perform experimental realizations of two dimensional turbulent flows [10; 26; 34; 52], some of them succeeding in the observation of one or both parts of the spectrum. However, as experimental realizations always involve the third component, care was taken to avoid 3D motion, by adding one of the previously mentioned mechanisms.

On the contrary, the focus on two dimensional turbulence, discouraged the consideration of more realistic quasi bidimensional turbulent flows until recently. Consequently, a statistical study of height fluctuations in connection to coherent vortices is limited to turbulent soap films [26] and liquid metal experiments [16].

2.4 Fluids with a free surface

Equations (2.17) and (2.18) hold in the bulk of the fluid and correspond to the conservation of mass and momentum, respectively. But they represent only the half of the history for free–surface flows. For fluids with a free surface, specific boundary conditions must be respected. These conditions were presented, for instance, by Tsai & Yue [53] or by Sarpkaya [48] and are summarized here. For simplicity, we restrict ourselves to the case where the influence of the upper fluid can be neglected. Therefore we can refer the interface simply as a free surface[5].

For free surface flows, there is no mass flux across the surface. Thus, any fluid element at the surface stays at the surface. If we define $F(x, y, z, t) = z - \eta(x, y, t)$, with (x, y, z) the spatial coordinates, and $\eta(x, y, t)$ the position of the interface (which varies both in space and time), this condition means

$$\frac{DF}{Dt} = 0, \tag{2.26}$$

[5]Despite our experiment corresponds to the –more general– case of two immiscible fluids separated by an interface, the influence of the upper fluid can be neglected because: (a) the high contrast in the density and viscosity of the fluids, and; (b) there is no forcing applied to the upper fluid.

or its equivalent:

$$\frac{\partial \eta}{\partial t} + u_1 \frac{\partial \eta}{\partial x} + u_2 \frac{\partial \eta}{\partial y} = u_3, \tag{2.27}$$

which is known as *kinematic boundary condition.*

We consider now the dynamic boundary conditions: continuity on tangential velocities; and continuity of tangential and normal stresses. However, for the case considered here: with only one dynamically relevant fluid and no gradients of surface tension (a point considered in detail by Sarpkaya [48]), the only relevant condition is the one on normal stresses, also known as the *pressure condition*:

$$\mathbf{T} \cdot \mathbf{n} = (\gamma\kappa + p_0)\mathbf{n} \quad \text{on} \quad z = \eta(x, y, t), \tag{2.28}$$

were γ is the surface tension coefficient, κ the local curvature, p_0 the atmospheric pressure, $\mathbf{n}$ the vector normal to the interface, and $\mathbf{T}$ the stress tensor. $\mathbf{T} = p\mathbf{I} - \mu\mathbf{E}$, in which $\mathbf{E}$ has the elements $E_{ij} = \left(\frac{\partial v_i}{\partial x_j} + \frac{\partial v_j}{\partial x_i}\right)$.

Equation (2.28) can be written as $p - p_0 = \mu(\mathbf{n} \cdot \mathbf{E}) \cdot \mathbf{n} + \gamma\kappa$, allowing us to interpret the Young-Laplace law $\Delta p = \gamma\kappa$ as the particular case of inviscid or stationary fluids.

2.4.1 Dimensionless pressure condition [7; 49]

To be consistent with the dimensionless expression of the Navier Stokes equation (2.18), we have to write the boundary condition in terms of the dynamic pressure introduced together with equation (2.18). Thus,

$$p_d - \rho g z = \mu(\mathbf{n} \cdot \mathbf{E}) \cdot \mathbf{n} + \gamma\kappa + p_0.$$

Now we use exactly the same change of variables introduced to write the dimensionless Navier Stokes equation (2.19). To recall it: $\mathbf{r} = L_0\tilde{\mathbf{r}}$, $\mathbf{u} = U_0\tilde{\mathbf{u}}$, $t = L_0/U_0\tilde{t}$ and $p = \rho U_0^2\tilde{p}$, with U_0 and L_0 the typical velocity and length scales of the problem. We perform the transformation first in the dynamic pressure, in the same way as for usual pressure $p_d = \rho U_0^2 \tilde{p}_d$, thus,

$$\tilde{p}_d = \tilde{p} + \frac{gL_0}{U_0^2}\tilde{z},$$

and the complete equation reads

$$\tilde{p}_d - \frac{gL_0}{U_0^2}\tilde{z} = \frac{\nu}{U_0 L_0}\mathbf{n} \cdot \tilde{\mathbf{E}} \cdot \mathbf{n} + \frac{\gamma}{\rho U_0^2 L_0}\tilde{\kappa} + \tilde{p}_0,$$

taking into account that $\mathbf{E}$ has dimensions of velocity over length (or frequency), that $\mathbf{n}$ is an unitary vector with no dimensions, and that κ has dimensions of an inverse length. Therefore, together with the Reynolds number (2.20), here we should define two more dimensionless groups: the *Froude* number

$$Fr = \frac{U_0^2}{gL_0}, \tag{2.29}$$

and the *Weber* number

$$We = \frac{U_0^2 L_0 \rho}{\gamma}. \tag{2.30}$$

In this way, we can alternatively write the dimensionless pressure condition as

$$\tilde{p}_d - \frac{1}{Fr}\tilde{z} = \frac{1}{Re}\mathbf{n}\cdot\tilde{\mathbf{E}}\cdot\mathbf{n} + \frac{1}{We}\tilde{\kappa} + \tilde{p}_0 \quad \text{on} \quad \tilde{z} = \tilde{\eta}(\tilde{x},\tilde{y},\tilde{t}). \tag{2.31}$$

The Froude number can be seen as the ratio between kinetic and potential energy, or even as the ratio between the flow velocity and the group velocity of gravity waves. Small Froude number implies that the restoring effect of gravity is strong and the surface is nearly flat. However, by considering analogies between the Froude and the Mach number (i.e. between hydrodynamics and acoustics), wave generation can be expected at Fr or M numbers as small as 0.05 [45]. On the other hand, as noticed in [6], for $Fr \sim O(1)$, potential and kinetic energies are comparable on the surface, and one can expect rich deformation dynamics. Finally, when $Fr \to \infty$, gravity has no more influence on the surface, because kinetic energy is too high.

The Weber number on the other hand, gives account of the restoring action of capillarity. It represents kinetic energy over cohesion energy (as discussed, for instance, by Clanet in the context of water-bells produced from jets [8]). For $We \to 0$, the accompanying term in equation (2.31) dominates over those of Re and Fr. Thus, one gets Young-Laplace equation, characteristic of static equilibrium. For small –but non zero– We, wave-like behavior could be expected, as it will be apparent in equation (2.43). This should be the case until $We \sim O(1)$, where both kinetic and cohesive energies balance [6]. For large We, cohesive energy becomes very important and a deformed surface can break into droplets. Finally, for $We \to \infty$, surface tension has no more influence on the surface, compared with the kinetic energy of the flow.

As it can be seen, a large variety of surface features can be observed, and it will be the subject, in particular, of chapters 5 and 6. A qualitative classification of this phenomenology will be given below, in section 2.5.1.

2.4.2 Linear waves on the free surface [1; 50]

Now we focus our attention on the simplest solutions for free surface flows. After stating some hypothesis, we will study the evolution of a very small perturbation, that can be described by linearized equations. This is called the linear theory for water waves. We will see then, that even these very simple computations will allow us to obtain important conclusions. Indeed, some of these results are the basis of the wave turbulence theory to be studied later.

The linear theory of water waves was developed in the context of inviscid ($\nu = 0$) and irrotational ($\nabla \times \mathbf{u} = 0$) fluid motion. The first assumption is generally valid, as long as one is concerned with wavelengths larger than few centimeters. When dissipation is taken into account (Lamb [29]), it produces an exponential decay in wave amplitudes with a factor $-2\nu k^2$, thus having considerable impact only at large wave-numbers.

In the turbulence context on the other hand, the second assumption can be hardly acceptable. Nevertheless, as the most general free surface problem could include turbulence

and waves, it is better to keep this hypothesis for the moment, and to study the classical results of the theory.

For inviscid fluids (where $\nu = 0$), Navier Stokes equation (2.18) becomes Euler equation. By considering that $(\mathbf{u} \cdot \nabla)\,\mathbf{u} = (\nabla \times \mathbf{u}) \times \mathbf{u} + \nabla(\mathbf{u}^2/2)$, and defining the vorticity $\omega = (\nabla \times \mathbf{u})$, Euler equation reads

$$\frac{\partial \mathbf{u}}{\partial t} + (\omega \times \mathbf{u}) = -\nabla \left(\frac{p}{\rho} + \frac{1}{2}\mathbf{u}^2 + gz \right). \tag{2.32}$$

We have the incompressibility condition (2.17)

$$\nabla \cdot \mathbf{u} = 0;$$

as noticed before, for inviscid fluids the pressure condition reduces to the Young–Laplace law (valid on the surface)

$$p - p_0 = \gamma\kappa, \tag{2.33}$$

and the kinematic boundary condition (2.27) remains unchanged.

We have to include also the boundary condition at the bottom, that follows from the assumption of impermeable bottom: $\mathbf{u} \cdot \nabla\{z + h(x, y)\}$ at a depth $z = -h(x, y)$. By assuming a flat bottom, the condition simply becomes

$$u_3 = 0 \quad \text{on} \quad z = -h. \tag{2.34}$$

Now, when considering irrotational motion ($\omega = \nabla \times \mathbf{u} = 0$), we can define a velocity potential $\phi(\mathbf{x}, t)$ such that

$$\mathbf{u} = \nabla\phi. \tag{2.35}$$

This means that the problem is reduced to find the potential solving the Laplace equation

$$\nabla^2\phi = 0 \tag{2.36}$$

that comes from the incompressibility condition. By including the velocity potential into the Euler equation (2.32), and writing the pressure as equation (2.33), we get a *potential* version of the pressure condition at the surface:

$$\frac{\partial \phi}{\partial t} + \frac{1}{2}|\nabla\phi|^2 + g\eta = \frac{\gamma}{\rho}\kappa. \tag{2.37}$$

Thus, the complete set of (nonlinear) equations are (2.36) for the bulk, (2.27) and (2.37) at the surface and (2.34) at the bottom. Now, the linearized version of these equation are, respectively

$$\nabla^2\phi = 0, \quad \text{in the bulk,} \tag{2.38}$$

$$\frac{\partial \eta}{\partial t} = \frac{\partial \phi}{\partial z}, \quad \text{on} \quad z = 0, \tag{2.39}$$

$$\frac{\partial \phi}{\partial t} + g\eta = \frac{\gamma}{\rho}\,\nabla^2\eta, \quad \text{on} \quad z = 0 \quad \text{and} \tag{2.40}$$

$$\frac{\partial \phi}{\partial z} = 0 \quad \text{on} \quad z = -h, \tag{2.41}$$

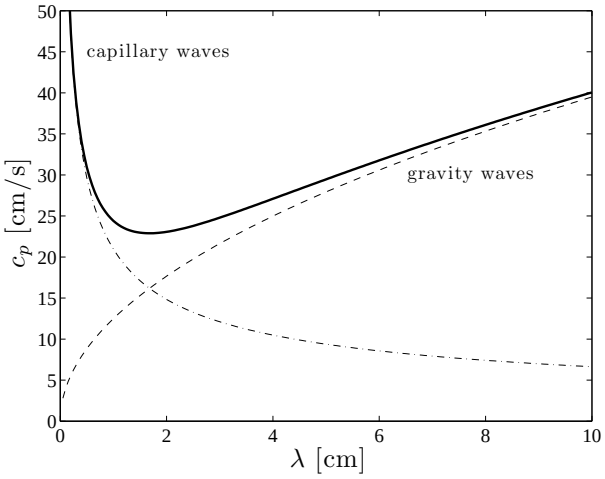

Figure 2.1: Phase velocity c_p for gravity-capillary waves in deep water, for the air-water interface (thick line). Dashed lines are limits in which only one of the dominant processes is considered.

in which we also considered that the surface is located, to leading order, at $z = 0$. Also, we used the linearized version of the curvature radius $\kappa = \nabla^2\eta$. In general, κ is defined in terms of the two local curvature radii R_1, R_2 as $\kappa = (1/R_1 + 1/R_2)$ and it could be highly nonlinear.

We consider a simple, sinusoidal, propagative perturbation of the surface,

$$\eta = a\cos(kx - \omega t),$$

where a is the (small) amplitude of the perturbation, ω is its angular frequency (please do not confuse with the vorticity ω), $k = 2\pi/\lambda$ is the wavenumber and λ the wavelength. A consistent velocity potential should have the form $\phi(x, y, z, t) = f(z)\sin(kx - \omega t)$, with f satisfying both the equation $f'' - k^2 f = 0$ and the bottom boundary condition (2.41). By evaluating equation (2.39) we find the explicit form of the velocity potential:

$$\phi(x, y, z, t) = \frac{a\omega\cosh(kh + zh)}{k\sinh(kh)}\sin(kx - \omega t).$$

Finally, we evaluate (2.40) on $z = 0$, where the condition is valid. This give us the so–called dispersion relation for gravity–capillary waves for water of arbitrary depth:

$$\omega^2 = \left(gk + \frac{\gamma}{\rho}k^3\right)\tanh(kh). \tag{2.42}$$

From this relation, we can notice:

- $\omega(k)$ has the dimension of inverse time (frequency), and k of inverse length. Thus, if we want to construct a velocity, a natural candidate is $\omega/k = c_p$. This is the phase velocity for a wave of wavelength $\lambda = 2\pi/k$, and represent the speed at which the crest of the wave travels. As it is presented in figure 2.1, ω varies with λ (or k):

waves with different wavelength travel with a different c_p developing a dispersion of the original wave packet. That is why equation (2.42) is called dispersion relation. This is why in the ocean, the farther the waves were created, the more coherent is the observed wave train, because the waves have the time to clearly isolate the observed λ. A second velocity that is relevant for wave propagation is the group velocity $c_g = \partial\omega/\partial k$: the velocity at which the whole wave packet travels.

- If we vary k from very small values to larger ones, the relative importance of the two terms on the parenthesis in equation (2.42) radically changes: for very small k, gravity is the dominant restitution effect. On the contrary, for large k, capillarity becomes more important. In the middle both effect can be relevant, and there is a particular length–scale at which they are exactly equal. This is the so–called capillary length $l_c = \sqrt{\gamma/\rho g}$, that depends only on fluid properties.

- The term $\tanh kh$ in equation (2.42) take into account the fluid depth. The most common limit case is the one of *deep water*, where $\tanh kh = 1$. It correspond to wave–lengths much smaller than the fluid depth. The opposite limit is also significant: the so–called *shallow water* limit for $kh \to 0$. It corresponds to very large waves compared with the fluid depth. In this case $\tanh kh \to kh$ and it is naturally accompanied with vanishing effects of surface tension (as k is small). Here, equation (2.42) is reduced to $\omega = \sqrt{ghk}$ which is non–dispersive ($c_p = c_g = \sqrt{gh}$).

- As we did for the Navier–Stokes equation and for the boundary condition at the surface, it could be interesting to perform the linear–waves analysis in a dimensionless form. This is equivalent to consider the dimensionless dispersion relation, which after introducing the dimensionless variables $\omega = U_0 L_0^{-1}\tilde{\omega}$ and $k = L_0^{-1}\tilde{k}$ reads (in deep water)

$$\tilde{\omega}^2 = \frac{1}{Fr}\tilde{k} + \frac{1}{We}\tilde{k}^3. \tag{2.43}$$

  The practical interest of this relation is not completelly clear. However, by having in mind both forms of the dispersion relation (eqs. (2.42) and (2.43)), we can gain insights about Fr and We numbers for wavy surfaces: small Froude number suggest that large scale surface deformation are dominant. Small Weber number suggest small scale deformations as the dominant ones.

2.5 Turbulence at the free surface

2.5.1 A qualitative description

For turbulence in free surface flows, we are not able to construct a simple picture on the basis of only one dimensionless parameter (as one can do with Re for classical turbulence). Indeed, in equation (2.31), we saw that 3 independent parameters are necessary to describe the system.

To overcome this difficulty, one can assume that the flow is turbulent, and then focus the attention only on the other two dimensionless parameters. This is implicit in the extensive description of strong free surface turbulence by Brocchini & Peregrine [6], to

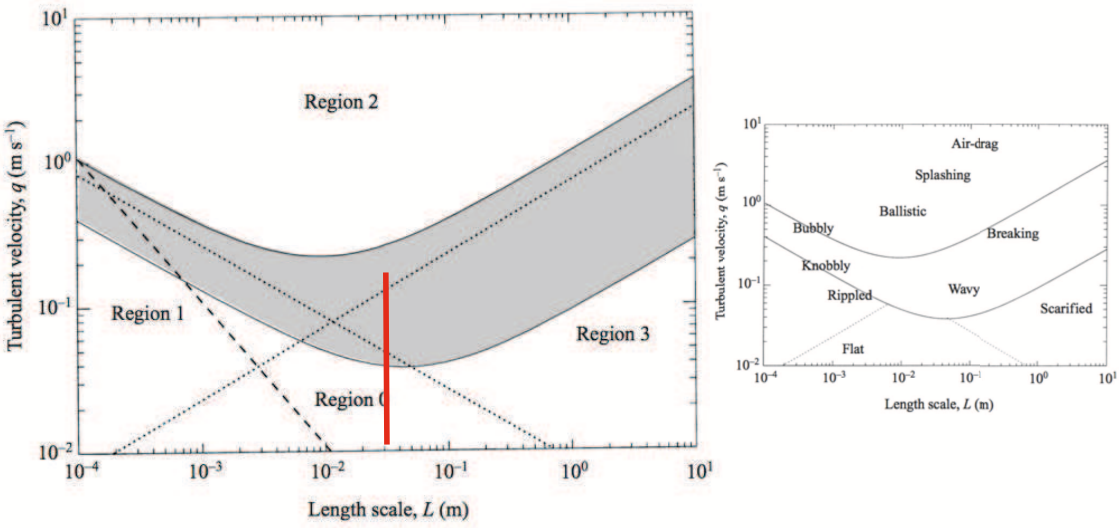

Figure 2.2: Dimensional diagram to regrouping the vast world of free surface turbulent flows into four different regions (see text). It is reproduced from [6]. L and q represent characteristic length-scale and velocity, respectively. Red line present a very roughly estimate of our experiment in this diagram. The smaller version of the diagram present some terminology to describe the different observed deformation features.

be recalled here. Although they develop a dimensional description (in terms of a length scale L and a velocity q), the dimensionless numbers of Froude and Weber are constantly evoked.

Brocchini & Peregrine started their discussion by considering the most frequent features that appear in free surface flows:

- A passive response to fluctuations in the pressure. We can interpret them as being a direct consequence of horizontal fluid motions (where the vorticity field is perpendicular to the surface). The paradigmatic example is an idealized vortex, in which an uniform rotation results in a lower pressure at the center, deforming the free surface. This kind of deformations are well supported by experimental observations nowadays [54; 2; 3] (see also the vortex in figure 1.1–top).

- Water waves: They are the natural response of a fluid under perturbations of the surface. But also, as noticed in [6], in a turbulent flow it is plausible to have velocity fluctuations that become irrotational –in particular by the influence of the free surface–, in which wave generation may occurs. On the other hand, as it can be noticed from figure 2.1, the phase velocity has a minimum of around $c_p = 23$ cm/s at $\lambda = 1.7$ cm, for the air water interface[6]. It is argued (in the sense of a necessary condition) that for velocities larger than this value, the presence of waves may be expected.

[6]The values for the galinstan-acid interface to be considered experimentally, are slightly different: $\min(c_p)$=21 cm/s at $\lambda = 1.9$ cm. This is a consequence of the two involved densities, and the different coefficient of interfacial tension γ.

- Flows where their streamlines are attached to the free surface. Typical examples are fluid motions in which the vorticity field is principally parallel to the surface, forming elongated depressions on the surface. A visual example of this are irregular deformations in the bottom–right in figure 1.1–top.

For a more systematic description, they constructed a diagram based on typical length and velocity scales. It is reproduced in figure 2.2. On this basis they identify four fundamental regions:

- A region where gravity is dominant and surface tension is unimportant (Region 3). It corresponds to small Fr and large We. This is the region where the previously described features are generally observed.

- A region of *weak turbulence*[7] (Region 0). Here both Fr and We are sufficiently small to preclude significant surface deformation. However, it is noticed that such gentle turbulence could have an effect on wave propagation.

- A region where surface tension is dominant and gravity is unimportant (Region 1). It corresponds to large Fr and small We. As gravity is not efficient as restoring mechanism, capillarity rules the dynamics, resulting in rounded surfaces. Low gravity environments should enter in this region [13; 20; 15]

- A region for very strong turbulence (Region 2), where neither Fr nor We are small enough to stabilize the surface. Thus, essentially two-phase flow phenomenology is observed.

Another (and the last we mention) valuable point in their discussion are the cases delimiting the smoothness of the surface. One limit corresponds to drop ejection from a very steep deformation (see for instance [25]). The opposite one corresponds to air entrainment from an a very strong depression (see for instance [2]). These limits are developed in order to estimate velocity and length scales defining the region in the center of their diagram.

In figure 2.2, the red line represent very rough estimates for our experiment: they are based on the forcing length scale and estimations of the velocity. This is developed further in section 3.2. This suggest that our experiment ranges between *weak turbulence* (low Fr and low We) and *gravity–dominated turbulence* (low Fr and large We) regimes.

2.5.2 Quantifying free surface turbulence: The continuous spectrum

There is no much doubt about the pertinence of performing a statistical description of free surface turbulence, in an analogous way as it is done for classical turbulence. Consider the picture 2.3 showing a sea state created artificially in the wave tank of École Centrale de Nantes. Two features can be noticed in particular: (i) No clear correlation can be stablished between two points in the surface. (ii) Even if it is a single picture, there is a

[7] Do not confound with weak turbulence theory, the alternative name of wave turbulence theory.

large variety of length-scales involved in the free surface motion. Similar arguments can be developed for the time when looking to a single point in the oceanic free surface, as noticed in [43]. The reader is encouraged to verify last sentence in his (her) next visit to his (her) preferred coast, specially in winter time.

For classical turbulence, we discussed the existence of inertial ranges, in which non-linearity allows the transfer of conserved quantities into scales different from the ones of injection. Similar phenomenology is observed in the case of water waves in the turbulent ocean, in the form of a continuous spectra (both in the frequency and length-scale domains). This means that there is a flux of energy between scales (see for instance the frequency spectrum given as an inset in figure 2.3). Since Phillips [43], there were many attempts to describe these continuous spectra from a mathematical point of view. First on the basis of dimensional grounds [43], and later by the development of a wave interaction theory, as reviewed recently by Nazarenko [40], and Newell & Rumpf [41].

We will consider now dimensional arguments for the spectra of free surface turbulence. Thus we will first define these spectra: The frequency spectrum of the surface displacement for a fixed point $\eta(\mathbf{x}, t)$ is

$$S_\eta(\omega) = \frac{1}{2\pi} \int_{-\infty}^{\infty} \langle \eta(\mathbf{x}, t)\eta(\mathbf{x}, t+\tau)\rangle e^{-i\omega\tau} d\tau, \tag{2.44}$$

where $\langle\cdot\rangle$ denotes ensemble average. This spectrum has dimensions $[S_\eta(\omega)] = L^2T$, where L represents the dimension of length and T the one of time.

The instantaneous wavenumber spectrum of $\eta(\mathbf{x}, t)$ on the other hand, reads

$$S_\eta(\mathbf{k}) = \frac{1}{2\pi^2} \int \langle \eta(\mathbf{x}, t)\eta(\mathbf{x}+\mathbf{r}, t)\rangle e^{-i\mathbf{k}\cdot\mathbf{r}} d\mathbf{r}. \tag{2.45}$$

This spectrum has dimensions $[S_\eta(\mathbf{k})] = L^4$, because we are concerned by a surface, the free surface of water.

Other dimensional quantities of interest are of course frequency $[\omega] = T^{-1}$ and wavenumber $[k] = L^{-1}$, but also gravity $[g] = LT^{-2}$; the ratio between surface tension and density $[\gamma/\rho] = L^3T^{-2}$ and the energy flux[8] $[\varepsilon] = L^3T^{-3}$.

2.5.3 Phillips spectrum

As we see in picture 2.3, most of the water surface is continuous, even when the turbulence is well developed. And if there is some wave breaking, it is restricted to small areas in the surface. In this particular picture, however, we do not see any. What we actually see are some very sharp crests representing the extreme condition in which the surface is still attached. After, wave breaking may come into play. Phillips argued that it is the attachment condition what governs the spectrum in the inertial range of oceanic turbulence generated by wind.

[8]This energy flux ε corresponds to P/ρ where P is the –perhaps better known– rate of energy transfer through a surface. Thus P has units of (energy)/(time · area) and gives the presented units for ε [17].

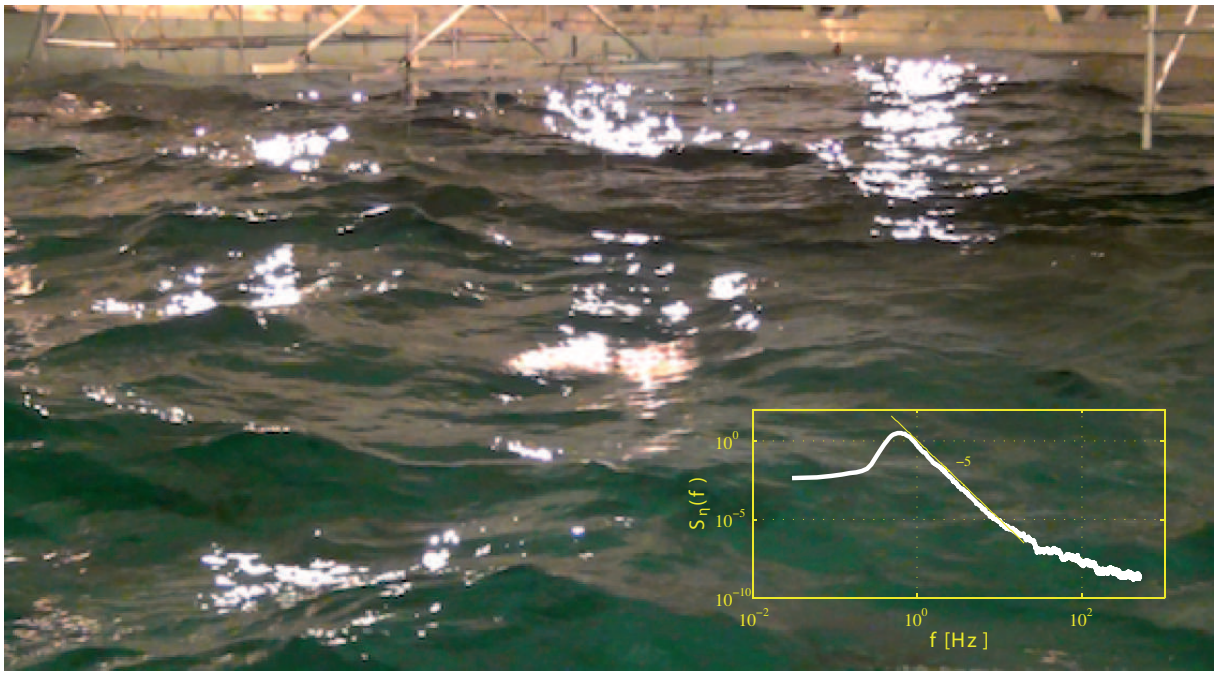

Figure 2.3: *Main:* Example of a sea state created artificially in the wave tank of École Centrale de Nantes. *Inset:* Frequency spectrum of the height η, measured with capacitive probes.

In a well developed and gravity dominated turbulent ocean, one can neglect the effects of surface tension and consider that fluid density enter as a dimensionless ratio[9]. Thus the physical parameters involved in the problem are only the surface roughness length z_0, wind velocity u_* and gravity g. As it is expected that the roughness length varies with velocity, Phillips proposes (referring to Ellison) the scaling $z_0 \sim u_*^2/g$. But more importantly, he argues that, once the inertial range is developed, it cannot depend on velocity. This is because the limiting surface shape –in which the surface is still attached– is given by a maximal downward acceleration equal to g. The wind velocity u_* can only affect the rate at which a wave reach its limiting shape.

Thus, the only possible combination of frequency and gravity giving the same dimensions of the frequency spectrum reads

$$S_\eta(\omega) \sim g^2\omega^{-5}. \tag{2.46}$$

And based on the same kind of dimensional grounds, the wavenumber spectrum can be obtained directly as

$$S_\eta(\mathbf{k}) \sim k^{-4}, \tag{2.47}$$

which is also justified as the asymptotic spectrum for a function with discontinuities in one or more points: when discontinuities are present in a spatial signal, its Fourier spectrum

[9]Actually, for the interfacial problem concerning fluids of densities ρ_1 and ρ_2 with $\rho_1 > \rho_2$, the dispersion relation is modifyed by changing gravity g by Ag, where $A = \rho_1 - \rho_2/\rho_1 + \rho_2$ is a dimensionless factor called Atwood number. Densities enter, however, together with surface tension, as in the usual dispersion relation (2.42).

converges to k^{-2}. As the wavenumber spectrum of η is proportional to the squared Fourier spectrum, the proposed spectrum follows.

At that time, some field measurements sustained the scaling of the frequency spectrum, for instance the work of Burling (reproduced in [43]).

2.5.4 Wave turbulence theory

As we already saw, classical turbulence theory is concerned with the nonlinear transfer of energy between scales of motion. In a somehow analogous way, wave turbulence theory deals with the transfer of conserved quantities[10] produced by the (weak) nonlinear interaction of waves. Thus, it is not a theory restricted to water waves, although its origin comes from them. One of its principal advantages is that, doing perturbative analysis in terms of a small parameter, one can explicitly compute the interaction coefficients and derive analytical expressions for relevant quantities (wave spectra for instance). Our goal in this section, however, is neither to give a complete description of the theory nor to derive explicit formulas, but only to present its results concerning the equilibrium spectra, again from dimensional grounds. Nowadays there are much more complete reviews available, in particular the one of Le Bellac [31], the experimentally focused one of Falcon [17], and the textbooks by Craik [11] and Nazarenko [40].

The most fundamental points of the theory –in my point of view– are two: (i) The universal dependence of the spectrum on the number of interacting waves and; (ii) How many waves interact for each particular kind of system.

We will consider the first point as a statement: The equilibrium range is shaped by the scaling of the energy flux ε, which depends itself on the number N of waves involved in the interaction. Thus, for the spectra of height fluctuations one has:

$$S_\eta \sim \varepsilon^{\frac{1}{N-1}}. \tag{2.48}$$

Let us consider now the number N of interacting waves. For a nonlinear theory to be relevant, the minimum number is 3. But in general, any system may involve a large number of interacting waves. However, for a N-wave interacting system, the evolution of each wave amplitude involve the amplitude of the N others (see [11] for instance). As we are concerned by a weak amplitude limit, the larger is the number of waves, the lower is their contribution to the wave amplitude. Thus, in the more general setting, it is usually a 3-wave interaction process

$$\omega_k = \omega_{k_1} + \omega_{k_2}, \quad \mathbf{k} = \mathbf{k}_1 + \mathbf{k}_2, \tag{2.49}$$

which is dominant. However, sometimes happen that the 3-wave interaction coefficients vanish (actually it happens when (2.49) do not hold) and the dominant nonlinearity involves 4-wave resonances

$$\omega_{k_1} + \omega_{k_2} = \omega_{k_3} + \omega_{k_4}, \quad \mathbf{k}_1 + \mathbf{k}_2 = \mathbf{k}_3 + \mathbf{k}_4. \tag{2.50}$$

A graphical way to see when 3-wave resonances are possible (or not) is to consider the dispersion relation of the particular system (see figure 2.4): One consider two original

[10] Energy in particular, but also the so-called wave action.

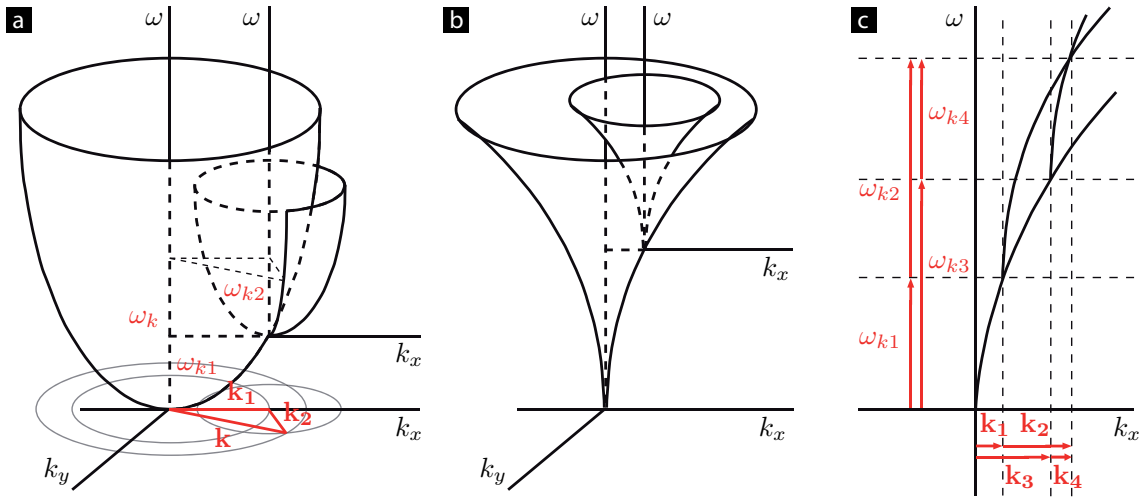

Figure 2.4: Graphical representation for dispersion relations in the form $\omega \sim k^\alpha$. (a) For $\alpha > 1$, 3-wave resonance is allowed in the intersection of surfaces. (b) As $\alpha < 1$, 3-wave resonance is not allowed (c) For the same $\alpha < 1$ as in (b), 4-wave resonance is possible. Figure adapted from Le Bellac [31].

waves, each following the dispersion relation $\omega \sim k^\alpha$. Thus, 3-wave interaction is allowed when there is an intersection between both surfaces $\omega \sim k^\alpha$, where the third wave can emerge (figure 2.4a). This is possible only if $\alpha > 1$. 4-wave resonances are possible whatever is the structure of the dispersion relation (see figure 2.4c). This is why it is not common to be faced to systems with more waves than 4.

It have to be noticed that the water wave problem in deep water is a particular one because it involves two different dynamical regimes: one dominated by gravity and the other dominated by capillarity. Indeed, following the graphical construction we conclude that capillary waves ($\alpha = 3/2$) present a 3-wave resonance and gravity waves ($\alpha = 1/2$) a 4-wave resonance. To face this problem, the common procedure is to consider each regime separately, developing the theory for each case. Moreover, experimental measurements have shown agreement with this picture, in the sense that two different power laws have been observed in the spectrum: one corresponding to gravity waves and other to capillary waves (see [18] for instance).

Dimensional derivation of the surface level spectra [17; 14; 9]: Let us first discuss the frequency spectrum [17; 14], because it is –typically– more accessible in experiments. As we already notice it has dimensions $[S_\eta(\omega)] = L^2T$.

The part of the spectrum concerned with only gravity waves (with $[g] = LT^{-2}$) exhibits the scaling characteristic of 4-wave resonances: $S_\eta(\omega) \sim \varepsilon^{1/3}$. As we has two dimensionless groups: $S_\eta(\omega)\omega^3/\varepsilon^{2/3}$ and $g^3/\varepsilon\omega^3$, the only combination of them respecting the scaling for the energy flux gives

$$S_\eta(\omega) \sim \varepsilon^{1/3} g\, \omega^{-4} \qquad \text{for gravity waves.} \tag{2.51}$$

For capillary waves on the other hand, the frequency spectrum $S_\eta(\omega)$ follow the scaling of 3-wave resonances: $\varepsilon^{1/2}$. Here the dimensionless groups are $\frac{\gamma}{\rho}\frac{\omega}{\varepsilon}$ and again $S_\eta(\omega)\omega^3/\varepsilon^{2/3}$.

As before, by looking a combination of these groups that involves the spectrum and the correct scaling for the energy flux, we obtain

$$S_\eta(\omega) \sim \varepsilon^{1/2} \left(\frac{\gamma}{\rho}\right)^{1/6} \omega^{-17/6} \qquad \text{for capillary waves.} \tag{2.52}$$

In order to discuss the wave-number spectrum for gravity and capillary waves, we have to notice that the bidimensional spectrum $S_\eta(\mathbf{k})$ is somehow impractical when performing transformations –via the dispersion relation– between frequency and wave-number domains. Because of this, and doing an implicit hypothesis of isotropy, we will consider the one-dimensional wave-number spectrum $S_\eta(|\mathbf{k}|) = S_\eta(k)$, with dimensions of L^3.

For both gravity waves and capillary waves, we can obtain the scalings starting from equations (2.51) and (2.52) respectively. We perform transformations between frequency and wave-number following the respective dispersion relation $\omega = \sqrt{gk}$ (gravity) and $\omega = \sqrt{\gamma/\rho}\ k^{3/2}$ (capillarity), and we carefully included powers of g or γ/ρ in order to maintain dimensional consistence. We obtain

$$S_\eta(k) \sim \varepsilon^{1/3} g^{-1/2}\ k^{-5/2} \qquad \text{for gravity waves, and} \tag{2.53}$$

$$S_\eta(k) \sim \varepsilon^{1/2} \left(\frac{\gamma}{\rho}\right)^{-3/4} k^{-15/4} \qquad \text{for capillary waves.} \tag{2.54}$$

These predictions for the surface level spectra of gravity–capillary waves, represent a fundamental result of the wave turbulence theory for water waves, and they demonstrate the ability of the theory to describe spectral fluxes in wave systems. Nevertheless, as the water wave case was formulated on a potential theory, it could be hardly appropriate to describe turbulence–generated surface deformation in a general way.

As discussed, the related Phillips spectrum, gives a more phenomenological prediction based on wave singularities. Thus, it has a wider scope than the Wave Turbulence predictions.

In summary, this chapter was devoted to a presentation of turbulence: first we presented classical turbulence (3D, homogeneous and isotropic) as it is the general context of hydrodynamical turbulence. Then we moved to a description of 2D turbulence, with a brief discussion of the experimental difficulties to reach it, in particular for free surface flows. Then we focused on free surface flows, exploring its formulation, its simplest wave-like solutions and some attempts to describe turbulent motion of free surface flows.

Next chapter concerns the experimental setup we use to study a turbulent flow with free surface. After a presentation of the conditions offered by our setup, we will be in a better position to place our experiment in relation to the discussed facets of turbulence.

2.6 Bibliography

[1] Acheson, D. J. *Elementary Fluid Dynamics*. Oxford University Press, 1990.

[2] Andersen, A., Bohr, T., Stenum, B., Juul Rasmussen, J., and Lautrup, B. Anatomy of a Bathtub Vortex. *Physical Review Letters 91* (2003), 104502.

[3] Andersen, A., Bohr, T., Stenum, B., Juul Rasmussen, J., and Lautrup, B. The bathtub vortex in a rotating container. *Journal of Fluid Mechanics 556* (2006), 121–146.

[4] Balkovsky, E., Falkovich, G., and Fouxon, A. Intermittent Distribution of Inertial Particles in Turbulent Flows. *Physical Review Letters 86* (2001), 2790–2793.

[5] Barenblatt, G. I. *Similarity, self-similarity, and intermediate asymptotics*. Consultants Bureau, 1979.

[6] Brocchini, M., and Peregrine, D. H. The dynamics of strong turbulence at free surfaces. Part 1. Description. *Journal of Fluid Mechanics 449* (2001), 225–254.

[7] Bush, J. W. M. Surface Tension Module, 1.63J/2.21J Fluid Dynamics course. MIT. Available on (link checked on april 2013) `http://web.mit.edu/1.63/www/Lec-notes/Surfacetension/Lecture1.pdf`.

[8] Clanet, C. Waterbells and Liquid Sheets. *Annual Review of Fluid Mechanics 39* (2007), 469–496.

[9] Connaughton, C., Nazarenko, S., and Newell, A. C. Dimensional analysis and weak turbulence. *Physica D 184* (2003), 86–97.

[10] Couder, Y. Two-dimensional grid turbulence in a thin liquid film. *Journal de Physique Lettres 45* (1984), 353–360.

[11] Craik, A. D. D. *Wave interactions and fluid flows*. Cambridge University Press, 1985.

[12] Cressman, J. R., and Goldburg, W. I. Compressible Flow: Turbulence at the surface. *Journal of Statistical Physics 113* (2003), 875–883.

[13] Düring, G., and Falcón, C. Symmetry Induced Four-Wave Capillary Wave Turbulence. *Physical Review Letters 103* (2009), 174503.

[14] Falcón, C. Private communication., 2009.

[15] Falcón, C., Falcon, E., Bortolozzo, U., and Fauve, S. Capillary wave turbulence on a spherical fluid surface in low gravity. *EPL 86* (2009), 14002.

[16] Falcón, C., and Fauve, S. Wave-vortex interaction. *Physical Review E 80* (2009), 056213.

[17] Falcon, E. Laboratory experiments on wave turbulence. *Discrete and Continuous Dynamical Systems 13* (2010), 819–840.

[18] Falcon, E., Laroche, C., and Fauve, S. Observation of Gravity-Capillary Wave Turbulence. *Physical Review Letters 98* (2007), 094503.

[19] Falkovich, G., Weinberg, A., Denissenko, P., and Lukaschuk, S. Floater clustering in a standing wave. *Nature 435* (2005), 1045–1046.

[20] Franco, A., and Falcón, C. Spatial Statistics of Capillary Wave Turbulence. submitted, 2013.

[21] Fridman, A. M., Polyachenko, E. V., Torgashin, Y. M., Yanchenko, S. G., and Snezhkin, E. N. On the possibility of experimental detection of the over-reflection instability. *Physics Letter A 349* (2006), 198–211.

[22] Fridman, A. M., Snezhkin, E. N., Chernikov, G. P., Rylov, A. Y., Titishov, K. B., and Torgashin, Y. M. Over-reflection of waves and over-reflection instability of flows revealed in experiments with rotating shallow water. *Physics Letter A 372* (2008), 4822–4826.

[23] Frisch, U. *Turbulence*. Cambridge University Press, 1995.

[24] Gibert, M., Xu, H., and Bodenschatz, E. Where do small, weakly inertial particles go in a turbulent flow? *Journal of Fluid Mechanics 698* (2012), 160–167.

[25] Goodridge, C. L., Tao Shi, W., and Lathrop, D. P. Threshold dynamics of singular gravity-capillary waves. *Physical Review Letters 76* (1996), 1824–1827.

[26] Greffier, O., Amarouchene, Y., and Kellay, H. Thickness Fluctuations in Turbulent Soap Films. *Physical Review Letters 88* (2002), 194101.

[27] Herterich, K., and Hasselmann, K. The Horizontal Diffusion of Tracers by Surface Waves. *Journal of Physical Oceanography 12* (1982), 704–711.

[28] Kamp, L. P. J. Strain-vorticity induced secondary motion in shallow flows. *Physics of Fluids 24* (2012), 023601.

[29] Lamb, H. *Hydrodynamics*. Cambridge University Press, 1895.

[30] Landau, L., and Lifchitz, E. *Mécanique des Fluides*. Mir, 1971.

[31] Le Bellac, M. An introduction to Zakharov theory of weak turbulence. In *Peyresq Lectures on Nonlinear Phenomena*. World Scientific, 2000.

[32] Lighthill, J. *Waves in Fluids*. Cambridge University Press, 1978.

[33] Lukaschuk, S., Denissenko, P., and Falkovich, G. Nodal patterns of floaters in surface waves. *The European Physical Journal Special Topics 145* (2007), 125–136.

[34] Marteau, D., Cardoso, O., and Tabeling, P. Equilibrium states of two-dimensional turbulence: An experimental study. *Physical Review E 51* (1995), 5124–5127.

[35] Maxey, M. R. The gravitational settling of aerosol particles in homogeneous turbulence and random flow fields. *Journal of Fluid Mechanics 174* (1987), 441–465.

[36] Miles, J. W. On the reflection of sound at an interface of relative motion. *Journal of the Acoustical Society of America 29* (1957), 226–228.

[37] Moisy, F., Morize, C., Rabaud, M., and Sommeria, J. Decay laws, anisotropy and cyclone–anticyclone asymmetry in decaying rotating turbulence. *Journal of Fluid Mechanics 666* (2011), 5–35.

[38] Monchaux, R., Bourgoin, M., and Cartellier, A. Preferential concentration of heavy particles: A Voronoï analysis. *Physics of Fluids 22* (2010), 103304.

[39] Monchaux, R., Bourgoin, M., and Cartellier, A. Analyzing preferential concentration and clustering of inertial particles in turbulence. *International journal of multiphase flow 40* (2012), 1–18.

[40] Nazarenko, S. *Wave Turbulence*. Springer, 2011.

[41] Newell, A. C., and Rumpf, B. Wave Turbulence. *Annual Review of Fluid Mechanics 43* (2011), 59–78.

[42] Ouellette, N. T., and Gollub, J. P. Dynamic topology in spatiotemporal chaos. *Physics of Fluids 20* (2008), 064104.

[43] Phillips, O. M. The equilibrium range in the spectrum of wind-generated waves. *Journal of Fluid Mechanics 4* (1958), 426–434.

[44] Phillips, O. M. The Kolmogorov spectrum and its oceanic cousins: a review. *Proc. R. Soc. Lond. A 434* (1991), 125–138.

[45] Polvani, L. M., McWilliams, J. C., Spall, M. A., and Ford, R. The coherent structures of shallow-water turbulence: Deformation-radius effects, cyclone/anticyclone asymmetry and gravity-wave generation. *Chaos 4* (1994), 177.

[46] Ribner, H. S. Reflection, transmission, and amplification of sound by a moving medium. *Journal of the Acoustical Society of America 29* (1957), 435–441.

[47] Sanli, C., Lohse, D., and van der Meer, D. From antinode clusters to node clusters: The concentration dependent transition of floaters on a standing Faraday wave. submitted, 2013.

[48] Sarpkaya, T. Vorticity, free surface, and surfactants. *Annual Review of Fluid Mechanics 28* (1996), 83–128.

[49] Savelsberg, R. *Experiments on free-surface turbulence*. PhD thesis, Technische Universiteit Eindhoven, 2006.

[50] Segur, H., and Grimshaw, R. Course Lectures, 2009 Program of Studies: Nonlinear Waves. WHOI-2010-01. Whoods Hole Oceanographic Institution. January 2010. Available on (link checked on april 2013) `http://www.whoi.edu/main//gfd/proceedings-volumes/2009`.

[51] Sommeria, J. Experimental study of the two-dimensional inverse energy cascade in a square box. *Journal of Fluid Mechanics 170* (1986), 139–168.

[52] Tabeling, P. Two-dimensional turbulence: a physicist approach. *Physics Reports 362* (2002), 1–62.

[53] Tsai, W. T., and Yue, D. K. P. Computation of nonlinear free-surface flows. *Annual Review of Fluid Mechanics 28* (1996), 249–278.

[54] Vivanco, F., and Melo, F. Experimental study of surface waves scattering by a single vortex and a vortex dipole. *Physical Review E 69* (2004), 026307.

Chapter 3

Generation and measurements in our Magnetohydrodynamical flow

This chapter is devoted to the description of the experimental setup that allowed us to create a confined-free-surface turbulent flow. It also includes a discussion about the expected characteristics of the flow, and the description of the experimental techniques we used to perform quantitative measurements.

We will start with a global view of the experimental setup, in order to introduce the possibilities of our Magnetohydrodynamical forcing. Next we will enter into the details of the main elements in the setup, including the physical properties of the conducting fluid used to perform experiments. Then we will discuss some important dimensionless numbers relevant to our experiment.

Concerning measurement techniques, in a recent review about Magnetohydrodynamical Turbulence, published in the *Annual Review of Fluid Mechanics*, Knaepen & Moreau wrote [15]:

> Accurate measurements in MHD flows are challenging and hardly achievable. Most of the liquids concerned are either opaque, corrosive, or very hot. [...]

With this encouragement, we will present the techniques we retained: for velocity measurements we used particle tracking velocimetry (PTV); to measure the surface elevation we performed both punctual measurement using an inductive sensor and measurements along a line by using an original optical method.

We will finish this chapter giving some place to a complementary experiment that allowed us to obtain the experimental value of the interfacial tension.

3.1 Experimental setup

We perform experiments using a magnetohydrodynamical forcing to create fluid motion. This means that instead of a mechanical excitation we induce a body force: The Lorentz force (also known as Laplace force) $\mathbf{F}_L = \mathbf{J} \times \mathbf{B}$, where $\mathbf{J}$ is the density of current and $\mathbf{B}$ the magnetic field. In order to impose an electrical current defining $\mathbf{J}$, the fluid medium

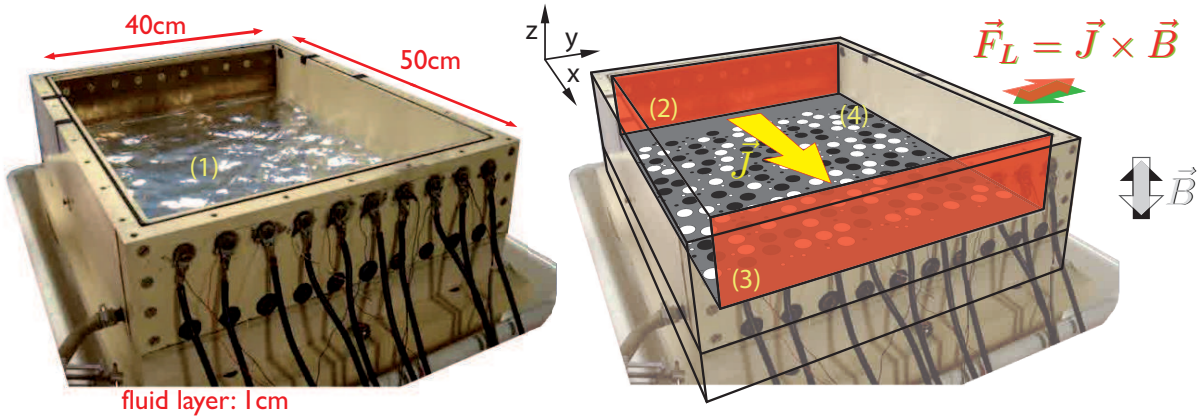

Figure 3.1: General view of the experimental setup, and principle of the forcing.

should conduct electricity, and the more conductive it is, the more effective the forcing will be. Similarly, the stronger the magnetic field, the stronger the forcing will be. But as homogeneous **J** and **B** will produce an homogeneous F to be compensated by pressure gradients, it is important to include some variability in **J** or **B** or in both.

In figure 3.1 there is a schematic representation of our experiment and the fundamental elements that allows us to have free-surface turbulent motion. (1) corresponds to the conducting fluid (a liquid metal in this case) in which current is able to go through. (2) and (3) are two electrodes which are connected to the conducting fluid in a way that promotes a homogeneous distribution of current. Beneath the fluid layer, (4) there is an array of permanent magnets which are arranged in a heterogeneous manner, in the same spirit as the experiments initiated by Bondarenko and collaborators [5] and pursued by Tabeling *et al.*[32]. This arrangement defines the geometry of the principal component of F, which in our configuration is in the $y-$direction.

It should be noticed that by using this kind of forcing, there is almost no risk of suffering parasite mechanical vibrations, because the only motion visible in the lab is the one of the fluid. The experimentalist is usually moving around also, but he has a strong interest in not perturbing the experiment.

We now move on to a more detailed description of the previously mentioned elements, as well as of the setup characteristics.

3.1.1 Container

We use a rectangular container of available volume $40 \times 52 \times 12$ cm^3, bounded by insulating plastic walls. x and y walls are 3 cm thick. Two brass electrodes are placed at the walls in $y-$direction and the use of ten perfectly impermeable connectors (also made of brass) allows to connect the electrodes from the interior to external wires, without any risk of leaking. At the top of the container we usually put a plexiglass plate, in order to keep the surface of the fluid visible. The bottom wall is thin (0.8 cm), in order to minimize the

Figure 3.2: Power supply.

distance to the magnets, while still keeping the mechanical resistance against buckling. Beneath this layer, there is a drawer system, which allows to easily change from one array of magnets to another.

The maximal working area is 40×50 cm^2 considering 1 centimeter to each electrode, and it could be reduced (adding plastic blocs to x-walls) in order to get different aspect ratios.

When placing the whole system on the table, we carefully control horizontally by regulating its 3 supports.

3.1.2 Electrical Current

A *Sorensen DHP Series* Power Supply allows us to have an electrical current I between two electrodes placed at opposite $x-$walls. Given the good conductivity properties of the fluid, I could go from 0 to 600 A with less than a Volt. By dividing the electrical current in the 10 wires connected to each electrode (see figures 3.1 and 3.2 back), we expect a nearly homogeneous density of current $\vec{J}$ in the y direction. Provided the use of a J3 connector (see figure 3.2 back), we can both remotely control the current input, and record the temporal signal of the output current and voltage.

For an imposed electrical current of 300 A, we present the response of the circuit in figure 3.3. We present a typical raw signal of current I recorded on an acquisition card, as well as the corresponding frequency spectrum for both current and voltage. The black line in figure 3.3a shows the recorded signal for one second. As it seems very fluctuating one can ask the question about the influence of fluid motion in the electrical circuit. As fluid motion needs both electrical current and magnetic field, we left out the magnetic field to answer this question. In figures 3.3a, 3.4 and 3.5 we considered both cases: when there is fluid motion (in black) and when the fluid is static (in blue), because the magnetic field is absent.

From figure 3.3a, one can see that current signals are qualitatively identical with and without fluid motion. Indeed, power spectral densities (PDS) of these signals show no important content at low frequencies, as it is shown in figure 3.3b for the case in black, when there is fluid motion. PDS for the static case show no perceptible difference (not shown). In conclusion high frequency fluctuations come from the Power Supply and are independent of the flow conditions. This precludes a detailed consideration of the statistics

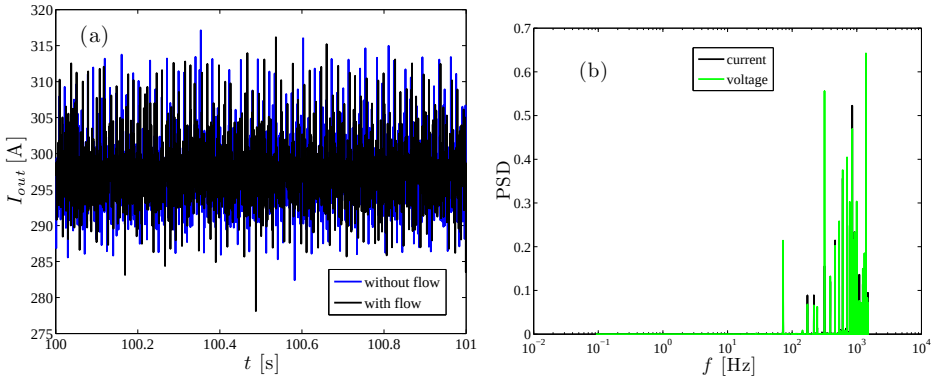

Figure 3.3: Example of the response of the system under imposed electrical current; and comparison between typical experimental condition (with magnetic field and fluid motion) and only the electrical circuit (without magnetic field and no fluid motion). (a) Signal of electrical current without fluid motion (blue) and with fluid motion (black). (b) Power Spectral Density of current (black) and voltage (green) signals for the case with magnets.

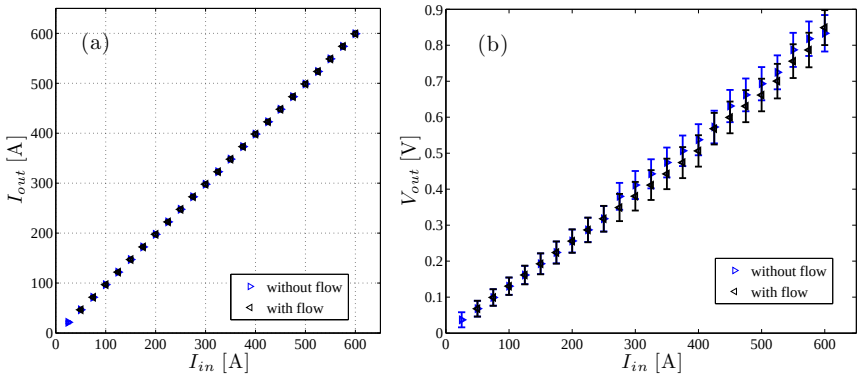

Figure 3.4: Response of the system as a function of the imposed current. (a) Output current as measured with the interface, as a function of imposed current. Imperceptible error-bars are included. (b) Output voltage as a function of imposed current. Error-bars are included based on standard deviation about the mean value.

of injected power, for instance.

However, as there are not many low frequency fluctuations, signals can be considered as stationary. This feature can also be seen when considering the mean registered value of the current

$$I_{output} = \overline{I} = \frac{1}{T}\int_0^T I(t)dt, \tag{3.1}$$

and its standard deviation

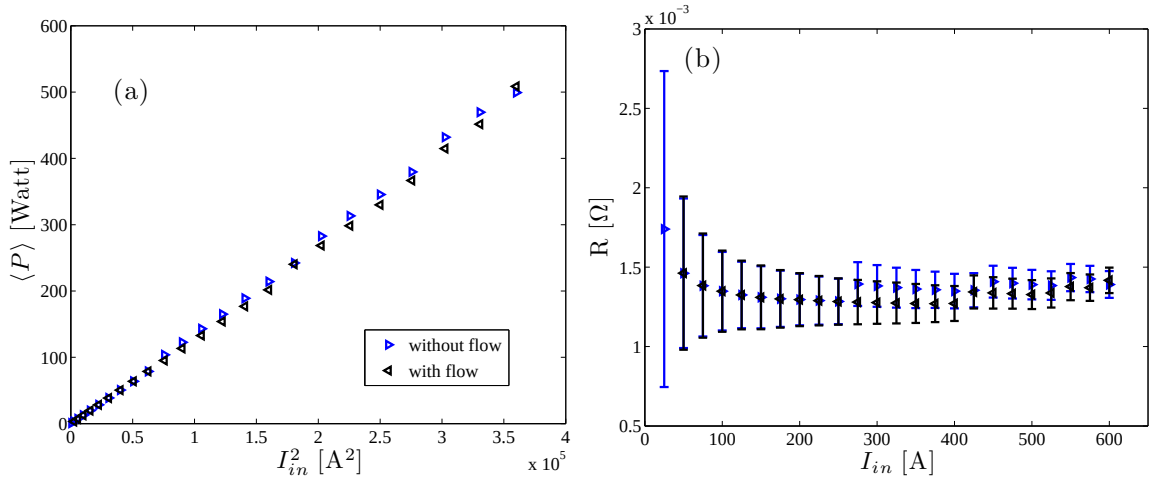

Figure 3.5: Power and Resistance. The electrical circuit (without flow) is compared with typical experimental conditions (with flow), as in figure 3.4. On the left there is the electrical Power $P = I \cdot V$ as a function of I^2. On the right there is the Resistance $R = V/I$ as a function of I.

$$\sigma_I = \sqrt{\frac{1}{T}\int_0^T (I(t) - \overline{I}\,)^2 dt}, \tag{3.2}$$

where $T = 300$ s. This I_{out} is plotted in figure 3.4a, for a set of imposed currents I_{in}, together with error bars computed from σ_I for each case. They are typically of a few Amperes, which correspond to symbol sizes in this series. They are thus imperceptible. A clear 1 slope is observed. Therefore, the electrical current seem a reliable parameter to control the experiment. This will be referred later as a measure of the forcing strength.

Figure 3.4b shows the equivalent analysis for the recorded voltage signals, in which it is apparent that voltage is generally less than 1 Volt. We can also see that standard deviation is larger, which is not surprising as we control the current.

The electrical resistance of a linear circuit is given by the relation

$$R = V/I, \tag{3.3}$$

in which R fluctuates in the same way as I and V do. Although some variability can be observed in figure 3.5b, one can consider its mean value is

$$\overline{R} = 1.4 \cdot 10^{-3}\ \Omega,$$

as a reference. The injected electrical power can be obtained in a similar way

$$P = I \cdot V \tag{3.4}$$

and it appears to fit reasonably well the expression $\langle P \rangle = \overline{R} \cdot I^2$, as shown in 3.5a.

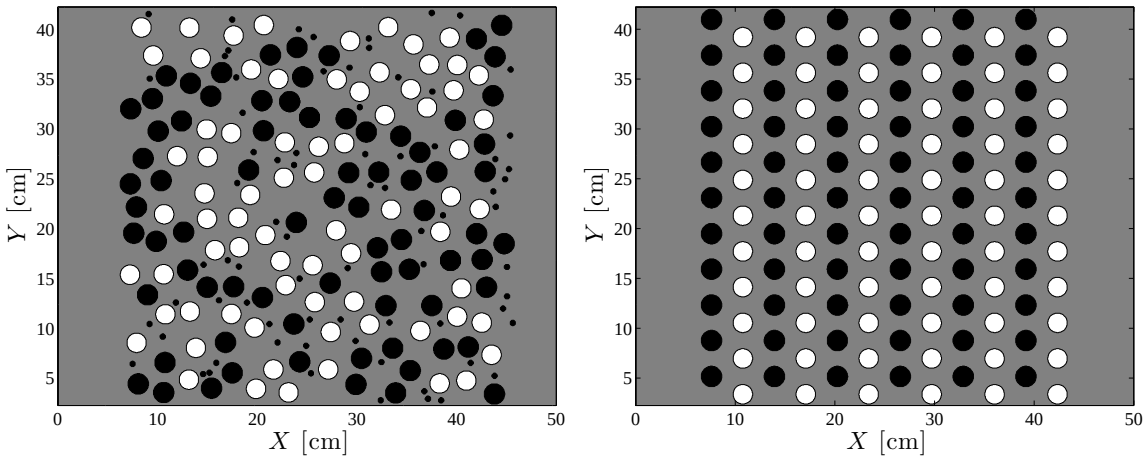

Figure 3.6: Arrangement of magnets used in the experiment. Black and white correspond to different polarities. The arrangement are called *Random* (left) and *Regular* (right).

3.1.3 Magnetic field

Beneath the container, we put a set of permanent magnets arranged in a specific way. The arrangement is characterized by the positions, sizes and polarities of the magnets. They define the spatial distribution of the magnetic field $\mathbf{B}$, fixing the geometry of the forcing (as $\mathbf{J}$ is roughly homogeneous and perpendicular to the vertical component of $\mathbf{B}$).

We use strong neodynium iron magnets of two sizes: Large ones are 2 cm in diameter, with a maximum magnetic field of 3000 Gauss (or 0.3 Tesla) at their surface. The small ones are 0.5 cm in diameter with a maximum magnetic field of 500 Gauss.

We arranged the magnets in two ways: one regular as presented in figure 3.6–right and the other random 3.6–left. For the regular case we fixed the positions in a hexagonal pattern and we used only the larger magnets.

For the random array of magnets, the positions (x, y) were chosen as random variables, respecting a balance of polarity and including the two magnet sizes, in order to reduce the size's spectral signature. In this way, we expect to produce a flow less dependent of the forcing, and more appropriate to observe cascade phenomena.

However, in order to better describe the obtained flow, it is useful to get a typical length scale for the forcing. To do so, we measure the distances between centers of the magnets (considering only the large diameter ones), and we compute the mean value for both arrangements:

$$L_m = 3.63 \text{ cm} \quad \text{for the random array,}$$
$$L_m = 3.83 \text{ cm} \quad \text{for the regular array.}$$

At the surface of the container, 8 mm above the surface of the magnets, the magnetic field of a permanent magnet is measured to be of 1200 Gauss. In one case (for the random array), we performed a careful spatial measurement of the magnitude of the vertical component of the magnetic field (figures 3.7 and 3.8): Using a personal computer, we controlled the position of a probe connected to a Gaussmeter *LakeShore*, and we

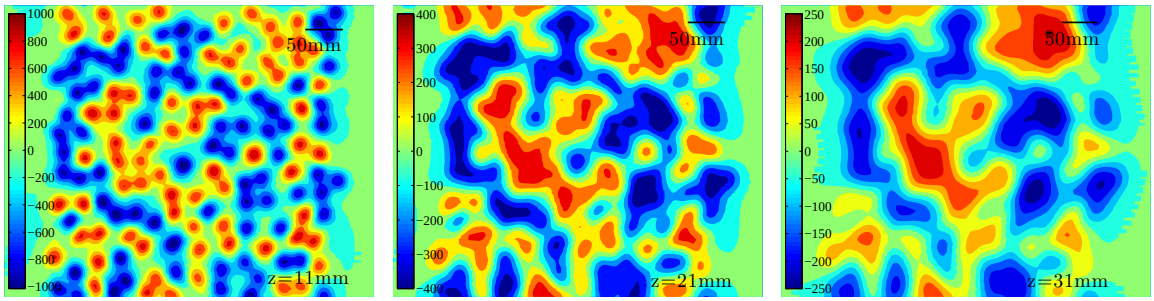

Figure 3.7: Measured magnetic field $B_z(x, y, z)$ for the random forcing, at three distances from the magnets. $z_1 = 11$ mm (left), $z_2 = 21$ mm (middle) and $z_3 = 31$ mm (right). Note that the color code is different in each figure.

simultaneously recorded one scalar value of the magnetic field (B_z in this case). After reconstruction, we ended up with a complete cartography of B_z in the plane (x, y) for a given height z, as shown in figure 3.7, for three values of the distance from the magnet's surface z: $z_1 = 11$ mm, $z_2 = 21$ mm and $z_3 = 31$ mm. In this way, the first plane 3.7a corresponds to the field in the core of the flow, but still close to the bottom of the cell (at 3 mm in distance). The second plane 3.7b is slightly above the surface of the liquid metal, and the third plane 3.7c is still further. This shows that we are far from having a $z-$homogeneous magnetic field. Instead, we have non negligible magnetic gradients.

A process of homogenization is apparent from figure 3.7: B_z evolves in z in a quite diffusive way: the original strong horizontal gradients of the vertical magnetic field evolve in z towards a more homogeneous (and weak) field.

To emphasize the vertical decrease of B_z (already visible from the color bars in figure 3.7), we show its representation in figure 3.8a: this time the colorbar is fixed, in order to see that the magnitude of B_z strongly reduces as z increases. This is also visible in the cut at $y = 133$ mm (figure 3.8b). Figure 3.8c shows a punctual measurement above a magnet, in which the z dependence is fitted with an exponential

$$|B_z(x_0, y_0)| \sim \exp(-\lambda z),$$

with $\lambda = 1.28$.

One would have expected, as a zero order approximation, a resulting magnetic field being a linear superposition of independent dipoles associated to each magnet position. Such a situation implies a decrease on z^{-3}. Nevertheless, even for a single magnet, the picture seems to be an over simplification. Indeed Figueroa *et al.* [10] measured a $\lambda = 2.05$ for a MHD experiment with electrolyte. In our experiment, this decrease could be reenforced by a kind of collective effect on the decay process.

Moreover, by simulating a diffusive evolution[1] of the magnetic field starting from its spatial shape at the origin (figure 3.6), we accurately recover the spatial structure of B_z as measured with the Gaussmeter at different heights (figure 3.7), and we can determine

[1]We considered $\partial B_z/\partial z = D_{\text{sim}}\nabla^2 B_z$, where D_{sim} is a constant determined by comparing the simulation results with the experimental measurements of figure 3.7.

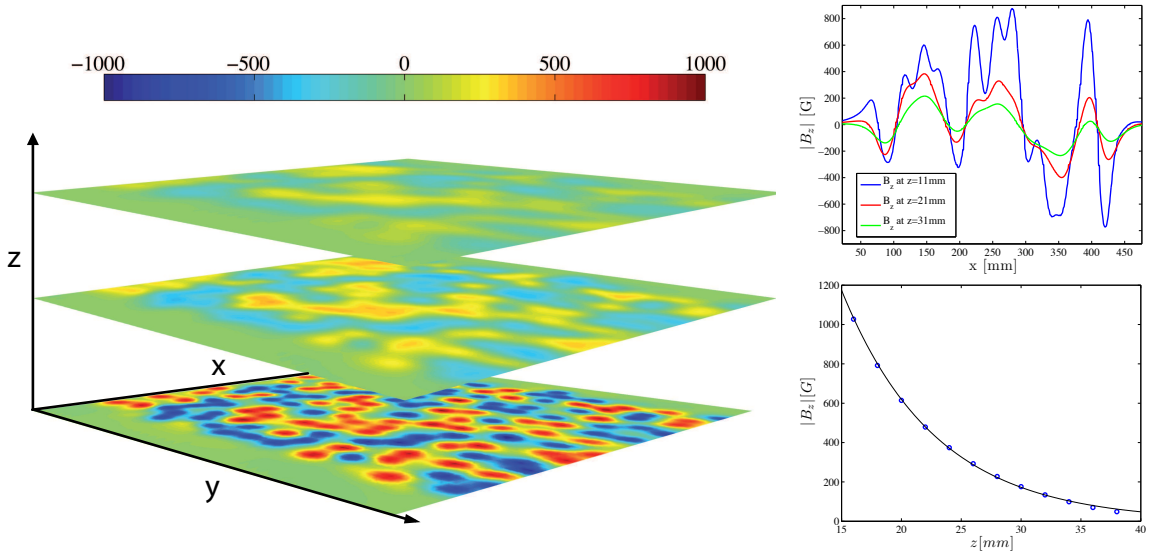

Figure 3.8: Variation of the magnetic field $B_z(x, y, z)$ on z. (a) schematic representation (not on scale). (b) Cut at fixed y. (c) Measurement above a magnet: Blue points correspond to the experimental measurement, and the black line is an exponential fit (see text).

an empirical diffusion coefficient D_{sim}. By using this coefficient, we know the shape of $B_z(x, y, z)$ for any forcing geometry. In particular for the regular one (not shown). However, as we noticed, the physical origin of this phenomenon remains unclear and deserves further consideration.

3.1.4 Conducting Fluid

The conducting fluid we use is a liquid metal known as Galinstan (or GaInSn). It is an alloy made of 68.5% of Gallium, 21.5% of indium, 10% of Tin, which is liquid above –19° C, and in particular at room temperature.

The density of galinstan is $\rho_g = 6440$ kg/m^3; its electrical conductivity is $\sigma_e = 3.46 \times 10^6$ S/m; its kinematic viscosity is $\nu = 3.73 \times 10^{-7}$ m^2/s.

In contact with the air, the surface of the liquid metal oxides, drastically changing the surface properties. Indeed a solid layer rapidly forms. To prevent this effect we cover the surface with Hydrocloric acid (HCl) in low concentration ($< 1\%$). As we do not want to perturb the galinstan-acid interface by the acid-air (or acid-plexiglas) interface, the depth of acid we put should exceed 5 cm in order to keep the acid in a deep water regime. Usually we put as much acid as we are able to put in the cell, which is close to 10 cm in depth.

As the density of the acid is essentially the one of water, which is 6 times lower than the galinstan's, the surface can be considered stress free. The interfacial tension of this acid–galinstan interface can be measured to be 0.5 N/m (the procedure to measure it will be described in section 3.5).

For comparison, the properties are summarized in the table 3.1, together with the values for other conducting fluids.

3.2 Dimensionless numbers and expected values

We have presented the characteristic magnitudes of the experiment for the given density of current J, the magnetic field B and the length scale L. For this last one, several choices are possible (container's size, mean distance between magnets, or fluid depth). We also have presented some important physical properties of our liquid metal. Now we have all the necessary ingredients to estimate the dynamical properties of the flow.

The equations of MHD, that govern the velocity field $\mathbf{u}$ and the magnetic field $\mathbf{B}$ are, (i) the Navier Stokes equation 2.18 with the Lorentz force

$$\rho\left(\frac{\partial \mathbf{u}}{\partial t} + (\mathbf{u}\cdot\nabla)\,\mathbf{u}\right) = -\nabla p_d + \mu\nabla^2\mathbf{u} + \mathbf{J}\times\mathbf{B}, \tag{3.5}$$

and (ii) the induction equation

$$\frac{\partial \mathbf{B}}{\partial t} + (\mathbf{u}\cdot\nabla)\,\mathbf{B} = (\mathbf{B}\cdot\nabla)\,\mathbf{u} + \frac{1}{\mu_0\sigma_e}\nabla^2\mathbf{B}, \tag{3.6}$$

where $\mu_0 = 4\pi\cdot 10^{-7}$ N/A^2 is the vacuum permeability (constant); and σ_e is the electrical conductivity of the fluid. The induction equation is obtained from Maxwell's equations and Ohm' law $\mathbf{J} = \sigma_e(\mathbf{E}+\mathbf{u}\times\mathbf{B})$, and it show how the magnetic field can be advected by the velocity field, depending with the parameters associated to the system (we will come back to this).

From equation 3.5, it is possible to construct a characteristic velocity by considering the balance between the advection and forcing terms $\rho\,(\mathbf{u}\cdot\nabla)\;\mathbf{u} \sim \mathbf{J}_0\times\mathbf{B}_0$, meaning that the forcing is fundamentally translated into fluid motion by non-linearity. This gives the estimate

$$U_0 = \sqrt{\frac{J_0 B_0 L}{\rho}}, \tag{3.7}$$

which implicitly assumes stationarity (at least in a statistical sense), and that the forcing dominates over dissipation (gravity does not enter into the analysis, as the mean direction of the forcing is orthogonal).

Table 3.1: Comparison of the physical properties for different liquids and liquid metals. ρ is the density, ν is the kinematic viscosity, γ is the surface tension and σ_e is the electrical conductivity.

	ρ [kg/m^3]	ν [m^2/s]	γ [N/m]	σ_e [1/Ω m]
Galinstan	6440	3.73×10^{-7}	0.5	3.46×10^{6}
Gallium	6080	3.24×10^{-7}	0.7	3.7×10^{6}
Mercury	13600	1.1×10^{-7}	0.4	
Sodium	930	10^{-6}	–	10^{7}
Water	1000	10^{-6}	0.073	

If we consider $L \sim 3$ cm, corresponding approximately to the magnets scale, one has

$$6\,\mathrm{cm/s} < U_0 < 30\,\mathrm{cm/s},$$

but if we take $L = 50$ cm (container size), the velocity will be about one order of magnitude larger. In the following evaluations we will stay with the former.

We retained the scaling (3.7) and not the alternative, linear one: $U_0 = J_0 B_0 L^2/\rho\nu$, valid for a flow dominated by viscous damping (considering this time $\rho\nu\triangle\mathbf{u} \sim \mathbf{J}_0 \times \mathbf{B}_0$). This is because it gives an estimate of U_0 larger than 360 m/s, which is inconsistent with a flow dominated by viscosity.

3.2.1 Hydrodynamical numbers

The first dimensionless number we consider is Reynolds number

$$Re = \frac{U_0 L}{\nu} = \sqrt{\frac{B_0 L^3 J_0}{\nu^2 \rho}}, \tag{3.8}$$

which in our system corresponds to

$$5 \cdot 10^3 < Re < 2.5 \cdot 10^4.$$

The flow is turbulent in this sense.

It can be noticed that the expression $Re = \sqrt{B_0 L^3 J_0/\nu^2\rho}$ contains almost only fixed parameters, with the exception of the control parameter $J_0 = I_0/S$, with S the surface of the electrodes in contact with the fluid (also fixed). This means that we have a clear expected growth of Re as $\sqrt{I_0}$, valid for turbulent flows.

For a thin layer of fluid –two dimensional in first approximation–, friction at the bottom can play an important role in the flow dynamics and energy transfer, since it acts as a linear damping modifying the bidimensional Navier-Stokes equation. The damping is of order $\nu/(H\delta)$, where δ is the characteristic length scale of the bottom boundary layer and H the layer's thickness. The flow is then quantified by $Re_h = (H\delta/L^2)Re$. As this friction can strongly affect the energy cascade process, it has to be taken into account when the properties of two dimensional turbulence are concerned [34].

As discussed in section 2.4, the free surface adds two extra dimensionless numbers: Froude Fr and Weber We numbers. These numbers quantify how effective gravity and capillarity are against surface deformation and allows a description of the resulting surface features.

In our experiment, Froude number reads

$$Fr = \frac{U_0^2}{gL} = \frac{B_0 J_0}{g\rho}, \tag{3.9}$$

and it ranges as

$$0.01 < Fr < 0.36.$$

Weber number, on the other hand

$$We = \frac{U_0^2 L \rho}{\gamma} = \frac{B_0 J_0 L^2}{\gamma}. \tag{3.10}$$

goes as

$$1.4 < We < 35$$

in our case.

On the light of [6] (see section 2.4), our parameter's set (Re, Fr, We) places us between the regimes referred to as *weak turbulence* (low Fr and low We) and *gravity–dominated turbulence* (low Fr and large We); the latter being the most common regime found in nature. This is consistent with qualitative observation. For low forcing one can observe gentle surface deformation (but still visible thanks to the reflective properties of the surface) and the development of stronger deformation when the forcing is increased. Also, it can be recalled that our Fr numbers are compatible with the hydrodynamical analog of wave generation by turbulence, expected at around 0.05 [28].

The quantification of the deformation features observed in the experiment is the subject of chapter 5.

We have also introduced the capillary length l_c. In our case, a pertinent way to obtain it is from the interfacial dispersion relation, as the crossover length scale for which gravity contribution $(gk\,(\rho_1 - \rho_2)/(\rho_1 + \rho_2))$ equals capillarity contribution $(\gamma k^3\,/(\rho_1 + \rho_2))$:

$$l_c \equiv \frac{1}{k} = \sqrt{\frac{\gamma}{(\rho_1 - \rho_2)g}} = 3 \text{ mm}. \tag{3.11}$$

In other words, deformations smaller than l_c deal with capillarity, and those larger than l_c are treated by gravity. For comparison, a water–air interface has $l_c \sim 2.7$ mm and a mercury–air $l_c \sim 1.7$ mm, so all these 3 interfaces have quite comparable values. In the frequency domain, the crossover between capillary and gravity dominated regimes occurs for

$$f_c = \frac{1}{2\pi}\sqrt{\frac{2g^{3/2}(\rho_1 - \rho_2)^{3/2}}{\sqrt{\gamma}(\rho_1 + \rho_2)}} \sim 11 \text{ Hz}.$$

3.2.2 Magnetohydrodynamical numbers

For conducting fluids, the magnetic field is governed by the induction equation (3.6), as velocity is governed by the Navier-Stokes equation. Also, in an analogous way, the relevance of magnetic field's induction can be described by the so-called Magnetic Reynolds number:

$$Rm = \frac{U_0 L}{\eta_m} = \frac{\tau_{\eta_m}}{\tau_u}, \tag{3.12}$$

where $\eta_m = 1/\mu_0\sigma_e$ is the magnetic diffusivity. $\tau_{\eta_m} = L^2/\eta_m$ gives account of the time scale on which perturbations of the magnetic field diffuse. We compare it to the time scale of advection imposed by the flow. When this ratio is large, the flow has strong action on the magnetic field, and advection overcomes diffusivity. In the limit of $Rm \to \infty$,

magnetic field lines freeze with the streamlines of the flow. This limit can be found in astrophysical flows and in the flows on the earth's core. One effect that is characteristic of this limit –the Dynamo effect– has been observed in laboratory experiments: In the so called von Kármán configuration (a cylinder with two rotating coaxial impellers, one on each side) filled with liquid sodium, one can get Rm of order 70. As the Dynamo onset was reached, the spontaneous emergence of a magnetic field was observed, triggered by turbulent fluctuations of the liquid metal [23; 3].

In the opposite case, for small Rm, disturbances of the magnetic field diffuse very fast (as $\tau_{\eta_m} \ll \tau_u$), so the flow has no effect on the magnetic field. In others words, the induced magnetic field (by the flow of conducting fluid) is negligible compared to the imposed one. Indeed, from equations (3.5) and (3.6), one can see that in this limit (as advection terms in (3.6) are negligible) the magnetic field is decoupled from the velocity field, although this later is still subjected the magnetic field, by means of the Lorentz force.

This small Rm is what we get in most industrial applications and laboratory experiments. It is also our case, as we get

$$0.01 < Rm < 0.04.$$

However, Rm does not tell the whole story about magnetohydrodynamics. Actually, one can estimate the induced current by the imposed magnetic field B_0 and the flow velocity U_0, which roughly opposes the imposed current J_0. It gives $J_{ind} = I_{ind}/S \sim \sigma_e U_0 B_0$, which gives values for I_{ind} that can be as large as 500 A! Indeed, the induced currents are of the same order of magnitude as the imposed one.

What happens is that in the bulk of the fluid (at least in zones where the imposed magnetic field is intense), the electrical current is smeared out by induction into the very thin layer in which velocity vanishes because of viscosity (where induction vanish as well). This creates a boundary layer for the current, the so-called Hartmann boundary layer. We can estimate the thickness of this Hartmann boundary layer as

$$\delta = \sqrt{\frac{\nu\rho}{\sigma_e}}\,\frac{1}{B_0} = 0.22 \text{ mm}. \tag{3.13}$$

This means that, at least in the zones around the magnets (which have a diameter of 2 cm), the forcing is confined into the thin Hartmann layer. So, even if in principle the forcing was expected to be in the volume, it actually acts only in this very restricted vertical zone.

The dimensionless number that compares the thickness δ of the Hartmann boundary, to the height of the fluid layer $h = 10$ mm, is the Hartmann number

$$Ha = \frac{h}{\delta} = 45. \tag{3.14}$$

A very challenging question comes naturally: If the current is concentrated into a thin boundary layer for zones in which B_0 is intense, what happens elsewhere? Does the current have any preference between going into the boundary layer, or completely avoiding regions in which the magnetic field is intense? In any case, it is clear that the interplay of J, B and U in our system is quite complex. In fact, very little is known about

the magnetohydrodynamics for non uniform magnetic fields, despite it being a common forcing tool nowadays.

There is a similar –but opposite– alternative to create a Lorentz force: a uniform strong magnetic field, together with a spatially dependent distribution of current (entering in the liquid metal by an array of punctual electrodes in the bottom of the container). It was studied in detail by Sommeria in the eighties [31] and recently by Gallet, Herault and collaborators [12]. For this configuration the argument given before holds: the current is restricted to the thin Hartmann boundary layer, which is uniform in this case. As explained before, in this case the forcing is restricted to the boundary layer on the walls perpendicular to **B**, and the flow in the bulk can be treated as being free of forcing and dissipation. However, this time it is the distribution of currents that contributes with its complexity.

The development of similar Hartmann boundary layers was recently discussed experimentally for a Taylor–Couette–like configuration by Boisson *et al.* [4]. There, they were able to easily control both the intensity of current and magnetic field in order to get a fixed Lorentz force $|F_0| = |J|\,|B|$. They revealed a non trivial difference between doing so with a strong J (and small B) or with a strong B (and small J). Plausibly the difference comes from the effect of magnetic boundary layers, which develops only for strong B.

We have stated the expected velocities for our experiment, together with its expected surface deformation regimes. Now we present the techniques to be used in order to obtain quantitative measurements.

3.3 Velocity measurements using particle tracking

Particle tracking is a conceptually simple technique to obtain a two dimensional velocity field perpendicular to the plane of observation. The basic idea is to have a set of objects moving in a plane –the *particles*–, and to take pictures of them for consecutive times t and $t + \Delta t$. Then one can find their positions at each time and reconstruct their trajectory, by which one can estimate their velocity during the interval Δt.

To give an illustrative example, we applied this idea to two pictures (figure 3.9) of cars, people and a metro which are moving across a bridge[2], so they are restricted to moving in one direction each, and roughly on a single plane. We approximatively know the time interval between both frames (chosen by hand for a standard camera: around 1 second in this case) and the distance could be obtained by considering reference objects of the photo and comparing them to available tabulated data, from google maps for instance. As a result, for each *object* we obtain an estimation of its mean velocity, for the corresponding interval of time: $v \sim 48$ km/hr for the metro, $v \sim 44$ km/hr for both cars, and $v \sim 5$ km/hr for people. This is why people prefer to take the metro instead of walking (even if the person under study walks very fast), and, as metro and car's speeds are quite similar, this give us some idea of why cars are still so popular in crowded cities.

This example is extremely simple, in the sense that the movement is only one-dimensional, and especially because we can easily identify each *object* by its singular shape, size and

[2]Bir-Hakeim bridge, in Paris

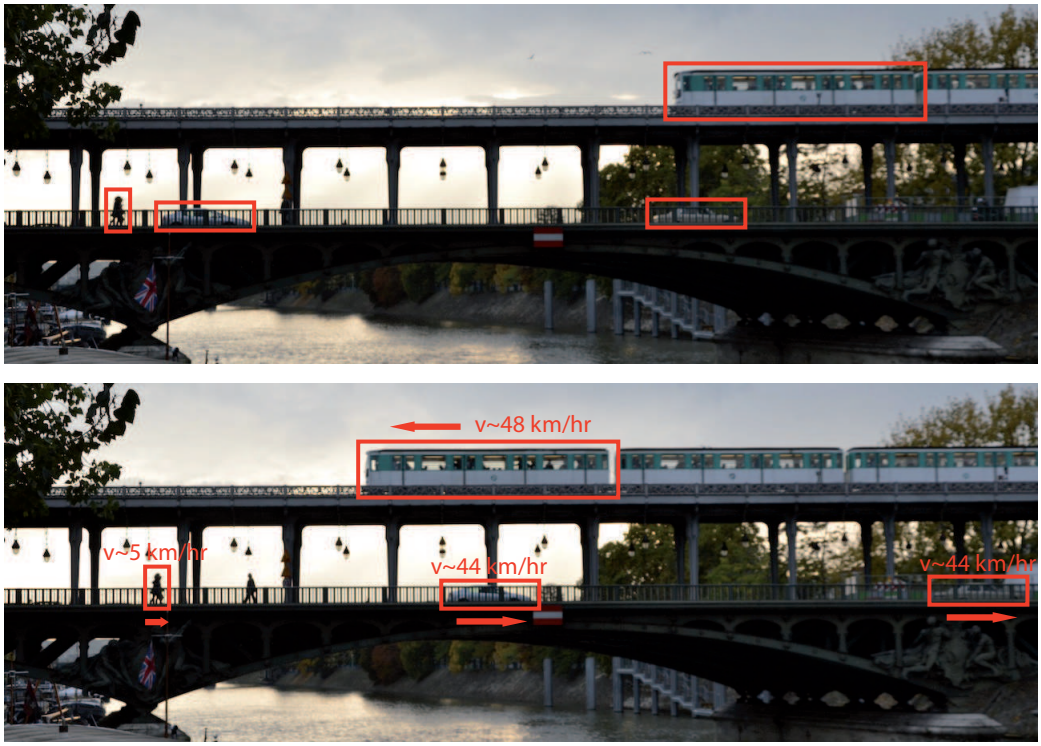

Figure 3.9: The idea behind particle tracking velocimetry.

color. Usually in an experimental tracking problem we do not have those advantages and we have to compensate them by taking very short time intervals in order to chose the correct path followed by each object.

In our case, most of the time we used particles of 1 mm in diameter, with a density of $\rho_p = 2000\ \mathrm{kg/m^3}$, which is close to a third of the density ρ_g of the liquid metal, and around twice the one of the acid. Particles are thus floating on the acid-Galinstan interface. We acquired images of the whole cell of 2000×1700 pixels^2 using a Dalsa camera (model PT–41–04M60–med). This gives particles of around 4 pixels in diameter. Acquisitions were performed at 50 Hz and stored on real time on a PC. As images include the borders of the container, we use its dimensions to obtain coordinates in real units.

We track around 200 particles in each frame, so the filling fraction is very small. In this regime, collision of particles are rare, and it also allows us to successfully reconstruct trajectories instead of the limited acquisition frequency of the camera. Nevertheless, as we will see later, we are not able to consider the evolution between two frames as a complete picture of the velocity field.

Since that the surface of the flow is a deformable mirror, care was taken on lighting, in order to obtain a good contrast between particles and the background (figure 3.10a). For each snapshot, we perform high pass filtering to remove wavy intensity fluctuations in length-scales larger than particle's diameter (figure 3.10b). Then we compute intensity contours of the image and identify particles as the superposition of at least 4 concentrical circles (figure 3.10c). This procedure gives us the position pairs (x, y) within a subpixel resolution. Moreover, for our conditions, this procedure is much more robust than simple

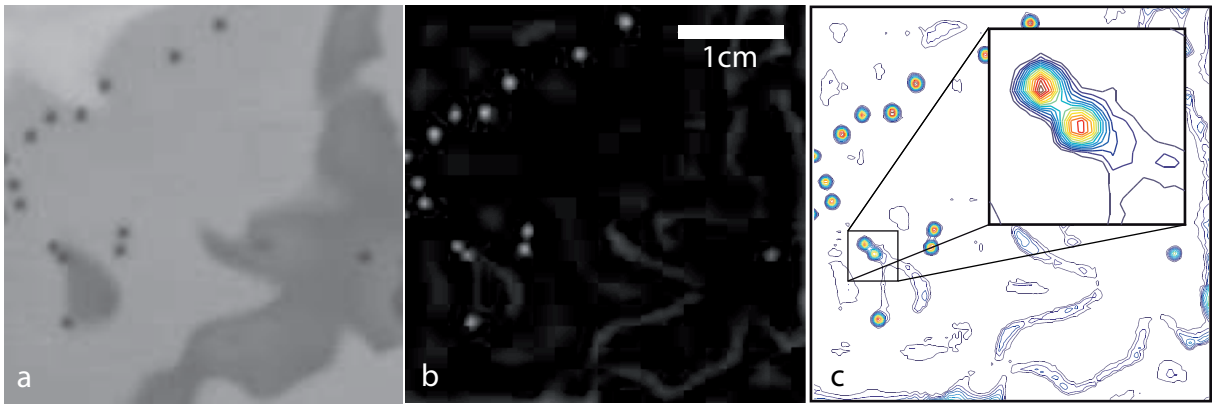

Figure 3.10: Stages of particle's detection using intensity contours: (a) is a part of a typical snapshot; (b) is the same image after the high pass filtering stage, in which wavy intensity fluctuations are removed; (c) shows the intensity contours of (b), from which particles will be identified.

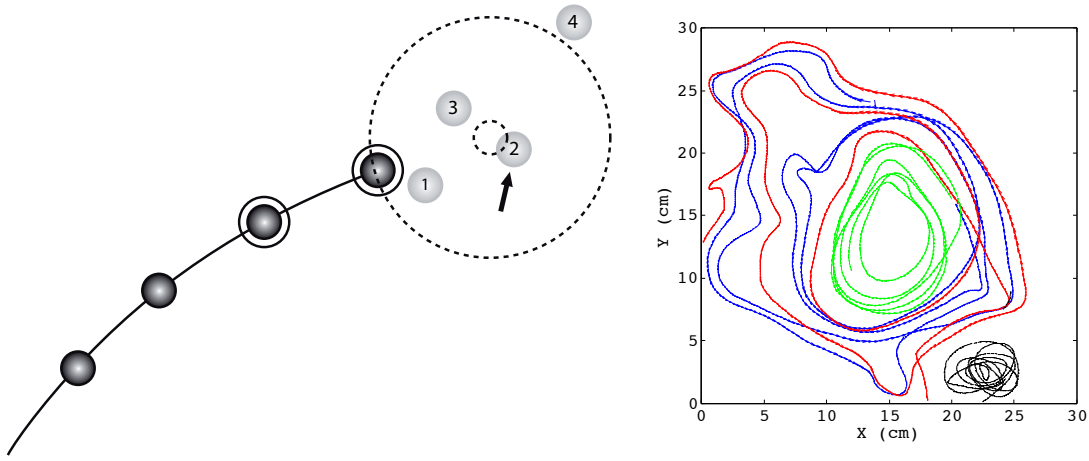

Figure 3.11: Reconstruction of trajectories. (a) Idea of the multi-frame predictive tracking algorithm (adapted from [27]): we drew already reconstructed trajectory points (in black) and some of the points in the next frame, which are candidates to be the subsequent trajectory point (light gray). From last two positions (circled black points) one predicts the expected one (open circle) and then we choose the closest to it (nº 2). In (b) we plot four of the reconstructed trajectories together with its velocities, each one in a different color.

thresholding, because of the strong intensity fluctuations of the background. Although, it is very expensive in terms of the computation time, in particular because the program interpolates the intensity profile when computing several contours, as we do in order to get accurate results (see the inset in 3.10c).

From this data, we compute trajectories using a matlab–implemented multi-frame *predictive tracking algorithm* (PRT) [25; 27]. This algorithm has two principal stages: It

performs a prediction for the position of particles in a frame on the basis of the movement of particles between the previous two frames. Then it chooses the compatible movement of the whole set of particles by minimizing distances between predictions and real positions found, within a given radius. The idea of the method is schematized in figure 3.11a, in which already-found-trajectory-points are drawn in black, together with some of the next-frame-points in light gray (which are the candidates to be the subsequent trajectory point). From the last two positions (circled black points) one predicts the expected next position (open circle) and then we choose the point which is closest to it (nº 2, with the arrow), and we add it as the next point in the trajectory of that particle. Under conflicts, the algorithm stop the trajectories involved, and restarts them as new tracks. If necessary, those trajectories could be re-connected by performing a second *high dimensional* tracking, now in the position-velocity space (instead of only position's space, as we do), as suggested by Xu [38].

It is worth noticing that with a *nearest neighbor tracking algorithm* (NNT), the chosen particle would be nº 1, which is likely to be wrong. That is why a predictive algorithm seems to be more adapted to tracking problems in fluid mechanics. At least it is the case in our experiment, where we performed the comparison between PRT and NNT. A second advantage of this algorithm is its lack of intrinsic velocity cutoffs, as particles are always searched consequently to their previous movement. A detailed comparison between tracking methods in fluid mechanics could be found in [27]. Given the set of trajectories, one can use a convolution kernel in order to obtain directly a filtered velocity field, instead of performing both velocity computation and filtering separately [24].

In summary, from the several alternatives to do particle tracking, we retained the following: The horizontal movement of particles is filmed with a single camera. Particles' position are obtained from snapshots using an intensity's contours technique. From position's data, we reconstruct trajectories using a multi-frame predictive tracking algorithm, from which we compute velocities for each trajectory. As we noticed, both the detection algorithm, and the tracking algorithm were chosen after numerous tests carried out in our experimental data, where those algorithms revealed as the most optimal for our conditions.

3.4 Height measurements

From simple observation of the experiment, one can see interesting features concerning the surface deformation. This is expected because, in opposition to experiments carried out to study two dimensional flows with a similar forcing ([19; 26] for instance), we do not make any effort to reduce vertical motion, and consequently surface deformation is expected to play an important role.

Now we will describe two techniques to measure the surface deformation. The first one is by using a *punctual* inductive sensor, and the second one is an original optical setup that allows to record the deformation along a line.

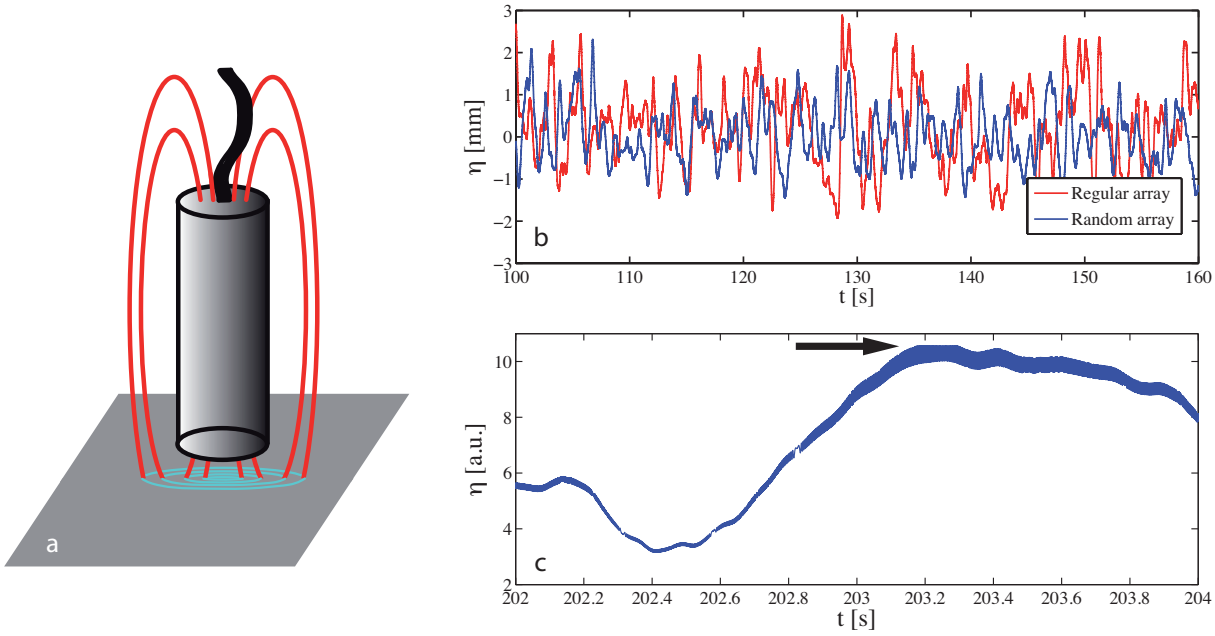

Figure 3.12: Inductive sensor. (a) is a representation of the sensor's principle (see text), in which an induced magnetic field interacts with a conducting material. If the proximity of the material varies, one can observe temporal signals as (b) and (c). (b) shows few seconds of the temporal evolution of the surface height, as detected by a sensor EMD 1003 (diameter 17 mm) for two independent experiments: for the regular forcing (in red) and for random forcing (in blue). In both cases $I = 450$ A. (c) shows an example of saturation for a sensor EMD 1043 (diameter 8 mm) and a rather low imposed current $I = 100A$.

3.4.1 *Punctual* measurement with an inductive sensor

An inductive sensor is a non-intrusive sensor that measures the distance to electrically conducting objects, typically plane rigid ones. It was developed (and is widely used nowadays) in industrial production chains, because it allows to control distances with high precision, and to check the presence/absence of objects without physical contact, even through layers of non-conducting materials.

The working principle is as follows: a high frequency alternative current travels through a coil in the main part of the sensor, generating a time varying magnetic field. When a conducting material is approached, an eddy current is induced on it, dissipating some of the imposed current, implying a change on the resistivity of the circuit. The smaller is the distance between the sensor and the conducting material, the larger is the current dissipation on the sensor circuit. Therefore one can obtain an electrical signal proportional to that distance. An schematic representation is given in figure 3.12a.

For (fast moving) liquid metals, Falcon *et al.*[9] have shown that the response of the sensor is linear with the distance, and that its sensitivity could be better than 1 V/mm. Typical temporal traces are given in figure 3.12b for I = 450 A and for the two forcing geometries.

Its measurement range is proportional to the diameter d of the sensor, starting at the

end of the sensor. Thus it should be placed close to the measured sample. Also, the measured height is the result of the implicit filtering over the area of its section, $\pi\,(d/2)^2$. In fact, the *point* in this *punctual measurement* could be actually huge (around 230 mm^2 for a d=17 mm). The frequencial cut-off associated with the filtering length-scale could be estimated from the dispersion relation (see equation 3.16). Because of this, there is an equilibrium to find between the measurement range and the implicit filtering.

We have tried two sensors of sizes $d_1 = 8$ mm (EMD 1043) and $d_2 = 17$ mm (EMD 1003). One can see that the small sensor starts to saturate at I = 100 A (see the arrow in figure 3.12c), which is close to the smallest forcing we used. Consequently, it is not suitable for our requirements. On the other hand, from visual inspection one could expect height deviations from the mean level as large as 5 mm. In order to avoid saturation at those large deformations, we finally worked with the large sensor. In this case, $\lambda = 17\,mm = 2\pi/k$, corresponds to a frequency of 12 Hz: this is the upper limit at which frequencies can be trusted. It is very close to the crossover frequency between gravity and capillary waves ($f_{CO} = 10.9$ Hz, as discussed in section 3.2), thus we cannot trust the temporal spectrum of capillary waves as obtained with this sensor.

The principal advantages of this local measurement are: (a) It is very easy to use. It only needs to be installed, plugged in and it is ready to measure. However, as an eventual influence of the local magnetic field was not carried out yet, we preferred to perform a calibration at each different measurement position. (b) It requires no post–processing, therefore the data analysis is very fast. (c) The signal can be recorded in real time, thus in this sense it has no practical limitation in temporal resolution. (d) It is non intrusive, as the model we use can be placed far enough from the surface.

The drawbacks of this sensor are: (a) As it is local, it provides no information about spatial structure of the surface deformation. However, as well resolved temporal measurements can give fundamental information about a flow, this could be not a major restriction. (b) Because of its working principle, this sensor performs an intrinsic spatiotemporal filtering defined by its area. As we noticed, the model we used has a diameter of d =17 mm and filter frequencies at around 12 Hz. This is, by far, the most significant drawback of this method.

3.4.2 Global measurements of the surface deformation

Punctual measurements of the fluid height give relevant information (see chapter 5), and in particular with a good time resolution. However, they have some disadvantages: First, the chosen point is somehow arbitrary, and consequently one cannot know a priori if it is a privileged one. Nevertheless, this problem can be tackled by considering more than one point and check whether the results are reproducible, at least in a statistical sense. But a second, and more crucial disadvantage, is that one cannot say anything about the spacial dependence of the height.

Specially to address the question about the spacial dependence of the height for a free surface flow, several non-intrusive techniques have been developed in recent years. It could be interesting to briefly mention some of them:

- *Laser scanning device for measuring the surface gradient on a line:* The idea is to send a vertical laser beam from one side of the free surface (lets say from the

bottom), and to record the deflection of the beam produced by the curvature of the surface. By using both a position sensitive scan, and a rapidly oscillating mirror, it is possible to scan an entire line with a very high temporal resolution. This method, developed by Savelsberg *et al.* [29], was used to study the surface deformation produced by grid turbulence in a channel of water [30].

- *Free-surface synthetic Schlieren:* Moisy *et al.* [22] developed a method that uses the difference in refractive index between two transparent liquids sharing a common interface: a deformed fluid interface can act as an irregular lens that amplifies/reduces any image depending on the local slope of the interface.

  Technically, they image a pattern of random dots, which is amplified/reduced by the deformed interface. By computing correlations with a reference image, they obtain the displacement field, which can be integrated to reconstruct the instantaneous shape of the interface. This method was used to study cross-waves induced by a vertically oscillating plate below a water-air interface [21].

- *Diffusing Light Photography:* This method was introduced by Wright *et al.* [36], pioneering the study of capillary wave turbulence in water. The idea is to put polystyrene particles of 1 μm and to illuminate the fluid from the bottom. As light is scattered by particles, it diffuses through the water. In this way, the camera on the other side will receive an amount of light that is inversely proportional to the local depth: the larger the depth, the larger will be the *loss* of light by diffusion. An important advantage of this technique is that there is no problem with caustics, so it is not limited by large slopes (until there is no true superposition of liquid as when waves break). More recently, this method was used to study over-reflexion of waves [11] and capillary wave turbulence [2]. More details of the method should be found in [35].

- *Fourier transform profilometry:* This method was proposed by Takeda and Mutoh in the eighties [33]: It consist in projecting a fringe pattern over a deformed surface (static at that time), and comparing it to an undeformed reference. The comparison leads to a phase map from which the deformed profile can be reconstructed. More recently, since the contributions of Cobelli and collaborators [7; 20], its applicability was extended to rapidly evolving fluid surfaces. Then it becomes a widely used technique in fluid mechanics [16; 13], as well as in the study of vibrating plates or surface deformation in foams [18]. All those materials having a light-diffusing surface. In particular, reference [7] present a reproducible protocol to turn diffusive the fluid free-surface.

However, all those appealing techniques make use of either light transmission properties or light diffusion properties of the fluid. Liquid metals, on the other hand, are completely opaque, so there is no transmission of light, and the diffusion of light in the surface is very small (but not zero). So the previously mentioned techniques are not suitable to measure the height in liquid metals.

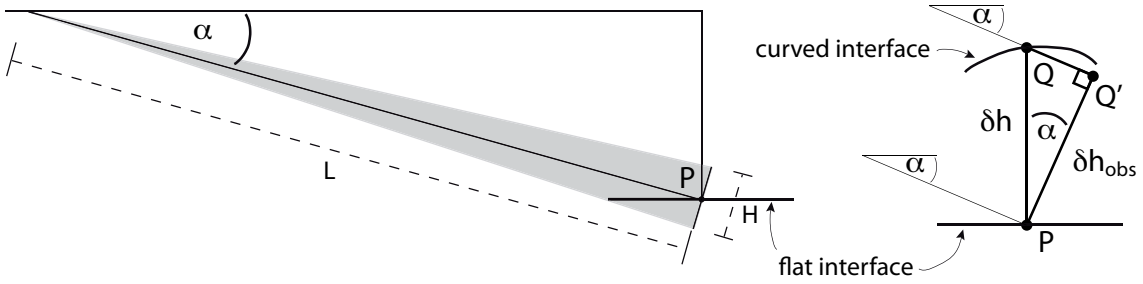

Figure 3.13: Geometry linking the observed displacement δh_{obs} and the vertical displacement δh, in the paraxial approximation.

3.4.3 Line measurement with *single camera stereoscopic method*

In our case, we will perform a direct optical measurement of the surface deformation along a line, by means of a simple triangulation technique.

The triangulation principle is given in figure 3.13. We consider the paraxial approximation $\beta_{max} \approx H/L \ll 1$, as the distance L between the camera and the measurement area, is much larger than the maximal measured deformation H.

In this approximation, one can consider a reference point P, lets say on the flat interface. Then, when the interface deforms, the point in the same vertical, Q will be perceived as being Q'. The vertical displacement $\overline{PQ} \equiv \delta h$ and the observed displacement $\overline{PQ'} \equiv \delta h_{obs}$ are related by the relation

$$\delta h = \delta h_{obs} / \cos\alpha,$$

were α is the angle between the camera orientation direction and the horizontal (see figure 3.13). From the technical point of view, we consider the diffusive part of a laser beam projected vertically from the top. This diffusive part traces the fluid elements that are in the interface.

The natural extension of the punctual measurement presented until now, is to have a spatially extended laser beam, and to use a camera to obtain the displacement along a line defined by the direction $\hat{r}$,

$$\delta h(r) = \delta h_{obs}(r) / \cos\alpha. \tag{3.15}$$

To do so, we place a cylindrical lens in the path of the laser, in order to get a diffusing line instead of a single point, together with a focusing lens (before the cylindrical one) in order to concentrate the light at the fluid surface. This is both to reduce the line thickness (improving the resolution of the height measurement), and to increase diffused light.

We take images of the (primarily) diffused line at 60 Hz with a high resolution Dalsa camera that gives 2000×1700 pixels^2 images. When taking pictures of a line of 40 cm, one can get 5 pixels/mm as horizontal resolution. Vertical resolution depends on the angle α but it is limited by the laser line thickness, which can be estimated as a half millimeter.

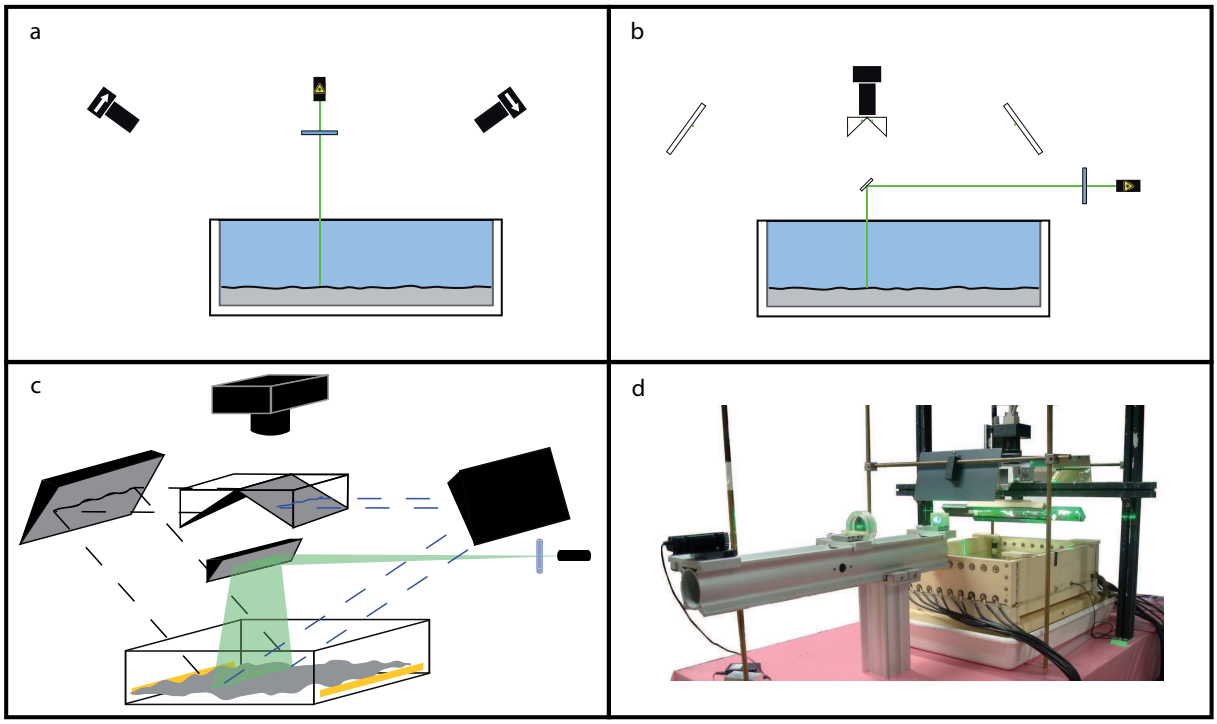

Figure 3.14: Setup for the *single camera stereoscopic method*. (a) is the configuration using two cameras and (b) is the equivalent one using a single camera. (c) is a schema 3d and (d) a photo of the actual setup.

The vertical resolution is found to be 3 pixels/mm. It was obtained by measuring the profile of a well calibrated stairway-shaped object[3].

The angle α is typically of the order of 45 degrees (50 for the results discussed in chapter 5). In that way we record preferentially the diffused part of the laser beam. On the other hand, specular reflexion of the laser beam is defined by the local slope of the fluid surface, which can be small for gentle forcing. But when the forcing is increased, the local slope increases consequently and one starts to record strong light spots –due to specular reflexion– in the part of the line where the normal direction matches the direction of the camera (see figure 3.14).

Until this stage, the description was based on the use of only a single camera, which is an standard procedure. It can be found as a commercial instrument to obtain the profile of diffusing objects (including metallic ones) within a good precision. But, because of the previously described limitation, this setup is not suitable for the strong deformation regimes we are interested in. This is why we propose a simple improvement to this technique in order to tackle the specular reflexion problem and to, consequently, be able to measure a strongly deformed surface.

The improvement consists in considering two opposite recording views instead of one. In that way, when the normal vector of the surface is directed into one of the recording views, necessarily it will not be directed into the opposite one. Then, in the post-

[3]©Padilla inc.

processing stage, one will be able to reconstruct all the line by discarding the saturated parts of both simultaneous records. In practice, as the vertical deformation of the line could be registered within a few pixels (in around 20 or 30, compared to 1700 that are available), we decided to use a set of mirrors in order to register both views in a single picture (see figure 3.14b–d for the actual setup, and the equivalent setup using two cameras in figure 3.14a). This trick has also the advantage of avoiding camera synchronization. As it is actually a stereoscopic measurement and it is performed with a single camera, we will adopt the name of *single camera stereoscopic method*.

As we already noticed, the vertical displacement $\delta h(r)$ can be directly obtained from the displacement of the laser line as perceived by the camera. So one has to isolate the coordinates (x, z) of the line from the raw images, despite both strong deformations of the line (tracing the strong deformations of the surface) and dazzles produced by specular reflexion. This post-processing stage is composed of several straightforward computations:

1. *Make both views superposable:* As the optical arrangement should be perfectly symmetric in order to produce no distortion between both views, in practice one can find a relative translation / rotation / elongation between them. It can be corrected in a single transformation, and once it is found for a single image–pair, it could be applied to the whole set performed measurements. To have both superposable views will be important in step 3.

2. *Make both views binary, by computing a local threshold:* Also for step 3, it is better if both views are binary. And as the intensity of the line can vary a lot in a single image (see raw pictures, figure 3.15, (a) and (c)), we preferred to compute a local threshold. This corresponds to taking thresholds in the mean value of a set of $N \times N$ neighbors pixels, with N the chosen value (in our case, $N = 17$ gives satisfactory results). In the zones where the contrast is high, this method gives good results (around the line for instance), but in zones with poor contrast, the threshold becomes arbitrary, resulting in the addition of noise. Nevertheless, this noise can be filtered in a later step (4).

3. *Assemble both views into a mutually filtered one:* This is the fundamental step, as here we take advantage of having two views, in which at least one of them should not exhibit saturation locally.

   From steps 1 and 2, one has similar lines everywhere excepting saturated zones. In that zones, one has the normal line (1 in binary code) surrounded by no information (0) for the first picture A. For the second picture B, on the other hand, the binary saturated image will exhibit 1 in a region larger than the line. So, when we perform the multiplication of A and B, pixel by pixel

   $$c_{ij} = a_{ij} * b_{ij},$$

   (equivalent to operation $C = A. * B$ for matrices in matlab), the resulting image C will present no saturations, as mutual corrections are applied locally.

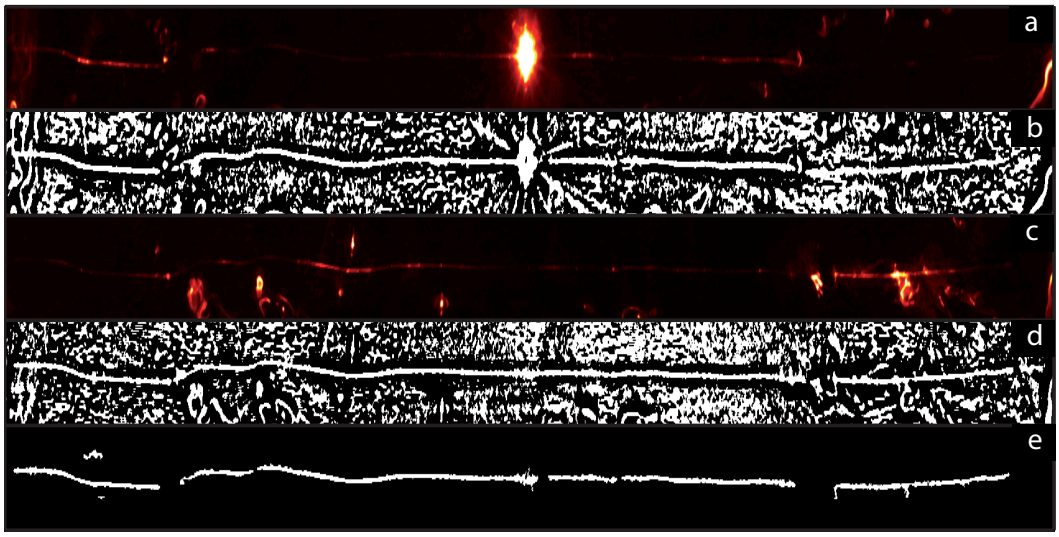

Figure 3.15: Image processing for both views of the line: (a) is the left view and (b) is the local threshold applied to it; (c) is the right view and (d) is the local threshold applied to it; (e) is the multiplication of (b) and (d) after removing most of the features generated by noise. In the left view (a) one can see a typical light spot produced by specular reflexion, which is successfully removed with the complementary view (c). Nevertheless we loose the line where the light intensity is too low in both views.

4. *Remove noise:* The noise carried in C (produced by the local thresholding) can be removed by a shape analysis. This is possible because the line has a clearly distinguishable elongated shape.

5. *Return into gray scales:* As a binary line only allows for a rough approximation of the $h_{obs}(r)$ profile, it is better to return into the gray scale. Doing so, one can take advantage of the more subtle intensity profile produced by the laser. Here again we multiply pixel by pixel the resulting binary image C with both original views, obtaining a gray scale line only in the pixels allowed by step 3.

6. *Convolve with a gaussian profile to improve the detection:* In gray scale, the convolution with a gaussian profile allows for a better estimation of the peak's maximum.

The advantages of this method (at least, by comparing it with inductive local measurements) are the natural ones of a measurement extended in space: (a) It allows the study of spatially varying quantities, in particular to the wavenumber spectrum of the surface deformation. (b) As one record several points at the same time, the statistics can be better than those of a local measurement for equivalent measurement time. (c) More particular to our case, the technique is non intrusive. As we record the diffusion of light at the surface, we have no need to introduce particles or other additives that could affect fluid properties. (d) Spatial resolution (in the horizontal place) is essentially limited by the thickness of the laser layer we use, of about half a millimeter.

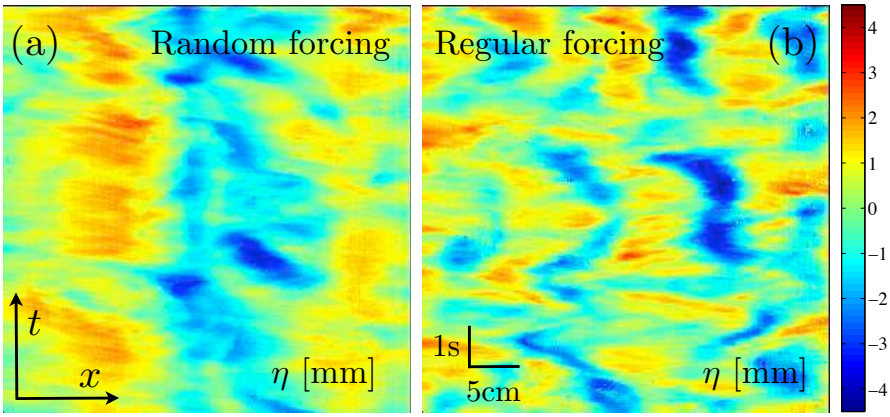

Figure 3.16: Examples of the obtained $h_{obs}(x)$ for sequences of images, resulting in a spatiotemporal diagram of the surface deformation field η. (a) corresponds to the random array and (b) for the regular one. The forcing is $I = 350$ A in both cases. A more detailed study of the deformation field will be presented later in chapter 5.

Its drawbacks come both from the fact of dealing with spatially resolved measurements and from the fact that this particular technique deals with diffusion of light in a medium which is only slightly diffusing. They are: (a) the spatiotemporal resolution is limited by the camera which is used. In our case we used a camera with high spatial resolution (in the best case we can measure a line of around 2000 pixels, which is good) but with not very high temporal acquisition frequency (60 Hz). Also, acquisition length T is also limited by the hardware[4]. We observed that for acquisitions of one minute at 60 Hz, the acquisition frequency was respected. (b) Vertical resolution of surface deformation is very limited. It is not larger that 4 pix/mm. (c) Data analysis is very time consuming. As most of the data analysis routines are home made, results should be controlled almost at each step and residual errors are to be corrected in a post-processing stage. (d) Finally the range of measurement is smaller than for inductive sensors, as for strong forcing there is an important increase of specular reflections, reducing the contrast for the line and making the more difficult the detection.

The drawbacks (c) and (d) can be overcome by changing the detection part in our simple data analysis, by more sophisticated ones. For instance the one of *active contours* seems promising: here one consider the image intensity as a topography –or potential well in 2D–. Then the active contour is defined as a deformable line with given tension and rigidity. It is initialized as a straight line and it is imposed to relax on the topography, until the line recover the shape defined for the maxima of intensity on the image [14; 37]. However, as the implementation in our particular data is not direct, this change is kept as a perspective for the near future.

Examples of the obtained temporal evolution of the $h_{obs}(x)$ profile are given in figure

[4]This time by the transfer/writing speeds of the hard disk on the acquisition PC, which are dependent on the available hard disk space. Thus, we followed a given protocol to trust the imposed acquisition frequency.

3.16 and a more systematic analysis is postponed to chapter 5.

It is worth giving a final remark concerning the possibility of performing measurement of the whole deformation field: it could be envisaged to develop a *really stereoscopic* measurement, in the spirit of the oceanographic techniques (see Cox and Munk [8] and also a more contemporary attempt by Benetazzo[1]). This seems reasonable, as by looking the surface with room lighting conditions, one can clearly notice the height fluctuations. But as the human eye is a complex optical instrument, and the implementation of such method could imply a lot of work, we keep this proposal on the perspectives of this thesis. Another perspective would be to try a first attempt by using the previously introduced stereoscopic setup. Eventually, it should be possible to implement 3D particle tracking methods with floating particles, in order to get a Lagrangian reconstruction of the deformation field.

3.5 Measurement of the interfacial tension γ for the acid–Galinstan interface

As we cover the liquid metal with low concentration acid to prevent oxidation, we are in very particular experimental conditions. In this case surface tension could not be assumed to be known[5] and it should be measured. One possible way to obtain its value is to consider the dispersion relation for waves on the interface of two fluids with infinite depth [17]:

$$\omega^2 = \frac{\rho_1 - \rho_2}{\rho_1 + \rho_2} gk + \frac{\gamma}{\rho_1 + \rho_2} k^3, \tag{3.16}$$

were ω is the angular frequency, $k = 2\pi/\lambda$ is the wavenumber, λ the wavelength, g is gravity (which one consider 9.81 ms^{-2} as a reasonable approximation for the earth surface, and in particular for our laboratory), γ is surface tension, and ρ_1, ρ_2 are the densities of both fluids ($\rho_1 > \rho_2$), which could be related by the Atwood number

$$A = \frac{\rho_1 - \rho_2}{\rho_1 + \rho_2}.$$

If one has access to most of those values, either because they are known or because one can measure them, one can obtain an unknown quantity. In our case, as we are interested in obtaining the value of γ, we would like to know all the rest. As we said, g could be assumed as known, together with ρ_1 and ρ_2. Now the challenge is to know k and ω.

A simple way to obtain both k and ω is to perform the Faraday experiment: This means to submit a fluid to a vertical sinusoidal excitation at a given frequency $f = \omega/2\pi$ and amplitude. When the control parameters are chosen in order to pass an instability threshold –the Faraday threshold–, the system exhibit stationary waves with a temporal periodicity that corresponds to the half of the forcing frequency, and a spatial structure that could be very complex, depending on the boundary conditions and the control parameters.

[5]Even if a value can be found in wikipedia: $\gamma_{wiki} = 0.718$ N/m, there is no clear statement of the interface under consideration.

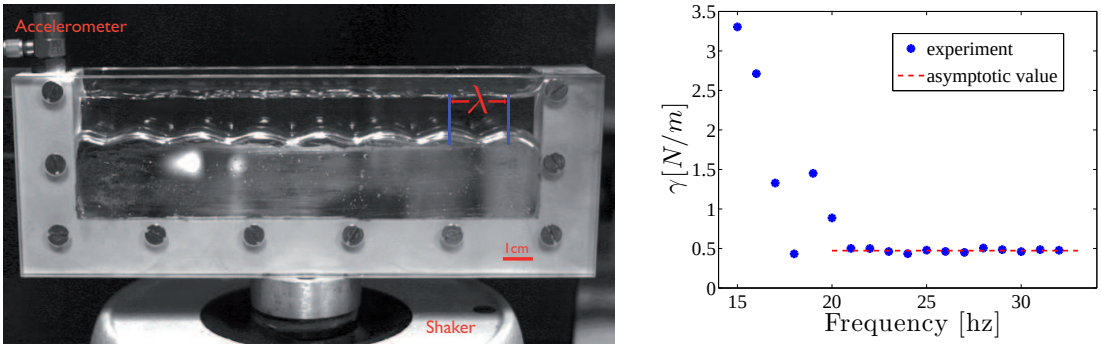

Figure 3.17: Faraday experiment to measure the surface tension γ for the Galinstan-acid interface. On the left there is a typical snapshot from which one can obtain the wavelength λ. On the right we plot (as blue points) the measured value of surface tension, as obtained by the expression (3.17), given the frequency of waves and measured λ. The asymptotic value 0.5 is plotted as a red dashed line.

For our purposes, we choose to work in a quasi-one-dimensional configuration, meaning that the most relevant dynamics are well described by a single spatial coordinate x, even if some movement is still present in the perpendicular direction y. The dimensions of the container are $16 \times 2 \times 5$ cm^3 (see figure 3.17a). Galinstan ($\rho_1 = 6440$ kg m^{-3}) fills the container until a height $h_1 = 2.57$ cm (at rest), which corresponds to the deep water limit. In fact $\tanh(kh_1) > 0.99$ for the whole set of frequencies used. On the top of Galinstan we put acid ($\rho_2 = 1000$ kg m^{-3}) in the same way as we do for the magnetohydrodynamical experiment. Using an electromagnetic shaker LDS (see figure 3.17a), we forced the system at frequencies going from 15 Hz to 32 Hz. For each frequency we chose an amplitude large enough to cross the instability threshold, but still trying to avoid nonlinear effects in the waves. Once the subharmonic wave develops (with frequency $f_s = f/2$), we take pictures to measure its mean wavelength λ, or the corresponding k. Then, in figure 3.17b we plot the expression

$$(\rho_1 + \rho_2)(-Agk + (2\pi f_s)^2)/k^3, \tag{3.17}$$

which corresponds to the experimental value for γ. From the same figure, on can see that γ takes an asymptotic value for large frequencies:

$$\gamma = 0.5 \text{ N/m}. \tag{3.18}$$

For low forcing frequencies, however, there is an important deviation from the asymptotic value. It could be interpreted as a strong influence of the container's boundaries, as only a few wavelengths are allowed. Then, when more wavelengths are possible, boundary effects become negligible.

3.6 Bibliography

[1] Benetazzo, A. Measurements of short water waves using stereo matched image sequences. *Coastal Engineering 53* (2006), 1013–1032.

[2] Berhanu, M., and Falcon, E. Space-time-resolved capillary wave turbulence. *Physical Review E 87* (2013), 033003.

[3] Berhanu, M., Verhille, G., Boisson, J., Gallet, B., Gissinger, C., Fauve, S., Mordant, N., Pétrélis, F., Bourgoin, M., Odier, P., Pinton, J. F., Plihon, N., Aumaître, S., Chiffaudel, A., Daviaud, F., Dubrulle, B., and Pirat, C. Dynamo regimes and transitions in the VKS experiment. *The European Physical Journal B 77* (2010), 459–468.

[4] Boisson, J., Klochko, A., Daviaud, F., Padilla, V., and Aumaître, S. Travelling waves in a cylindrical magnetohydrodynamically forced flow. *Physics of Fluids 24* (2012), 044101.

[5] Bondarenko, N. F., Gak, M. Z., and Dolzhanskiy, F. V. Laboratory and theoretical models of plane periodic flow. *Izvestiya, Atmospheric and Oceanic Physics 15* (1979), 711–716.

[6] Brocchini, M., and Peregrine, D. H. The dynamics of strong turbulence at free surfaces. Part 1. Description. *Journal of Fluid Mechanics 449* (2001), 225–254.

[7] Cobelli, P. J., Maurel, A., Pagneux, V., and Petitjeans, P. Global measurement of water waves by Fourier transform profilometry. *Experiments in Fluids 46* (2009), 1037–1047.

[8] Cox, C., and Munk, W. Measurement of the Roughness of the Sea Surface from Photographs of the Sun's Glitter. *J. Opt. Soc. Am. 44* (1954), 838–850.

[9] Falcon, E., Laroche, C., and Fauve, S. Observation of Depression Solitary Surface Waves on a Thin Fluid Layer. *Physical Review Letters 89* (2002), 204501.

[10] Figueroa, A., Demiaux, F., Cuevas, S., and Ramos, E. Electrically driven vortices in a weak dipolar magnetic field in a shallow electrolytic layer. *Journal of Fluid Mechanics 641* (2009), 245–261.

[11] Fridman, A. M., Snezhkin, E. N., Chernikov, G. P., Rylov, A. Y., Titishov, K. B., and Torgashin, Y. M. Over-reflection of waves and over-reflection instability of flows revealed in experiments with rotating shallow water. *Physics Letter A 372* (2008), 4822–4826.

[12] Gallet, B., Herault, J., Laroche, C., Pétrélis, F., and Fauve, S. Reversals of a large-scale field generated over a turbulent background. *Geophysical & Astrophysical Fluid Dynamics 106* (2012), 468–492.

[13] Herbert, E., Mordant, N., and Falcon, E. Observation of the Nonlinear Dispersion Relation and Spatial Statistics of Wave Turbulence on the Surface of a Fluid. *Physical Review Letters 105* (2010), 144502.

[14] Kass, M., Witkin, A., and Terzopoulos, D. Snakes: Active Contour Models. *International Journal of Computer Vision 1* (1988), 321–331.

[15] Knaepen, B., and Moreau, R. Magnetohydrodynamic Turbulence at Low Magnetic Reynolds Number. *Annual Review of Fluid Mechanics 40* (2008), 25–45.

[16] Lagubeau, G., Fontelos, M., Josserand, C., Maurel, A., Pagneux, V., and Petitjeans, P. Flower Patterns in Drop Impact on Thin Liquid Films. *Physical Review Letters 105* (2010), 184503.

[17] Lamb, H. *Hydrodynamics*. Cambridge University Press, 1895.

[18] Le Goff, A., Cobelli, P. J., and Lagubeau, G. Supershear Rayleigh waves at a soft interface. *Physical Review Letters 110* (2013), 236101.

[19] Marteau, D., Cardoso, O., and Tabeling, P. Equilibrium states of two-dimensional turbulence: An experimental study. *Physical Review E 51* (1995), 5124–5127.

[20] Maurel, A., Cobelli, P. J., Pagneux, V., and Petitjeans, P. Experimental and theoretical inspection of the phase-to-height relation in Fourier transform profilometry. *Applied optics 48* (2009), 380–392.

[21] Moisy, F., Michon, G.-J., Rabaud, M., and Sultan, E. Cross-waves induced by the vertical oscillation of a fully immersed vertical plate. *Physics of Fluids 24* (2012), 022110.

[22] Moisy, F., Rabaud, M., and Salsac, K. A synthetic Schlieren method for the measurement of the topography of a liquid interface. *Experiments in Fluids 46* (2009), 1021–1036.

[23] Monchaux, R., Berhanu, M., Bourgoin, M., Moulin, M., Odier, P., Pinton, J. F., Volk, R., Fauve, S., Mordant, N., Pétrélis, F., Chiffaudel, A., Daviaud, F., Dubrulle, B., Gasquet, C., Marie, L., and Ravelet, F. Generation of a Magnetic Field by Dynamo Action in a Turbulent Flow of Liquid Sodium. *Physical Review Letters 98* (2007), 044502.

[24] Mordant, N., Crawford, A. M., and Bodenschatz, E. Experimental Lagrangian acceleration probability density function measurement. *Physica D: Nonlinear Phenomena 193* (2004), 245–251.

[25] Ouellette, N. T. Programs available on `http://leviathan.eng.yale.edu/software_tracking.html`.

[26] Ouellette, N. T., and Gollub, J. P. Dynamic topology in spatiotemporal chaos. *Physics of Fluids 20* (2008), 064104.

[27] Ouellette, N. T., Xu, H., and Bodenschatz, E. A quantitative study of three-dimensional Lagrangian particle tracking algorithms. *Experiments in Fluids 40* (2005), 301–313.

[28] Polvani, L. M., McWilliams, J. C., Spall, M. A., and Ford, R. The coherent structures of shallow-water turbulence: Deformation-radius effects, cyclone/anticyclone asymmetry and gravity-wave generation. *Chaos 4* (1994), 177.

[29] Savelsberg, R., Holten, A., and van de Water, W. Measurement of the gradient field of a turbulent free surface. *Experiments in Fluids 41* (2006), 629–640.

[30] Savelsberg, R., and van de Water, W. Experiments on free-surface turbulence. *Journal of Fluid Mechanics 619* (2009), 95–125.

[31] Sommeria, J. Experimental study of the two-dimensional inverse energy cascade in a square box. *Journal of Fluid Mechanics 170* (1986), 139–168.

[32] Tabeling, P., Burkhart, S., Cardoso, O., and Willaime, H. Experimental study of freely decaying two-dimensional turbulence. *Physical Review Letters 67* (1991), 3772–3775.

[33] Takeda, M., and Mutoh, K. Fourier transform profilometry for the automatic measurement of 3-D object shape. *Applied Optics 22* (1983), 3977–3982.

[34] Tsang, Y.-K., and Young, W. R. Forced-dissipative two-dimensional turbulence: A scaling regime controlled by drag. *Physical Review E 79* (2009), 045308(R).

[35] Wright, W. B., Budakian, R., and Putterman, S. J. See reference 17 of [36].

[36] Wright, W. B., Budakian, R., and Putterman, S. J. Diffusing light photography of fully developed isotropic ripple turbulence. *Physical Review Letters 76* (1996), 4528–4531.

[37] Xu, C., and Prince, J. L. Snakes, Shapes, and Gradient Vector Flow. *IEEE Transactions on Image Processing 7* (1998), 359–369.

[38] Xu, H. Tracking Lagrangian trajectories in position–velocity space. *Measurement Science and Technology 19* (2008), 075105.

Chapter 4

Basic flow's properties

In this chapter we will focus on simple quantities allowing us to describe the different regimes we studied with our setup. More precisely, we will stress the properties of the flow in terms of the control parameters we explored: Forcing strength, controlled by varying the intensity of current; and forcing geometry, varied by changing the distribution of magnets.

We look to the properties of the velocity field at the surface, as measured by PTV, and then, we will focus into the basic properties of the surface deformation. A more detailed study of the surface deformation, in particular its relation to wave turbulence is postponed to chapters 5 and 6. The study of more subtile effects on particles at the Galinstan-acid interface is given in chapter 7.

But before going into the quantitative picture of the flow, it is useful to give an informal description of the regimes we explored.

4.1 Qualitative description

Although they are inconvenient for optical quantitative measurements, the reflecting properties of the surface allow to a good qualitative observation, especially in terms of the surface deformation. In this sense, and considering the imposed forcing strength and forcing geometry, one can distinguish different surface deformation regimes.

4.1.1 Random geometry of forcing:

In general terms, random forcing has the counter-intuitive tendency to generate a highly coherent velocity field (as we discuss later in this chapter). It corresponds to a large scale coherent structure surrounded by smaller scale vortices (see for instance figure 4.1-a). This coherent configuration is still time dependent, in the sense that vortices have no fixed position, despite the number of vortices does not varies a lot. Vortices are in continuous interaction, sometimes merging into a larger vortex (or even equally sized), sometimes fragmenting from one to two. The rotational orientation of vortices seems to be stationary (at least for the large scale vortex, which is easily identifiable): we do not

observe reversals, even for large waiting times. This is confirmed by taking independent realizations of the same experiment, giving rise to the same rotational orientation.

The origin of small-scale temporal dynamics is the impossibility to respect at the same time the complex spatial structure –although fixed– of the Lorentz force ($\mathbf{F}_L \approx F_L\,\hat{y}$) in the presence of lateral walls. This means that we do not have a base state with vortices of a size clearly identifiable with the forcing scale, as in the case of the flow produced by a checkerboard array of magnets (square array with alternating polarities) [8], or by a square distribution of current [7; 1]. For low forcing, vortices are easily identifiable, as well as their interaction. Surface deformation comes essentially from the depression at vortex cores, and it becomes as complex as the interaction between vortices can be.

For more intense forcing, one can observe a similar large scale structure in the flow, although the motion is faster and with more small-scale temporal fluctuations. When vortices are clearly identifiable, surface deformation comes again from depression in vortex cores. This time, however, one can see the development of regions with strong shear, surrounded by zones where small scale surface deformation can be seen, recalling capillary waves that forms in the front of steep gravity waves (see for instance Longuet-Higgins [4]).

4.1.2 Regular geometry of forcing:

As we already saw in the magnetic field description (section 3.1), magnets' positions for the regular forcing are in an hexagonal lattice. In spite of this, magnets' polarities alternate forming stripes, generating a magnetic field with almost one dimensional dependence. A forcing dependent of only one coordinate is known as Kolmogorov flow. Our forcing, however, has some departure from this dependence as near the walls, bands are not completely equivalent. A Kolmogorov forcing gives rise to a periodic shear flow, which is stable for very small Reynolds number [2]. In our case, we only observe this for very short transient regimes when the forcing is switched on. Very likely because of our departure from the one dimensional case. What we actually observe for gentle forcing, is the presence and interaction of vortices of a well defined size, comparable to the distance between magnet's centers. Contrary to the random forcing, here we obtain a more uniform distribution of vortices with also more uniform sizes.

For intermediate and strong forcing regimes, vortices become difficult to observe, because of the strongly time fluctuating flow, although some apparent spacial periodicity is reminiscent from the forcing geometry. For stronger regimes the surface deformation seems to be larger than for the equivalent forcing with the random array, and one can also perceive the development of small scale capillary waves close to steep waves, indeed in a stronger manner than in the random case.

4.2 Velocity at the surface

4.2.1 Lagrangian picture

In top panels of Figure 4.1 we present a collection of trajectories obtained using the PTV technique already described in section 3.3: They were obtained by following the displacement of particles that are floating at the surface of the liquid metal. Thus they

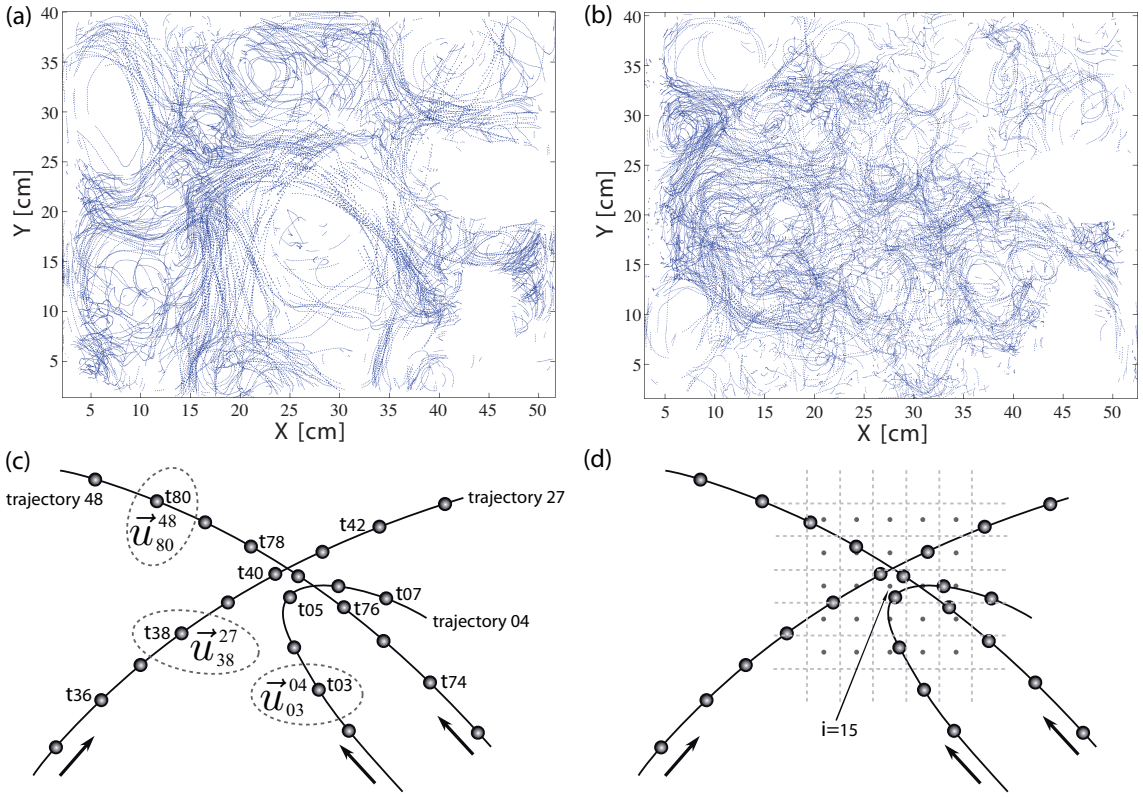

Figure 4.1: Top panels: particles' trajectories on the surface of the flow. (a) Obtained with the random forcing, at a forcing strength of I = 275 A. (b) Similar observation as (a), but for the regular forcing. Bottom panels present schemas to describe how we quantify the velocity field (c) for a Lagrangian description, and (d) for a time averaged eulerian description (see text for more details).

trace the velocity field on that surface. The panel (a) corresponds to the flow produced with the random array of magnets, for a current intensity of I = 275 A. Panel (b) present the equivalent field for the regular array of magnets. In both cases we plotted trajectories of particles within 6 seconds of acquisition, in order to keep trajectories visible. Notice that these figures correspond to the whole experimental cell.

From these figures one can already appreciate some differences between both forcing protocols: the random forcing produces more coherent trajectories, recalling the presence of large vortices. On the contrary, for the regular forcing trajectories do not seems to present any spatial structure. Bellow, we will return to a more precise spacial description of these flows.

Due to the discrete nature of PTV measurements, it seems pertinent to introduce some notation, as presented in Figure 4.1c, which is a schematic zoom of a small part of the top panel's pictures. Three segments of trajectory are presented here, recorded at different times: the criterion for grouping these trajectories is spacial proximity rather than temporal coincidence. This is the very same approach used in top panel's pictures, and implies an implicit *time averaging* process.

We will index the velocity of each particle on the basis of their time and given trajectory, so the velocity $\mathbf{u}_t^l$ corresponds to the velocity in the trajectory N° l at the instant t. Of course, the number assigned to trajectories is completely arbitrary, whereas the time is not. In this way, a Lagrangian trajectory l is composed by a collection of instantaneous samples, measured at consecutive particle positions

$$\begin{aligned}\mathbf{u}^l &= \{\mathbf{u}_{t1}^l, \mathbf{u}_{t2}^l, \cdots, \mathbf{u}_{t_{\max}}^l\} \\ &= \{\mathbf{u}_{t1}^l(x(t1), y(t1)), \cdots, \mathbf{u}_{t_{\max}}^l(x(t_{\max}), y(t_{\max}))\}.\end{aligned}$$

Notice that $\mathbf{u}_t^l$ was measured on a plane, parallel to the bottom. Thus it is unambiguously defined by the position $(x(t), y(t))$, and it has only two components, as we have not measured the vertical displacement.

We are now in position to consider the standard deviation σ_u of the whole set of sampled particles' velocities on the surface of the flow, which can be written as

$$\sigma_u = \frac{1}{N_t\, N_l}\sqrt{\sum_{t=1}^{N_t}\sum_{l=1}^{N_l}(\mathbf{u}_t^l - \langle\overline{\mathbf{u}}\rangle)^2}, \tag{4.1}$$

where N_t is the total number of considered frames, N_l is the total number of trajectories, and

$$\langle\overline{\mathbf{u}}\rangle = \frac{1}{N_t\, N_l}\sum_{t=1}^{N_t}\sum_{l=1}^{N_l}\mathbf{u}_t^l \tag{4.2}$$

is the global mean. Notice that $\langle\overline{\mathbf{u}}\rangle \approx 0$ due the absence of fluxes though lateral walls and the fact that we are considering the whole cell.

We show in Figure 4.2-left the dependence of the Reynolds number

$$Re_\sigma = \sigma_u L/\nu$$

on the forcing strength controlled by the intensity of imposed electrical current I. L is the length scale defined by the magnet's array (see section 3.1), ν is the fluid viscosity and σ_u is considered as a characteristic velocity scale for experiment performed at a given intensity of current, after the statistically steady state is reached. The red curve corresponds to the regular forcing, the blue one to the random forcing and we also included the line with 1/2 slope in log-log scale, which corresponds to a scaling as $\sqrt{I}$. As discussed in section 3.2, a scaling for the velocity going as

$$U_0 = \sqrt{J_0 B_0 L/\rho}$$

is expected from the balance of the Lorentz force and the advection term in the Navier-Stokes equation. Thus we also plotted in Figure 4.2-right the ratio

$$\sigma_u/U_0,$$

representing the departure of the measured velocity of particles at the surface from the expected values.

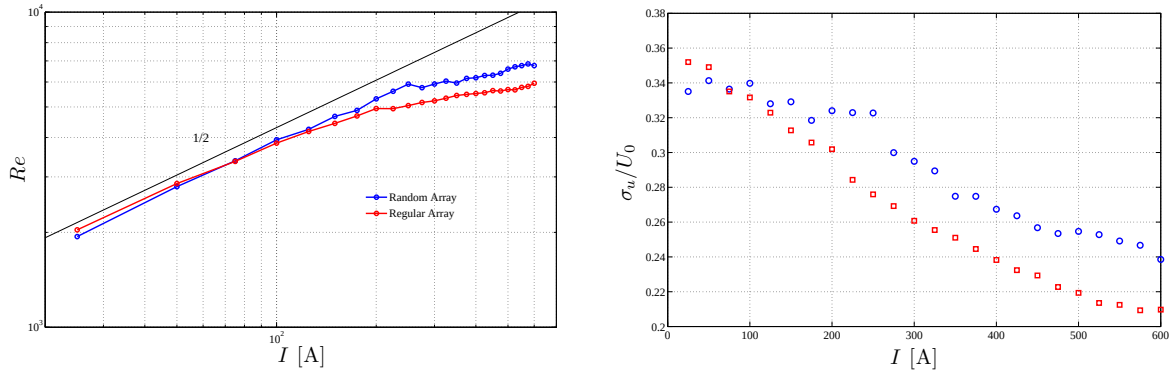

Figure 4.2: Influence of forcing on particles' velocities. On the left we plotted $Re = \sigma_u L/\nu$ as a function of the forcing strength I. σ_u is the standard deviation of particles' velocities over all particles' trajectories. The plot in log-log scale allows to appreciate the scaling on $\sqrt{I}$ represented by the black line with slope 1/2. On the right we plotted again σ_u, but this time over the expected velocity $U_0 = \sqrt{J_0 B_0 L/\rho}$ introduced in section 3.2.

From Figure 4.2-left one can see that the scaling 1/2 is more or less respected for both forcing protocols at low forcing: In the best case, for the random forcing, one could say that the scaling is respected until I = 250 A. This can be interpreted as the regime in which Lorentz force –that acts meanly in the plane– is efficient to inject energy in a two-dimensional flow. On the other hand, as it can be seen from Figure 4.2-right, the velocity σ_u is less than about a third of the one expected from scaling arguments, which was clearly over-estimated. This can be due to several reasons: To construct the estimate, we used the maximal magnetic field B_0 whereas it is far from being homogeneous; σ_u corresponds to the standard deviation, then it is a modest estimate, as some velocities actually reach the expected value U_0. Finally, it has to be recalled that we are looking to the velocity *of particles transported by the velocity field* instead of the velocity field itself, thus an effective filtering due to particles's inertia can be argued. However, these arguments can explain why the curves are globally lower than 1, although they do not explain the evolution in terms of the forcing intensity, which is also expressed by the departure from the 1/2 scaling for strong forcing in Figure 4.2-left. One possible explanation is that our measurement do not take into account the vertical displacement of the surface –and then the one of particles–, which may become very important for strong forcing.

4.2.2 Time averaged Eulerian picture

The global analysis in terms of σ_u does not take into account the spatial structure of the flow, which seems to be non-trivial when looking the trajectories in Figure 4.1. One possible way to take space into account is to consider instantaneous pictures of the flow. This in not possible in our case, as we have chosen to track a limited number of particles in order to avoid interactions between them. Thus, within our experimental conditions, a more reliable way to consider space is to perform a temporal average of the flow. The

schematic representation of this process is given in Figure 4.1d: We define a grid over the measurement area, with typical side Δ and we compute the statistics over the particles that were at each defined cell, regardless of the time. Thus, we can compute an average velocity, as well as the fluctuations over that value. We did that for every grid point, given the fact that after a transient period, particles have explored almost the whole experimental area.

We have then N cells defined by the coordinates of the regular grid (x_i, y_i), so we can call $\mathbf{v}_i = \mathbf{v}(x_i, y_i)$ the set of velocities corresponding to that position. In the example of Figure 4.1 (panels (c) and (d)), we have that $\mathbf{v}_{15}$ is composed by three instantaneous velocities $\mathbf{u}\,{}^{27}_{40}$, $\mathbf{u}\,{}^{04}_{05}$ and $\mathbf{u}\,{}^{48}_{77}$. For each cell, the mean value will be referred as $\overline{\mathbf{v}_i}$ and the standard deviation as σ_{v_i}.

Typical *Eulerian mean flows* $\overline{\mathbf{v}_i}$ are presented in Figure 4.3: Both were constructed from the data sets presented in the top panels of Figure 4.1: on the left we present the flow produced by the random array of magnets and on the right the one produced by the regular array. Forcing strength corresponds to I = 275 A in both cases. Here we used a coarse graining length $\Delta = 8$ mm. A similar structure is observed independent of the forcing strength under consideration.

Although already identifiable from the superposed trajectories in figure 4.1-a, from Figure 4.3-left the presence of a large scale vortex is undeniable. It has a radius of around 7 cm which is larger than both the magnet's array length scale and the layer thickness. This vortex is surrounded by some smaller vortices until the whole cell is filled. This large scale vortex recalls the observations by Sommeria [7] and later by Gallet *et al.* [1] in the context of two-dimensional turbulence. Starting from several vortices with sizes comparable to the typical forcing scale, these vortices experience merging events producing larger vortices, to end up with one –or few– large scale vortices of size comparable to the one of the container. Their large-scale vortices are observed to experience *reversal* phenomena: abrupt inversions of sense of rotation happening at *random* time intervals. In this way the original symmetry of the system is statistically recovered. Our case, on the other hand, appears to be very different from the one of two dimensional turbulence: we observe that our large scale vortex is present from the very beginning of the experiment (or after a short time transient) and although it is not static, it is insensitive to merging events of small vortices that happen regularly. Therefore, in our case, the sense of rotation of the large-scale vortex is fixed and it seem to be defined by the forcing.

For the regular forcing (figure 4.3-left), one can observe some vortices and stronger bands close to walls, suggesting also a large scale circulation. However, the spatial structure is less clear than for the random case, and a partial explanation of this will be given next.

On the basis of both the mean flow $\overline{\mathbf{v}_i}$ and the temporal fluctuations σ_{v_i}, one can quantify the distribution of the energy in the velocity field. For each cell one can define the fraction of energy contained in the mean flow

$$e_i = \frac{\overline{\mathbf{v}_i}^2}{\overline{\mathbf{v}_i}^2 + \sigma_{v_i}^2},$$

going between 0 when fluctuations concentrate the energy ($\sigma_{v_i}^2 \gg \overline{\mathbf{v}_i}^2$), to 1 when it is

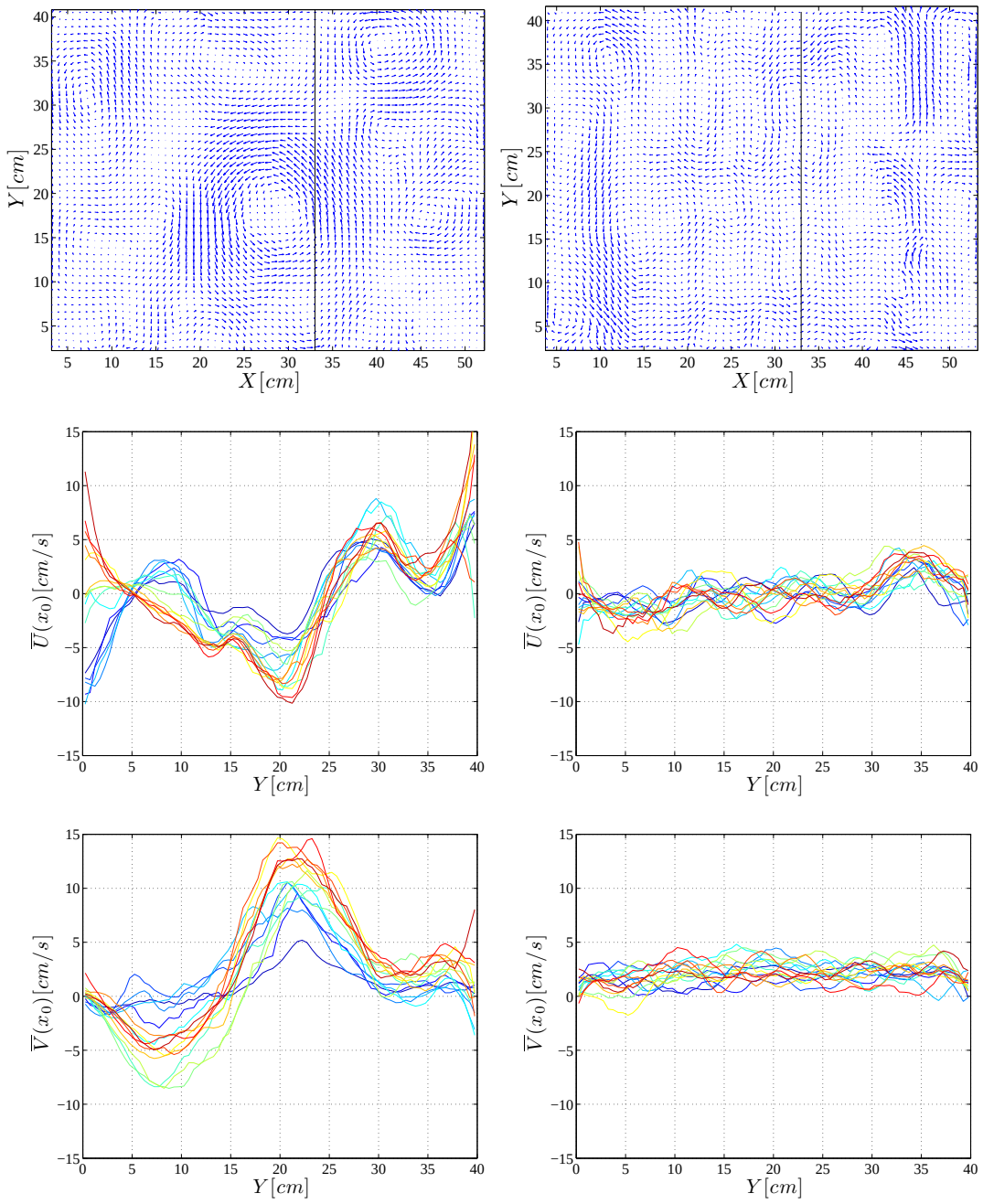

Figure 4.3: Time averaged Eulerian representation of the flow. Top panels present the whole eulerian velocity field for I = 275 A. Black line correspond to $x_0 = 33$ cm, where surface deformation measurements where performed. U component of the averaged velocity is presented on the middle and V component on the bottom. All figures on the left correspond to random forcing, and those on the right to regular forcing.

concentrated in the mean flow ($\overline{\mathbf{v}_i}^2 \gg \sigma_{v_i}^2$). Then one can consider the spacial average of

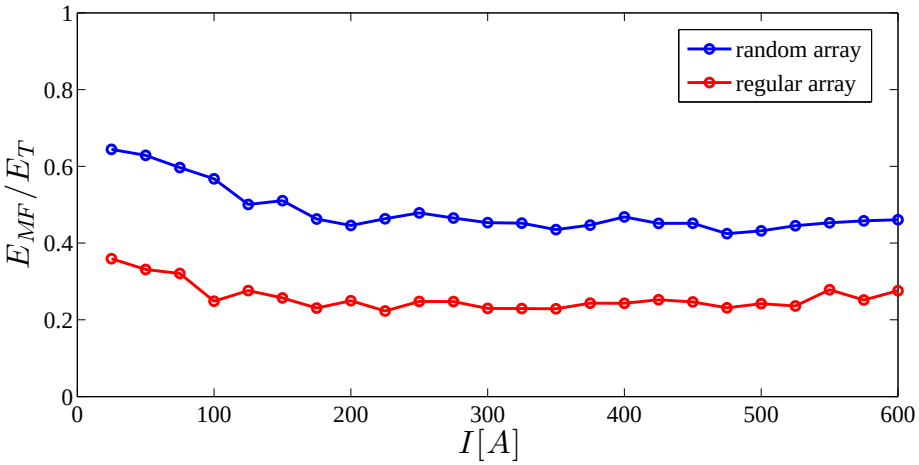

Figure 4.4: Energy distribution as a function of the forcing strenght: E_{MF}/E_T is 1 when all the energy is contained in the time averaged *mean flow*, and it is 0 when all the energy correspond to temporal fluctuations. The random forcing is in blue, and the regular one in red.

this quantity

$$\frac{E_{MF}}{E_T} = \langle e_i \rangle = \frac{1}{N}\sum_{i=1}^{N} e_i$$

over the whole coarse–grained measurement area. It has the same limits as the local case, and it gives a global comparison of the energies involved in the flow.

In Figure 4.4, we plotted E_{MF}/E_T as a function of the imposed current I (the forcing strength), again for the two forcing geometries. As a general feature, one can appreciate that the fraction of energy on the mean flow does not changes a lot, despite the increase of the supplied power. However some variation is present until roughly 200 A. In this low forcing regime, the fraction of energy in the mean flow is more important, which is not surprising as the flow seems to be more coherent. The most remarkable feature, however, is the important difference between both forcing protocols: For the random forcing, around a half of the energy is in the mean flow; for the regular array on the contrary, most of the energy corresponds to temporal fluctuations.

This result emphasizes the fundamental difference between the two considered forcing geometries. It also gives a partial explanation of the less clear spatial structure of the flow produced with the regular forcing (compared to the one of the random forcing): It is just because the energy contained in the mean flow is of the same order of magnitude of temporal fluctuations.

Finally, we focus our attention in the vorticity field, defined from the Eulerian velocity field $\mathbf{v}$, as:

$$\omega = \nabla \times \mathbf{v}. \tag{4.3}$$

In particular, the vertical component of the vorticity $\omega_z = \partial_x v_y - \partial_y v_x$ depends only of

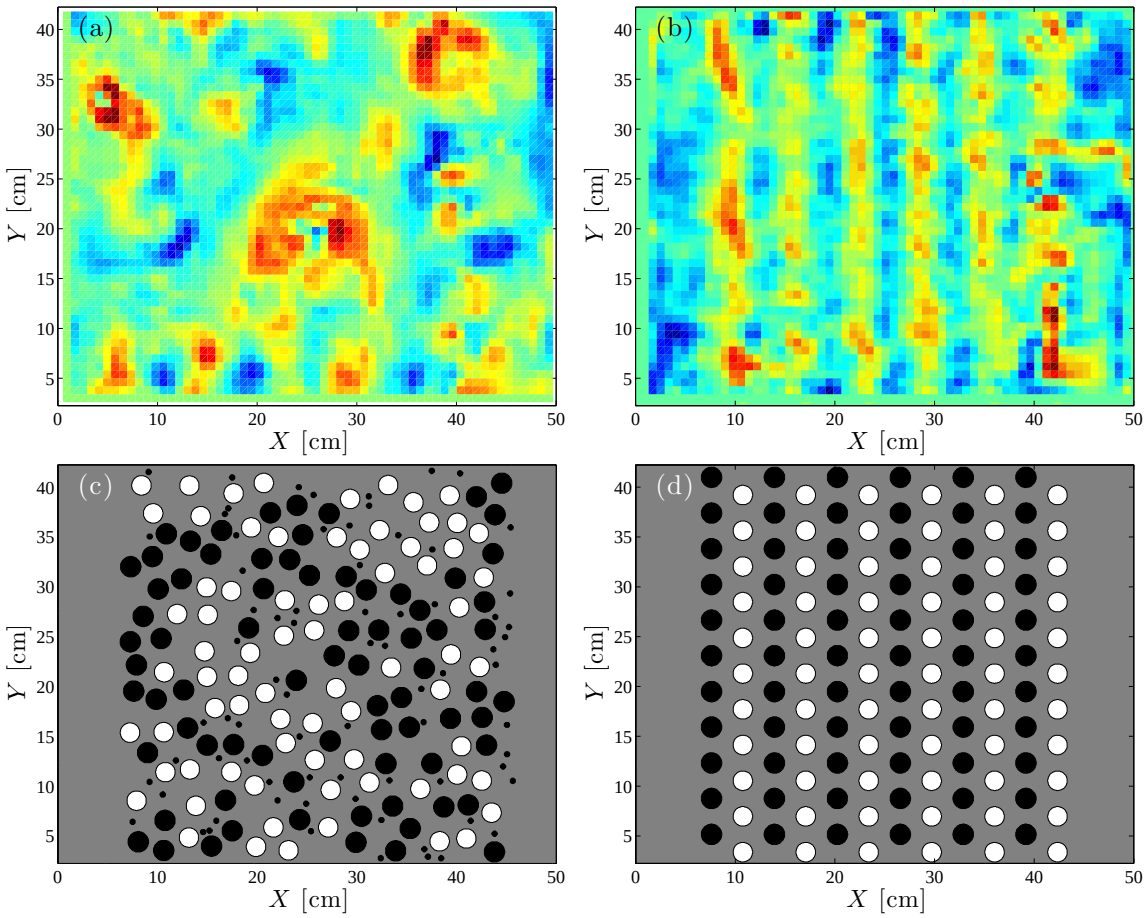

Figure 4.5: Relation between vorticity (top panels) and magnetic fields (bottom panels). The regular forcing is on the right, and the random forcing is on the left. Both vorticity field (on the top) correspond to a forcing of I = 300 A, the color-bar range from –10 s^{-1} (blue) to 10 s^{-1} (red).

the velocity field on the plane. Thus it can be obtained from our measurements after taking spatial derivatives of the mean Eulerian velocity field. In figure 4.5 (a) and (b) we present two examples of mean vertical vorticity field, as it is obtained from the time averaged Eulerian representation of the flow $(v_x, v_y) = (\overline{\mathbf{v}_i} \cdot \hat{x}, \overline{\mathbf{v}_i} \cdot \hat{y})$. Panel 4.5a presents the random forcing and and panel 4.5b presents the regular one. Bottom panels show the corresponding magnetic fields. Particularly when considering the regular case (compare right panels 4.5b and 4.5d), one can observe in the vorticity a clear reminiscence of the imposed magnetic field, which here corresponds to shear bands. For the random array (left panels 4.5a and 4.5c), the relation is less evident but it is still present, and suggest the distribution of magnets as a suitable explanation to the large scale vortex. It have to be noticed that these features become visible only when considering time averaged flows: they are not evident from an instantaneous observation of the flow.

Some authors already discussed the flow's dependence on the forcing's geometry in

the context of a two layer configuration of stably stratified fluids (in which fluid motion is produced as in our case: with permanent magnets and an homogeneous electrical current, but using electrolites instead of liquid metals). The common conclusion is that there is little difference when looking to statistical quantities, especially when the forcing is strong enough [5; 6]. This would not be surprising if one considers stratified turbulent flows as a close approximation to two dimensional turbulence, where the transfer of energy into larger scales should smear out any signature of the forcing.

However, Williams *et al.* [9] pointed out that after taking long time averages of the instantaneous velocity field, the trace of the forcing geometry becomes visible again, even for a strongly fluctuating flow. Recently, this trace of the original forcing was explored in more detail for unstationary flows with relatively low Reynolds number (until ~ 300) by Liao *et al.* [3]. They found that, for their experimental conditions, the symmetries present in the forcing determine the distribution of the energy in the flow. Specifically, they show that a square lattice of magnets (of alternating polarities) produces strongly fluctuating kinetic energy, whereas stripes of magnets (also of alternating polarities) drive stronger velocity gradients.

Although the resolution of our measurements do not allow such a detailed quantification, we share the general conclusions of the referred works: there is a strong connection between the magnetic field and the resulting two dimensional velocity field. Moreover, our results represent an extension to [9; 3], in the sense that they are valid for much more intense turbulent flows, and even when bidimensionality is not imposed (i. e. in the presence of important surface deformation). Under these conditions, we no longer expect the rough independence on forcing conditions observed also with stably stratified flows [5; 6].

4.3 Fluctuations on the surface level

For our present purpose of giving an elementary description of the observed flows, we will consider only one series of local elevation measurements carried out using the inductive sensor (section 3.4). We consider here the amplitude of surface level fluctuations, as quantified by the standard deviation (more precisions will be given in next chapter, in particular in equation 5.4). It is presented in figure 4.6, again as a function of the intensity of electrical current I, and for both forcing geometries.

From the figure 4.6, one can see that –in this series– fluctuations of the surface level increase roughly linearly, with a rate of $2 \cdot 10^{-3}$ mm/A, although it depends on the forcing protocol. The linearity of this growth seems to be dependent of the measurement point, as will be noticed in the next chapter. However, one observation appears to be confirmed by all our measurements: level fluctuation are more important for the regular forcing. This suggest, and it is not surprising, that the flow obtained with the regular forcing is more fluctuating both in terms of kinetic energy and in terms of surface level. The flow produced with the random forcing, on the other hand, present smaller surface level fluctuations, as it is more coherent and have a stronger mean flow.

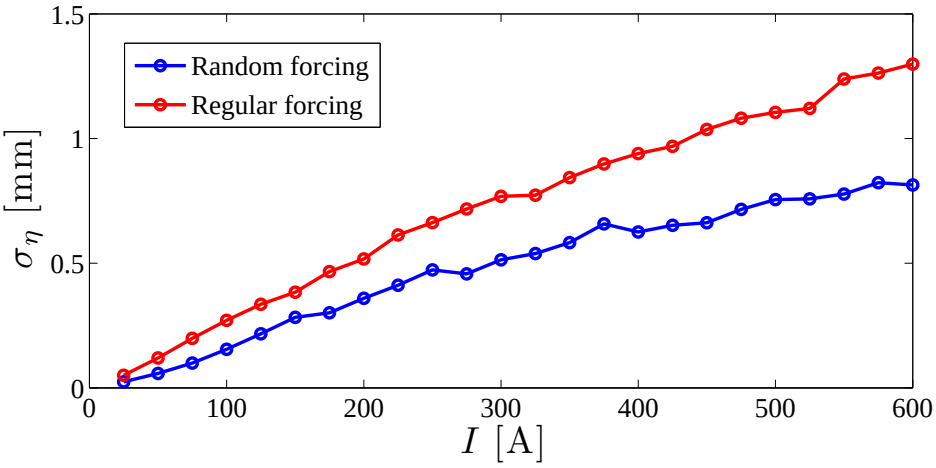

Figure 4.6: Fluctuations of the height level measured on a single position. It is one of the curves presented in 4.6. Random forcing is in blue, and the regular one in red.

4.4 Summary: different turbulent flows

In conclusion, in this chapter we emphasized the distinctive features of the flows accessible with the experimental setup presented in the previous section. We can summarize them as follows:

- We are able to produce two qualitatively different flows. The first one (produced by a random forcing) is characterized by a strong mean flow that develops larger velocities and in which, consequently, fluctuations of the surface level are relatively small compared to the second one. The second flow (produced by a regular forcing) is characterized by intense velocity fluctuations, as well as by large surface level fluctuations. These features are controlled by the imposed forcing geometry defined by the magnetic field. In both cases, the geometry of the imposed forcing is recovered in the time averaged velocity field.

- An increase of the velocity fluctuations and of surface level fluctuations is observed when the forcing strength is increased. There is a partial agreement with the expected growth of the velocity as $\sqrt{I}$. As surface deformation increases, it is accompanied by interesting wave-like features, as it can be seen in figure 5.1 for the regular forcing case.

- In our experiment the Lorentz force is mainly horizontal; and the thickness of the fluid layer is small compared with the container size (1 cm compared with 40 or 50 cm). This two conditions impose the structure of our flow: It is a flow where horizontal motion is dominant over the vertical one. Indeed vertical velocities are measured (locally) to be of around 10% of horizontal ones. In this sense it tempting to consider our flow as being two-dimensional.

However, as noticed before, we also observed rich surface deformation as a consequence of the complex interplay between the horizontal force, rigid walls and bottom effects (friction and boundary layers as a consequence). Moreover, in order to get a fully two dimensional flow, one should constraint the flow by using density stratification or strong uniform magnetic fields, which is out of the purpose of this study. Indeed we are interesting in how the surface is deformed as a consequence of a bulk turbulent flow, and this will be the subject of next chapter.

4.5 Bibliography

[1] Gallet, B., Herault, J., Laroche, C., Pétrélis, F., and Fauve, S. Reversals of a large-scale field generated over a turbulent background. *Geophysical & Astrophysical Fluid Dynamics 106* (2012), 468–492.

[2] Kelley, D. H., and Ouellette, N. T. Using particle tracking to measure flow instabilities in an undergraduate laboratory experiment. *American Journal of Physics 79* (2011), 267.

[3] Liao, Y., Kelley, D. H., and Ouellette, N. T. Effects of forcing geometry on two-dimensional weak turbulence. *Physical Review E 86* (2012), 036306.

[4] Longuet-Higgins, M. S. Capillary rollers and bores. *Journal of Fluid Mechanics 240* (1992), 659–679.

[5] Marteau, D., Cardoso, O., and Tabeling, P. Equilibrium states of two-dimensional turbulence: An experimental study. *Physical Review E 51* (1995), 5124–5127.

[6] Ouellette, N. T., and Gollub, J. P. Dynamic topology in spatiotemporal chaos. *Physics of Fluids 20* (2008), 064104.

[7] Sommeria, J. Experimental study of the two-dimensional inverse energy cascade in a square box. *Journal of Fluid Mechanics 170* (1986), 139–168.

[8] Tabeling, P., Burkhart, S., Cardoso, O., and Willaime, H. Experimental study of freely decaying two-dimensional turbulence. *Physical Review Letters 67* (1991), 3772–3775.

[9] Williams, B. S., Marteau, D., and Gollub, J. P. Mixing of a passive scalar in magnetically forced two-dimensional turbulence. *Physics of Fluids 9* (1997), 2061–2080.

Chapter 5

The effect of turbulence on surface deformation

In this chapter we will discuss our measurements of the surface deformation. After introducing the general motivations of this study (section 5.1), we present some details about the experimental tools we used (section 5.2) focusing on their advantages and drawbacks. Then we move to experimental results (section 5.3). At this point it is pertinent to underline that more measurements should be performed in order to make our statistical results undeniable. Finally we present a summary of the results together with a conjecture explaining our results.

5.1 Introduction: Can a quasi–bidimensional turbulent flow generate surface waves?

A couple of general observations can be recalled (from previous chapters) about the flow we obtain by using the electromagnetic forcing:

- As the principal component of the force is horizontal, and the thickness of the fluid layer is small, the flow is primarily bidimensional. Let us call it quasi–bidimensional. As a consequence the dominant component of the vorticity field is the vertical one.

- Despite the dominant bidimensional motion, rich surface deformation can be recognized, in particular by looking to figure 5.1.

Under this conditions, a natural question comes: Can a quasi–bidimensional turbulent flow generate surface waves?

Indeed, this question motivate the study presented though this chapter.

5.1.1 Arguments to expect wave generation

In the context of sound waves, Lighthill considered the possibility of spontaneous generation of sound by vortical motion [9]. In analogy to this, authors as Cerda & Lund [1],

or Ford and collaborators [6; 16] considered spontaneous wave generation by bidimentional vortical flows in shallow water. Generation of non-dispersive waves is predicted for small Froude numbers, and it is indeed observed in numerical simulations [16] for a Froude number of 0.05. To our knowledge there is no generalization or these theoretical results to dispersive waves in deep water[1]. Therefore it is pertinent to ask the question about wave generation in our experiment, were the Froude number is estimated to range between 0.01 to 0.36.

Another –cruder– argument can be given by considering that phase velocity has a minimum at the crossover between gravity and capillarity dominated regimes (see section 2.4). It correspond to 23 cm/s at $\lambda = 1.7$ cm for the water-air interface and 21 cm/s at $\lambda = 1.9$ cm for the Galinstan-acid interface under our consideration. The argument behind this can be traced back to the context of waves generated by turbulent wind (see for instance [15; 8]). In particular, Phillips [15] understand it as a resonance process happening a these values. On the other hand, we may notice that this is also the onset of wave resistance: faster moving objects generate waves [17].

In our experiment, the characteristic –horizontal– velocity is roughly estimated as $U_0 = \sqrt{I_0 B_0 L/S_0 \rho}$, where B_0 is the fixed magnetic field, L is a characteristic length-scale of the forcing and S_0 is the area at which the electrical current I_0 goes thought. As I_0 is used as control parameter, it turns out that the minimum phase velocity of waves is reached at

$$I_0 \approx 300 \text{ A}.$$

This estimate seems consistent with qualitative observation of our experiment, as shown in figure 5.1, although some variability appears as a function of the forcing parameters.

Experimental results of Savelsberg & van de Water [18; 19], on the other hand, suggest that waves can be observed for lower mean velocities.

5.1.2 Statistical features of nonlinear waves

A classical, yet simple analysis to quantify the relevance of wave nonlinearities, is to study the third order moment in hight level distributions: the Skewness. These ideas can be traced back to the fifties, when Longuet-Higgins introduced a result that became a cornerstone for the sea-waves community: when random linear waves are considered, the surface elevation follows a gaussian distribution [10],

$$p(\eta) = \frac{1}{\sqrt{2\pi}\sigma_\eta} \exp\left(-\frac{\eta^2}{2\sigma_\eta^2}\right). \tag{5.1}$$

The sea surface is considered in the form $\eta(\mathbf{x}, t) = \sum_n c_n \cos\left(\mathbf{k}_n \cdot \mathbf{x} + \omega_n t + \phi_n\right)$ where ϕ_n are random phases and c_n are random variables that respect the condition $\sigma_\eta^2 = \int S_\eta(\mathbf{k}) d\mathbf{k}$, with $S_\eta(\mathbf{k})$ the continuous spectrum of surface elevation.

Thus, for surface deformations that are symmetrical around the most probable value, the distribution (5.1) is clearly symmetric. The skewness, which is the measure of the distribution asymmetry, is zero in this case, by definition.

[1] Although Coste & Lund extended the theory for gentle departures from shallow water [3].

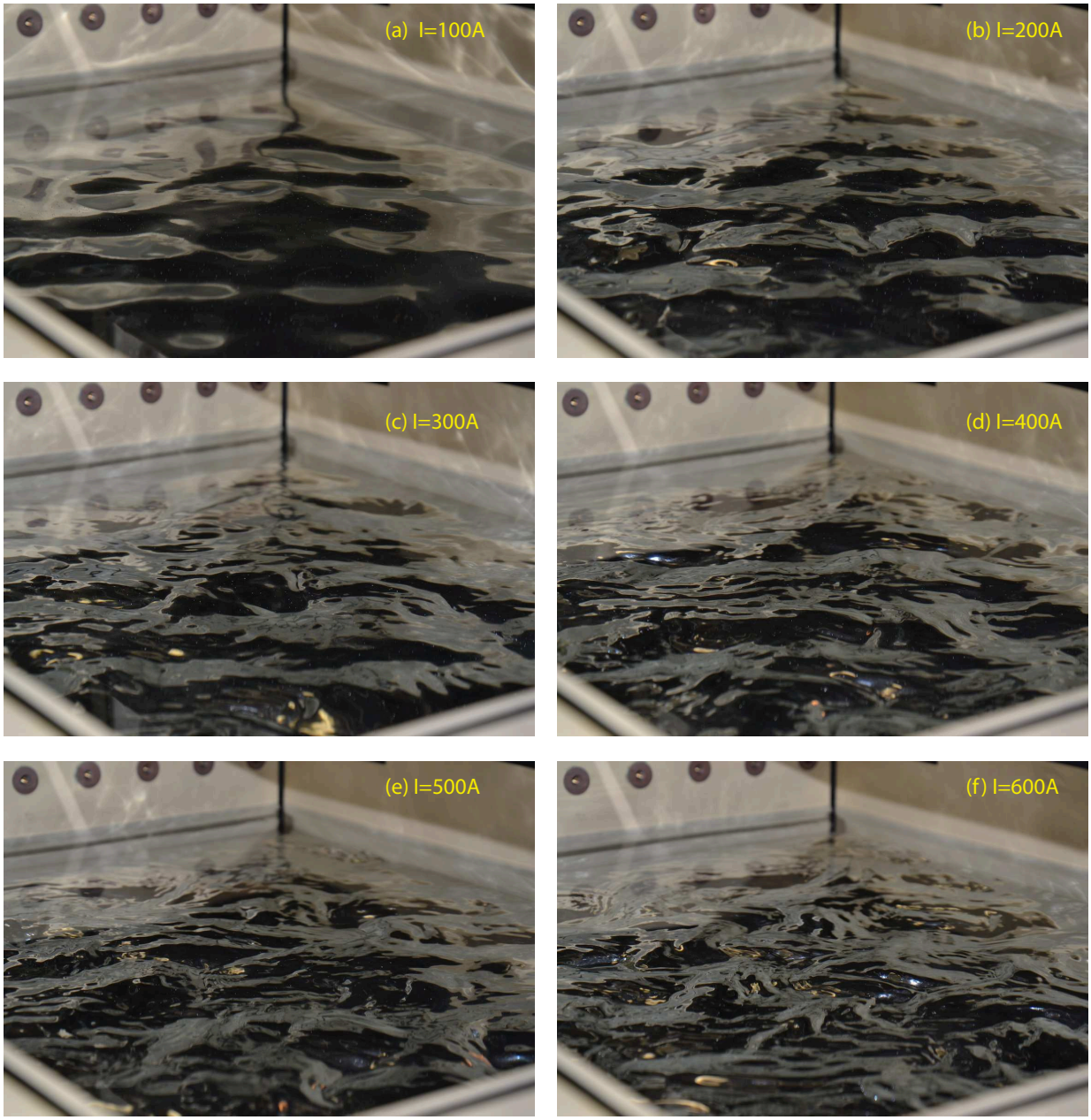

Figure 5.1: Photos of the experiment for increasing forcing strength, Regular forcing.

One may think this distribution as the consequence of simultaneous knowledge of the shape of individual elements forming the surface (sinusoidal waves in this linear case) and the statistical distribution of its amplitudes.

The linear result was extended to *weakly nonlinear* waves [11], in an approximation that takes advantage of a linear formalism, although including nonlinear interaction between components. Consideration of weakly nonlinear wave profiles result in a skewness

[11] as

$$\text{Skewness}(\eta) = 3k_p\sigma_\eta, \tag{5.2}$$

where k_p is the wavenumber of the spectral peak (remember that we are placed in the sea-wave context), and σ_η is the standard standard deviation. Both quantities, k_p and σ_η, are always positive, and thus the skewness is positive in this context.

This estimate was confirmed later by Tayfun when he introduced its celebrated distribution [20]. Tayfun distribution is widely accepted nowadays in the oceanographical context as it present a successful fit for the surface level distribution when nonlinear interacting waves are involved. It depends only on the wave steepness $k_p\sigma_\eta$. In particular it show very good agreement with wave turbulence experiments [5; 4] and large Basin measurements [13], where peaked waves are observed.

Therefore, to consider the skewness of a hight level distribution give statistical indications about the symmetry of surface deformations. Moreover, positive skewness may be related with the presence of nonlinear waves.

5.2 Measurement methods

In order to try a quantitative answer to the introductory question, we performed two kinds of measurement of the fluid level:

Local measurements by using an inductive sensor:

We briefly recall the principal advantages of this local measurement (the principle of this sensor is given in section 3.4): (a) It is very easy to use and data analysis is straightforward. (b) It is non intrusive, as the sensor we use can be placed far enough from the surface. (c) There is no practical limitation in temporal resolution, so we can perform very long and well resolved measurements.

Its drawbacks, on the other hand are: (a) It provide no information about spatial structure of the surface deformation. (b) It perform an intrinsic spatiotemporal filtering defined by its horizontal section. As we used a model with d =17 mm, one estimates its frequencial cutt-off at around 12 Hz (see section 3.4). This filtering is, by far, the most significant drawback of this method.

We performed measurements using this sensor at different points and under different conditions, which are specified in table 5.1. Each M in the table correspond to a whole series of measurements, spanning several forcing strengths.

Measurements along a line:

In order to access the spatial structure of the surface deformation, we developed a measurement method along a line. As for the previous case, here we recall few points. For the detailed description of the technique see section 3.4. The advantages of the technique are that: (a) It allows the study of spatially varying surface deformation. (b) As one record several points at the same time, the statistics can be better than those of a local measurement for equivalent measurement time. (c) The technique is non intrusive. (d) Spatial resolution is limited by the thickness of the laser layer we use, of about half a millimeter. Its drawbacks are: (a) spatiotemporal resolution is limited by the camera which is used. In our case we used a camera with high spatial resolution but with an acquisition frequency of just 60 Hz. Also, acquisition length T is limited by the material.

(b) Vertical resolution of surface deformation is very limited (about 4 pix/mm). (c) Data analysis is very time consuming. (d) Finally, the range of measurement is smaller than for inductive sensors.

Given the advantages and drawbacks of these two techniques, whenever it is possible, we performed both kind of measurements. When it is the case, we will discuss their results in parallel. However, other measurements were only possible with only one of the two methods, in particular the spatial and spatiotemporal analyses.

5.3 Experimental Results

5.3.1 General observations

5.3.1.1 Temporal, spatial and spatiotemporal evolution

The temporal evolution of the surface level at a given point $\mathbf{x_0}$ is shown in figure 5.2. Four different experimental conditions are presented, showing natural changes. For instance, fluctuations are larger and faster when the forcing is increased (in figure 5.2, compare (a) and (c) with (b) and (d)). However, every signal show erratic motion, signature of the underlying turbulent motion.

When we consider measurements resolved both in space and time, erratic motion is visible again, as expected. This is accompanied with coherent motion, evoking in particular the vortical origin of the surface deformation. This is shown in figure 5.3, where two instantaneous profiles of the deformation field are presented. Both profiles contain a vortex, which core is placed at different points (see the caption). As the measurement is along a line, we cannot be sure if the profile corresponds exactly to a vortex core. However, they were chosen as the –local– maximal depletions in the spatiotemporal diagram.

In order to consider spatiotemporal measurements, we should notice that the deformation field is composed from two components:

$$\eta(x,t) = \delta\eta(x,t) + \overline{\eta}(x), \tag{5.3}$$

where $\delta\eta(x,t)$ are fluctuations with zero mean, and $\overline{\eta}(x)$ are time averages over the whole measurement period.

Table 5.1: Specifications of local series of measurements. The coordinate system is the same as for PTV measurements (see top panels in figures 4.1 and 4.3). T is the total acquisition time and $f_{acq.}$ is the acquisition frequency.

Measurement	x_0 $[cm]$	y_0 $[cm]$	T [min]	$f_{acq.}$ [Hz]	Forcing	Comments
M1	5	34	5; 40	3012	regular	close to border
M2	15	23	5	3012	regular	
M3	28	17	5	3012	regular	
M4	24	19.5	5; 40	3012	regular	
M5	12	18	5	4986	regular/random	
M6	44	24	5	4986	regular/random	close to border

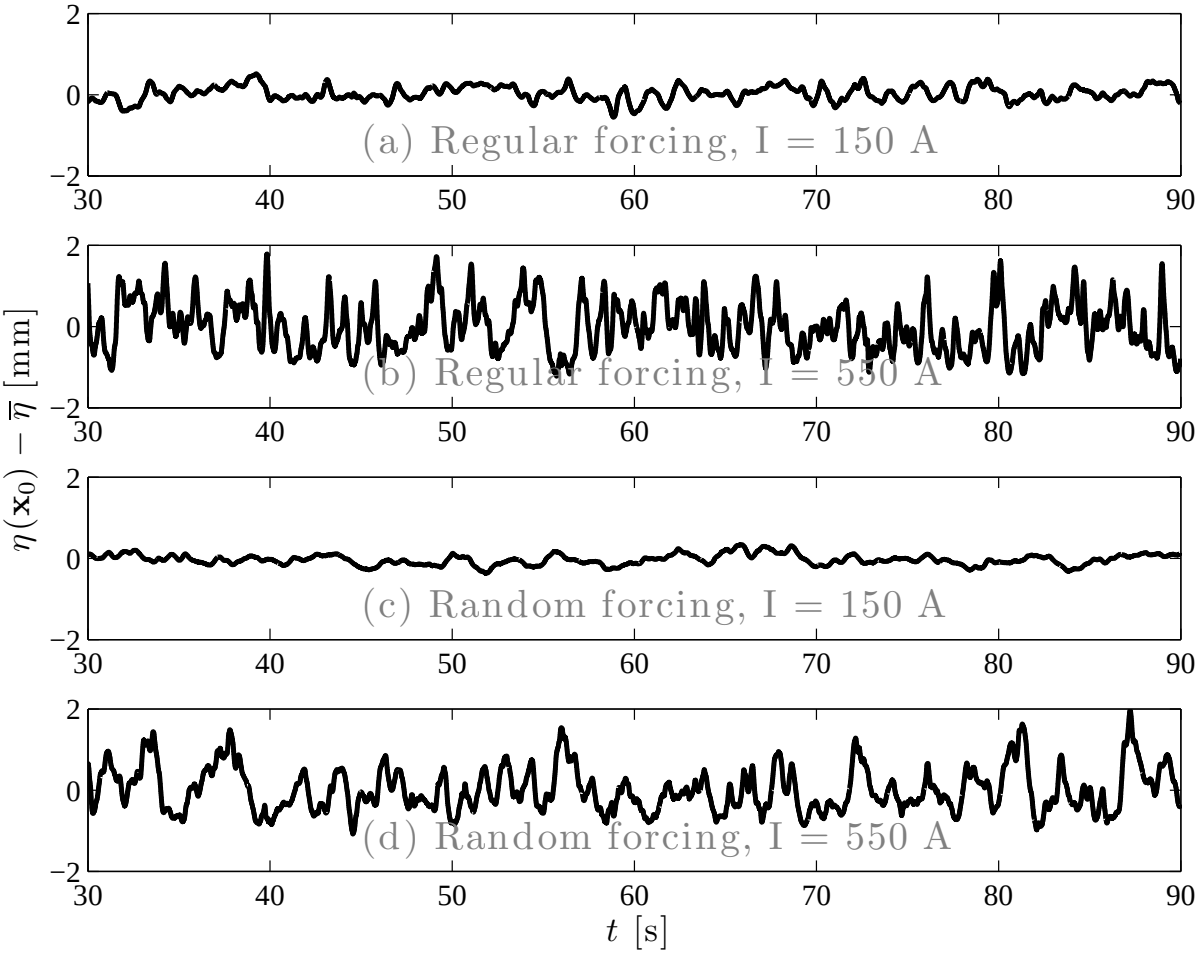

Figure 5.2: Examples of temporal traces of the surface level η at a fixed point (from series M5). Forcing conditions are as follows: (a) $I = 150$ A, regular forcing; (b) $I = 550$ A, regular forcing; (c) $I = 150$ A, random forcing; and (d) $I = 550$ A, random forcing.

The spatiotemporal evolution of $\delta\eta$ is presented in figure 5.4. Each figure correspond to 10 seconds and almost the whole container length $L_x = 40$ cm. Top panels correspond to a forcing strength of I = 150 A, for the random forcing (a) and regular one (b). Both panels share a common color–bar symmetric around 0. Bottom panels correspond to a forcing strength of I = 350 A. Color–bar (again symmetric around 0) span larger values in this case. As in the temporal traces of figure 5.2, we can see here that fluctuations increase with the forcing as expected, and that the deformation become faster. We may notice that the regular forcing seems to present richer dynamics than the random one.

Time averages $\overline{\eta}(x)$ are presented in figure 5.5. Here again random forcing is on the left and regular one on the right. The color–code here is related to the forcing strength, going from I = 100 A (in dark blue) to I = 400 A (in dark red). Along this chapter we will maintain the color convention going from blue to red as the forcing is increased.

In opposition to temporal fluctuations $\delta\eta$, random forcing present much stronger time averaged deformation. These features recall those from the velocity field: random forcing

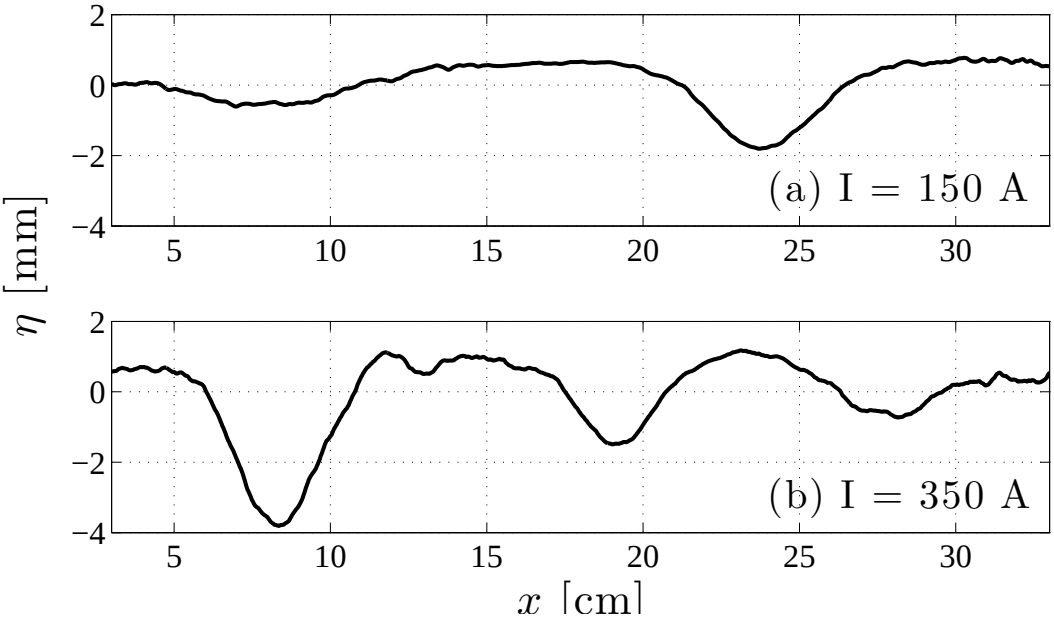

Figure 5.3: Examples of instantaneous profiles of the surface level η when a vortex is present. (a) corresponds to a forcing of $I = 150$ A and the vortex core is placed at $x_0 \sim 24$ cm. (b) corresponds to $I = 350$ A and the vortex core is placed at $x_0 \sim 8$ cm. In both cases the forcing is regular.

is more coherent, in opposition to regular one, which is more fluctuating. It is plausible to expect a more coherent deformation field from the more coherent velocity field. Indeed, one may see –qualitatively– a strong correlation between the averaged deformation $\overline{\eta}(x)$ and the corresponding averaged velocity profiles, presented in previous chapter (see figure 4.3, which is obtained on the same line as deformation measurements).

Therefore, as the time averaged profiles strongly depend on the forcing conditions, in what follows, we will focus our attention only in the fluctuations $\delta\eta$.

5.3.1.2 Amplitude of fluctuations of the surface level

We will focus now on statistical quantities, suitable for the problem under our consideration.

We consider first the standard deviation:

$$\sigma_\eta = \sqrt{\frac{1}{N_C}\int (\delta\eta)^2 \, d\Omega}, \tag{5.4}$$

where $\delta\eta = \eta - \overline{\eta}$ are fluctuations of the surface level; $d\Omega$ is the integration domain (just dt for time evolving signals or $dt\,dx$ for signals evolving in space and time) and N_C is the corresponding normalization constant.

The measured standard deviation is presented in figure 5.6. Colors represent the forcing protocol: regular forcing is in red and random forcing in blue. This color notation

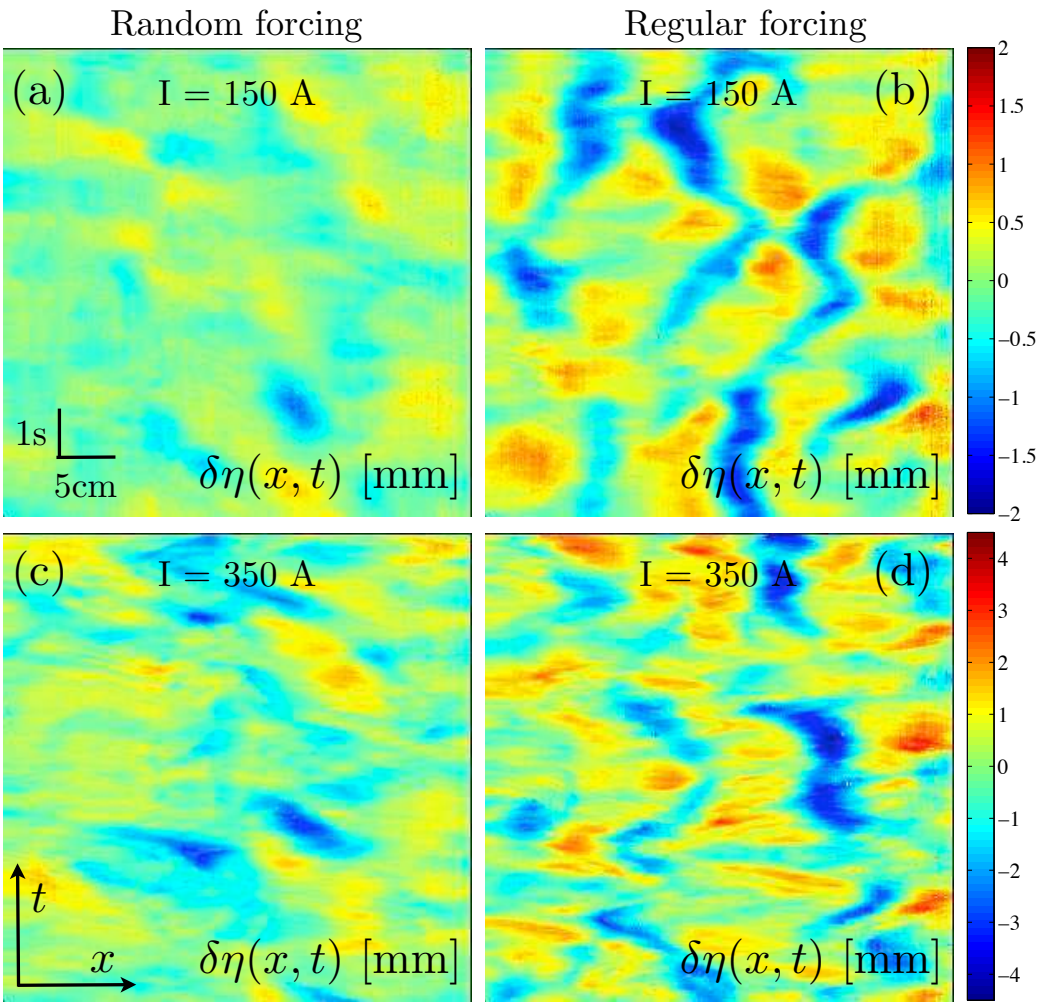

Figure 5.4: Spatiotemporal evolution of the fluctuating part of the deformation field $\delta\eta$. Panels on the left are for the random forcing, and those on the right for the regular one. (a) and (b) correspond to a forcing of $I = 150$ A, although (c) and (d) to a stronger one of $I = 350$ A.

will be respected all along this chapter. For each forcing strength (defined by the intensity of electrical current I) we performed measurements resolved in space and time. With the data we can get a global value for the fluctuations. However, using the same data set, we performed a coarse–graining process on a given spatial window, in order to estimate the error–bars shown in the figure.

One of the differences between random and regular forcing –discussed before in a qualitative manner– is now quantified: the regular forcing produces strong temporal fluctuations, growing at a rate of about $3 \cdot 10^{-3}$ mm/A; on the other hand, the random forcing develops weaker fluctuations, growing at a rate of about $2 \cdot 10^{-3}$ mm/A.

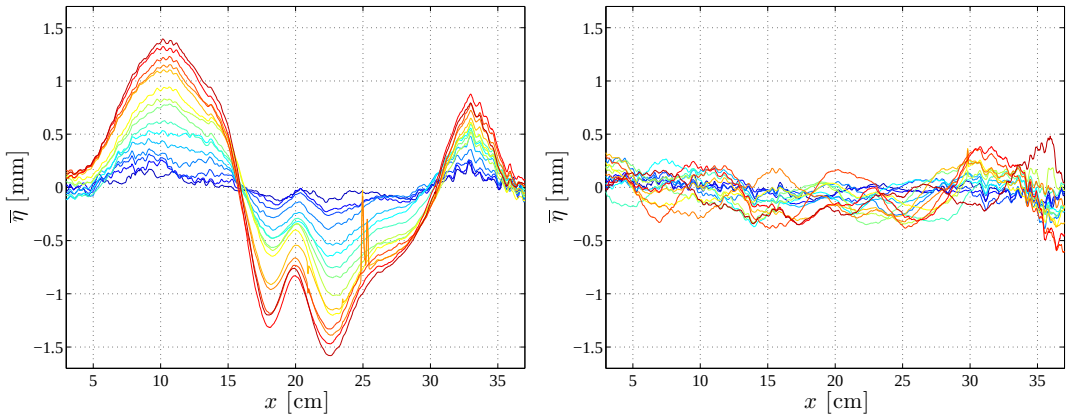

Figure 5.5: Time averaged part of the deformation field $\overline{\eta}$. Panel on the left is for the random forcing, and the one on the right for the regular one. Color–code evolves with the intensity of forcing, going from a weak one ($I = 50$ A, in dark blue) to a stronger one ($I = 400$ A, in dark red).

5.3.2 Surface level spectra

The next feature to consider when studying erratic signals, is the spectral content. Indeed, heigh fluctuations in fluids with free–surface had shown nontrivial phenomena as power–law spectra, in analogous way as for turbulent motion (see, for instance, chapter 2, or Falcon *et al.* [5]). We are referring here to the so–called wave–turbulence theory, which is a natural framework to compare with our experimental results.

We measured first the frequency spectrum, obtained for the regular forcing and for several forcing strengths (as referred in the legend). Examples are presented in figure 5.7-left. They are obtained using the inductive sensor, as it has a better temporal resolution. We compute the Power Spectral Density (PSD) using the welch estimator. Typically we compute the PSD using a 2^{15} points window (acquisition frequency is 3012 Hz in most cases) overlapped 1/4 of its length. Thus the resulting PSD was averaged at least 100 times. We used a Hamming window in each section of the signal.

What we shown in figure 5.7-left are the PSDs of the normalized surface level $\delta\eta/\sigma_\eta$, that show a power-law dependence on the frequency from 1 or 2 Hz to 10 or 20 Hz. We also traced a reference power-law PSD$(f) \sim f^{-5}$ that appeared to be in qualitative agreement. We will come back to its interpretation.

To be more quantitative, we computed a linear fit in the log-log representation, thus assuming the power-law dependence on the frequency for the range from 2 Hz to 10 Hz. This is presented as the ω-slope in figure 5.7-right[2]. Error-bars were constructed over equivalent realizations (same forcing strength and same forcing protocol).

[2]We preferred to use a fixed range in order to make the comparison easier. This choice pushed us to exclude lower forcing strengths from the analysis, as the power-law dependence was not clear. The analysis was performed for local measurements presented in table 5.1, although we excluded measurements done close to the wall, as they present the trace of a peak identifiable with the container size, that made the fit more questionable.

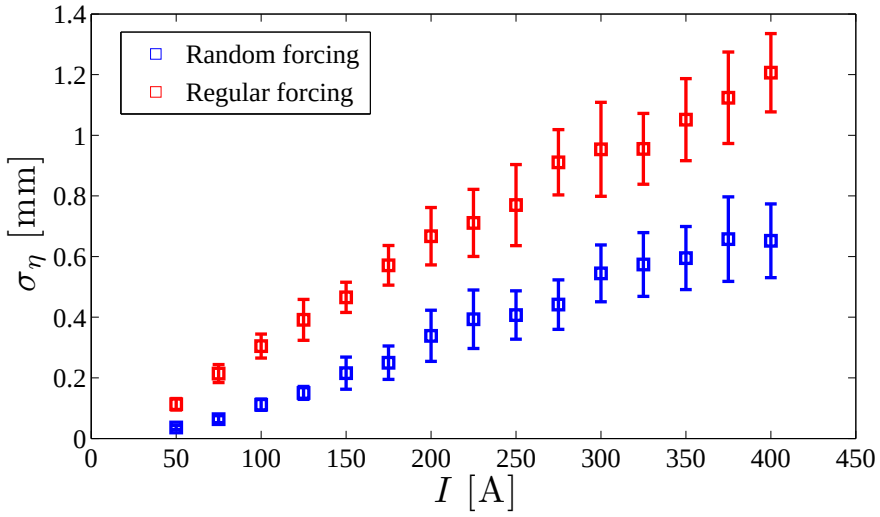

Figure 5.6: Standard deviation (STD) of the surface level $\delta\eta$ for spatial measurements. Error bars are constructed on spatial deviation (the space is divided on 25 zones). See more details on section 5.3.5.

Figure 5.8-left presents the spatial spectrum for the regular forcing. Here again we used the welch estimate of the PSD, but as this time signals correspond to images (of 1640 pixels of horizontal length), we computed the PSD in each frame along its whole length with no overlap. The PSD of the mean profile is subtracted in order to focus ourselves in fluctuations. The instantaneous PSD is averaged for the whole set of frames (3600). At low forcing there is a peak corresponding to $\lambda \sim 10$ cm, which is larger than the expected vortex size (this is not observed for the random forcing). However, we cannot discard a preferred scale –selected by the forcing– of separation between vortices. For larger forcing, we performed log-log fits between inverse length-scales from 0.13 cm^{-1} to 0.5 cm^{-1}, despite they are much more questionable than those for the ω–spectrum. The results are shown in figure 5.8-right.

In a general manner, we can say that the ω-slope (fig. 5.7-right) spans values from -6 to -4, and we can already notice that a comparable range of slopes was observed for the gravity spectrum in experiments of wave turbulence (see, for instance, Falcon *et al.* [5]). k-slope on the other hand (fig. 5.8-right) spans values from -4.8 to -2.7.

Both ω-slopes and k-slopes show the tendency to increase when the forcing is increased, although there is considerable difference concerning the forcing protocol: slopes for random forcing are higher than those observed with the regular forcing.

We can recall two paradigmatic predictions for the spectrum of gravity waves (already discussed in the introduction, section 2.5): wave turbulence theory predicts a power law spectrum as f^{-4} for the frequency and as $k^{-5/2}$ for wave-number. It is based on the weak interaction of (four) nonlinear waves and it is also dependent on the injected power. A second prediction is the one by Phillips [14], where the frequency spectrum scales as f^{-5}

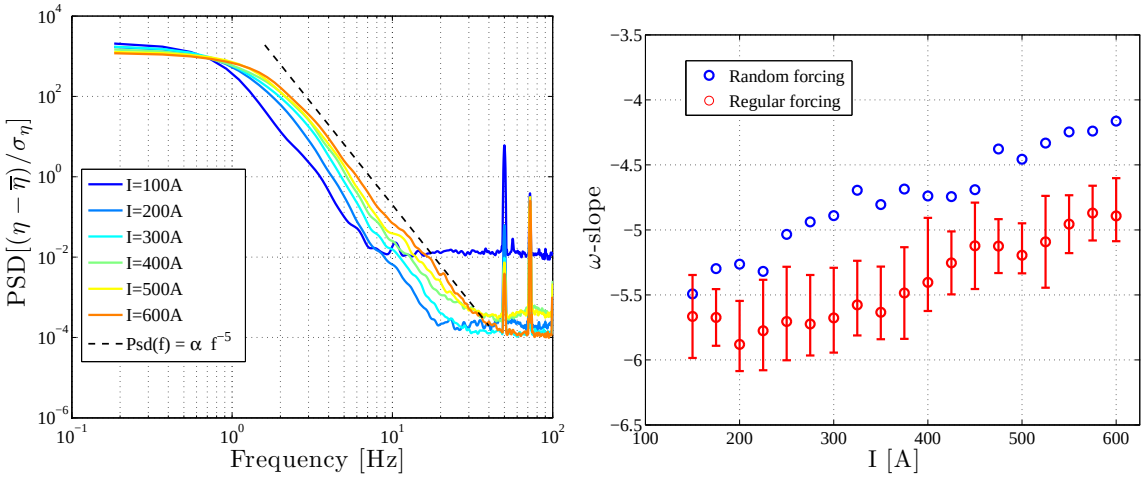

Figure 5.7: (a) Examples of Power Spectral Densities (PSDs) of the rescaled surface level $\delta\eta(x_0,t)/\sigma_\eta$ taken at position M4, roughly at the center of the container. We used the regular forcing with strengths referred in the legend. The power law f^{-5} is plotted as a reference. (b) ω-slopes obtained from the fit of the PSD between 2Hz and 10Hz; error bars were computed over realizations taken far from container borders.

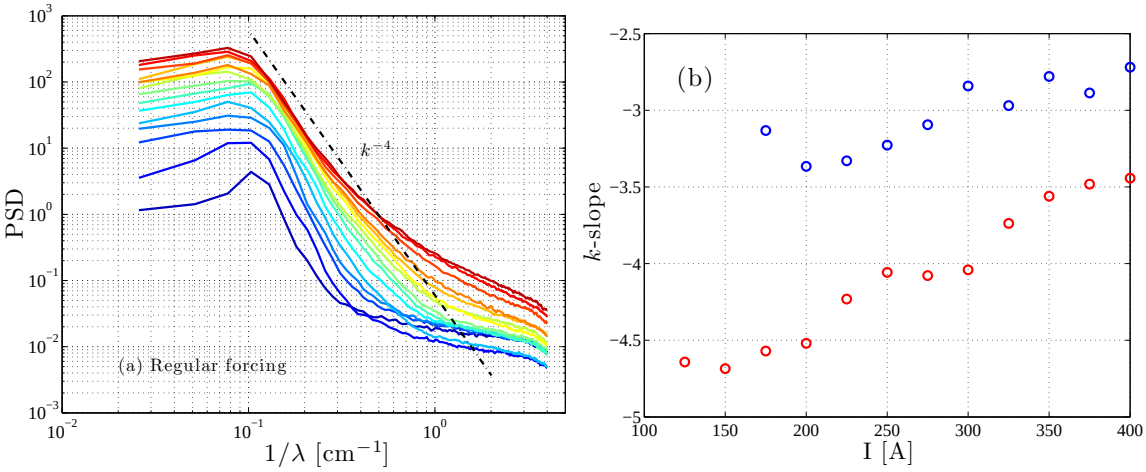

Figure 5.8: (a) Spatial PSD computed from measurements along the line $\delta\eta(x,t)$. Here colors go from $I = 50$ A (blue) to $I = 400$ A (red). The power law k^{-4} is plotted as a reference. (b) k-slopes obtained from the fit of the PSD between 0.13 cm^{-1} and 0.5 cm^{-1}.

and wave-number in k^{-4}. It is based on the limiting peaked shape of waves near breaking, thus it represent a more *geometric* picture. However, it should be noticed that for one dimensional measurements this spectrum should read k^{-3} as suggested, for instance, by Nazarenko *et al.* [12].

Phillips' prediction is not only the closest one to our experimental measurements. It can be formulated on discontinuity arguments, whatever the orientation of the discon-

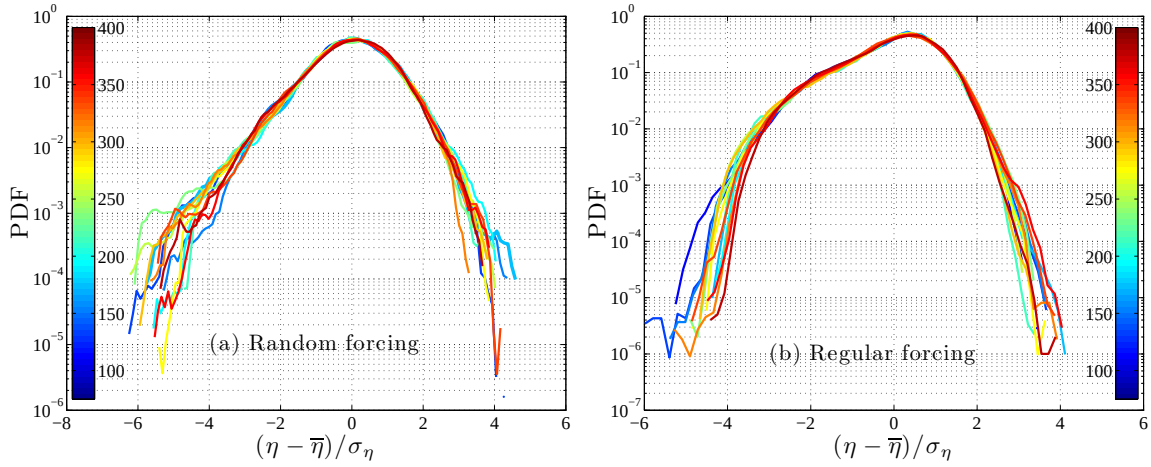

Figure 5.9: Probability distribution functions of $\delta\eta(x,t)$: (a) random forcing; (b) regular forcing. Color–code is the same as in figure 5.8.

tinuity is. Therefore it is valid for discontinuities coming both from strongly nonlinear waves, and from vortices cores, as those presented in figure 5.3. To this point, we cannot distinguish which of the two processes originate the Phillips' spectrum in our experiment, although vortices seem to be more plausible candidates.

5.3.3 Asymmetry in surface level distributions

Now we consider the distribution of hight fluctuations $\delta\eta$, in the form of normalized histograms or Probability Distribution Functions (PDFs). In figure 5.9 we present the PDFs obtained from spatially–resolved measurements. PDFs for the regular forcing are on the right and those for the random forcing on the left. As we already know the amplitude of fluctuations σ_η (see figure 5.6), we traced here the *normalized* PDFs: the distributions of $\delta\eta/\sigma_\eta$. By doing so, we focus on the shape of the distributions.

We can remark that distributions are asymmetric, and always concentrated through values below the mean. This feature can be quantified by considering the third order moment of the distribution, or skewness, which is actually a measure of the distribution symmetry. It is defined as

$$\text{Skewness}(\eta) = \left(\frac{1}{N_C} \int (\delta\eta)^3 d\Omega \right) / \sigma_\eta^3, \tag{5.5}$$

with the same notations used for equation (5.4). It is negative when the distribution has more values under the most probable value; zero when the distribution is perfectly symmetric (for example a gaussian); and positive when the distribution presents more values over the most probable one.

Thus, the asymmetry of our distributions is confirmed in figure 5.10. As for the computation of σ_η, we performed a spatial coarse–graining to get a more representative value and the corresponding error–bars. Then, the most salient feature is that the skewness is always negative and almost independent of the forcing. This quantification is consistent

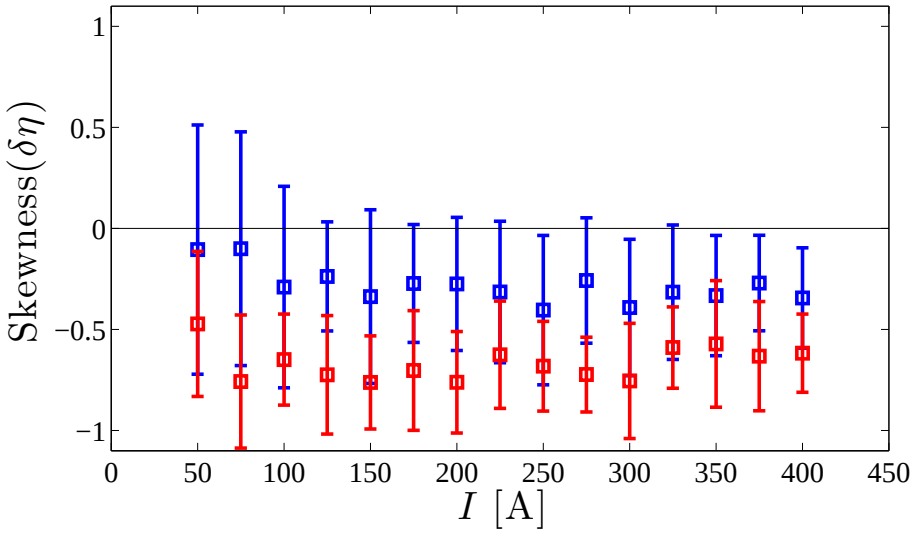

Figure 5.10: Skewness of $\delta\eta(x,t)$ for spatially resolved measurements. The black line at zero corresponds to a perfectly symmetric distribution. As in figure 5.6, error–bars are constructed by considering spatial variability.

with our observations of the PDFs. In particular it is interesting to emphasize the almost negligible changes in the shape of the distributions, which is why the skewness stay almost constant. We can notice that the shape of the distributions is more than fixed: it is also nontrivial, especially in the case of the regular forcing (figure 5.9b). Indeed, one may think that a second maxima is developing and eventually the distribution will become bimodal. But we check that the signals are not bistable. Another origin of this particular shape may be found when superposing selected profiles, as we do in figure 5.11. Here we superposed the same profiles from figure 5.3 after re–normalizing them on σ_η. This sug-

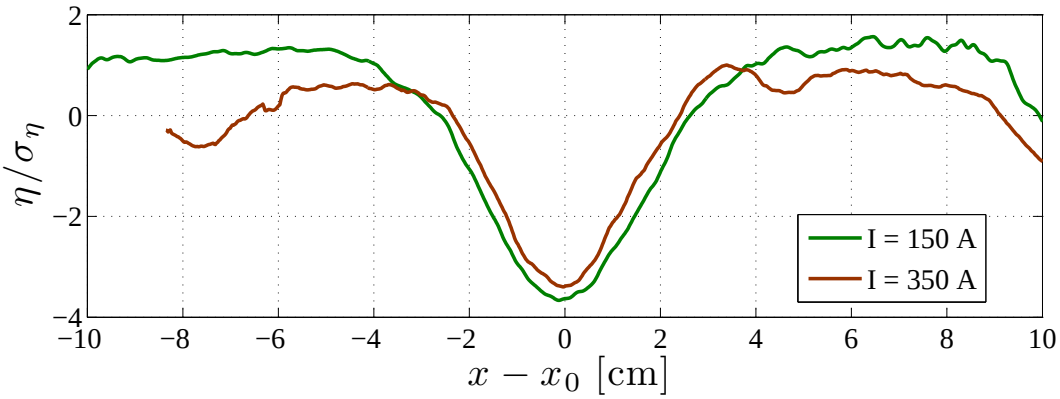

Figure 5.11: Vortices from figure 5.3 rescaled by the standard deviation.

gest the self–similar shape of depletions as another explanation for the non–trivial shape of distributions. However, more profound analysis should be done in order to confirm this hypothesis.

Let us return to the connection with wave–turbulence. First we should notice that in wave–turbulence experiments [5] and in for ocean waves [13], the skewness is always positive and increases linearly with the *forcing* (see equation (5.2)). Therefore, nonlinear wave theories are in complete disagreement with our observations. However, it is still true that a non zero skewness could be interpreted as the statistical signature of a nonlinear process shaping the distribution. In our experiment we observe a negative skewness and we saw the natural candidates: coherent vortices. Surface deformation of individual coherent vortices present a natural asymmetry though values under the mean level as a consequence of the lower pressure in vortices cores. Therefore, level depressions could have more statistical weight due to vortices, partially explaining our observed distributions.

Vortices are natural candidates to explain both the observed Phillips' spectrum, and the negative asymmetry of the height distributions. Therefore, it is tempting to see these two results as the statistical signature of vortices on the surface deformation.

5.3.4 On the possibility of wave generation

Despite the PDFs suggest vortices as the principal content in our deformation signals, the observed spectra give no indication about its origin –let us say, if they come from vortices or from nonlinear waves–. This is particularly true about Phillips spectrum.

On the other hand, for the arguments developed in the introduction of this chapter, we expect some generation of waves by the turbulent flow. Therefore, it is interesting to ask ourselves if the measured deformation respect the dispersion relation of linear waves. It was shown that it is the case for externally excited waves: monochromatic waves (see, for instance, next chapter); random nonlinear waves [7; 2] and in some experiments of channel flows [18; 19].

To study that, we consider is the joint (ω, k)-spectrum. It is obtained by applying the Fast-Fourier-Transform (FFT) to the spatiotemporal diagram $\delta\eta(x,t)$. As for the PSD calculations, Hamming windows is used. Despite the limited acquisition time (1 min), and as in this analysis the temporal resolution is not crucial, we divided the original signal in 6 shorter time windows that were overlapped in 1/4 of the period, in order to average few times. This result in a temporal resolution of $\Delta f = 0.1$ Hz, together with the spatial resolution that is kept unchanged at $\Delta\lambda^{-1} = 0.025$ cm^{-1}.

Few examples for different forcing conditions are given in figure 5.12, where the (ω, k)-spectrum (expressed in the non-angular variables (f, λ^{-1})) is plotted in logarithmic scales. Both frequency and inverse length-scale are in linear scale. Figures on the top correspond to moderate forcing (I = 150 A), and figures on the bottom correspond to a stronger forcing (I = 350 A); right panels correspond to regular forcing and those on the left to the random one. In every case we included the full dispersion relation for gravity-capillary waves, although only gravity waves are expected in the shown region.

All figures look very similar despite the differences in forcing conditions: In all cases the most energetic scales correspond to zero frequency (at least lower than 0.1 Hz) and small, but not necessary zero inverse length-scale. This spectral content is clearly not

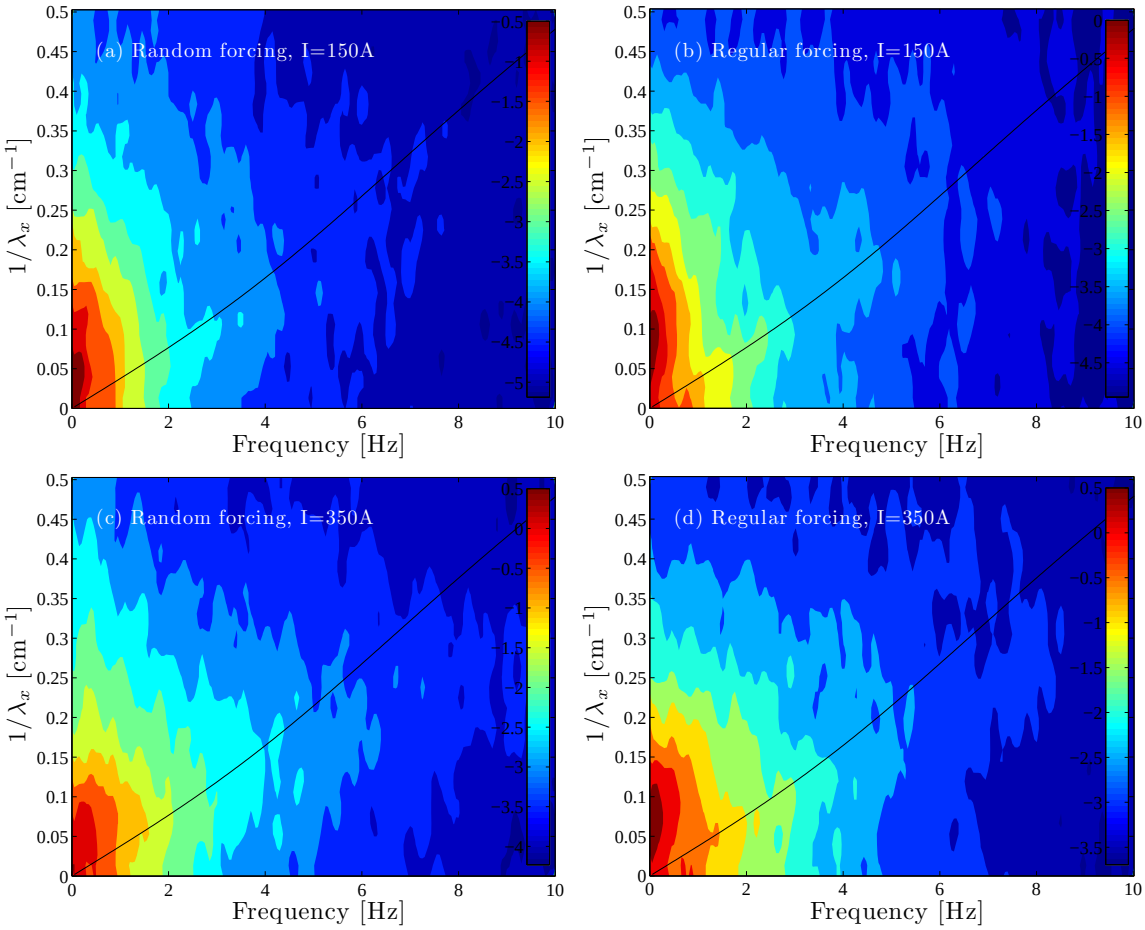

Figure 5.12: $(\omega, k)-$spectrum obtained from computing the FFT of the spatiotemporal diagram. It is plotted in logarithmic scale. (a) Random forcing at $I = 150$ A; (b) Regular forcing at $I = 150$ A; (c) Random forcing at $I = 350$ A; (d) Regular forcing at $I = 350$ A. In all cases we included the dispersion relation for gravity-capillary waves (black lines).

associated to waves and most likely to the vorticity field. However, careful observation at frequencies larger than 1 Hz, allows us to notice that part of the spectral content follow the dispersion relation, especially for the regular forcing. This give some indication of the presence of waves in our flow. However, this indications should be confirmed by complementary measurements and analysis. For instance, the data analysis of the measurement along a line may be reformulated (see the perspectives of the technique in section 3.4). By doing so, we could analyze stronger forcing, where the effect is expected to increase. On the other hand, global measurements may improve the statistics and make clearer any spectral signature of the waves.

5.3.5 Technical challenge: which measurement we trust?

We should discuss a still puzzling issue concerning height level measurements: there is a discrepancy between local and spatially resolved measurements. It seems to come from the

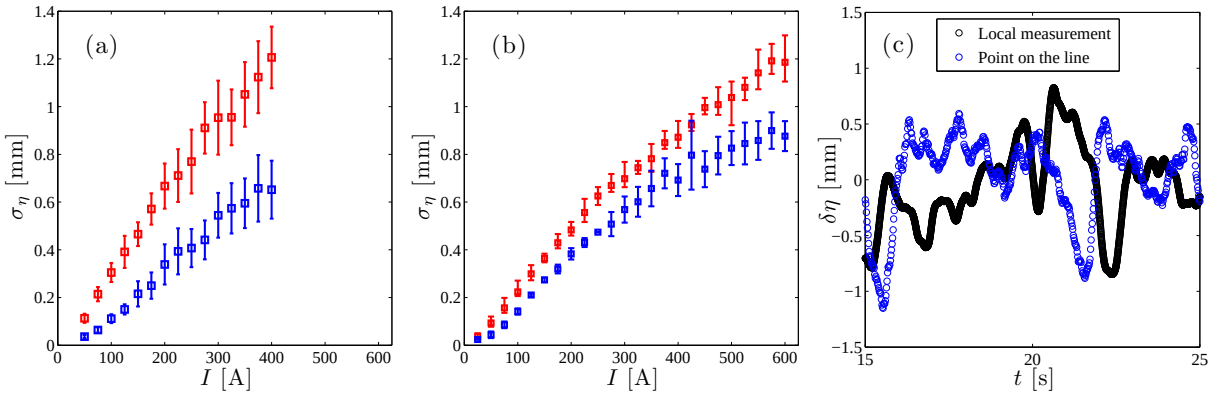

Figure 5.13: Discrepancy in measurement of σ_η. (a) Standard deviation of $\delta\eta(x,t)$ measured along a line (figure 5.6). The space is divided in zones of 17 mm where fluctuations are computed. Symbols represent the mean fluctuation amplitude and error–bars give account of the dispersion about this value. (b) Standard deviation of $\delta\eta(\mathbf{x}_0,t)$ measured with the inductive sensor. Error–bars are constructed over experimental realizations. (c) Temporal trace comparing local and spatially resolved measurements. Local signal is acquired at M4: $\mathbf{x}_0 = (24,19.5)$ cm. From spatially resolved measurement we choose a point at $\mathbf{x}_g = (25.3,20)$ cm. However, measurements are not simultaneous.

drawbacks of local measurements: (i) the inductive sensor we used performs averaging due to its large size; (ii) the somehow arbitrary position on which local measurements where taken. Now we present these discrepancies, together with a discussion of their possible origin.

In figure 5.13, we present the amplitude of fluctuations, as quantified with the standard deviation of the deformation field $\delta\eta$. Figure 5.13a is actually figure 5.6, and it is included again for comparison. It is obtained using space resolved measurements: once we have the deformation along the whole line, we divided it in few regions. Thus, for each region we obtain independent values of σ_η, from which error–bars are obtained. This procedure is similar to have several small sensors which perform averages over the given length scale at different places[3]. If we consider the line as a whole, we get a single –and slightly larger– value for the standard deviation. Figure 5.13b is the standard deviation obtained with *local* measurements. In this case, for each forcing strength, we performed measurements at different points (detailed in table 5.1). Symbols represent the mean value over all these measurements; and error-bars reflect maximum and minimum values for each forcing strength. In this way the region defined by error-bars covers the whole spanned values.

When comparing figures 5.13a and b, one may observe a significant increment on the values of σ_η measured with the line (a), compared with those obtained with local measurements (b). The possible reasons: (i) *local* measurements are performed at particular places. (ii) Spatially resolved measurements contain the fluctuating component $\delta\eta$ and a temporal average $\overline{\eta}$. (iii) *Local* measurements perform spatial average and give smooth

[3]Indeed, the scale we used is 17 mm: the diameter of the inductive sensor. However, the area considered in this coarse–graining is much smaller than the one used by the sensor.

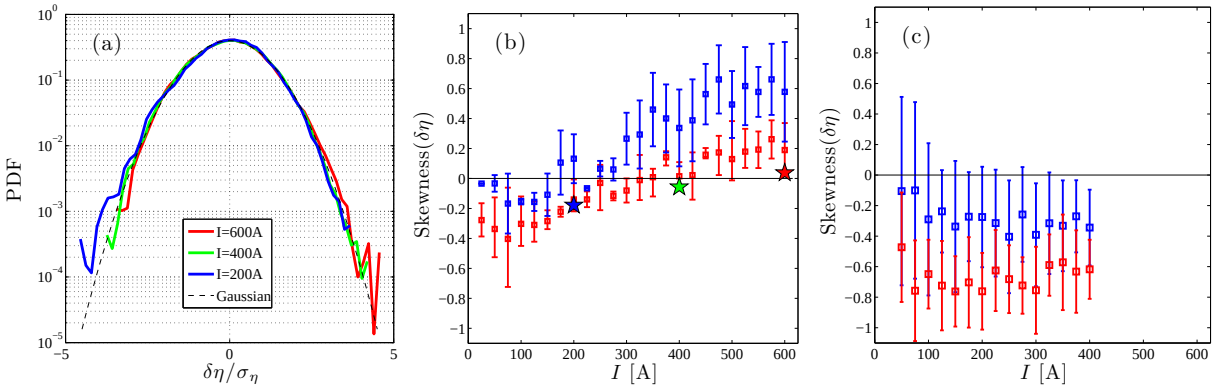

Figure 5.14: Discrepancy in asymmetry features of the PDFs. (a) Examples of PDFs of $\delta\eta(\mathbf{x}_0, t)$ for long measurements (40 minutes) taken at the center of the container, using the regular forcing. They are normalized by the corresponding standard deviation, and compared to a gaussian (black dashed line). (b) Skewness of $\delta\eta(\mathbf{x}_0, t)$. The black line at zero corresponds to a perfectly symmetric distribution. Error–bars are computed using the same procedure as for to those of the STD in figure 5.6. Colored stars correspond to example distributions (a). (c) Skewness of $\delta\eta(x, t)$. As in figure 5.13a, error–bars are computed over spatial variability.

signals. From these three, we should exclude the second one, as we concentrate all our analysis on $\delta\eta$. On the other hand, in figure 5.13c, we compare 10 seconds of *local* signal (in black) to part of the spatially resolved signal (in blue), despite the signals are neither simultaneous nor corresponding to the same point (see caption). We may see that blue signal captures peaked features in a better way the than black one, suggesting the filtering of *local* measurements as a very relevant one. We cannot discard the reason (i) although it cannot be evaluated without doing a more systematic study, which is a perspective.

It should be noticed, however, that the general qualitative features of the measurements remain unchanged. (1) Random forcing (in blue) produce smaller fluctuations than the regular forcing (in red). (2) The amplitude of fluctuations grow almost linearly with forcing, and get values of the order of a millimeter when the forcing is strong.

Now we focus on the asymmetry of the hight level distributions. In figure 5.14a, we show examples of PDFs of normalized fluctuation amplitudes $\eta(t)/\sigma_\eta$ obtained in long measurements (40 minutes) with the *local* inductive sensor. They are obtained using the regular forcing (at point M4) for three forcing strengths. The gaussian distribution with standard deviation equal to 1 is also shown as a reference (black dashed line). This three examples show some asymmetry, but they are much more symmetric than the PDFs obtained in spatially resolved measurements (figure 5.10). The skewness of *local* measurements is presented in figure 5.14b, considering all realizations (table 5.1), most of them performed during shorter times. This figure includes the values of the examples as stars of the corresponding color. For comparison, the skewness of spatially resolved measurements (figure 5.10) is presented again in figure 5.14c.

Three main features appear in figure 5.14b: (i) the regular forcing (in red) show lower skewness than the random one (in blue). (ii) There is an increase in the skewness with

the forcing strength. It is similar for regular and random forcing, and it is seems to be linear. (iii) As the skewness starts at negative values and increases with the forcing, there is a forcing at which the asymmetry changes in sign. Figure 5.14c only reproduces the first feature. Moreover, it replaces (ii) and (iii) by another, equally striking feature: the skewness is always negative and almost constant.

The possible explanations of the discrepancy are similar to those for σ_η. The filtering process performed by the inductive sensor seems a major element: it smooth the signals, turning them more gaussian. However, this cannot explain any evolution of the skewness through positive values. We have to notice that long measurements (as those presented in figure 5.14a and as stars in 5.14b), do show very small skewness, and those with poor statistics present larger values. One has to recall that high order moments –as the skewness– are very sensitive. They can only be trusted when statistics are significant. In this sense, the quality of statistics is expected to be less crucial in the case of σ_η. Finally, the fact that we measured only at given points, could be another source of disagreement.

To conclude, we presented and discussed the elements of discrepancy between the two methods of measurement we used. *Local* measurements are not precise enough to capture the details of peaked deformations, as those concerned in our study. Thus, in most of the quantities studied here, spatially resolved measurement give us more confidence. On the other hand, the very limited temporal resolution of our spatially resolved measurement make the local measurement a necessary complement. Even if some arguments were developed, discrepancies in the skewness are strong –both quantitatively and qualitatively– and deserves further analysis.

5.4 Summary and conclussion

In summary, in this chapter we considered the surface deformation produced by a quasi–bidimensional velocity field. By performing spatially resolved measurements, together with local ones –better resolved in time–, we acceded to the surface deformation and its statistics.

Fluctuations of the surface level increase when the forcing is increased. This is evaluated by the standard deviation σ_η. At strong forcing, σ_η exceed the millimeter, which corresponds to the 10% of the fluid layer thickness. Largest deformation can reach the half of the layer thickness, as it can be seen from Probability Distribution Functions (PDFs).

There are systematic differences between forcing protocols: random forcing produce smaller fluctuations ($\delta\eta$) than the regular forcing, although time averaged profiles ($\overline{\eta}$) are larger. Regular forcing present opposite features. This is consistent with the picture given by velocity fields –considered in the previous chapter–: random forcing produces a more coherent, large–scale time averaged velocity field (more important than its fluctuations). This induces strong average deformation profiles and smaller fluctuations. Regular forcing presents a less important time averaged velocity field, with larger temporal fluctuations. This is also translated into surface deformation.

When considering the spectrum of surface level fluctuations, we observe a frequency spectrum with clear power-law dependence on the frequency. ω-slopes are qualitatively close to -5 (quantitatively they range from -6 to -4). For the wave-number spectrum k-slopes range approximately from -4.8 to -2.7. Strong vortices that develop local singu-

larities, are expected to show a Phillips like spectrum (in k^{-3} and ω^{-5}).

Non trivial PDFs are observed. They show important asymmetries through values under the mode. This is quantified by the skewness of the surface level distribution, which is negative.

As we are dealing with the deformation of free surface subjected to gravity and capillarity, we discussed possible connections with wave–turbulence theory, developed in the same context. Here, ω-slopes are consistent with measurements in wave–turbulence experiments, although the asymmetry features in surface level distributions (PDFs) are completely different. On the other hand, the frequency spectrum close to -5 and the negative skewness corresponds to the statistical signature of surface deformation induced by vortical motion.

Finally, when looking the joint (ω, k)-spectrum, we observe a very modest part – although still visible– of the surface energy following the dispersion relation of gravity-capillary waves. This give some hope about observing waves in our setup, despite it seems necessary to perform global measurements of the deformation field in order to be conclusive about this point.

5.5 Bibliography

[1] Cerda, E., and Lund, F. Interaction of Surface Waves with Vorticity in Shallow Water. *Physical Review Letters 70* (1993), 3896–3899.

[2] Cobelli, P. J., Przadka, A., Petitjeans, P., Lagubeau, G., Pagneux, V., and Maurel, A. Different Regimes for Water Wave Turbulence. *Physical Review Letters 107* (2011), 214503.

[3] Coste, C., and Lund, F. Scattering of dislocated wave fronts by vertical vorticity and the Aharonov-Bohm effect. II. Dispersive waves. *Physical Review E 60* (1999), 4917–4925.

[4] Denissenko, P., Lukaschuk, S., and Nazarenko, S. Gravity Wave Turbulence in a Laboratory Flume. *Physical Review Letters 99* (2007), 014501.

[5] Falcon, E., Laroche, C., and Fauve, S. Observation of Gravity-Capillary Wave Turbulence. *Physical Review Letters 98* (2007), 094503.

[6] Ford, R. *Gravity wave generation by vortical flows in a rotating frame*. PhD thesis, University of Cambridge, 1993.

[7] Herbert, E., Mordant, N., and Falcon, E. Observation of the Nonlinear Dispersion Relation and Spatial Statistics of Wave Turbulence on the Surface of a Fluid. *Physical Review Letters 105* (2010), 144502.

[8] Janssen, P. *The interaction of Ocean Waves and Wind*. Cambridge University Press, 2004.

[9] Lighthill, M. J. On sound generated aerodynamically. I. General theory. *Proceedings of the Royal Society A 211* (1952), 564–587.

[10] Longuet-Higgins, M. S. The Statistical Analysis of a Random, Moving Surface. *Philosophical Transactions of the Royal Society A 249* (1957), 321–387.

[11] Longuet-Higgins, M. S. The effect of non-linearities on statistical distributions in the theory of sea waves. *Journal of Fluid Mechanics 17* (1963), 459–480.

[12] Nazarenko, S., Lukaschuk, S., McLelland, S., and Denissenko, P. Statistics of surface gravity wave turbulence in the space and time domains. *Journal of Fluid Mechanics 642* (2010), 395–420.

[13] Onorato, M., Cavaleri, L., Fouques, S., Gramstad, O., Janssen, P. A. E. M., Monbaliu, J., Osborne, A. R., Pakozdi, C., Serio, M., Stansberg, C. T., Toffoli, A., and Trulsen, K. Statistical properties of mechanically generated surface gravity waves: a laboratory experiment in a three-dimensional wave basin. *Journal of Fluid Mechanics 627* (2009), 235–257.

[14] Phillips, O. M. The equilibrium range in the spectrum of wind-generated waves. *Journal of Fluid Mechanics 4* (1958), 426–434.

[15] Phillips, O. M. Recent Developments in the Theory of Wave Generation by Wind. *Journal of Geophysical Research 67* (1962), 3135–3141.

[16] Polvani, L. M., McWilliams, J. C., Spall, M. A., and Ford, R. The coherent structures of shallow-water turbulence: Deformation-radius effects, cyclone/anticyclone asymmetry and gravity-wave generation. *Chaos 4* (1994), 177.

[17] Raphael, E., and de Gennes, P. G. Capillary gravity waves caused by a moving disturbance: Wave resistance. *Physical Review E 53* (1996), 3448–3455.

[18] Savelsberg, R., and van de Water, W. Turbulence of a Free Surface. *Physical Review Letters 100* (2008), 034501.

[19] Savelsberg, R., and van de Water, W. Experiments on free-surface turbulence. *Journal of Fluid Mechanics 619* (2009), 95–125.

[20] Tayfun, M. A. Narrow-band nonlinear sea waves. *Journal of Geophysical Research 85* (1980), 1548–1552.

Chapter 6

The effect of turbulence on wave propagation

6.1 Introduction

Fluid flows bounded by a free surface exhibit rich dynamics, from simple structures as waves or vortices, to strongly interacting turbulent regimes (see [3], chapter 2 and/or figure 1). Indeed, these strongly interacting regimes between *structures* of the same kind allowed the development of celebrated theories during last century: fully developed hydrodynamic turbulence, which studied and characterized the nonlinear interaction between *eddies* (vortical structures of characteristic length and velocity) [10] and later on wave turbulence, which studied and characterized the nonlinear interaction between *waves* [7; 14]. Despite its comparable fundamental interest [2; 4], the problem of *wave–eddy* interaction –known as Wave–Vortex interaction problem, where these two theories merge– has received considerably less attention.

The Wave–Vortex problem is properly an *interaction* problem, as waves can influence vortex dynamics[1], and vortices can affect wave propagation and their structure. As it could be expected under these circumstances, such a complex problem is far from being completely understood. Some progress, however, can be summarized in the different facets of the interaction:

- *Generation of vorticity by waves:* Wave breaking is the clearest mechanism by which waves generate vorticity in the oceanographical setting. It happens on at least two scales: On scales at the order of –or smaller than– the wavelength, as water enters vertically producing a sudden perturbation, with the consequent strong shear, horizontal vorticity and, eventually, air entrainment [11]. Wave breaking can also induce vertical vorticity that progressively transfers energy from small scale breaking waves to larger scale rotational motion, especially –but not exclusively– in the surf–zone [16; 6].

[1] In the following we will make no distinction between vortices, vorticity and turbulence, as they are intimately related.

Figure 6.1: Waves and a vortex in japanese art, by Utagawa Hiroshige ($\sim$ 1855).

- *Distortion/scattering of turbulence by waves:* The previous case deals with vorticity generation from otherwise calm and perhaps irrotational fluid (at least on the starting phase). In a more general situation the fluid may be already turbulent. In that case, waves can still modify turbulence by increasing its turbulent kinetic energy. Apart from wave breaking, other enhancing mechanism is the coupling between turbulent motion and Stokes drift, which increase the turbulent kinetic energy to the detriment of wave energy [20; 1; 19].

- *Generation of waves by turbulence:* As we discussed in chapter 5, this topic can be traced back to Lighthill [13] and to the vast context of wave generation by turbulent wind. It was considered later by Cerda & Lund [5] and by Ford [9], and more recently in a experiment by Savelsberg & van de Water [18].

- *Distortion/scattering of waves by vorticity:* This problem was addressed theoretically by Phillips in the fifties [17]. He considered gravity waves (of wavenumber k, wavelength λ, frequency ω and wave velocity c_w) over a turbulent background, only characterized by the (small) intensity of turbulent fluctuations (with typical veloc-

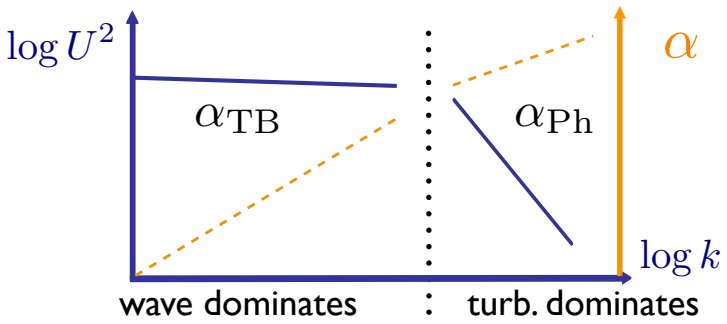

Figure 6.2: Schematic representation of the validity regions of the Phillips [17] and Texeira & Belcher [20] predictions for wave dissipation by turbulence.

ity U_t and length scale L). He found the directional distribution of the scattered wave, together with a prediction of the associated decrease of the wave amplitude during this process. One may model the propagation and dissipation of a wave as $\eta(x,t) = a_0 \mathrm{e}^{\alpha x} \sin(kx - \omega t)$, with a_0 the initial wave amplitude and α a spatial dissipation coefficient. Phillips predicted that dissipation scales as $\alpha_{Ph} \sim \epsilon^{2/3} k^{4/3}/g$ in the limit of small wavelengths compared to the typical scales of turbulence $\lambda \ll L$. More recently, Teixeira & Belcher considered –also theoretically– the opposite limit $\lambda \gg L$ and found a dissipation as $\alpha_{TB} \sim U_t^2 k^2/g$ [20]. Both theories also assumed $c_w \gg U_t$. We schematized them in figure 6.2, where we traced the energy spectrum (considering $U = c_w + U_t$) as a function of the wavenumber k, although only for the turbulence–dominated part the spectrum is well known: it scales as $U^2 \sim \epsilon^{2/3} k^{-2/3}$, as given by Kolmogorov theory. This scaling allowed us to notice that both predictions are actually part of the same picture, because if we extrapolate the Teixeira–Belcher scaling into the turbulence dominated part, we recover the Phillips prediction.

Experimentally, the influence of a turbulent flow on waves was studied by Ölmez & Milgram [15], and more recently –and under different conditions– by Falcón & Fauve [8]. Qualitatively, both experiments conclude that turbulent motion enhances wave dissipation. However, they do not access the spatial structure of the process. In other experiments, it was shown that a simple vorticity configuration (one or two vortices), leads to phase shifts of a surface wave that propagates over it [21; 22]. These attempts underlined the profound influence of turbulence on propagating waves, although a more general picture of the process is still lacking.

In chapter 5 we briefly discussed the possibility of wave generation by turbulent motion. This chapter will be devoted to another aspect of the Wave–Vortex Interaction problem: the influence of vorticity on monochromatic waves.

Despite hydrodynamics is perhaps the most natural context for the study of the interaction of waves with turbulence, it can be noticed that the problem is also relevant in the context of wave propagation in heterogeneous media.

6.2 The Experiment: MHD flow + mechanically induced waves

We used the very same Magnetohydrodynamical (MHD) forcing presented along this thesis, although we only consider here the regular forcing (section 3.1). The choice is based in our interest of studying a highly fluctuating turbulent flow, for what the regular forcing is better suited.

We excite waves on the liquid metal surface by means of an electromagnetic shaker controlled by a function generator. Therefore, a vertical sinusoidal vibration is applied to the liquid surface by a cylindrical paddle with horizontal extension of 11cm. This *source* of waves is placed on one corner of the working area, and measurements are performed on the diagonal (local measurements) and along the central line (see the setup schema in figure 6.3). We chose the vertical excitation as we expect to transfer most of the injected energy into wave modes. Horizontal excitation, on the other hand, is expected to transfer an important part of the energy into the velocity field. A drawback of this choice is the limitation of excited wave amplitudes because of the small fluid depth. A second limitation comes in general because of the formation of drops when the forcing is too strong.

As for the study of surface deformation, we measured the fluid level along a line using the stereoscopic detection (green line in figure 6.3), and *locally* by using an inductive sensor placed at the individual positions M1, M2 or M3 in figure 6.3.

The local measurements to be considered here are performed at points M3 and M2,

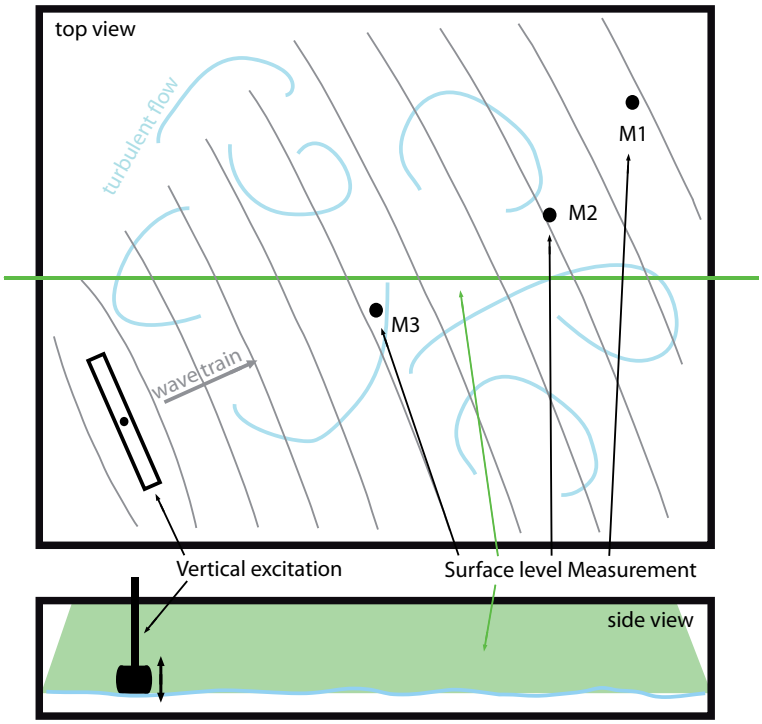

Figure 6.3: Experimental setup for study wave-vortex interaction.

Table 6.1: Detail of local measurements. M. Point is the measurement point, with coordinates (x_0, y_0); MHD forcing conditions are presented in terms of the imposed electrical current, in Amperes; a Label is given in order to distinguish from cases with only waves, only turbulence, or both.

M. Point	(x_0, y_0) [cm]	Wave conditions	MHD forcing	Label
M3	(28, 17)	f_0=7Hz	{0–400}A	M3W / M3WT
M3	(28, 17)	no excitation	{20–400}A	M3T
M2	(15, 23)	f_0=7Hz	{0–350}A	M2W / M2WT
M2	(15, 23)	no excitation	{25–350}A	M2T

Table 6.2: Scales involved in the experiment. Length scale can refer both to a wavelength λ (for excited waves), or to another physical dimension.

Source	Length scale [cm]	Frequency [Hz]
Container	40 & 50	0.67 & 0.53
Fluid thickness	1	23.16
MHD forcing (mean magnets separation)	3.8	5.92
Wave excited at 5 Hz	4.7	5
Wave excited at 7 Hz	3.1	7
Wave excited at 8 Hz	2.7	8

and their details are presented in table 6.1. As we are dealing both with a MHD forcing (producing irregular fluid motion) and with externally excited waves, sometimes we directly refer the flow produced by the MHD forcing as being turbulent, although is some cases (at low forcing) it is just unstationary.

Finally, we include in table 6.2 some relevant length and time scales involved in the experiment, specially those related to the forcing scale of turbulence, and those of the externally excited waves. Frequency and length scales presented here are linked by the dispersion relation

$$\omega^2 = \left(\frac{\rho_1 - \rho_2}{\rho_1 + \rho_2} gk + \frac{\gamma}{\rho_1 + \rho_2} k^3 \right) \tanh kh, \tag{6.1}$$

considering all length scales as being a wavelength. ω is the angular frequency, $k = 2\pi/\lambda$ the wavenumber, g is gravity, γ is surface tension, ρ_1 is the density of Galinstan, ρ_2 the one of acid and h is the fluid thickness.

6.3 Experimental results

6.3.1 Local measurements

In figure 6.4a, we present the standard deviation of height fluctuations. The four considered series presented in table 6.1 are included. We can see that there is not much

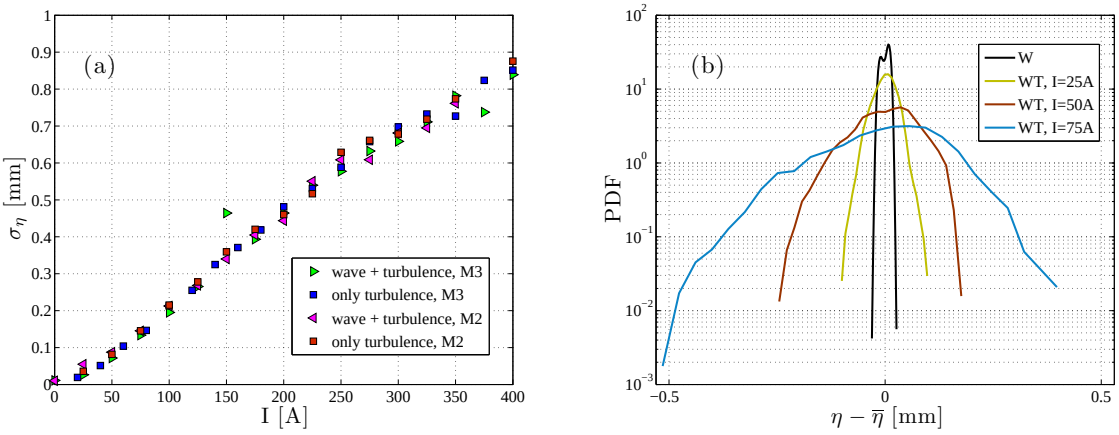

Figure 6.4: (a) Standard deviation of height fluctuations, for measurements referred in table 6.1. (b) Probability distribution functions for a case without turbulence (M3W, in black) and three cases including turbulence (M3WT, in colors).

influence of waves in the global amplitude of fluctuations. This is confirmed by the PDFs presented in figure 6.4b. Black line correspond to a case without turbulence (M3W). With a careful observation, one can appreciate that the distribution is bimodal, which is standard for a monochromatic sinusoidal oscillation. But it is also apparent that the amplitude is very small compared with those excited by the turbulent flow (M3WT, in colors) even when the forcing is not strong. Thus wave amplitude do not affect turbulent fluctuation amplitudes. Indeed, the imposed excitations are reflected as oscillations –at the given frequency f_0– superposed into larger scale height fluctuations produced by the MHD forcing. This can be seen in the spatiotemporal diagram in figure 6.6b.

In figure 6.5 we present the Power Spectral Densities (PSDs) of the corresponding measurements. They are computed using the same protocol as in chapter 5. In left panels we show the *Wave + turbulence* case (WT). Black lines correspond to I = 0 A, which is the case with no turbulence (W), and then, colors go from blue to red as the strength of the forcing is increased. Panel 6.5a is at point M3, and panel 6.5c is at point M2. Right panels present a selection of the WT cases (in circles), together with their turbulent (T) counterparts: the equivalent cases with no waves (thin lines of the corresponding color). Panel 6.5b is at point M3, and panel 6.5d is at point M2.

An intrinsic dissipation of waves over distance is expected. It can be recognized by comparing black curves in figure 6.5: we observe that the amplitude of the spectral peak at 7 Hz, associated to the excited wave, is around 5 times higher at M3 (top panels) than at M2 (bottom panel). M3 is closer to the wave source than M2. The quantification of this is given below.

For the cases with wave and turbulence, we can see that wave peaks measured at M3 persist until larger forcing than those measured at M2: from figure 6.5a one can distinguish the wave peak even at the larger forcing considered (I = 400 A in this case). At M2 the wave peak is no longer distinguishable from around I = 200 A (see the blue symbols in figure 6.5d). For cases were the wave peak is perceptible, it is accompanied by

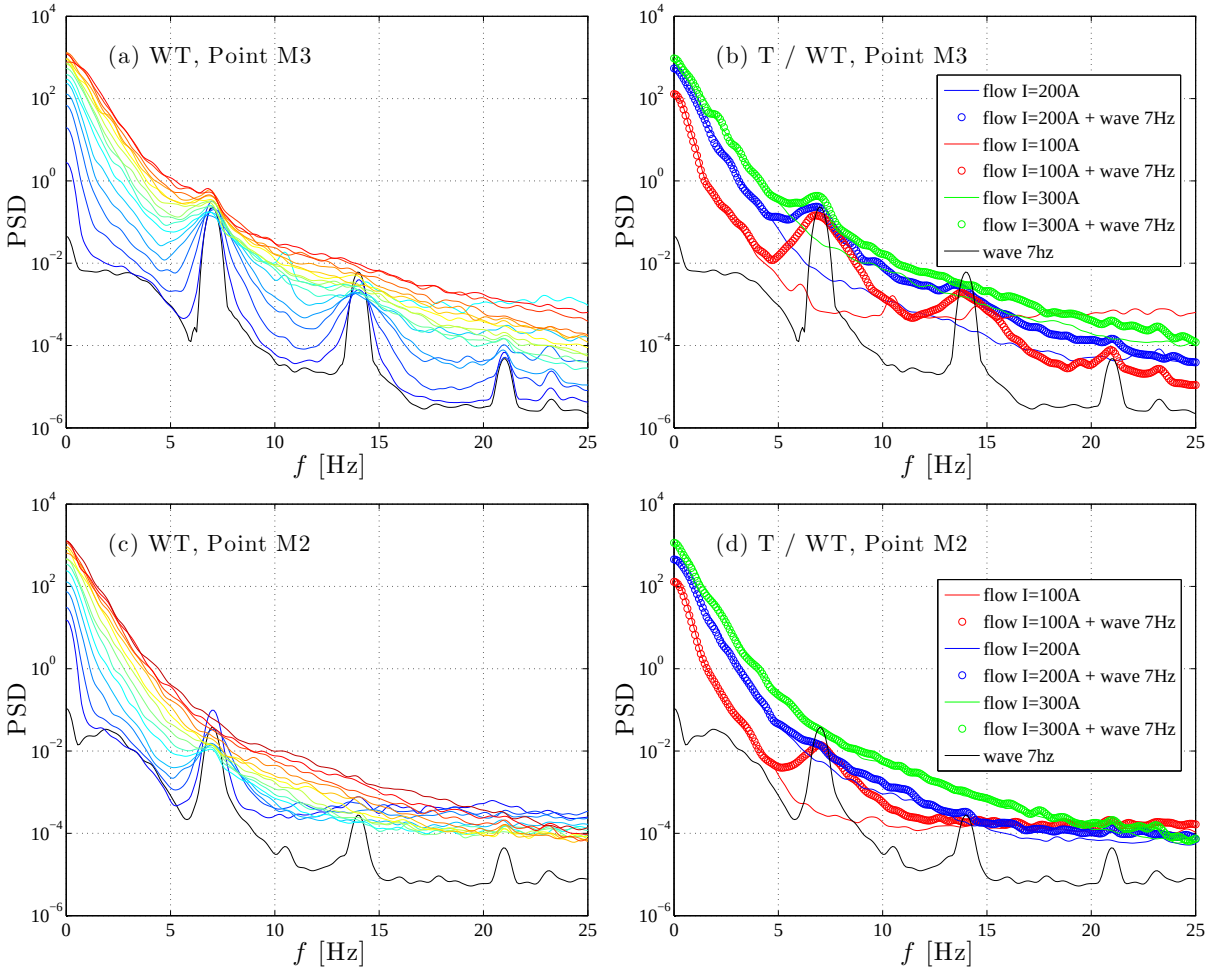

Figure 6.5: Power spectral densities (PSD). Top panels corresponds to M3, and bottom panels to M2. Figures on the left were obtained with turbulence and waves for all the explored forcing intensities. Those on the right are few examples when wave + turbulence (WT) is compared with the case with only turbulence (T).

the peak widening. These effects are the joint result of turbulence and dissipation over the distance traveled by the wave.

We can also compare cases with waves + turbulence and those with only turbulence by looking to the examples presented on right panels of figure 6.5. Solid lines (T) and symbols (WT) match very well until the frequencies associated to the peak induced by external excitation. Therefore one can conclude that the low frequency spectrum is the consequence of turbulent flow. For frequencies larger than the mechanically excited one, both spectra become different in general.

6.3.2 Spatiotemporal analysis

Although local measurements already show the effect of turbulence on wave dissipation, those resolved in space give further information about how it occurs, and allows alternative

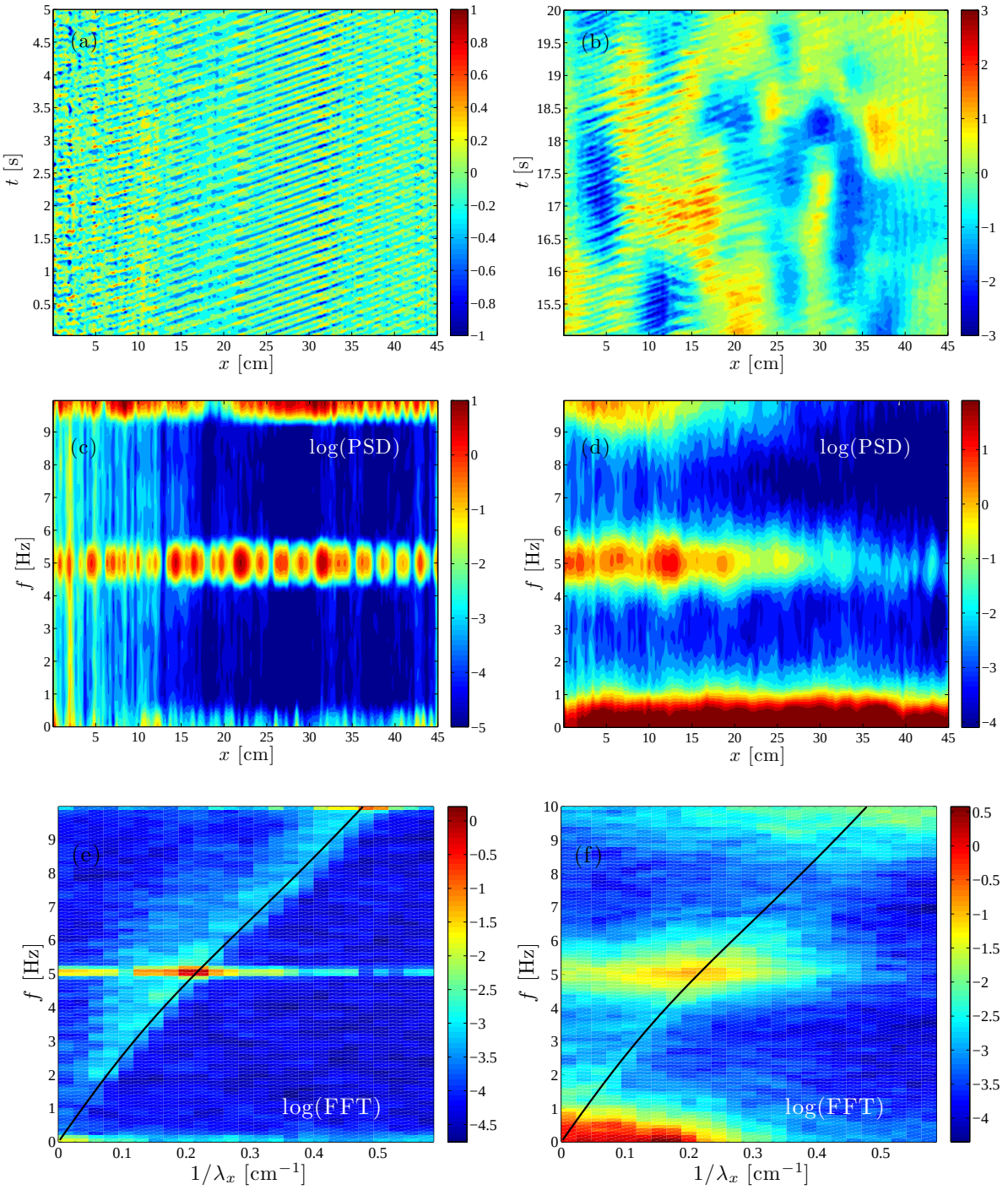

Figure 6.6: Spatiotemporal evolution of $\eta(x,t)-\overline{\eta}(x)$ and the corresponding spectral representations. The excitation is at $f_0 = 5$ Hz alone (left panels), and the MHD forcing is at $I = 080$ A (right panels). The spatiotemporal evolution is shown in top panels. Frequency spectra –computed at each x– is on the middle. Frequency–wavenumber spectrum is on bottom panels. It includes de dispersion relation for linear waves (black line).

quantifications. Thus we present now the spatially resolved measurements performed in the central line (see figure 6.3). The methodology used is similar to that presented in chapter 5: we acquire images of a line of diffused light produced with a laser sheet, at frame rate of 60 Hz. Then we post–process the images in order to get the evolution of the fluid height η. After interpolation of loss points, we performed an spatiotemporal filtering (low pass filter at 20 Hz for time, and at 2 or 5 mm in space), and we subtracted the time averaged profile. Thus, in what follows we are concerned only with height fluctuations $\eta(x,t) - \overline{\eta}(x)$, both produced by excited waves or by the MHD forcing.

Top panels in figure 6.6 present our typical observations. In 6.6a, there is only the mechanically excited wave (here at $f_0 = 5$ Hz). Although wave propagation appears very clear, the wave pattern is not completely trivial, both because the measurement line is not perpendicular to wave propagation, and because the wave train is not truly a plane wave. Panel 6.6b present the deformation of the surface when there are both a wave (again at $f_0 = 5$ Hz) and an underling fluid motion produced by MHD forcing at I = 80 A. In this case, the contributions to surface deformation are easy to identify: waves correspond to oblique lines (as in top–left panel), and the big red / blue zones corresponds to larger scale fluid motion. Interestingly, one can already notice here that waves are visible only until around $x \sim 25$ or 30 cm, as a consequence of the enhanced dissipation produced by fluid motion. Panels in the middle present the corresponding Power Spectral Densities (PSDs), which are computed at each spatial position. In panel 6.6c, where there are only waves, the peak at f_0 and its harmonics are the most important features, although some spatial modulation of the peak appears with no clear origin: it could be due in part to resolution limitations of the technique, but also to wave reflexions in walls or to the sources of spatial variability evoked just before. On panel 6.6d, there is the PSD corresponding to the data presented on panel 6.6b. One can see the f_0–peak very clear until the mentioned x, after which the wave contribution become of the same order of the background noise. One can also see that low frequencies are now very important but still clearly separated from f_0, as we already noticed.

Bottom panels present the frequency–wavenumber (or ω–k) spectrum. It is computed in the same way as for figure 5.12. The dispersion relation for linear waves (6.1) is shown as a black line. In the case without turbulence (panel 6.6e), the energy concentrates in the dispersion relation, specially around the excited frequency (5 Hz in figure 6.6) and its harmonics. When MHD forcing is added (panel 6.6f), there is an important spreading of the energy injected into wave modes. However, the local maximum is still on the dispersion relation. On the other hand, a *zero* frequency mode appears quite far from the dispersion relation. As we studied in the previous chapter, this mode comes as the consequence of turbulent motion.

In figure 6.7 we present the spatial average of the PSDs over all the points in the line. Top panels correspond to $f_0 = 8$ Hz and bottom ones to $f_0 = 5$ Hz. On the left we present the spectra of the wave alone (in black) and then the spectra when there is both the wave and MHD forcing (thick colored lined). We superposed the spectra of respective signals with only MHD forcing (thin dashed lines of the corresponding color). At very low frequency (less than 1 Hz), the wave + turbulence spectrum matches very well the one of only turbulence. On the contrary, for frequencies larger than 1 Hz, some differences are visible, especially for $f_0 = 5$ Hz (bottom–left panel). The f_0–peak characteristics will be

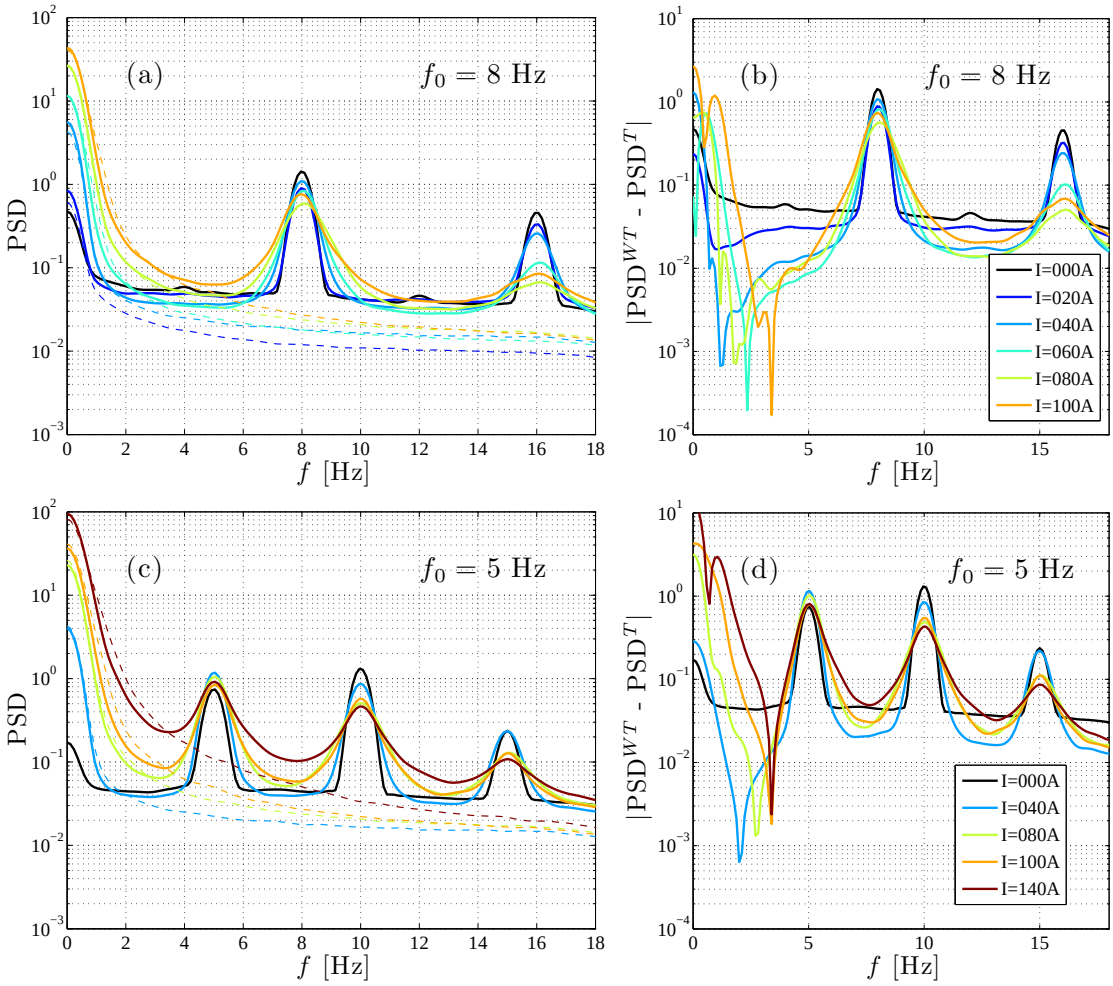

Figure 6.7: Spatially averaged PSDs. They are computed by averaging the PSDs obtained at every position in space. On the left, we compare the case with wave + turbulence (solid lines) to the one with only turbulence (dashed thin lines). On the right we *isolate* the wave contribution by subtracting the PSD of the turbulence case to the one with wave + turbulence. Top panels correspond to an excitation at $f_0 = 8$ Hz, and bottom ones to $f_0 = 5$ Hz. Black lines correspond to the case without turbulence, then colors go from blue to red as the MHD forcing is increased (see legends on the right).

considered in the section below.

In order to emphasize the wave contribution to spectra, we subtracted the turbulence spectrum to the one with wave + turbulence. This is presented on right panels. A residual low frequency components is present as as consequence of the differences between turbulence and wave + turbulence spectra. The specific correspondence of colors and the MHD forcing is shown in the legends on the right, and it will be used in further figures.

These spectra look similar to those obtained by local measurements, but this time we can understand their variations as the cumulative effect of turbulence over the averaging distance.

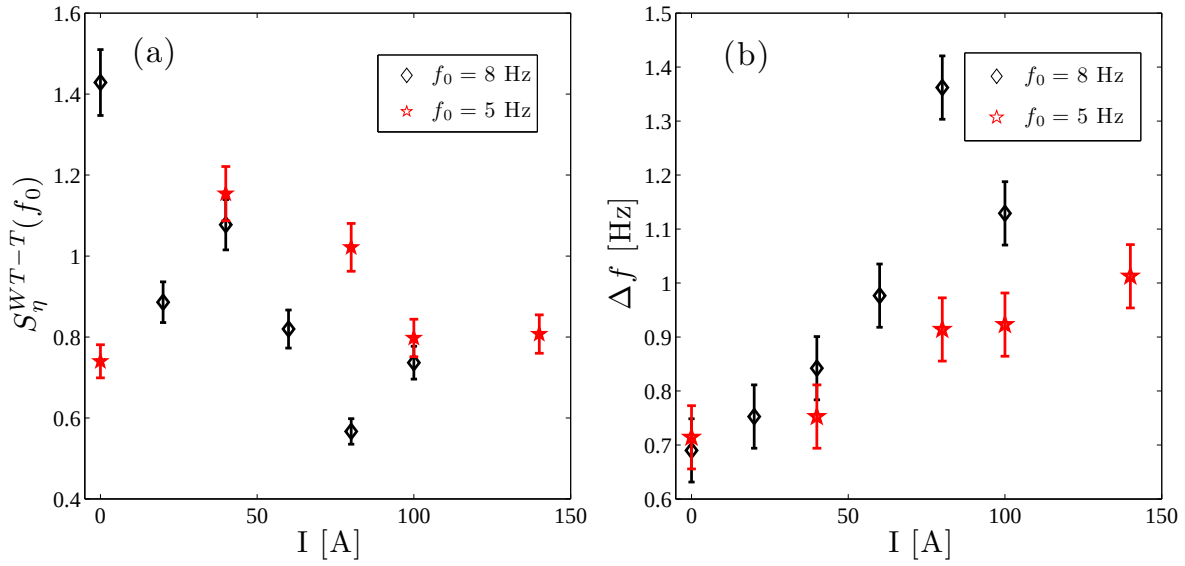

Figure 6.8: Evolution of the wave–spectral–peak as a function of the turbulence intensity. It is presented here as the f_0-peak characteristics obtained from the PSDs in right panels of figure 6.7. In (a) we present the peak's maximum height. In (b) we show the peak's width at half its height. Black diamonds correspond to a wave of $f_0 = 8$ Hz and red stars to one of $f_0 = 5$ Hz. Error-bars are constructed on the resolution of the spectrum computation: for (a), an estimation is done as the mean variation of the spectrum over the band $[f_0 - 2, f_0 + 2]$ Hz. For (b), it is the frequency resolution of the computation, given by the temporal window used (~ 8.5 s).

6.3.3 f_0–peak characteristics

Now we consider the evolution of the peak corresponding to the excited wave (at f_0), as a function of the MHD forcing. We focus on the spectrum S_η^{WT-T} obtained after subtracting the one of turbulence from the one of wave + turbulence (see right panels of figure 6.7).

The results are presented in figure 6.8. On (a) we present the local maximum of the spectrum S_η^{WT-T} around f_0. Most of the times the maximum is at f_0, although an slight shift can also be observed. Excluding the first point in the $f_0 = 5$ Hz series (in red)[2], the data show the tendency of a decrease in the maximum height, as the MHD forcing is increased. This tendency is confirmed by local measurements.

Then we consider the peak–width, defined as the width at the half height (the height being that of figure 6.8a). This is presented on figure 6.8b. Here the tendency is of an increase of the width as turbulence is increased. We can observe that the peak's widening is stronger for 8 Hz (black diamonds) than for 5 Hz (red stars).

These two results –peak reduction and peak widening– present good agreement with the observations of Falcón & Fauve [8], despite the experimental differences. They excite

[2]Unlike our expectations, the first point in the $f_0 = 5$ Hz series is smaller than the rest. It is indeed smaller than its harmonic, as it can be seen in figure 6.8c. Based on this figure, one may speculate about a subtile border effect strengthen the harmonic frequency to the detriment of the fundamental one. This effect being loss in the presence of MHD forcing.

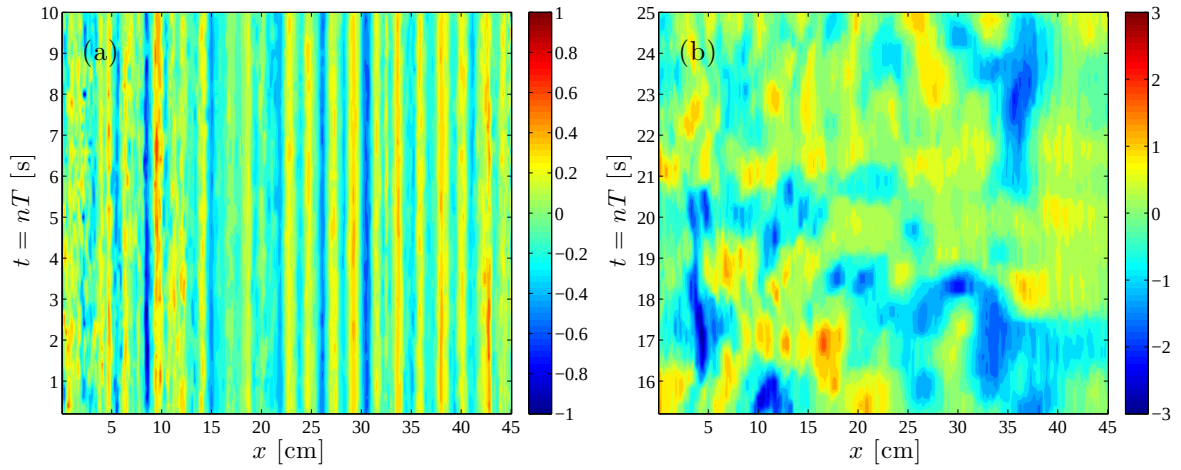

Figure 6.9: Spatiotemporal diagrams when considering t only at successive periods nT, with n an integer number. Flow characteristics are the same as in figure 6.6: (a) is for wave with no turbulence; and (b) is the wave with turbulence given by I = 080 A.

standing waves by means of the Faraday instability (produced by a vertical vibration at a frequency $2f_w$). Thus, there is no wave propagation. On the other hand, they excite spatiotemporal fluctuations using a MHD forcing, exactly as we do, but on a weaker level[3]. Peak reduction and widening is a clear part of their observations (see figure 8 in [8]) although the focus of the study was on the influence of fluctuations on the instability properties.

When considering the spatial variation of spectra at f_0 (what one may see by looking the line at 5 Hz in figure 6.6d), one would like to define a value of x for which waves are no longer measurable. This value is expected to be reduced when turbulence is increased. However, it seems difficult to quantify this, on the light of the high spatial variability of the signal. Therefore, we consider an alternative method to study such a spatial variation.

6.3.4 Spatial decrease of the wave contribution to η

In order to quantify the spatial decrease of the wave contribution to η, we can take advantage of its periodicity, together with the intrinsic randomness of the turbulence contribution. A sinusoidal wave is T–periodic: $\eta(x, t + nT) = \eta(x, t)$, with n an integer number. Thus, if we consider the time only at successive periods, the temporal dependence is lost, as it can be seen in figure 6.9a. Therefore, a *coherent average* of such a conditioned data set gives a clear sinusoidal pattern. When turbulence is included, although it can dominate the instantaneous dynamics (see figure 6.9b), it present no contribution to the coherent average. Thus we can focus on the wave contribution to η with confidence. We can model the coherent mean as

[3]In their experiment, the imposed electrical current are much smaller than ours, but the dimensions of the setup are smaller as well. Thus, any comparison should be done in terms of the density of current J_0: it spans values from 0.14 to 0.57 A/cm^2 in their case, and from 0.75 to 10 A/cm^2 in our experiment.

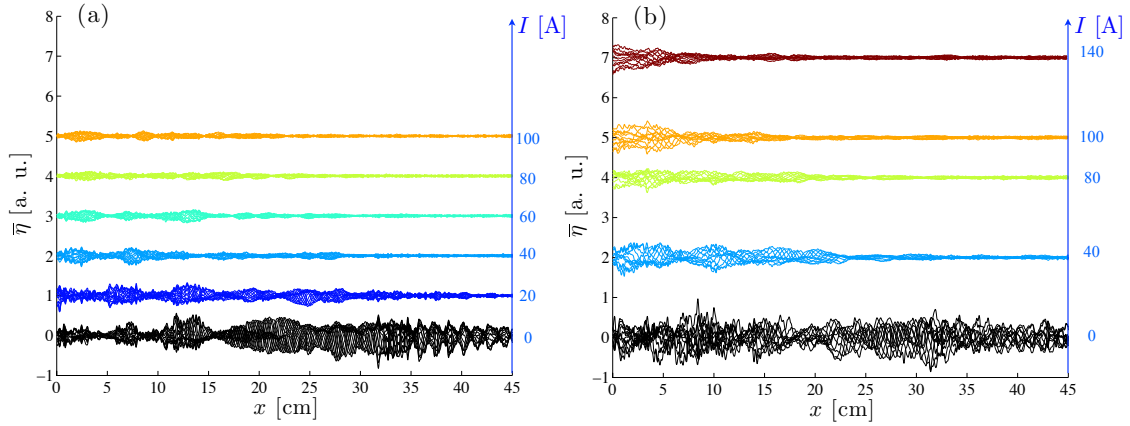

Figure 6.10: Coherent mean profiles as a function of the forcing. We compute a mean over frames at successive periods (example of data sets are those of figure 6.9). (a) Mean profiles for $f_0 = 8$ Hz. (b) Mean profiles for $f_0 = 5$ Hz. In each case, profiles of a given forcing are superposed (14 profiles for $f_0 = 8$ Hz and 11 for $f_0 = 5$ Hz). Profiles of different forcing have a different color, and they are shifted following the legend in blue.

$$\overline{\eta}(x) = a_0 \exp\left(-\alpha_I x\right) \sin\left(kx\right), \tag{6.2}$$

were a_0 is the excitation amplitude, k is the wavenumber and α_I is the dissipation coefficient due both to turbulence (quantified by the intensity I of the MHD forcing), or just to viscous dissipation [12]. It can be noticed that for viscous dissipation of linear waves in deep water, Lamb shown that $\alpha_0 = 2\nu k^2/c$, where ν is the kinematic viscosity of the fluid and c is the phase velocity. For turbulence, theoretical arguments give also a k^2 scaling, as noticed in the introduction. However, the validity of these arguments is restricted to very specific conditions between $\lambda = 2\pi/k$ and L (the typical length–scale of turbulent fluctuations).

In figure 6.10 we present the result of the coherent averaging for the two frequencies considered before: (a) 8 Hz; (b) 5 Hz. Several realizations are obtained from each data set, as averages are computed over frames separated by one period. Realizations of the same data set are just superposed and the color is related to the forcing, following the convention used in figure 6.7. Profiles of different forcing are shifted for clarity: upper profiles correspond to stronger forcing. The vertical shift is proportional to the intensity of the MHD forcing, in order to facilitate comparison between (a) and (b). The scale of fluctuations is always the same.

One can remark (specially on panel 6.10b) that as the forcing is increased, there is a reduction of the zone where wave amplitudes are significant. This is consistent with the model of equation (6.2). By comparing both panels in figure 6.10, one can see that the profiles at 8 Hz (a) decrease for a weaker forcing than those at 5 Hz (b). These features can be quantified by computing the variance of the profiles obtained by coherent average.

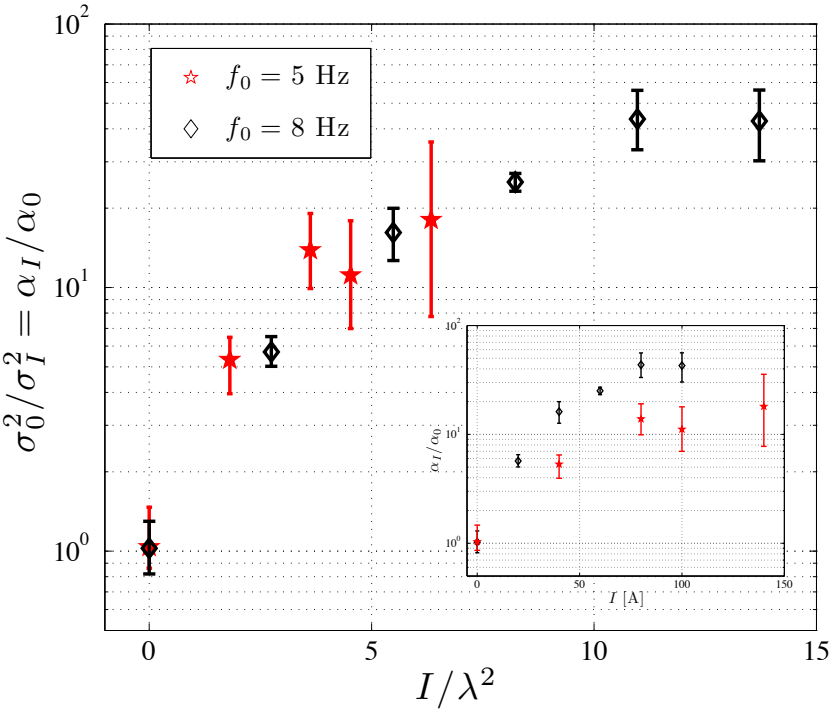

Figure 6.11: Increase of dissipation due to turbulence. Inset: we plot here the inverse of the variance of coherent mean profiles, as a function of the forcing. By normalizing by the variance of the wave alone, we access α_I/α_0 : a coefficient for the increase of wave dissipation (see details in the text). Main: both curves collapse by considering the ratio between the forcing I and the wavelength λ. λs are given in table 6.2: black diamonds correspond to a wave of $f_0 = 8$ Hz with $\lambda = 2.7$ cm; and red stars to one of $f_0 = 5$ Hz with $\lambda = 4.7$ cm. Error-bars give account of the variance's dispersion on equivalent profiles.

One has,

$$\mathrm{Var}(\overline{\eta}(x)) = \sigma^2 = \frac{1}{L}\int_0^L \overline{\eta}^2 dx = \frac{a_0^2}{L}\int_0^L \exp\left(-2\alpha_I x\right)\ \sin\left(kx\right)^2 dx, \tag{6.3}$$

where L is the distance over which dissipation is considered. Although this integral involve a complicated dependence[4] on k, for the waves considered here it is accurate enough to

[4]The exact expression for the integral reads

$$\sigma^2 = \frac{a_0^2}{4L(\alpha^2+k^2)}\left[\frac{k^2}{\alpha}\left(1-e^{-2\alpha L}\right) - 2\left(\alpha\sin\left(kL\right)^2 + k\sin\left(2kL\right)\right)e^{-2\alpha L}\right],$$

but the dependence on k is much reduced when neglecting finite size effects, which is reasonable whenever the wavelength λ do not exhibit quantization because of the walls. There one gets

$$\sigma^2 = \frac{a_0^2 k^2}{4L\alpha(\alpha^2+k^2)},$$

which should be considered as the reference expression. However, when $\alpha \ll k$, it can be further simplified to the form of equation (6.4). The validity of this limit was checked for the cases considered here.

use a the simpler expression:

$$\sigma_I^2 \sim \frac{a_0^2}{4L\alpha_I}. \tag{6.4}$$

Therefore, by considering the ratio σ_0^2/σ_I^2, we obtain a measure of how dissipation increases as a consequence of turbulence. We may underline the dissipative nature of this expression by noticing that it is equivalent to α_I/α_0. It is presented in figure 6.11 for the previously considered frequencies. If we consider only the dependence on the forcing (given by the current intensity I, as shown in the inset of figure 6.11), for $f_0 = 8$ Hz (in black) the dissipation starts *faster* and it saturates at a larger value, compared to the case at $f_0 = 5$ Hz (in red). These features are consistent with the qualitative observation of figure 6.10. Therefore, there is a dependence on f_0. As it cannot comes neither from the fluid properties nor from geometrical considerations, it should correspond to a frequency–dependent response of turbulence.

A dependence on k^2 is observed for these frequencies. This is shown in the main panel of figure 6.11, where both curves collapse when using the product I/λ^2. This dependence matches the theoretical one discussed in the introduction. For instance, Teixeira & Belcher proposed $\alpha_{TB} \sim U^2k^2/g$ [20][5]. However, the scaling on U^2 is less clear, as it implies a linear increase with I (see chapter 4).

This analysis complements the one of the f_0–peak. Indeed, general features are shared: (i) both analyses give account of the dissipative effect of turbulence on the excited wave. (ii) Waves at higher frequency (8 Hz) experience stronger attenuation. On the other hand, the coherent average analysis appears to be more robust to quantify the 0–MHD–forcing contribution, as it implicitly take into account the fundamental frequency and its harmonics. Also, it allows to gain a further insight into the frequency–dependent response of turbulence.

6.4 Summary and discussion

In this chapter we described our study on the influence of turbulence on wave propagation. By analyzing the height fluctuations under different conditions –specifically, by varying the intensity of the MHD forcing and the frequency of the excited wave– we observed the enhancement of wave dissipation by turbulence.

After describing the experimental conditions, we shown some flow features obtained with local measurements: specifically we shown that the large scale flow produced by the MHD forcing present the most important contribution to surface deformation η.

Then we focused on the frequency spectrum of η. From both local and spatially resolved measurements, we observe that the spectral peak corresponding to the excited wave (the f_0–peak) changes as a function of the turbulence produced by the MHD flow.

By analyzing the f_0–peak, we observe the decrease of its amplitude, accompanied by its widening. These two effects can be understood as follows: the decrease of the peak's amplitude may be due to the transfer of the wave energy into turbulent fluctuations, in

[5]We observed in the introduction that this theory is related to the Phillips' one [17]. However, the expression given by Teixeira & Belcher is easier to compare with our results.

particular through its closest scales. It implies higher spectral amplitudes of the contiguous scales, thus widening the original peak. Linear waves do not suffer of such a transfer. Therefore, turbulence triggers the nonlinear transfers of energy happen through contiguous scales.

This attenuation effect of turbulence on waves cumulates along the space. Therefore, to evaluate the spatial attenuation gives an alternative quantification of the effects of turbulence. We evaluate this by computing coherent averages of the spatiotemporal evolution of η, from which the variance can be linked to an attenuation coefficient. This analysis share the general features of the one of f_0–peak.

Both analysis (the one of f_0–peak and the one of coherent averaging) demonstrate the enhancement of dissipation by turbulence. They also shown a non trivial dependency of dissipation on f_0 (the frequency of the excited wave): waves of higher frequency are more efficiently attenuated by turbulence.

We contrasted our results with theoretical predictions, finding agreement with those of Teixeira & Belcher [20], although complementary measurements have to be done.

One may see these effects as an increase in turbulent dissipation. As we are far enough from molecular dissipation, the losses of wave–energy imply an increase of turbulent kinetic energy (TKE). Teixeira & Belcher proposed a scenario for this increase (valid in the limits of their theory, where turbulent scales are smaller than the wavelength): as waves propagates in a given direction, the Stokes drift would intensify and elongate the turbulent eddies in that direction. This can be seen as an alternative source for anisotropy for turbulence. However, we were unable to measure any increase in the TKE and it could be a very challenging perspective.

6.5 Bibliography

[1] Ardhuin, F., and Jenkins, A. On the interaction of surface waves and upper ocean turbulence. *Journal of Physical Oceanography 36* (2006), 551–557.

[2] Berry, M. V., Chambers, R. G., Large, M. D., Upstill, C., and Walmsley, J. C. Wavefront dislocations in the Aharonov-Bohm effect and its water wave analogue. *European Journal of Physics 1* (1980), 154–162.

[3] Brocchini, M., and Peregrine, D. H. The dynamics of strong turbulence at free surfaces. Part 1. Description. *Journal of Fluid Mechanics 449* (2001), 225–254.

[4] Bühler, O. Wave–Vortex Interactions in Fluids and Superfluids. *Annual Review of Fluid Mechanics 42* (2010), 205–228.

[5] Cerda, E., and Lund, F. Interaction of Surface Waves with Vorticity in Shallow Water. *Physical Review Letters 70* (1993), 3896–3899.

[6] Clark, D. B., Elgar, S., and Raubenheimer, B. Vorticity generation by short-crested wave breaking. *Geophysical Research Letters 39* (2012), L24604.

[7] Craik, A. D. D. *Wave interactions and fluid flows.* Cambridge University Press, 1985.

[8] Falcón, C., and Fauve, S. Wave-vortex interaction. *Physical Review E 80* (2009), 056213.

[9] Ford, R. *Gravity wave generation by vortical flows in a rotating frame*. PhD thesis, University of Cambridge, 1993.

[10] Frisch, U. *Turbulence*. Cambridge University Press, 1995.

[11] Kiger, K. T., and Duncan, J. H. Air-Entrainment Mechanisms in Plunging Jets and Breaking Waves. *Annual Review of Fluid Mechanics 44* (2012), 563–596.

[12] Lamb, H. *Hydrodynamics*. Cambridge University Press, 1895.

[13] Lighthill, M. J. On sound generated aerodynamically. I. General theory. *Proceedings of the Royal Society A 211* (1952), 564–587.

[14] Nazarenko, S. *Wave Turbulence*. Springer, 2011.

[15] Ölmez, H. S., and Milgram, J. H. An experimental study of attenuation of short water waves by turbulence. *Journal of Fluid Mechanics 239* (1992), 133–156.

[16] Peregrine, D. H. Large-scale vorticity generation by breakers in shallow and deep water. *European Journal of Mechanics - B/Fluids 18* (1999), 403–408.

[17] Phillips, O. M. The scattering of gravity waves by turbulence. *Journal of Fluid Mechanics 5* (1959), 177–192.

[18] Savelsberg, R., and van de Water, W. Experiments on free-surface turbulence. *Journal of Fluid Mechanics 619* (2009), 95–125.

[19] Savelyev, I. B., Maxeiner, E., and Chalikov, D. Turbulence production by nonbreaking waves: Laboratory and numerical simulations. *Journal of Geophysical Research: Oceans 117* (2012), C00J13.

[20] Teixeira, M. A. C., and Belcher, S. E. On the distortion of turbulence by a progressive surface wave. *Journal of Fluid Mechanics 458* (2002), 229–267.

[21] Vivanco, F., and Melo, F. Surface Spiral Waves in a Filamentary Vortex. *Physical Review Letters 85* (2000), 2116–2119.

[22] Vivanco, F., and Melo, F. Experimental study of surface waves scattering by a single vortex and a vortex dipole. *Physical Review E 69* (2004), 026307.

Chapter 7

The effect of turbulence on floating particles

In this chapter we will consider the effect of turbulence on floating particles. It appeared to us that particles' position do not recover the whole measurement area in an homogeneous way, giving the indication of a collective phenomena induced by the flow. Indeed, we observe the formation of clusters when considering the area of triangles defined by the position of nearest neighbors. By performing an statistical analysis of triangles' area, we got a powerful tool to decide which particles belong to a cluster. Indeed, clustered particles exhibit much stronger velocity and angular correlations than the unconditioned case.

As noticed in the introduction, several mechanisms are susceptible to induce clustering of floating particles: (i) particles' inertia, (ii) upwelling/downwelling flows and (iii) surface tension. For each mechanism we construct suitable quantities, which we correlate with time averaged velocity. These correlations suggest upwelling and downwelling motions as responsible for particles clustering.

Article's copie:

Experimental study on the clustering of floaters on the free surface of a turbulent flow*

Pablo Gutiérrez & Sébastien Aumaître

Abstract

We present an experimental study of the statistical properties of particles floating on the surface of a turbulent flow. Two random flows with different properties are generated in a layer liquid metal by an electromagnetic forcing. The forcing is strong enough to generate a 3D flow deforming the interface. The motion of hundreds of millimeter-size particles floating at the interface between the liquid metal and a diluted acid solution is followed by particle tracking and the surface level is recorded along a line. Basic properties of the flow, of the surface deformation and of the particle diffusion are given. Then a statistical procedure is proposed to evidence the clustering of floaters. Some dynamical properties of clusters are exposed. Hypotheses are proposed to explain clusters formation.

* We chosen to keep the original structure of the submitted paper, despite some sections were already presented in the manuscript.

7.1 Introduction

Floating objects on the sea surface, going from large containers to micrometer plankton and passing through algae and plastics litters, have a large economic and ecological impact [1]. Their tendency to agglomerate in large clusters is often observed, as testified by the plastic litter islands and huge garbage patches reported on all oceans [2]. However, the mechanisms of this clustering is far from being fully understood. The action of turbulent eddies and Stokes drift induced by swell have been evoked [3]. Indeed it has been suggested first by Kraichnan [4] that a passive scalar stretched and folded by the gradients of a turbulent velocity field, should have a more intermittent behavior than the velocity field itself (see also Appendix A). But floating objects are far to be passive bodies. Indeed they are less dense than the supporting fluid, thus sensitive to inertia. Inertial particles are known to form clusters in 3D turbulent flows [5; 6]. Moreover, the floaters experience a 2D surface flow $\mathbf{u}_s(x, y, z = h(t))$. It is a compressible flow since upward and downward motions of the underlying fluid, generate hill and subduction zones where $\partial_x u + \partial_y v = -\partial_z w \neq 0$ These zones act as shrinking and expanding areas for the floaters concentration [7]. Finally, a millimeter-size particle is sensitive to capillarity forces. It is attracted by particles with similar wetting [8] and sensitive to the surface curvature [9; 10].

We present here an experiment where some of these processes are relevant. The device consists of a layer of liquid metal placed over a magnet network and forced by a constant horizontal current. It can generate a fully turbulent flow that disturbs the liquid metal surface. To prevent the oxidation of the liquid metal surface, we cover it with an aqueous solution of hydrochloric acid at low concentration. In this study, we follow the trajectory of hundred millimeter-size spheres floating on the liquid metal. The first section is devoted to the description of the experimental device and the measurement procedures. In section 2 we give some basic properties of the surface flows experienced by the floaters. We especially underline the discrepancies between the flows generated by a regular and a random array of magnets. Then we focus on the statistical properties of the floaters in section 3. In this section we first consider diffusion properties of individual particles and the mixing efficiency of both magnet arrays, as the function of the applied current. Then we study the spatial distribution of the particles by using the Delaunay triangle linking three neighboring particles. Statistical properties of the area of these triangles show the clustering propensity and give us a clear criterion to define clusters. Using this criterion we are able to characterize the statistics of the number of particles per cluster and to underline the coherent dynamics inside clusters. Possible mechanisms of this clusterization will be discussed in the concluding section.

7.2 Experimental device and procedure

7.2.1 Flow generation

An electric current, of density $\mathbf{J}$, in addition to a magnetic field, $\mathbf{B}$, can generate a Lorentz force $\mathbf{F_L}$ inside a conducting body: $\mathbf{F_L} = \mathbf{J} \times \mathbf{B}$. This force has been used to stir conducting fluids since Bondarenko *et al* [11]. They used a uniform current an alternative magnetic strips to study 2D turbulence with a well-defined periodic forcing. Later, Sommeria [12] applies a strong uniform magnetic field and space-dependent distribution of current to generate an almost 2D flow and to study the transition between large scale structures. Then the technique becomes a common tool to study 2D turbulence, [13], instability [14; 15] and chaotic mixing [16] in 2D flows.

We adopted a similar forcing, albeit different objectives and experimental details. A sketch of the experiment is shown figure 7.1. The experiment is performed in a plastic (isolating) rectangular container, with a maximal working area of $L \times l = 40 \times 50 cm^2$. This cell is filled with $H = 1cm$ layer of gallinstan, a liquid alloy at room temperature made of gallium, indium and tin [17]. The use of liquid metal provides us to reach high density current up to 1.5×10^5 A/m^2 with no need of high power nor cooling (the applied voltage is less than a Volt). The current is supplied with *Sorensen DHP Series* Power supply by two brass electrodes placed along the cell end. Beneath the container, we can produce two vertical magnetic fields B. Their shape in space is constrained by arrays of strong permanent Neodymium Iron magnets about 20 mm diameter as shown in figure 7.1. One array is made with regular lines of alternating polarity and the second with randomly distributed magnets. Both have a mean distance between magnets of the order of 35 mm. At the

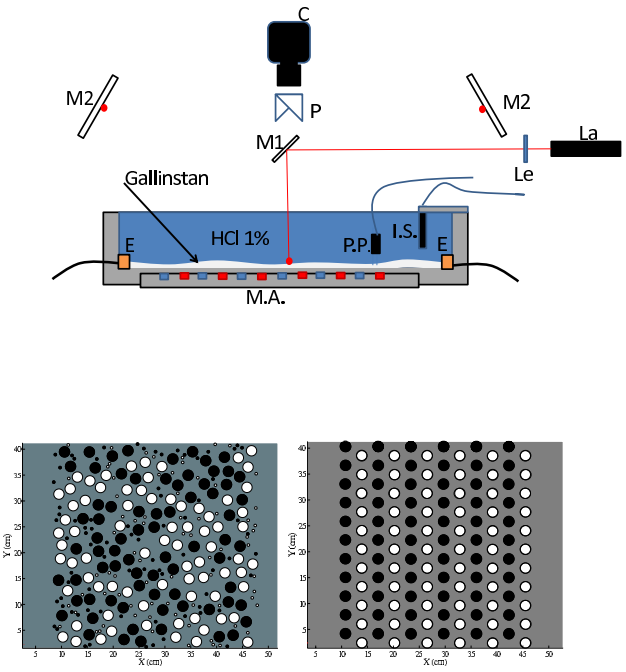

Figure 7.1: The experimental device. **Top :** Sketch of the experimental cell. A 1 cm layer of Gallinstan (GaIn Ti) is placed between two electrodes (E), over a magnet array (MA) in a cell of 50 × 40 cm. The potential probe (PP) puts under a magnet, gives an estimate of the local velocity fluctuations and the inductive sensor (I.S) gives access to the local elevation. The beam of the Laser diode (La) is transformed into a laser sheet by the cylindrical lens (Le) and projected on the surface of a mirror (M1). A line diffused on the surface is made by the laser sheet on the Gallinstan surface is tracked with 2 opposite angle by a single Camera(C) by the two mirrors (M2) and the prims (P). **Bottom :** Sketch of the random and regular magnets array used in the experiment. The black and white indSicate the magnet polarity.

bottom of the container, the magnetic field of each permanent magnet is around 1200 Gauss. Both generated flows are briefly compared in the next section. To prevent the oxidation of the surface which creates a thin solid film, the Gallinstan is surmounted by a layer of Chlorite Acid solution (at concentrations lower than a percent). The layer is thick enough (about 10 cm) in order to make the Gallinstan–Acid interface insensitive to the boundary condition at the top of the Acid layer.

In the context of two layers of stratified fluid, some authors already discussed the susceptibility of such a flow to the forcing geometry. A common conclusion is that almost no differences appear as long as statistical quantities are concerned especially under strong forcing [20; 22]. This seems in agreement with the 2D turbulence framework, in which the detail of the forcing geometry has to be smeared out by inverse cascade transferring energy to large scales. However Williams *et al* pointed out that after an average over a time long enough, the trace of the forcing becomes visible again, even in strongly fluctuating flows [21]. Recently, this trace was explored in more details (again under stable stratification) at moderate Reynolds number (until 300) by Liao *et al.* [23]. They claim that under their experimental conditions, the symmetries of the forcing are determinant for the energy distribution of the flow. In contrast to these previous works, we did not try to maintain a 2D flow with a flat surface. Instead, we want to reach a more natural fully developed 3D free surface flow with deformed interface. The surface elevation is measured either locally with an induction sensor or along a line with an optical device. Moreover our aim is the study floating objects on the liquid metal interface which is seeded with millimeter-size plastic spheres. The particles are tracked by using a Dalsa PT-41-04M60-med CMOS camera and their dynamics are obtained using usual Particle Tracking Velocimetry (PTV) algorithm described below. In contrast to [7], we are interested by the motion of these inertial particles moving on deformed interface and sensitive to capillarity force. Obviously our study will benefit from a close comparison with the one of a passive scalar moving on compressible flow with a flat interface [7] as well as the study of inertial particles moving in the bulk of a 3D or 2D turbulent flow [6; 21].

7.2.2 Dimensionless parameters

The dimensionless Navier–Stokes Equation driven by an electromagnetic Lorentz forcing, exhibits a natural velocity scale that balances advection term and the Lorentz force $U_o = \sqrt{JB\mathcal{L}/\rho} \sim 1$ m/s with $\mathcal{L}$ a characteristic length of the flow. Therefore, one gets the Reynolds number $Re = \sqrt{JB/\rho}\mathcal{L}^{3/2}/\nu$. With the relevant choice for $\mathcal{L}$, this scaling is efficient to describe electromagnetically forced flows in another geometry [24]. In our device the maximum Reynolds number accessible built on the global cell size $\mathcal{L} = L = 50$ cm is of order of $Re_L \sim 1.5 \times 10^6$ (corresponding to $U_o \sim 1$ m/s). Built on the characteristic length scale of

the forcing $l = 4$ cm, it will be limited to a more realistic value $Re_l = 3 \times 10^4$ (corresponding to $U_o \sim 30$ cm/s) and the flow will be still turbulent from this point of view.

In such a flow, an important phenomenon is the magnetic boundary layer, perpendicular to the applied field, where induction concentrates the electric currents and the velocity gradients in a thin layer near the boundary. Its depth, e_H is characterized by the Hartmann number $Ha = \sqrt{\sigma/\rho\nu}BH \leq 45$ with $e_H = H/Ha$ which can be as small as 0.2 mm. Bottom friction which linearly damps the horizontal velocity has also to be taken into account. It can be characterized by a Reynolds number built on the Hartmann layer depth thus $Re_H = Re_L/Ha \cdot H/L = \sqrt{JL/\sigma\nu B} \sim 3 \times 10^4$. Such a parameter plays an important role for the structure of the flow in the 2D approximation [25]. Another useful scale is the Kolmogorov scale $\eta = \nu^{3/4}/\epsilon^{1/4}$ where the mean energy flux can be estimated as $\epsilon = U_o^3/L$, hence $\eta \sim 3 \times 10^{-2}$mm. This scale η is the one at which viscous damping becomes efficient in the bulk of the flow. We have the following hierarchy of scales $L > l \sim H \gg e_H \gg \eta$. We can expect a fully developed turbulence in the bulk of a fluid driven through Hartmann's boundary layers by an electromagnetic forcing.

Finally, we studied an interface between Gallinstan–Acid for which we determined a surface tension of order of $\gamma = 0.5N/m$ by the use of Faraday surface instability. The capillary length is then $l_c = \sqrt{\gamma/(\rho - \rho_o)g} \sim 3$mm, with ρ_o the acid solution density. Thus our millimeter-size floaters are sensitive to capillarity. The surface deformation is thwarted by both capillarity and gravity force. At the centimeter forcing scale, l, where gravity dominates, one can estimate the Froude number $Fr = U_o/\sqrt{gl} \sim 0.2$. This means that advection by the flow is slower than the emitted gravity wave at that scale.

7.2.3 Measurement techniques

7.2.3.1 Surface velocity field

PTV is a conceptually simple technique to obtain a two dimensional velocity field. The basic idea is to have a set of particles moving in a plane, and to take pictures of them for consecutive times t and $t + \Delta t$. Then one can find their positions at each time and reconstruct their trajectory, by which one can estimate their velocity during the interval Δt. In our case, we use particles of $a = 1$ mm in diameter, with density $\rho_p = 2000$ kg/m^3: less than the density ρ of the liquid metal, and more than the density of the acid. Therefore particles stay in the Acid-Galinstan interface. We acquired images of the whole cell of 2000×1700 pixels^2. This gives particles of around 4 pixels in diameter. Acquisitions were performed at 50 Hz and stocked on real time on a personal computer. We track around 200 particles in each frame, so the filling fraction is very small. In this regime, collisions of particles are rare, so we can successfully reconstruct trajectories in spite of the relatively limited acquisition frequency of the camera. Nevertheless, as we will see later, we are not able to consider the evolution between two frames as a complete picture of the velocity field.

Since the surface of the flow is actually a deformable mirror, a special care was devoted on lighting, in order to obtain particles contrasting from background. Once the images are obtained, we perform high pass filtering to remove the intensity modulations at length scales larger than particles diameter. Then we compute intensity contours of the image and identify particles as the superposition of at least 4 concentric circles. This procedure gives us the position of the particles with a subpixel resolution. This method is very robust under noisy conditions, even if it is computationally expensive. And, as expected, when parasite lighting fluctuations matches shape and size of real particles, the method assumes them as being particles. Nevertheless those events are generally filtered by the tracking stage.

From the position data, we compute trajectories using multi-frame predictive tracking algorithm [26; 27]. The tracking of a particle has two principal stages: First the algorithm performs a prediction for the position of the particle in a given frame based on its motion within the previous two frames. Then the algorithm selects the real position of the tracked particle in the given frame by choosing the one minimizing its distance to predicted position. Such tracking is repeated for all the particles in the frame (a detailed description of the algorithm is given in [26]). Given the set of trajectories, we used a convolution kernel in order to directly obtain a filtered velocity field [27]. One important advantage of this predictive tracking algorithm is its lack of intrinsic velocity cutoffs, as particles are always searched consequently to their previous motion.

7.2.3.2 Surface elevation

Surface elevation in the vertical direction is sampled locally using induction sensor. This sensor measures its distance to an electrically conductive material including liquid metal [28]. It is well suited for measurement of motion perpendicular to its axis. However, it averages the vertical displacement on a horizontal area comparable to the sensor surface (about a cm^2). Therefore it is efficient to measure surface fluctuations having a horizontal wavelength much larger than the vertical displacement.

In addition to this local measurement, we measure the surface elevation along a line using a classical triangulation technique. This technique tracks the displacement of diffused light spots. However as the liquid metal interface is poorly diffusive and highly reflective, we need to use very sensitive camera to follow the diffused light. Therefore we have also to deal with direct reflective spots saturating the camera sensor. To do so, we record the line displacement under two opposite angles. Hence, the blinding reflective spot in one angle is not seen in the other. Then the all line displacement can be reconstructed.

7.3 General characteristics of the observed turbulent flows

As we focus the present study on the floaters dispersion properties, we postpone a precise description of the surface deformation generated by such flows to further studies. In this section, we will give first an overview of the basic properties of the surface that can be estimated from the floaters motion for both magnets arrays. Then a limited description of the basic properties of the surface elevation of the flow along a line is presented.

7.3.1 Average properties of the particles velocity field

Using PTV technique, we are able to follow about two hundred particles during more than 60 sec. Figure 7.2a–b shows the trace of these trajectories during 5 sec for both magnet arrays driven by an imposed electrical current of $I = 250$ A. The flow generated by the random array is shown Figure 7.2–a and the one generated by the regular array is shown on Figure 7.2–b. Fig 7.2–c presents the RMS velocity, $\sqrt{\langle \overline{V_p^2} \rangle}$, of all the floaters during the 60s of the experiment where V_p stands for the Lagrangian velocity of the particles measured by PTV, $\langle \ \cdot \ \rangle$ stands for spatial averaging and $\overline{\cdot}$ stands for time averaging. Velocities are normalized by the expected velocity $U_o = \sqrt{JBl/\rho}$ with l the characteristic length of the forcing. U_o over–estimates the measured velocity about a factor 2 or 3. This is not surprising since we overestimate the magnetic field by using its maximum to compute U_o, whereas we are considering the RMS velocity. Moreover, excepted the plateau below 200 A in the case the random array, $\sqrt{\langle \overline{V_p^2} \rangle}/U_o$ decreases with the forcing intensity. It means that the surface flow explored by the particles contains less and less of the energy injected by the Lorentz forcing. This could be interpreted as an increasing of tridimensional effects.

The trajectories shown in Figure 7.2a–b, give an idea of the stream-lines of the flow averaged over 5s. The flow generated by the random magnet array exhibits clear structures whereas it seems notto be the case for the one generated by regular array . This remains true even for larger time windows and it is observed at all driving intensities. This is due to the fact that the flows generated by the random array fluctuate less in time than the flows generated by the regular array. This is well illustrated by the Figure7.2–d. We plot on this figure the kinetic energy contained in the time–averaged flow of the particles $\langle \overline{u}^2 \rangle$ divided by the total kinetics energy, where $\overline{u}$ is the time–averaged Eulerian velocity deduced from the Lagrangian measurement of the particle. The Eulerian velocity field of the time–averaged flow contains almost all the energy in the case of the random magnet array, whereas it contains less 40% in the case of the regular array. In the first case, the magnet pattern anchors the structure of the flow. This discrepancy between both magnet arrays remains whatever the spatial resolution chosen to coarse–grain the Eulerian field (although the relative fluctuations decrease in both cases, when the resolution of the Eulerian field is decreased, as expected from the central limit theorem). Hence we are able to generate two distinct flows with different properties, one having much more temporal fluctuations than the other.

It has to be mentioned that the tracking methods give only access to the motions of the tracers, and thus the velocity field felt by the floater in our case. Although the averaged procedure used

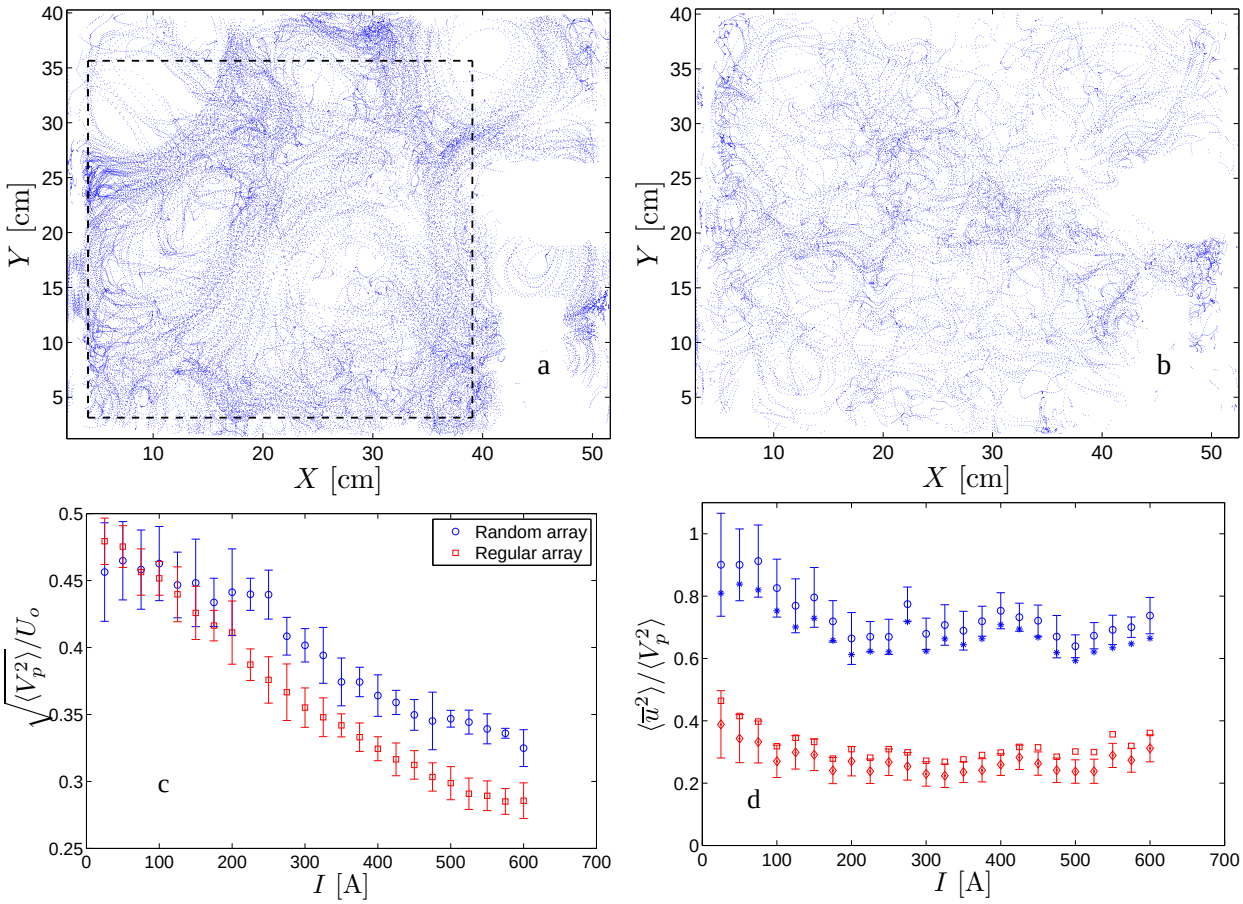

Figure 7.2: Flow characterization.**Top figures**: The dots give the positions of all the particles recorded during 5s at a rate of 50 Hz with a forcing current of I =250 A, a) for the random magnet array, b) for the regular magnet array. **Bottom figures** shows c) the evolution of RMS velocities of the floaters normalized by U_o versus the driving intensity I for the random magnet array (blue dots) and the regular magnet array (red squares), and d) shows the ratio of the kinetic energy contained in a time–averaged Eulerian flow, divided by the total kinetic energy as a function of I. Two spatial resolution of the Eulerian field are given for each magnets array : the random magnet array with a resolution of [50 × 50] (blue asterisks) and [100 × 100] (blue dots) and the regular magnet array at a resolution of [50 × 50] (red diamonds) and [100 × 100] (red squares)). Error bars are estimated from the fluctuations in time and redundant measurements.

to estimate the Eulerian field cancels the spatial inhomogeneity of the particles distribution, it is not clear how the floaters motion reproduces exactly the surface flow. At least, one can expect that it keeps a qualitative trace of the basic properties of the flow presented here.

7.3.2 Surface elevation

This difference between both magnet arrays is reflected in the study of the surface elevation along a line perpendicular to the imposed current density. We first study the variance of the elevation: $\langle \Delta h^2 \rangle = \langle (h - \langle h \rangle)^2 \rangle$, as a function of the imposed current. This is shown on figure 7.3-top in logarithmic axis (main panel) and linear axis (inset). Both magnet arrays seem to follow different power law with an exponent around 1.6 for the regular array and an exponent 2.2 for the random one. Especially for $I > 150$ A, the elevation increases faster for the random array. Moreover, the stationary part of the elevation is larger for the random array as already observed for the velocity field figure 7.2–d. Indeed as shown in the figure 7.3–bottom, the stationary deformation induces around 50 % of the surface elevation with the random magnet array whereas it is less 20% for the regular array. Moreover this part grows initially up to 200 A with the random array and then decreases slowly with intensity, whereas it continuously decreases for the regular magnet array. This change recalls the one observed in the

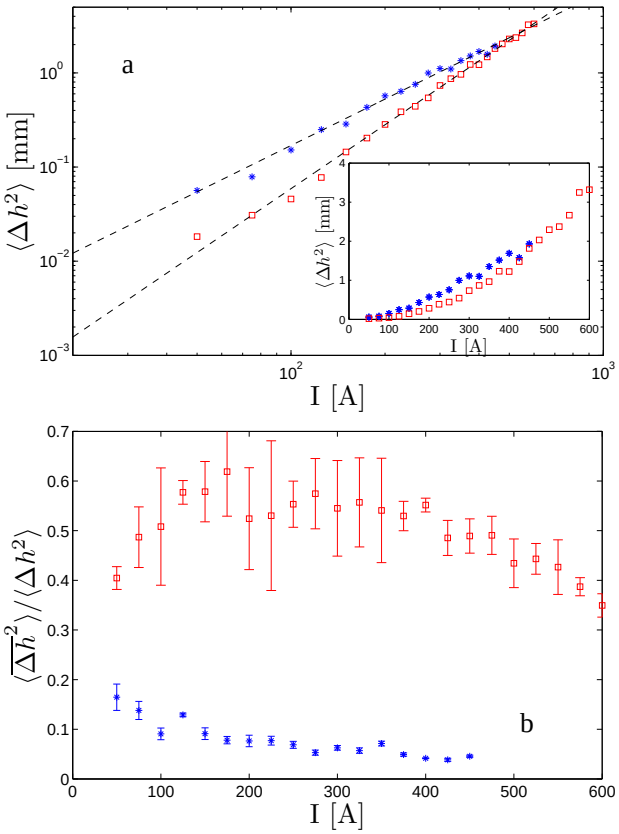

Figure 7.3: **Top**: Variance of the surface elevation Δh, in logarithmic (main panel) and linear axis (inset) at various driving electrical current I, for the regular (blue asterisks) and random (red circles) magnet array. The dashed lines represent a power law $\langle \Delta h^2 \rangle \propto I^{\alpha}$, fitted for $I > 200$ A. The deduced exponents are α =1.6 for the regular and 2.2 the random magnet array. Error bars are of order of the symbols size. **Bottom**: Ratio of variance of the time–averaged deformation divided by the total variance as a function of the driving current intensity for the regular (blue asterisks) and random (red circles) magnet array. Error bars are estimated from the fluctuations in time and redundant measurements.

kinetic energy in figure 7.2–c.

In order to quantify a characteristic correlation length scale of the surface deformation along a line, $h(x,t)$, we considered the normalized self-correlation function in space and averaged in time $G_h(\lambda)$:

$$G_h(\lambda) = \overline{\frac{1}{2L}\int_{-L}^{L} \delta h(x+\lambda)\cdot \delta h(x) dx / \langle \overline{h^2} \rangle} \quad (7.1)$$

In the main panel of figure 7.4, the time–averaged profile $\overline{h(x)}$ has been subtracted before the computation of the correlation function, i.e. in equation (7.1) one takes $\delta h(x) = h(x) - \overline{h(x)}$ where $\overline{h(x)}$ is shown on the left inset. For the driving current of 400 A used in the figure 7.4 the correlation length obtained for the fluctuations, λ_c, is about 1.6 longer for the random array. When the time–averaged profile is not subtracted, as shown on the right inset, then the correlation length, Λ_c, is almost unchanged for the regular array but is 50% larger for the random array. It illustrates that static correlations of longer range are involved in the latter. This last observation remains true whatever is the driving current and it is even stronger at lower driving.

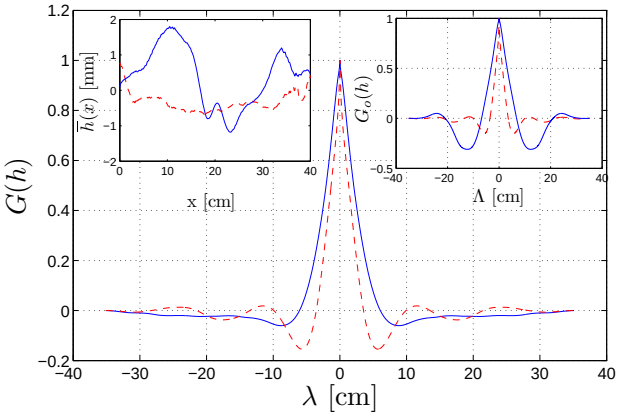

Figure 7.4: **Main panel**: Self-correlation function, in space of the elevation averaged in time, for a driving intensity of 400 A. Full lines are used for the random magnet array, and dashed lines are used for the regular array. The averaged profile shown **in the left inset** has been subtracted to obtain $G(\lambda)$. **On the right inset** is shown the selfcorrelation function in space of the elevation, averaged time, but whitout the substraction of the mean profile.

Figure 7.5, represents for both magnet arrays the correlation length λ_c, defined as the mid–width at the half maximum of self-correlation function, once that the time-averaged profile has been subtracted. It shows that, for the regular array, the values of the correlation lengths weakly depend on the forcing strength. Indeed λ_c fluctuates between 1.3 and 1.6 cm. The variations are more pronounced for the random array. Up to 200 A the correlation length scale strongly increases, from almost 0 up to 2.5 cm and then slowly decreases for subsequent increase of the current. Once again a change is observed around 200 A.

The correlations in time, averaged in space,

$$g_h(\tau) = \langle \frac{1}{2T}\int_{-T}^{T} \delta h(t+\tau)\cdot \delta h(t) dt \rangle / \langle \overline{h^2} \rangle \quad (7.2)$$

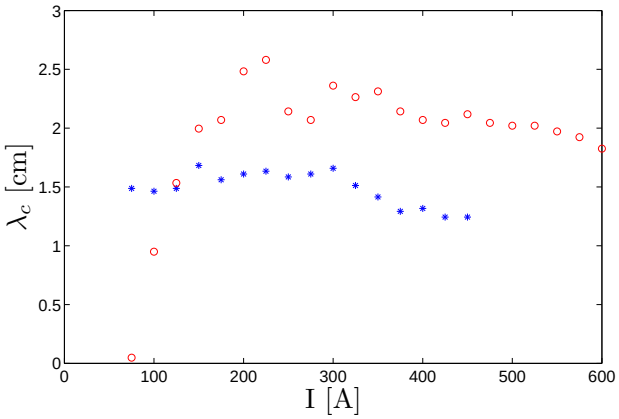

Figure 7.5: Correlation length λ_c as a function of the driving intensity for the regular (blue *asterisks*) and random (red circles) magnet array.

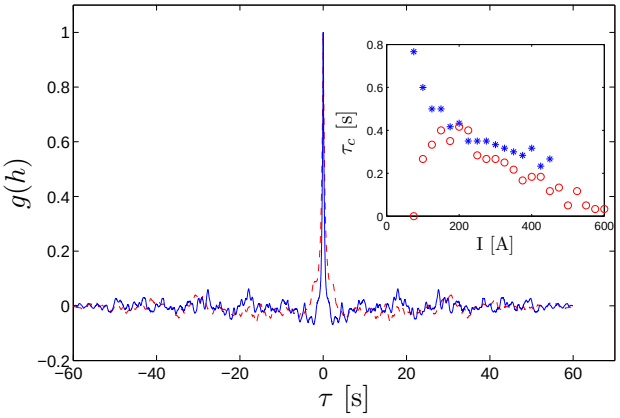

Figure 7.6: Self-correlation function in time of the elevation averaged in space for a driving intensity of 400 A. The full lines are used for the random magnet array, and dashed lines are use for the regular array. The inset shows the evolution of the characteristic correlation time with the driving intensity for the random magnet array (red circles) and the regular one (blue asterisks).

are shown on figures 7.6 for both magnet arrays at 400 A. At this driving intensity, the correlation time, τ_c, is about the same order for both arrays. It is defined as the mid–width at half the height of the self-correlation function. Actually, above 200 A, as shown in the inset, for both magnet arrays, the τ_c are similar and they decrease with a rate near 10^{-3}s/A. Below 200 A, the correlation time of the regular array decays faster, whereas the one of the random array grows. A more precise study of this transition in connection with the underlying flow as well as the spectral analysis of the elevation and the generation of surface wave, is postponed to a further publication where we will focus on surface deformation and wave turbulence.

7.4 Dynamical properties of the floaters

We focus now on the motion of the particles. The first thing to consider is the diffusion properties of a single particle in reference to the classical Brownian motion. Then we will compare the mixing properties of both generated flows. Finally, we will study the instantaneous spatial distribution of particles. To do so, we study the statistical properties of the Delaunay triangle linking the nearest neighbors. By comparing the distribution of triangles obtained experimentally with the one obtained from a homogeneous distribution of points, we are able to quantify the level of clustering and to determine a criterion defining clusters. Finally the properties of the particles velocity inside a cluster are explored.

7.4.1 Particles diffusion and mixing

We first study the statistical properties of $R(t) = \sqrt{(X(t)-X(0))^2+(Y(t)-Y(0))^2}$, the displacement of all the single particles that we are able to follow during a time t. For the well-known Brownian particles, one has $\langle R(\tau)^2\rangle = D\tau$ where diffusion coefficient is given by the Einstein formula : $D = \frac{2\langle V^2\rangle d^2}{18\nu}$ with ν the fluid viscosity and d the particle diameter. Figure 7.7**top** presents $\langle R(\tau)^2\rangle$ as a function of the dimensionless time $\tau\cdot\langle V^2\rangle/\nu$ in logarithmic axes. Comparison with the dot–dashed line proportional to τ and the dashed line proportional to τ^2, shows that we are closer to a ballistic regime than to a diffusive regime. Actually, one can compute an exponent γ such that $\langle R(\tau)^2\rangle \propto \tau^\gamma$. We made the estimate in a range of τ such that $\lambda\sqrt{\langle R(\tau)^2\rangle}L/2$, in order to be not too sensitive to the forcing length and to the cell size. Therefore, one gets $\gamma \sim 1.6$ for the regular array and $\gamma \sim 1.8$ for the random one. This almost ballistic behavior is confirmed on the Figure 7.7–**bottom**. Indeed a better collapse of the curves at different forcing strengths is obtained when a characteristic ballistic time, proportional to $l/\sqrt{\langle V^2\rangle}$, is taken to rescale the time unit, with l the characteristic length of the forcing. It has to be noticed that the range of scales between the forcing length and the cell size might be too small to reach the real diffusive regime.

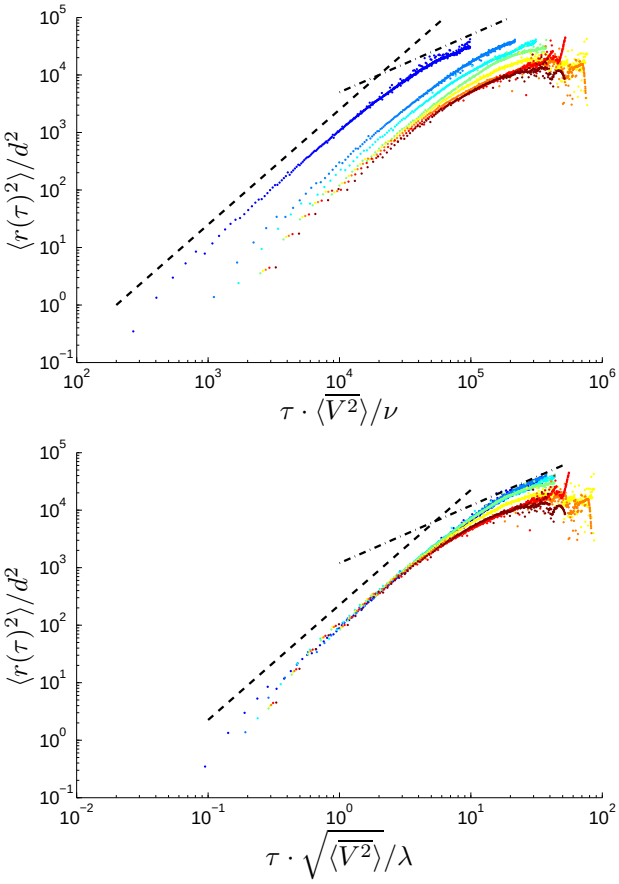

Figure 7.7: Single diffusion processes of the floating particles under different current intensities driving $I = [25, 100, , 175, 325, 400, 475, 575]$, for the random array of magnets. **Top**: The time is rescaled by the diffusive time $\nu/\overline{\langle V^2\rangle}$.**Bottom**: The time is rescaled by the characteristic ballistic time scale, $l/\sqrt{\langle V^2\rangle}$ is used, with l the characteristic length of the forcing. The dot-dashed line shows the linear scaling expected for diffusive processes, whereas the dashed line shows the quadratic behaviors expected for Ballistic transport.

However, from figure 7.2 a–b, one can expect that the flow generated by the regular array implies a better mixing of the trajectories of the particles. In order to get a quantitative check of this, we pixelate the cell in N_p squares and we compute the number of particles, n_i that can be found in each cell, i, during the experimental run and we divide it by the mean density. Then we use the usual tools to quantify the mixing : the variance of the relative density $\sigma(\rho_i)^2 = \langle \rho_i^2 - \langle \rho_i \rangle^2 \rangle$ with $\rho_i = (n_i/v_i) \cdot (V/N)$ the relative density in each cell. The smallest is $\sigma(\rho_i)^2$, the best is the mixing. Others tools to quantify a mixing, are the relative Rényi entropies [29]:

$$S_\alpha = \frac{1}{1-\alpha} \log \left(\sum_{i=1}^{N_p} \rho_i^\alpha \right),$$

ranging from 0 to 1. It reaches the limit $S_\alpha = 1$ for the perfectly homogeneous mixing. $\alpha = 1$ corresponds to the usual Shannon entropy, whereas S_2 is called the correlation entropy, and higher values of α give more importance to higher fluctuations [29].

The upper curve of figure 7.8 shows the concentration variance difference between the random array and the regular array , $\Delta\sigma(\rho_i)^2 = \sigma_{rg}(\rho_i)^2 - \sigma_{rd}(\rho_i)^2$, at various driving current intensities. The bottom curves show the Rényi entropies differences between both arrays at five successive values of α. These quantities are estimated during the 60 s of statistically stationary regimes of the experiment. It appears clearly that, above 200 A, the mixing is equivalent for both magnet arrays. Below 200 A, there is a discrepancy. It shows that the regular array performs a better mixing. This discrepancy is more important for higher values of α. It underlines that the difference is increased when the higher fluctuations of the concentration are concerned. It should be recalled that a transition around 200 A has been already observed in the kinetic energy of the particles driven by the random magnet array. Instead of the study of the mixing properties for a fixed duration, the same quantity can be estimated for a fixed average displacement. As we showed that the displacement is mainly ballistic and proportional to the RMS velocity, thus we have to estimate the mixing during a time $T(I) = T_o \cdot (\sqrt{\langle V(I_o)^2\rangle}/\sqrt{\langle V(I)^2\rangle})$, where T_o and I_o are respectively the duration and the intensity of the slowest experiment ($I_o = 25$ A). This procedure brings to the same conclusions although

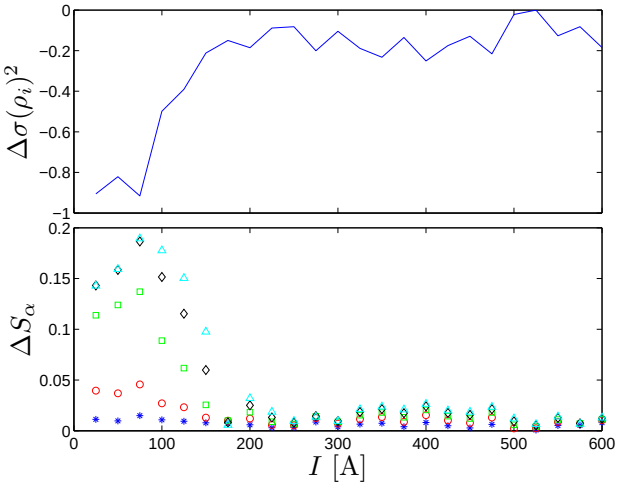

Figure 7.8: Mixing properties of both magnet arrays as a function of the applied driving currents for experimental runs of 60. **Top:** Difference between the particles concentration variance of the regular magnet array and the random magnet array as a function of the applied driving current. **Bottom:** The difference between the Rényi entropies, ΔS_α, of the regular magnet array and the random magnet array as a function of the applied driving current, with $\alpha = 1$, $*$; $\alpha = 2$, $\circ$;$\alpha = 3$, $\square$ $\alpha = 4$, $\diamond$; $\alpha = 5$, $\triangle$.

the curves of $\Delta\sigma(\rho_i)^2$, and ΔS_α (not shown) are more noisy.

7.4.2 Clustering

In the previous sections, the averaged behaviors of the particles are concerned. We are now going to focus on the instantaneous spatial distribution of the floaters. To do so, we borrow a tool usually used to study granular packing [30; 31], and successfully introduced to track cluster of inertial particles in fully developed 3D turbulence [6]. In order to quantify the floaters density at the surface, we use the area of the Delaunay triangles linking three nearest neighbors. Such triangulations are shown in figure 7.9, for a uniform distribution of 254 points (top) and for the same number of particles tracked on a snapshot of our experiment (bottom). In solid state physic and granular matter these tessellations of the surface are used to study amorphous states. In the case of a random set of point, the tessellation gives a gamma distribution $P(\mathcal{A})$ for the elementary triangles area, $\mathcal{A}$ [31] with:

$$P(\mathcal{A}) = \frac{b^a}{\Gamma(a)}\mathcal{A}^{a-1}\exp(-b\mathcal{A}), \qquad (7.3)$$

where $a = \langle\mathcal{A}\rangle^2/\sigma(\mathcal{A})^2$ and $b = \langle\mathcal{A}\rangle/\sigma(\mathcal{A})2$. For uncorrelated points uniformly distributed with a Gaussian distribution for $\mathbf{s_1} = (\mathbf{r_1}-\mathbf{r_2})/\sqrt{2}$ and $\mathbf{s_2} = (2\mathbf{r_3}-\mathbf{r_1}-\mathbf{r_2})/\sqrt{3}$, where vectors $\mathbf{r_1}$, $\mathbf{r_2}$, $\mathbf{r_3}$ define the triangle position, one expects an exponential distribution with $a = 1$ and $b = 1/\langle\mathcal{A}\rangle$ [32]. This is indeed the case to figure 7.9–a, excepting small deviations due to constraints imposed by the cell boundaries. This uniform distribution will be used as the reference state hereafter. All excess of a small area of this reference, can be considered as a trace of clusters of correlated particles. More precisely, an exponent $a < 1$ will be the signature of this excess of small areas, since this induces a negative power near 0 and a vanishing most probable value, whereas b will characterize the exponential cut–off.

We study the areas obtained for each snapshot of the experiment. As the number of followed particles and Delaunay triangles can change slightly from time to time, we normalized the area of each triangle, $\mathcal{A}_i$ by the mean area of triangles at each instantaneous tessellation: $A_i = \mathcal{A}_i \cdot L_x \cdot L_y/N_t$ where N_t is the number of triangles of the instantaneous tessellation. Hence $\langle A\rangle$=1. Figure 7.10 shows the Probability Density function (PDF) of these normalized areas obtained from 3000 successive snapshots of an experiment performed with the random array and with a driving intensity of I =300 A (blue crosses). It shows also the PDF of 3000 realizations of independent successive synthetic tessellations for sets of nearly 200 particles uniformly distributed. For both magnet array and all applied currents, the distribution of triangles areas follows perfectly a Gamma distribution (without any fitting parameters once mean and standard deviation are given). Notice that, if in the case of the synthetic uniform distribution one gets a and b close to one (within 20% of error due to cell boundary), in the case of the experimental PDF one gets $a = 0.311$. This value, smaller than one, is responsible of the cusp observed near 0. Smaller is a, the stronger is this cusp, i.e larger is the excess of small area. Thus a is indeed a signature of the clustering.

Figure 7.11 shows the value of a as a function of the driving current I for both magnet arrays. In both cases, excepted for the smallest intensity, one gets a decay with $0.24 < a < 0.5$. There is therefore always a strong clustering. In the case of the regular array, the decay is almost linear and a goes form 0.5 to 0.35. For the random array we can observe, here again, different behaviors below

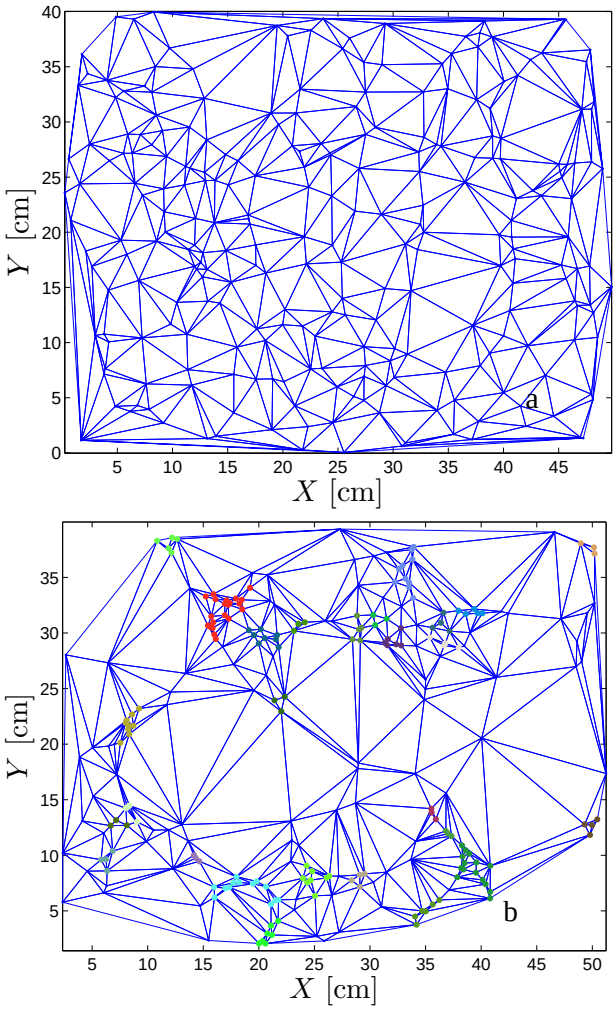

Figure 7.9: A snapshot of the position of 254 particles and the corresponding Delaunay tessellation, for particles uniformly distributed (a) and for an instantaneous measurement in the experiment with the random array for $I = 300$ A (b). In this last case, color marked points correspond to particles found in different clusters

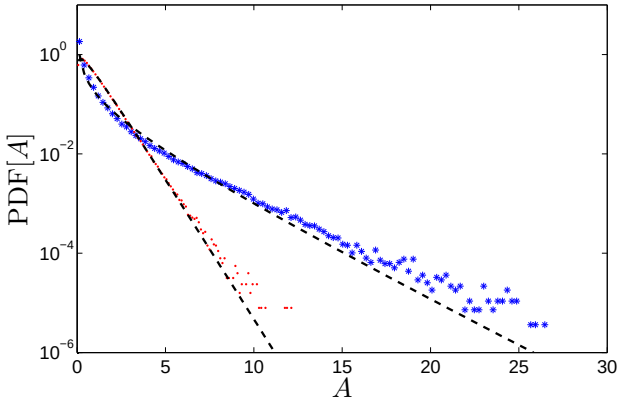

Figure 7.10: Probability Density Function of the normalized Delaunay triangle area obtained experimentally (blue crosses) and constructed from an uniform distribution of points (red dots). Dashed lines correspond to the Gamma distribution of same average and standard deviation.

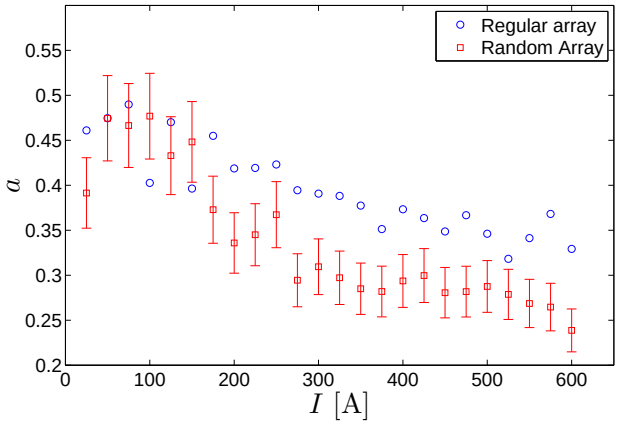

Figure 7.11: The values of the exponent a extracted from the fit of the PDF of the Delaunay triangles area, for both magnet arrays as a function of the driving current. Error bars are estimated from the level of accuracy of the fit of the experimental PDF by a Gamma distribution.

and above 200 A. Below 200 A, the decay of a, going form 0.5 to 0.35 in 150 A, is faster than for the regular array. Above 200 A, the decay rate becomes of the same order for both magnet arrays.

As the areas of the tessellation follow a Gamma distribution (7.3) for a set of points uniformly distributed (our reference) as well as for the experimental observation, one can easily find a criterion to define particles inside a cluster. We consider that a particle is in a cluster if it belongs to a triangle with an area A smaller than a critical value A_c. A_c is chosen such that $P_e(A \leq A_c) \geq P_r(A \leq A_c)$, where the indices r and e refer to the synthetic reference distribution and experimental distribution respectively. Using (7.3) and neglecting the exponential decay at large A one get:

$$A_c = \left(\frac{b_r^{a_r} \cdot \Gamma(a_e)}{b_e^{a_e} \cdot \Gamma(a_r)} \right)^{\frac{1}{a_e - a_r}} \tag{7.4}$$

(with a_r and b_r close but not exactly equal to 1). This criterion has been used to define the cluster shown in figure 7.9 for which $A_c = 0.14$.

We have now the tools to study clusters properties. We first checked the statistics of the number of particles per cluster, N_c, for the regular and random magnets arrays. For both magnets configurations, the PDF are identical and are compatible with a power law with an exponent near

2.5. However, this value is sensitive to the choice of the threshold value of the area defining the clusters. For an onset smaller than A_c, the cutoff cancels the power law. For an onset larger than A_c, huge clusters containing almost all the detected particles imply a bottleneck effect that pollutes the power law. Finally the relation between this exponent and the spatial intermittency is still an open question.

Knowing which particles belong to a cluster,we can compare the velocity fluctuations inside clusters with the unconditional global fluctuations. The top panel of figure 7.12, exhibits the PDF of the fluctuations of one component of the velocity of particles belonging to a cluster $\delta v_y = v_y - V_{cy}$ around the mean velocity, $\mathbf{V_c}$, of the cluster. These fluctuations are compared to the unconditioned case corresponding to the fluctuations V_y of all the particles in the cell. The conditioned PDF is narrower and its shape, with exponential tails, differs from the unconditioned one which is nearly Gaussian. The flatness

$$\langle(\delta v_y - \langle\delta v_y\rangle)^4\rangle/\sigma(\delta v_y)^4$$

of the fluctuations around the cluster velocity, is equal to 5.1 whereas the flatness of V_{cy} is 3.2 i.e. close to the value expected for Gaussian variables. These discrepancies imply a correlation between the velocity of a particle and the fact that it belongs to a cluster. The same ascertainment can be obtained from the other velocity component. One can also look for correlation in the direction of displacement by defining θ_c like the direction of the velocity compared to the one of the cluster. θ_c can be compared with θ the angle with a fixed arbitrary direction in the unconditioned case. The distribution of θ_c is narrower than the unconditioned one, θ (which is almost uniformly distributed) as shown in the bottom of the figure 7.12. Both results mean that, as expected, the motions inside the clusters are much more coherent that the unconditioned global ones, strengthening our definition of clusters.

Finally we can check how the coherence is conserved when the forcing is increased. Figure 7.13 shows the ratio between the standard deviation of conditional velocities and of angles belonging to clusters and the unconditional ones, for different intensity and both magnet arrays. The velocity fluctuation ratio is slightly higher in the regular array whereas the angle fluctuations are of the same order for both magnet arrays. Despite the noise, fluctuations seem to increase with the driving for the regular array whereas a transition between a decreasing and an almost constant behavior can be observed around 200 A for the random magnet array here again.

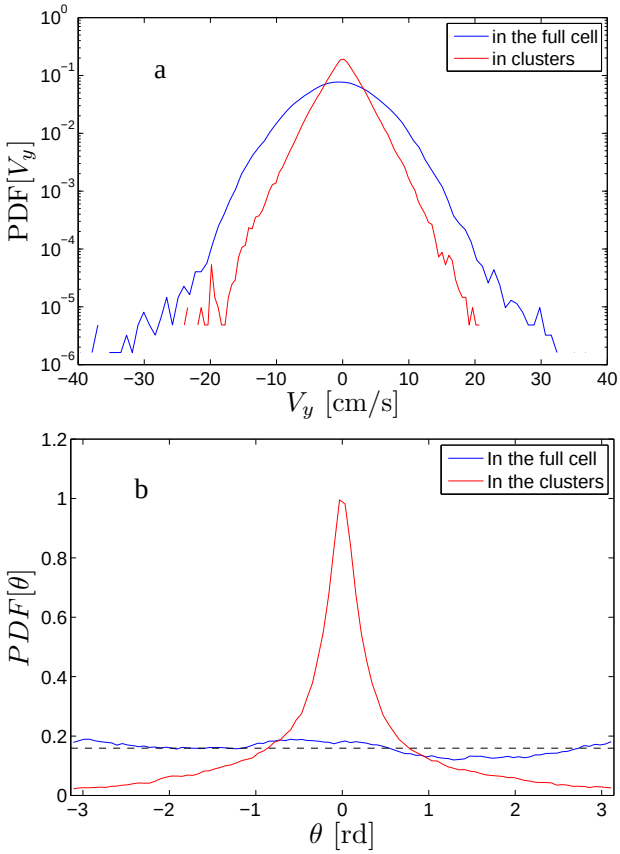

Figure 7.12: Statistics of the clusters dynamics. **Top** PDF of the fluctuations around the mean velocity of a cluster for the y–component of the velocity of particles belonging to the cluster (red) compared to the unconditional fluctuations (blue). **Bottom** Angle distribution of the direction of the particles displacements, belonging to a cluster, around the direction of the cluster (red). It is compared to the unconditioned distribution of direction (blue) and a uniform distribution of angles (dashed line).

7.5 Discussion

Before discussing possible mechanisms of clustering, let us summarize some of our experimental results. Using a liquid metal and an electromagnetic forcing, we are able to generate strongly fluctuating free surface flows. We used two kinds of magnet arrays. The first is made of regular strips of alternative polarities. The second is made with magnets put randomly. We apply to them an elec-

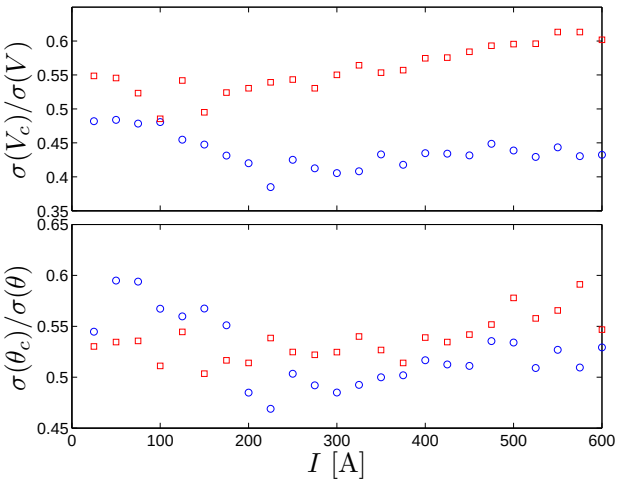

Figure 7.13: Relative fluctuation of velocity (top) and direction (bottom) for both magnet arrays versus the applied driving current.

trical current I going from 25 A to 600 A. Both magnet arrays have different level of fluctuations, i.e. the level of energy contained in the temporal fluctuations compared to the energy in the generated mean flow, is twice higher for the regular array. Equally, the surface deformation induced by the flow above the random array, has a larger stationary part. The stationary part induces long range correlations. The characteristic correlation length does not vary strongly with the forcing especially above 200 A. No transition emerges from the flow produced by the regular array, whereas the flow produced by the random magnet array presents several clues of a transition around 200 A. Indeed, kinetic energy of particles, characteristic correlation time, mixing properties or the ability to form clusters, behave differently below and above 200 A. Above this value, both magnet arrays seem to adopt similar behavior, except that the random array generates a more stationary flow. In any case, floaters do not mix uniformly but tend to form clusters that can be identified by the study of the distribution of the Delaunay triangles areas. The statistics of the area of the triangle linking neighbor particles, follow Γ–distributions. These distributions are singular near 0, illustrating the tendency to form clusters. Particles belonging to a same cluster have a coherent displacement.

Now, we try to explore the origin of the clustering. Several mechanisms can be identified. The first is related to the specificity of the surface flow where the particles are constrained to move. These flows are not purely 2D and a floater at the surface is subjected to a compressible 2D flow where

$$\partial_x u(x,y)|_{z=h(t)} + \partial_y v(x,y)|_{z=h(t)} = -\partial_z w(x,y)|_{z=h(t)}.$$

To quantify this compressibility, it has been introduced a criterion using the Eulerian velocity field:

$$\mathcal{C} = \langle(\partial_x u + \partial_y v)^2\rangle / \left(2\langle(\partial_x u - \partial_y v)^2\rangle\right)$$

with $\mathcal{C} = 1/2$ for an incompressible 2D flows [7].

The second mechanism is induced by the finite size of the floaters. Therefore, they can experience inertial effects. Inertial particles in 3D turbulent flow are known to form clusters. Indeed, in first approximation, the velocity $\mathbf{V}$ of the particles is not divergence free either. By using a first order expansion in terms of the Stokes time, $\tau_s = 2a^2(\rho_p - \rho_f)/(9\nu\rho_f)$, one gets for particles of density ρ_p immerged in a fluid of density ρ_f and of viscosity ν [6; 33]:

$$\nabla \cdot \mathbf{V} \sim -\tau_s \nabla \cdot (\mathbf{u} \cdot \nabla \mathbf{u}).$$

Although the effective mass of floating body is not easy to determine because it depends on the immersed portion of the body, on the wetting angle. One can try to estimate inertial effects by computing $\nabla \cdot (\mathbf{u} \cdot \nabla \mathbf{u})$.

The third mechanism is due to capillarity. Our particles are smaller than the capillarity length l_c, and thus, they are sensitive to the surface tension. Capillarity tends to make attractive particles of similar wetting. However, the attractive capillarity force between particles decays exponentially with the distance [10], and thus, they are significant on characteristics length of order of l_c. Therefore, this interaction length is an order of magnitude smaller than the mean free path between floaters. Hence, due to the low particle concentration, we expect that capillarity will be initially inefficient to agglomerate floaters. However, once the clusters are formed, the attraction could play a stabilizing role and it could affect the cluster cohesion. Capillarity force makes also particles sensitive to the surface curvature. In our experiment, the surface is far from being flat, since the standard deviation of the surface deformation can reach 20% of the layer depth of liquid metal. Although the characteristic radius of curvature of the surface deformation is much higher than l_c, it can tend to move and to concentrate particles by capillary effect. This was reported as the Cheerios effect [10; 8]. Considering this capillarity effect combined with Stokes drift, clustering

has been observed in a Faraday wave experiment and in surface wave turbulence [19; 34]. However, in our device, surface deformation is mainly associated with vertical vortices. The motion of a particle subject to centrifugal forces, to gravity and to surface tension acting on a curved surface is a subject of studies by itself. However, with non-wetting particles lighter than the fluid, as our floaters, a simple force balance tends to exhibit a net force pointing to the center of the vortex. In contrast, in our experiment, we observed that the particles are repelled from vortex cores, as shown below. Hence, we assume that the capillarity forces are not at the origin of the cluster formation, although it could contribute to the cluster cohesion.

In order to estimate the first effect, we have to evaluate $-\partial_z w(x,y)|_{z=h(t)}$ for our surface flow. Therefore, we need to know the Eulerian velocity field at the surface. In order to have only few collisions and small interactions between floaters, and to be able to track particles without a high speed camera, we choose to have large mean free path between floaters and thus a relatively small number of particles Therefore, we are not able to get the instantaneous Eulerian field with a good spatial resolution. However, as shown figure 7.2–d, the time averaged mean flow reproduced with 80 % of accurate the flow when we use the random array of magnet. Moreover, at high current, both magnet arrays seem to share similar clustering properties. Thus, we compute in a pixilated grid of N_p squares of $5 \times 5\text{mm}^2$,

$$\begin{aligned}\alpha_i = & \quad \partial_z \overline{w_i}(x_i,y_i)|_{z_i=h(t)} \\ = & \quad -\partial_x \overline{u_i}(x_i,y_i)|_{z_i=h(t)} - \partial_y \overline{v_i}(x_i,y_i)|_{z_i=h(t)},\end{aligned}$$

where the subscript i refers to the cell i of the pixilated image. Then, we estimate the correlator, r_α, between this quantity and the normalized time-averaged density $\rho_i = n_i/v_i$ previously introduced with

$$r_\alpha = \langle \Delta\alpha_i \cdot \Delta\rho_i \rangle / (\sigma(\alpha_i) \cdot \sigma(\rho_i)),$$

where the averages $\langle \ \cdot \ \rangle$ are taken on the spatial distribution and where ΔX means $X - \langle X \rangle$. Figure 7.14 shows the spatial distribution of the normalized $\Delta\rho_i/\sigma(\rho_i)$ and $\Delta\alpha_i/\sigma(\alpha_i)$ as well as their product $\Delta\rho_i/\sigma(\rho_i) \cdot \Delta\alpha_i/\sigma(\alpha_i)$ for a driving current of 400 A. Although they are not identical, some similar patterns emerge in both figures 7.14a–b. Moreover, clear patches where both quantities are highly correlated appear in 7.14–c. The global correlator $r_\alpha = 0.35$ is not huge but still significant, considering the noise introduced by the coarse-grained gradient and the decoherence induced by the time averaging.

A crude estimate of the compressibility criterion gives $\mathcal{C} - 1/2 \sim 0.05$, i.e. the surface flow appears nearly incompressible. Hence, it seems relevant to assume in first approximation that the measured time-averaged surface flow $\mathbf{u}$ is a 2D incompressible flow. Thus, one can try to compute the inertia effect by computing $\nabla \cdot \overline{\mathbf{V_i}} \sim -\tau_\mathbf{s}\beta_\mathbf{i}$ with

$$\beta_i = \nabla \cdot (\overline{\mathbf{u_i}} \cdot \nabla \overline{\mathbf{u_i}}).$$

In comparison with figure 7.14 the spatial correlations are less obvious. Indeed, in figure 7.16–bottom the product $\Delta\rho_i/\sigma(\rho_i) \cdot \Delta\beta_i/\sigma(\beta_i)$ is larger than one over 9% of the studied surface only. In contrast, in figure 7.14–bottom the product $\Delta\rho_i/\sigma(\rho_i) \cdot \Delta\alpha_i/\sigma(\alpha_i)$ is larger than one on 19.4 % of the surface of the pixilated image. Therefore, the spatial coherence between α_i and ρ_i is larger than the spatial coherence between β_i and ρ_i. This is confirmed the spatially averaged correlators. In the case of a driving $I = 400$ A one gets $r_\alpha = 0.35$ and $r_\beta = 0.07$. It underlines that the upwelling/downwelling flows have a more significant contribution to clustering than inertial effect.

It has to be noticed that due to the secondary upwelling flow in the vortex core and downwelling flow at the vortex hedge [35], α_i is highly correlated to vorticity as shown figure 7.15. The correlator $r_\Omega = \langle \Delta\Omega_i \cdot \Delta\alpha_i \rangle / (\sigma(\alpha_i) \cdot \sigma(\Omega_i))$ is equal to 0.83, where $\Omega_i = (\partial_x v - \partial_y u)_i$ is the vorticity in the cell i. Thus Ω_i is also correlated with the density ρ_i although the correlator is slightly smaller and negative (-0.30 compared to $r_\alpha = 0.35$). Moreover, one expects that inertia drives particles lighter than the fluid to the center of the vortex by centrifugal effect, which is the opposite of what we observe. In shallow water limit, the secondary vertical flow is assumed to be smaller than the horizontal one, since one expects $\langle w \rangle \propto (h/R)^3 \langle \mathbf{u_h} \rangle$ [36], with w the vertical velocity components (near the vortex core), $\mathbf{u_h}$ the horizontal velocity field, h the fluid layer and $R \sim 2\lambda_c \sim 5h$ is the characteristic radius of the vortex. However, in our cases where (h/R) is about 1/3, it seems that the downwelling flow, at the vortex edge, acts as a particle attractor whereas the vortex core, acts as a Repeller. Moreover as the stretching is large at the vortex edge, particles cluster in elongated structures where they have coherent velocities and directions of displacement.

To summarize this part, we used the station-

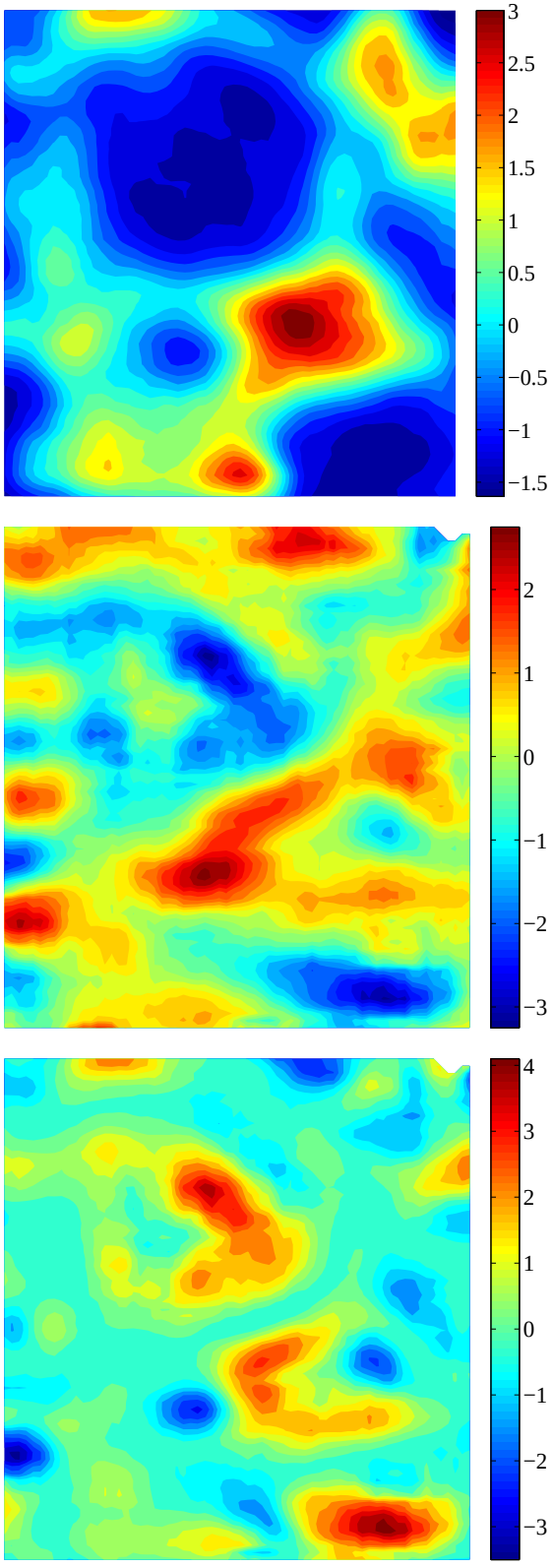

Figure 7.14: Spatial repartition of the normalized density $\Delta\rho_i/\sigma(\rho_i)$ (top), $\Delta\alpha_i/\sigma(\alpha_i)$ (middle) and the product $\Delta\rho_i \cdot \Delta\alpha_i/(\sigma(\rho_i)\sigma(\alpha_i))$ for a driving current $I = 400$ and the random array.

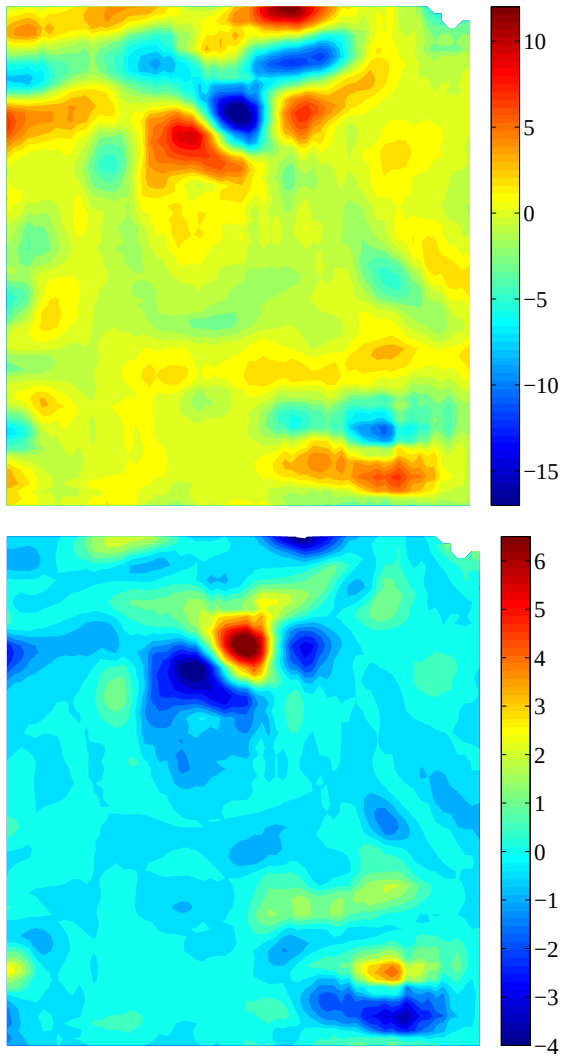

Figure 7.15: Spatial repatition of $\Delta\beta_i/\sigma(\beta_i)$ (top) and the product $\Delta\rho_i \cdot \Delta\beta_i/(\sigma(\rho_i)\sigma(\beta_i))$ for a driving current $I = 400$.

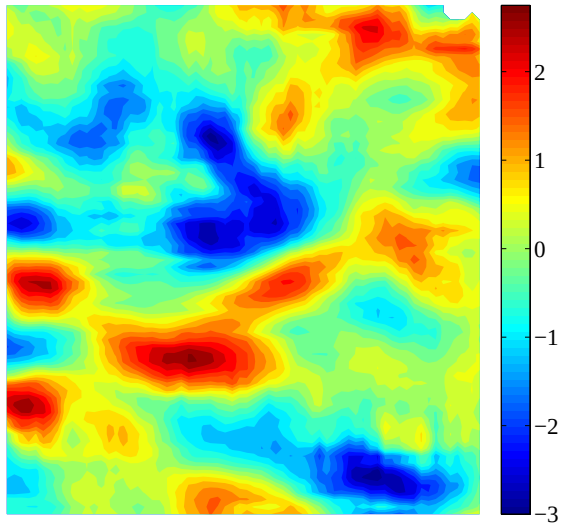

Figure 7.16: Spatial repatition of $\Delta\Omega_i/\sigma(\Omega_i)$ for a driving current $I = 400$.

arity property of the random array to explore the clustering mechanism. To do so, we check the local and global correlation between the spatial distributions of the particle averaged in time, with (i) the compressible part of the time-averaged surface flow, (ii) the inertia effects and (iii) the vorticity. Our analysis shows that the particles concentrate along the compressi downwelling part of the flow. The downwelling and upwelling parts of the flow are highly correlated to the vorticity. Thus, the vorticity is correlated with the particle density distribution as well. However vorticity and inertia should have the tendency to concentrate light floaters near the vortex core, in contrast to our observatiosn. This is the major difference between floaters and inertial particles in a 3D flow. However it has to be mentioned that the action of the upper fluid is still unknown. Some experiments are planned in a device devoted to this study.

The last issue is how spatial inhomogeneity of the floaters reflects the intermittent property of the underlying flow. In Appendix A, we propose an argument sustaining the conjecture of Kraichnan claiming that the passive scalar has to be more intermittent than the underlying flow. The high intermittency of the passive scalar stretched and folded by the velocity gradient is revealed by the anomalous scaling of the structure function of the concentration field [4]. It has been related to the ramp and cliff inhomogeneous structure of the passive scalar density [37]. We do not reach a resolution accurate enough to compute the structure function of the concentration field of floaters in our experiment. However, it has been shown that some properties of turbulent flow, or others complex stretched flows, are enclosed in the time evolution of the shape of triangles in 2D (or tetrads in 3D) delimited by Lagrangian points passively advected by the flow [32; 38; 39]. Therefore a forthcoming work will be devoted to the study of the time evolution of such distorted triangles, delimited by floaters, in order to underline discrepancies with the passive scalar case [32; 39]. Moreover, with the tool introduced to define particles belonging to a cluster, we should be able to study the triangle distortion evolution in relation to the particles ability to enter or escape from the clusters and thus to relate spatial inhomogeneity and intermittent properties.

Appendix: Intermittence of the passive scalar

It was argued in [4] that the concentration field of a passive scalar will be intermittent even if the advective velocity field is not. Here we give an argument sustaining this conjecture using the constraints imposed by the stationarity on the self-correlation function in time of concentration field. We consider a passive scalar θ (like temperature fluctuations, salt or contaminant concentration) transported by a homogeneous and uniform turbulent velocity flow $\mathbf{u}$ at high Reynolds Number, Re. We assume that the velocity field $\mathbf{u}$ follows the K41 scaling theory in the inertial range. Therefore in this intermediate range of scales, the energy flux ϵ through the scales is conserved and the Fourier components of all quantities become independent of the dissipation and injection energy processes; Thus they will depend only on ϵ and on the wave number k . The dimensional analysis implies $\langle \hat{u}_k|^p \rangle \propto (\epsilon/k)^{p/3}$. For a passive scalar in a statistically stationary state one can write

$$\partial_t \theta + u_i \partial_i \theta = S + D \partial_{jj} u_i \qquad (7.5)$$

where S is a large scale source term, compensating the diffusive lost (e.g. a maintained large scale temperature or concentration gradient). For moderately small Schmidt Numbers $Sc = \nu/D$ such that the Péclet number $Pe = Sc \cdot Re$ is large, the passive scalar has to be transported through the inertial range upto the diffusive scale η_D. η_D is defined such that $Pe_{\eta_D} = \delta u_{\eta_D} \eta_D / D$ is nearly 1 with δu_{η_D} a typical velocity increment on the diffusive scale. One can consider the quantities coarse–grained up to a scale $K = 1/l$ in the inertial range by using a low pass filtering on the velocity field. Thus one has the following balance for the coarse–grained field $\mathbf{u}_K$ and θ_K :

$$\partial_t \langle \theta_K^2/2 \rangle = P_o + \Pi_K \qquad (7.6)$$

where P_o is a large scale injection term, independent of K and Π_K is the concentration flux through the scale $K = 1/l$ in the inertial range. It is assumed to be independent of the large scale L and the small scale η_D. Stationarity imposes that in $\overline{P_o} = \overline{\Pi_K}$ and the dimensional analysis imposes the only time scale $(1/K\hat{u}_K)$ in the inertial range. It implies : $\langle |\hat{\theta}_K^2| \rangle \propto P_o/(K\hat{u}_K) \propto P_o K^{-2/3}/\epsilon^{1/3}$. Hence the usual non-intermittent scaling will be :

$$\langle |\hat{\theta}_K^{2p}| \rangle \propto P_o^p K^{-2p/3}/\epsilon^{p/3}. \qquad (7.7)$$

However stationarity does not only impose the equality between the time average of I_o and Π_K but also the equality of the time integral of their self-correlation function as demonstrated in [40]. Applying the previous dimensional analysis to the equality

$$\begin{aligned}\tau_{P_o}\sigma(P_o)^2 &= \int_0^\infty \overline{\Delta P_o(t)\cdot\Delta P_o(t+\tau)}d\tau \\ &= \int_0^\infty \overline{\Delta\Pi_K(t)\cdot\Delta\Pi_K(t+\tau)}d\tau \\ &= \tau_{\Pi_K}\sigma(\Pi_K)^2 \qquad (7.8)\end{aligned}$$

with $\Delta X = X - \langle X\rangle$ and where we define the correlation time of the variable X as: $\tau_X = 1/\sigma(X)^2 \int_0^\infty \overline{\Delta X(t)\cdot\Delta X(t+\tau)}d\tau$. The lhs of (7.8) does not depend on the scale K whereas the dependence in K of rhs, can be estimated using dimensional analysis. Thus one gets $\langle|\hat{\theta}_K^4|\rangle \cdot K\hat{u}_K \propto \sigma(P_o)^2\tau_{I_o}$, hence

$$\langle|\hat{\theta}_K^4|\rangle \propto \sigma(P_o)^2\tau_{P_o}K^{-2/3}/\epsilon^{1/3}.$$

This result is far from the expected scaling (7.7) although the velocity follows a normal scaling. Parts of the scaling hypothesis have to be released in order to agree with observations. Moreover such kind of constrains could explain the saturation of the structure function exponents of the passive scalar, noticed in the no-intermittent inverse cascade regime of the 2D turbulence [37] or compressible flows [41].

Acknowledgments

We would like to thank V. Padilla for building of the setup, C. Wiertel–Gasquet for helping at the automation of the experiment, Raphael Candelier for performing the algorithm used to define clusters, F. Daviaud, M. Bonetti and G. Zalczer for helpful discussions. We are indebted to Aurelie Heyries and Daphne Heyries for their works on the first stage of the experiment.This work is supported by the ANR Turbulon. PG received also the support from the triangle de la physique and CONICYT.

7.6 Bibliography

[1] P. G. Ryan, C. L. Moloney, Nature **361** 23 (1993)

[2] http://en.wikipedia.org/wiki/Marine_debris

[3] K. Herterich and K. Hasselmann, J. Phys. Oceanogr. **12** (1982) pp704.

[4] R.H. Kraichnan, Phys. Rev. Lett. **72**, 1016 (1994)

[5] E. Balkovsky, G. Falkovich, A. Fouxon, Phys. Rev. Lett. **86**–13, 2790 (2001)

[6] R. Monchaux, M. Bourgoin, A. Cartellier Phys. Fluids **22**, 103304 (2010)

[7] Cressman, J. R., Davoudi, J., Goldburg, W. I., and J. Schumacher, J.: Eulerian and Lagrangian studies in surface flow turbulence. *New J. Phys.* **6**, 53, 2004.

[8] Dalbe, M. J., Cosic, D., Berhanu, M. and Kudrolli, A.: Aggregation of frictional particles due to capillary attraction. *Phys. Rev. E* **83**, 051403, 2011.

[9] P. Denissenko, G. Falkovich, S. Lukaschuk Phys. Rev. Lett.**97**, 244501 (2006)

[10] Vella, D. and Mahadevan, L.: The cheerios effect. *Am. J. Phys* **73** 817, 2005.

[11] N.F. Bondarenko, M.Z. Gak, F.V. Dolzhanskiy, Izvestiya Atmospheric and Oceanic physics, **10**, 711 (1979)

[12] Sommeria, J.: Experimental study of the two–dimentional inverse energy cascade in a square box. *J. Fluid Mech.* **170**: 139–168, 1986.

[13] Tabeling, P., Burkhart, S., Cardoso, O. and Willaime, H.: Experimental Study of Freely Decaying Two–Dimensional Turbulence. *Phys. Rev. Lett.* **67**: 3772–3775, 1991.

[14] P. Tabeling, B. Perrin, S. Fauve, Europhys. Lett. **3** –4, 459-465 (1987)

[15] T. Dauxois, Phys. Fluids **6**, 1625 (1994);

[16] G.A. Voth, G. Haller, J. P. Gollub, Phys. Rev. Lett. **88**, 254501 (2002)

[17] From the safety datasheet acc, Guideline 93/112/EC of Germatherm Medical AG, the galinstan is made of 68.5 % of Gallium, 21.5 % of indium, 10 % of Tin. Its density is $\rho = 6.440\times10^3$ kg/m^3, its kinematic viscosity is $\nu = 3.73\times10^{-7}$ m^2/s, its electrical conductivity $\sigma = 3.46\times10^6$ (S/m)

[18] Savelsberg, R., van de Water, W.: Experiments on free-surface turbulence. *J. Fluid Mech.* **619**: 95, 2009.

[19] Falkovich, G., Weinberg, A., Denissenko, P. and Lukaschuk, S.: Floater clustering in a standing wave. *Nature (London)* **435**, 1045, 2005 (see in particular the supplementary material); Denissenko, P., Falkovich, G. and Lukaschuk, S.: How waves affect the distribution of particles that float on a liquid surface. *Phys. Rev. Lett.* **97**, 244501, 2006; Lukaschuk, S., Denissenko, P. and Falkovich, G.: Clustering of Floating particles by surface waves. *J. Low Temp. Phys.* **145**, 297, 2006; Lukaschuk, S., Denissenko, P. and Falkovich, G.: Nodal patterns of floaters in surface waves. *Eur. Phys. J. Special Topics* **145**, 125, 2007.

[20] Marteau, D., Cardoso, O. and Tabeling, P.: Equilibrium states of two–dimensional turbulence: An experimental study. *Phys. Rev. E* **51**: 5124–5127, 1995.

[21] Williams, B. S., Marteau, D. and Gollub, J. P.: Mixing of a passive scalar in magnetically forced two-dimensional turbulence. *Phys. Fluids* **9**: 2061–2080, 1997.

[22] Ouellette, N. T. and Gollub, J. P.: Dynamic topology in spatiotemporal chaos. *Phys. Fluids* **20**: 064104, 2008.

[23] Liao, Y., Kelley, D. H. and Ouellette, N. T.: Effects of forcing geometry on two–dimensional weak turbulence. *Phys. Rev. E* **86**: 036306, 2012.

[24] J. Boisson, A. Klochko, F. Daviaud, S. Aumaître, Phys. Fluid **24**–4, 044101 (2012)

[25] Y.K. Tsang, W.R. Young, Phys. Rev. E **79**–4, 045308 (2009)

[26] Ouellette, N. T.: Programs available on `http://leviathan.eng.yale.edu/software_tracking.html`.

[27] Ouellette, N. T., Xu, H. and Bodenschatz, E.: A quantitative study of three-dimensional Lagrangian particle tracking algorithms. *Exps. Fluids.* **40** 301, 2006.

[28] E. Falcon, C. Laroche, S. Fauve, Phys. Rev. Lett. **89**–20, 204501 (2002)

[29] E. Gouillard, PhD thesis :*Etude de l'advection chaotique dans des mélangeurs à tiges, en écoulements ouverts et fermés*, tel-00204109, (2008)

[30] D. Bonamy, F. Daviaud, L. Laurent, M. Bonetti, and J. P. Bouchaud, Phys. Rev. Lett. **89**, 034301 (2002)

[31] T. Aste, T. Di Matteo, Phys. Rev. E **77**–2, 021309 (2008)

[32] P. Castiglione and A. Pumir, Phys. Rev. E **64** 056303 (2001)

[33] M. Maxey and J. Riley, Phys. Fluids **26** , 883 (1983) .

[34] E. Shröder, J.S. Andersen, M.T. Levinsen, P. Alstrom, W.I. Goldburg, Phys. Rev. Lett. **76**–25, 4717 (1996)

[35] L.P.J. Kamp, Phys. Fluids **24** 023601 (2013)

[36] Notice that this sacling can explain why at the same energy input, the random array that anchors larger strucutre R has faster two dimensional surface flow with less hight fluctuations. Indeed since the ratio w/u_h will be smaller for the random array, it will be more 2 dimensionnal.

[37] A. Celani, A. Lamotte, A. Mazzino and M. Vergassola, Phys. Rev. Lett **84**–11 (2000) pp 2385

[38] A. Pumir, B.I.Shairman, M. Chertkov, Phys. Rev. Lett. **85**–25 (2000) pp5424

[39] S.T. Merrifield D.H. Kelley, N.T. Ouellette , Phys. Rev. Lett **104** 254501 (2010)

[40] J. Farago, J. Stat. Phys. **118** (2004) pp 373

[41] J. Bec, K. Gaweędzhi P. Horvai, Phys. Rev. Lett. 92–22 224501 (2004)

Chapter 8

Conclusions and Perspectives

8.1 Summary and Conclusions

During this thesis several results were presented, and they can be summarized in four main parts:

1) We characterized a turbulent flow produced with a MHD forcing.

   By imposing simultaneously a homogeneous horizontal electrical current and a heterogeneous vertical magnetic field, we generate fluid motion in a thin layer of conducting fluid. The signature of the forcing geometry (as defined by the magnetic field) rules fundamental characteristics of the resulting flows. Therefore, we are capable to create two very different flows. (i) A flow in which the velocity field present a much larger time averaged component than its temporal fluctuations. As the flow show a coherent large scale structure, surface deformations have a time averaged component of the same order as fluctuations about the mean profile. (ii) Another flow where fluctuating components concentrate most of the flow energy: temporal fluctuations of velocity are larger than time averaged velocity and the equivalent relation is also valid for the surface deformation.

   For the two flows, there is an increase both on velocity and in the amplitude of surface deformation, despite the discussed differences. Horizontal velocities are much larger than vertical ones, thus the flow can be considered as primarily two-dimensional.

2) We considered the influence of turbulence on surface deformation:

   We studied the surface deformation generated by a primarily horizontal turbulent flow. At gentle forcing (with imposed electrical current from 50 A to around 200 A) we clearly distinguished coherent vortices: (i) qualitatively from temporal and spatiotemporal traces of surface deformation, and (ii) in statistical terms, as they introduce an asymmetry through values below the mean surface level, as a consequence of their characteristic shape.

   For stronger forcing, there are some indications of the existence of –spontaneously generated– waves in our experiment: the observation of an asymmetry to values larger than the most probable value in local measurements; and indications of a small part of the energy concentrated around the dispersion relation of waves. At this stage, we can –weakly– conclude that waves are spontaneously generated in our experiment. However, more experiments

should be carried out –in order to make statistics more reliable– and further data analysis should be performed in order to quantify wave contributions in our measured fields.

3) We considered the influence of turbulence on wave propagation:

   By analyzing the height fluctuations under different conditions –specifically, by varying the intensity of the MHD forcing and the frequency of an externally excited wave– we observed the enhancement of wave dissipation by turbulence.

   We performed two complementary analyses: one based on the spectral signature of the excited wave, or f_0–peak in the frequency spectrum; and a second analysis that consist in computing coherent averages of the spatiotemporal evolution of η, from which the variance can be linked to an attenuation coefficient. As we increase the intensity of the forcing –implying stronger turbulent fluctuations–, the analysis of the f_0–peak, reveals the decrease of its amplitude, accompanied by its widening. A transfer of the wave energy into turbulent fluctuations of close scales may explain the simultaneous decrease and widening of the peak. This enhancement of wave dissipation by turbulence is confirmed by the analysis of the coherent average. Both analyses shown a non trivial dependency of dissipation on the frequency of the excited wave: waves of higher frequency are more efficiently attenuated by turbulence.

4) We considered the influence of turbulence on floating particles:

   When particles float a the surface of a flow, they are subjected to a specific constrains: first they have to stay at the surface; then they experience the action of surface tension and of other surface motions. Therefore, floating particles experience an effective compressibility. As a consequence, we observe the phenomenon of preferential concentration of floating particles. We first develop statistical tools that allows us to identify clustering of particles. As expected, we observe strong velocity and angular correlations between particles belonging to a cluster. Then, we constructed suitable quantities to rely flow characteristics to the cumulated concentration of particles. As we found that upward-downward flow present larger correlations than particles' inertia or surface deformation, we propose it as the responsible mechanism for preferential concentration of particles.

8.2 Perspectives

We can mention some *short term perspectives*, as they are a natural continuation of the presented works.

Concerning the dynamics of particles, we focused on the statistics of clusters by taking each time as independent. Thus, a natural perspective of our work is to extend the analysis to the temporal evolution of clusters. In particular, the evolution of the area defined by three particles can be contrasted with prediction stated for two dimensional flows.

We observed that several processes are involved in the evolution –and clustering– of floating particles, from which turbulent motion is perhaps the most complex. Thus, we started simpler experiments excluding turbulence: we put particles in a parabolic fluid surface, as obtained when a cylindrical contained is subjected to rotation about its vertical axis. We observe slow non-trivial motions as a consequence of surface tension and particle's inertia. This preliminary experiments are still to be understood, and then, the interaction of several particles under these conditions will be considered.

We presented an scenario where upward-downward flows are responsible both from preferential concentration of particles and from their tendency to go outside vortices cores. However,

an alternative scenario could be the one where particle dynamics is ruled by the acid instead of liquid metal (because particles are heavier than the acid). This scenario must be tested. This is difficult to do in the presented experiment, thus, it will be necessary to make a complementary one, on the spirit of the one mentioned in the previous paragraph.

Concerning surface deformation, it is necessary to improve the statistics obtained, in particular to understand the observed differences between local and space-resolved measurements. It is also relevant to develop more delicate analysis of the spatiotemporal measurements of surface deformation, in order to distinguish potential from rotational contributions and clarify the existence of waves.

As *longer term perspectives*, there are different directions that could be followed:

During this thesis, we emphasized the richness of the MHD forcing to generate a turbulent flow with a free surface. This is an important advantage of working with liquid metals: because the high conductivity of the fluid, the Lorentz forcing is a very effective one. However, despite our efforts, we experienced strong limitations at the moment of performing measurements. Therefore one perspective is to develop an optical method to obtain the full two dimensional surface deformation in reflective surfaces –perhaps by properly correlating stereo images–.

On the other hand, for transparent electrolytes (that reach weaker turbulent regimes), it could be interesting to test the available techniques to measure global surface deformation. In this way, we can also take advantage of standard velocimetry techniques –like Particle Image Velocimetry (PIV)– to go deeper into the spatiotemporal characterization of the flow, and to compute correlations with surface deformation.

We explored in detail two aspects of the wave-turbulence problem: the one of wave generation by a turbulent flow; and the influence of turbulence on wave propagation. There is still many others aspect to be explored in experiments, in particular how the nonlineal interaction of turbulent waves is affected by vorticity. Another, related and interesting problem, not yet explored experimentally to my knowledge, is how a velocity field is affected by a wave that travels on the surface.